Numerical Simulations of Black-Hole Spacetimes

Thesis by

Tony Chu

In Partial Fulfillment of the Requirements

for the Degree of

Doctor of Philosophy

California Institute of Technology

Pasadena, California

2012

(Defended July 8, 2011)

Acknowledgements

This thesis would not have been possible without the wisdom and guidance of many people.

First, I thank my thesis advisor Mark Scheel, for allowing me to take part in the excitement of numerical relativity, and for teaching me valuable lessons along the way. I am indebted to him for his kindness and encouragement throughout my graduate studies. His door was always open, and he was never too busy to entertain my many naive questions and whimsical ideas. Each time I left his office, physics made a lot more sense.

I thank Harald Pfeiffer, who was my mentor when I first came to Caltech and was still clueless about numerical relativity. He had no hesitations in helping me to get started, and was infinitely patient in providing detailed explanations of important concepts, supplemented by his sharp insight. His resourcefulness never ceases to amaze me, and I am truly fortunate to have crossed paths with him.

I thank Rana Adhikari and my formal advisor Yanbei Chen for serving on my candicacy and thesis committees, Lee Lindblom for serving on my candidacy committee, and Christian Ott and Béla Szilágyi for serving on my thesis committee. The time and care they have given me are deeply appreciated. I also thank Kip Thorne, my advisor before his retirement, who nudged me in the direction of numerical relativity upon my arrival at Caltech, and conveyed to me the wonder of gravitation.

I thank my fellow relativity students for brightening and enlightening my days: Kristen Boydstun, Jeffrey Kaplan, Keith D. Matthews, David Nichols, Huan Yang, Fan Zhang, and Aaron Zimmerman. I am especially grateful to my officemates David and Keith for frequent and helpful interactions, and to Keith for being my travel companion to physics conferences. I also thank the many others whose knowledge I have benefited from in the last several years: Michael Boyle, Jeandrew Brink, Alessandra Buonanno, Michael Cohen, Marc Favata, Chad Galley, Tanja Hinderer, Nathan Johnson-McDaniel, Geoffrey Lovelace, Haixing Miao, Samaya Nissanke, Robert Owen, Yi Pan, Christian Reisswig, Ulrich Sperhake, Sherry Suyu, Heywood Tam, Nicholas Taylor, Saul Teukolsky, Anil Zenginoglu, and anyone else I may have inadvertently left out.

I thank Yanbei Chen, Harald Pfeiffer, Mark Scheel, and Kip Thorne for writing recommendation letters for my postdoctoral applications, and JoAnn Boyd for making sure that I did not miss any deadlines. I thank JoAnn Boyd and Shirley Hampton for sorting out all sorts of administrative stuff, so that I never had to worry about them. I also thank Chris Mach for setting up new computers for me, and for fixing them whenever they misbehaved.

I thank Alan Weinstein for having enough faith to admit me into the physics graduate program. I thank the physics department for supporting me as a teaching assistant during my first year at Caltech, and the Brinson Foundation and Sherman Fairchild Foundation for supporting me as a research assistant in subsequent years. I also acknowledge support from NSF grants PHY-0601459, PHY-0652995, and DMS-0553302 and NASA grant NNX09AF97G.

I thank Kenneth Chang and Geoffrey Ho, who are my best friends, comrades, and partners in crime, for the fun-filled times we have had together. They are thoroughly absurd, in the best possible way. I cannot recount all of the numerous occasions on which they have compelled me to burst out in laughter.

And of course, I am eternally thankful for my mother, for giving me a reason to always be able to smile, and for blessing me with more than I deserve. Somehow she has maintained an inexhaustible confidence in me and has supported every one of my endeavors, even when they were far-fetched and she clearly knew so. Among the things I have dreamed of doing, perhaps studying black holes was not so crazy after all.

Abstract

This thesis covers various aspects of the numerical simulation of black-hole spacetimes according to Einstein's general theory of relativity, using the Spectral Einstein Code (`SpEC`) developed by the Caltech-Cornell-CITA collaboration.

The first topic is improvement of binary-black-hole initial data. Chapter 2 is primarily concerned with the construction of binary-black-hole initial data with nearly extremal spins. It is shown that by superposing two Kerr metrics for the conformal metric, the spins remain nearly constant during the initial relaxation in an evolution, even for large spins. Other results include non-unique conformally-flat black hole solutions to the extended-conformal-thin-sandwich equations. Chapter 3 presents work in progress, and builds on the method of the previous chapter to add physically realistic tidal deformations in binary-black-hole initial data, by superposing two tidally deformed black holes to compute the freely specifiable data. The aim of this is to reduce the junk radiation content, and represents a first step in incorporating post-Newtonian results in constraint-satisfying initial data.

The next topic is the evolution of black-hole binaries and the gravitational waves they emit. Chapter 4 presents the first spectral simulation of two inspiralling black holes through merger and ringdown. The black holes are nonspinning and have equal masses. Gravitational waveforms are computed from the simulation, and have the lowest numerical error to date for this configuration. Gauge errors in these waveforms are also estimated. Chapter 5 extends this work to perform the first spectral simulations of two inspiralling black holes with moderate spins and equal masses, including the merger and ringdown. Two configurations are considered, in which both spins are either anti-aligned or aligned with the orbital angular momentum. The high accuracy of the gravitational waveforms for the nonspinning case is found to carry over to these configurations. Chapter 6 uses the waveforms from these simulations to make the first attempt to calibrate waveforms in the effective-one-body model for spinning, non-precessing black-hole binaries.

The final topic is the behavior of quasilocal black-hole horizons in highly dynamical situations. Chapter 7 discusses simulations of a rotating black hole that is distorted by a pulse of ingoing gravitational radiation. For large distortions, multiple marginally outer trapped surfaces appear at a single time, and the world tubes they trace out are all dynamical horizons. The dynamical horizon and angular momentum flux laws are evaluated in this context, and the dynamical horizons are contrasted with the event horizon. The formation of multiple marginally outer trapped surfaces in the Vaidya spacetime is also treated.

Contents

List of Figures

List of Tables

Chapter 1

Introduction

The existence of black holes, regions of spacetime in which gravity is so strong that even light cannot escape from them, is one of the most fascinating predictions of Einstein's general theory of relativity. Far from being of purely mathematical interest, surmounting observational evidence has firmly established their astrophysical relevance [1, 2, 3, 4, 5]. Furthermore, black hole spacetimes provide an ideal setting to understand the dynamics of strong gravity, beyond the realm of small deviations from Newtonian physics.

Despite the beguilingly simple form that the Einstein equations can be cast in,[1]

$$G_{\mu\nu} = 8\pi T_{\mu\nu}, \tag{1.1}$$

where the Einstein tensor $G_{\mu\nu}$ describes the curvature of spacetime and the stress-energy tensor $T_{\mu\nu}$ describes the distribution of matter, they are in fact a complicated set of coupled, nonlinear partial differential equations that can be solved exactly only for solutions that possess a high degree of symmetry. Since nature is rarely so kind, numerical methods are imperative to unlocking the mysteries in gravity's hold. This undertaking is the field of numerical relativity.

Numerical relativity has experienced a tremendous amount of progress in the last few years, largely driven by the exigency to model the merger of two inspiralling black holes. Such an event is expected to generate a burst of energy in the form of gravitational waves, which observatories such as LIGO and VIRGO will detect in the near future [6], thereby

[1] Throughout this thesis, unless otherwise noted, we use geometrized units in which the speed of light $c = 1$ and the gravitational constant $G = 1$. We also use the convention that the spacetime metric signature is $(-+++)$. In this chapter, Greek indices are spacetime indices running from 0 to 3, while Latin indices are spatial indices running from 1 to 3.

ushering in a new era of gravitational wave astronomy. However, the signal due to the black-hole binary's gravitational radiation is extremely weak and buried in a sea of noise. In this regard, accurate gravitational waveforms from numerical simulations are crucial, since they can serve as templates that are then cross-correlated with the detectors' data, enhancing the probability of detection [7].

The numerical simulation of black holes has many elements, such as the construction of astrophysically realistic initial data, a suitable formulation of the Einstein equations to evolve, and the choice of gauge or coordinate conditions to use. Initial data provides the starting point of a black hole evolution, and so must adequately capture the essential features of the physical spacetime. For instance, to model the last several orbits of a black-hole binary, it is desirable for the initial data to possess very low eccentricity, since it is expected that the orbits will have already circularized from the emission of gravitational waves [8]. One should also be able to specify pertinent mass ratios and spins.

There is no unique way to formulate the Einstein evolution equations, and in fact some ways are much more preferable than others. The various formulations such as the Arnowitt-Deser-Misner (ADM) system [9], the Baumgaurte-Shapiro-Shibata-Nakamura (BSSN) system [10, 11], and the generalized harmonic system [12] differ in their definition of dynamical variables, the addition of constraints to the evolution equations, whether equations are first-order or second-order in time, etc. Even though the formulations are equivalent on an analytical level when the constraints are exactly satisfied, their numerical behaviors can be quite different. In particular, small violations of the constraints may grow exponentially when the system is not well-posed, leading to unstable evolutions.

Similarly, there is no unique way to fix the gauge in the Einstein equations. They are freely specifiable, which can be a blessing and a curse. The choice may simply be dictated by convenience. However, for sufficiently complex situations like a binary black hole merger, a suitable choice is not obvious, and one that is poorly motivated can hinder the interpretation of the physics, or cause the simulation to fail altogether.

This thesis covers various aspects of the numerical simulation of black holes, using the Spectral Einstein Code (`SpEC`) developed by the Caltech-Cornell-CITA collaboration [13]. The focus is primarily on black-hole binaries. Chapters 2 and 3 are concerned with improving the construction of binary-black-hole initial data, while chapters 4, 5, and 6 discuss binary-black-hole evolutions and assess the gravitational waveforms calculated from the simulations. Of course numerical relativity is not confined to studying black-hole binaries, but is an indispensable venue for exploring strong gravity in general. As a further application of

numerical relativity, chapter 7 investigates the dynamics of quasilocal black-hole horizons for single strongly distorted, rotating black holes.

1.1 Binary-black-hole initial data

In their usual form, space and time are treated on an equal footing in the Einstein equations. From the perspective of performing a numerical evolution however, it is much more intuitive to make a clear distinction between space and time, and to treat spacetime as a time sequence of spatial hypersurfaces. The usual approach to doing this is to introduce a $3+1$ decomposition of the spacetime metric $g_{\mu\nu}$ [14, 9],

$$
\begin{aligned}
{}^{(4)}ds^2 &= g_{\mu\nu} dx^\mu dx^\nu, && (1.2)\\
&= -N^2 dt^2 + g_{ij} \left(dx^i + \beta^i dt\right) \left(dx^j + \beta^j dt\right), && (1.3)
\end{aligned}
$$

where g_{ij} is the spatial metric of a hypersurface of constant time t, N is the lapse function that measures proper time between neighboring hypersurfaces along their timelike unit normals n^μ, and β^i is the shift vector that determines how coordinate labels move between each hypersurface. Along with the definition of the extrinsic curvature $K_{\mu\nu} = -\frac{1}{2}\mathcal{L}_n g_{\mu\nu}$, the Einstein equations (shown for $T_{\mu\nu} = 0$) split into a set of constraint equations,

$$
\begin{aligned}
R + K^2 - K_{ij} K^{ij} &= 0, && (1.4)\\
\nabla_j \left(K^{ij} - g^{ij} K\right) &= 0, && (1.5)
\end{aligned}
$$

and a set of evolution equations,

$$
\begin{aligned}
\partial_t g_{ij} &= -2N K_{ij} + \nabla_i \beta_j + \nabla_j \beta_i, && (1.6)\\
\partial_t K_{ij} &= N \left(R_{ij} - 2K_{ik} K^k{}_j + K K_{ij}\right) && (1.7)\\
&\quad - \nabla_i \nabla_j N + \beta^k \nabla_k K_{ij} + K_{ik} \nabla_j \beta^k + K_{kj} \nabla_i \beta^k.
\end{aligned}
$$

In the above, R_{ij} is the Ricci tensor of g_{ij}, $R = R_{ij} g^{ij}$, $K = K_{ij} g^{ij}$, and ∇_i is the covariant derivative compatible with g_{ij}. The initial value problem consists of solving the constraint equations for (g_{ij}, K_{ij}) on an initial spatial hypersurface.

Chapter 2 is mostly concerned with the construction of initial data for black holes in the context of the extended-conformal-thin-sandwich formalism, which was done in collaboration with Geoffrey Lovelace, Harald Pfeiffer, and Robert Owen. In this formalism, the

initial value problem constitutes solving five elliptic equations for the conformal factor ψ, the lapse N or conformal lapse $\tilde{N} = \psi^{-6}N$, and the shift β^i (see chapter 2 for details on the conformal decomposition and the explicit equations that are being solved). This formalism has become increasingly popular, because the freely specifiable data are particularly appealing when quasiequilibrium solutions are sought after, such as for the early stages of a binary-black-hole inspiral. The free data consist of the conformal metric $\tilde{g}_{ij}$, its traceless time derivative $\tilde{u}_{ij}$, K, and $\partial_t K$. For quasiequilibrium, it is natural to set $\tilde{u}_{ij} = \partial_t K = 0$, and the choice of K is related to the temporal gauge. For simplicity, the conformal metric, which is related to the physical spatial metric by $g_{ij} = \psi^4 \tilde{g}_{ij}$, is usually taken to be the flat metric, $\tilde{g}_{ij} = \delta_{ij}$. This type of initial data is said to be conformally flat. However, we show that even though it is possible to construct conformally flat black-hole initial data with spins very close to their maximum value of unity, in an evolution the spins will quickly relax to a value of about 0.93. Because astrophysical black holes may have spins larger than this [15, 16], a better choice for $\tilde{g}_{ij}$ is needed.

For single black holes, the way around this issue is trivial, since one can simply choose $\tilde{g}_{ij}$ and K to correspond to an exactly known Kerr solution, with the spin parameter set as close to unity as desired (assuming sufficient numerical resolution). This idea is taken a step further in chapter 2 to construct binary-black-hole initial data by specifying $\tilde{g}_{ij}$ and K from a superposition of two Kerr solutions,

$$\tilde{g}_{ij} = \delta_{ij} + \sum_{a=1}^{2} e^{-r_a^2/w_a^2} \left(g_{ij}^a - \delta_{ij} \right), \tag{1.8}$$

$$K = \sum_{a=1}^{2} e^{-r_a^2/w_a^2} K_a. \tag{1.9}$$

The quantities g_{ij}^a and K_a are the spatial metric and the trace of the extrinsic curvature, respectively, for the individual Kerr black holes. The Gaussians $e^{-r_a^2/w_a^2}$ with weight factors w_a, as functions of Euclidean distance r_a around each hole, ensure that the spacetime becomes nearly flat away from the holes. In an evolution of such initial data, initially large spins only change by a few parts in 10^4 as the geometry relaxes, making this type of initial data well-suited to model highly spinning black-hole binaries.

My main contribution to chapter 2 was the construction of conformally flat, maximally sliced initial data for single black holes as described in section 2.3.2, including finding non-unique solutions to the extended-conformal-thin-sandwich equations, and the computation of embedding diagrams to facilitate the comparison with puncture data. In addition, I

aided in running the apparent horizon finder to locate the inner, super-extremal marginally outer trapped surfaces in the superposed-Kerr-Schild initial data of section 2.4.2. The work involving superposed-Kerr-Schild data and the scalar-curvature spin was primarily done by Geoffrey Lovelace, that involving puncture data by Harald Pfeiffer, and that involving approximate Killing vectors by Robert Owen.

While being a substantial improvement over conformally flat initial data, the superposed-black-hole initial data described above still does not account for many features of a physical black-hole binary. For example, a black hole in a binary is not exactly a Kerr black hole, but is tidally deformed by the presence of its companion. Also, the initial data should contain the binary's outgoing gravitational radiation, which is absent if the conformal data approaches that for a flat spacetime away from the holes. Such deficiencies give rise to a burst of spurious gravitational radiation, commonly referred to as junk radiation, early on in an evolution of the initial data. This junk radiation contaminates the actual gravitational waveforms of interest that are computed in the evolution, and degrades their accuracy. One way to remedy this problem is to make use of results from post-Newtonian theory [17] in the construction of initial data, which has been done in works such as [18, 19, 20]. In all previous attempts to include post-Newtonian results though, the Einstein constraint equations were not fully solved, so that the initial data had rather large constraint violations.

Chapter 3 presents work in progress to incorporate post-Newtonian results in (nonspinning) binary-black-hole initial data that satisfy the constraint equations, with a focus on including realistic tidal deformations of the black holes. The high-frequency components of the junk radiation are expected to be partly due to the oscillations of the black holes at early times before they have relaxed, because they do not have the correct geometry in the initial data. The inclusion of realistic tidal deformations aims to address this concern. By building on the procedures of the previous chapter, initial data is constructed by superposing the tidally perturbed Schwarzschild metrics as determined in [19]. I am responsible for the work in this chapter, but I have especially benefited from helpful discussions with Nathan Johnson-McDaniel.

1.2 Binary-black-hole evolutions

The evolution of two orbiting black holes can be divided into the inspiral, merger (including plunge), and ringdown phases. The inspiral and ringdown can be well approximated by post-Newtonian theory [17] and black hole perturbation theory [21], respectively. However,

an accurate description of the merger requires the power of numerical relativity. Developing the ingredients to successfully perform a full binary-black-hole evolution has proven to be a long and arduous task.

A major breakthrough was achieved by Frans Pretorius [22] with the first stable evolution of a black-hole binary that lasted for about one orbit, followed by the merger and ringdown. A central technique he employed was a generalized harmonic evolution system. In this formulation of the Einstein equations, the coordinates are specified via the gauge source function $H_\mu = g_{\mu\nu}\nabla_\lambda\nabla^\lambda x^\nu$, which implies evolution equations for the lapse N and shift β^i [12]. In Pretorius's work, H_μ was promoted to an independent dynamical field, with H_t satisfying an evolution equation that prevented the N from collapsing to zero, while $H_i = 0$.

The early successes of binary-black-hole evolutions were based on finite difference methods, but recent progress with spectral methods has shown great promise. Spectral methods are far more efficient and offer superior accuracy for smooth solutions [23]. Unfortunately, the merger has been particularly more difficult to handle. In spite of this, the efforts of the Caltech-Cornell-CITA collaboration have lead to the most accurate long-term evolution to date of two equal-mass, nonspinning black holes [24]. This work is presented in chapter 4.

My main contribution to chapter 4 was performing the merger evolutions, under the guidance of Mark Scheel, and determining a suitable gauge condition that prolonged the evolutions until the formation of a common horizon as described in section 4.2.3. This gauge condition was inspired by that of Pretorius, but with H_i also satisfying an evolution equation that drives β^i toward zero near the black holes,

$$\nabla^\nu\nabla_\nu H_t = f(x,t)\xi_1\frac{1-N}{N^\eta} + \xi_2 n^\lambda\partial_\lambda H_t, \tag{1.10}$$

$$\nabla^\nu\nabla_\nu H_i = g(x,t)\xi_3\frac{\beta_i}{N^2} + \xi_2 n^\lambda\partial_\lambda H_i, \tag{1.11}$$

where $\nabla^\nu\nabla_\nu$ is the scalar wave operator, and η, ξ_1, ξ_2, ξ_3, $f(x,t)$, $g(x,t)$ are adjustable parameters. The effect of the equation for H_i was to increase the coordinate size of the black holes, and helped to delay the formation of coordinate singularities. I also extracted the gravitational waveforms from the merger evolutions, and estimated the gauge errors present in the waveforms at late times. For this purpose, I introduced an error measure of the waveforms that does not require splitting each (l,m)-mode into an amplitude and phase, which is ill defined whenever the amplitude very nearly or does vanish. The waveforms from these simulations were also used in the first NINJA project [25, 26], a collaboration between the numerical relativity and data analysis communities in which numerical waveforms were

shared and embedded in colored Gaussian noise, which were then analyzed using search and parameter-estimation pipelines.

The efforts above were extended to accommodate equal-mass, spinning black holes, which are presented in chapter 5. Two non-precessing cases involving moderate spins of about 0.44 were considered, with both spins either anti-aligned or aligned with the orbital angular momentum. Low-eccentricity initial data were constructed for the two cases, in which the black holes had approximately the same separation. The anti-aligned case went through 10.6 orbits before merger, while the aligned case went through 15.6 orbits, demonstrating the orbital hang-up effect. The spins of the final merged holes in both cases were along the direction of the orbital angular momentum during inspiral, demonstrating the phenomenon of spin-flips in the anti-aligned case. Encouragingly, the high accuracy of the waveforms for the nonspinning case carried over. In the process of simulating the mergers though, it became apparent that the type of gauge condition used in the nonspinning case were not robust, but required much fine-tuning of the associated parameters. Nevertheless, the anti-aligned case was successfully completed, and is detailed in the main text of chapter 5. Shortly afterwards, a more robust alternative, the so-called damped-harmonic gauge, was developed by Béla Szilágyi, Lee Lindblom, and Mark Scheel [27]. This was used in the merger and ringdown evolutions of the aligned case. Since the other details are very similar to the anti-aligned case, the major results of this simulation are summarized at the end of chapter 5.

I am responsible for most of the work in chapter 5, which was done under the guidance of Harald Pfeiffer and Mark Scheel. Fan Zhang extrapolated the waveforms for the anti-aligned case, using a variant of the code developed by Michael Boyle and Abdul Mroué [28]. Michael Boyle extrapolated the waveforms for the aligned case. I have also repeated the merger and ringdown evolutions of the anti-aligned case with the damped harmonic gauge. Waveforms from these new simulations, and those from the aligned case, are being used in the NINJA2 project [29].

1.3 Effective-one-body formalism

Black-hole binaries may have a wide range of mass ratios and spins, and building a bank of template waveforms that covers a significant region of this parameter space is much too computationally expensive to rely on numerical simulations alone. A possible, practical solution is the effective-one-body formalism [30, 31], which combines information from post-

Newtonian theory, black hole perturbation theory, and numerical simulations to produce analytical waveforms covering the inspiral, plunge, and ringdown. The aim is that by performing a manageable number of simulations, an analytical template bank can be built that interpolates the parameter space between simulations [32, 33].

The effective-one-body formalism maps the real motion of two bodies (with masses m_1 and m_2) to the motion of a single body (with reduced mass $\mu = m_1 m_2/(m_1 + m_2)$) in an effective background spacetime. This mapping is accomplished by determining the correspondence between the Hamiltonians of the real and effective problems,

$$H_{\rm real} = M\sqrt{1 + 2\nu\left(\frac{H_{\rm eff}}{\mu} - 1\right)}, \tag{1.12}$$

where $M = m_1 + m_2$ and $\nu = \mu/M$. To go beyond describing the conservative dynamics, a radiation-reaction force F_i is added to Hamilton's equation for the relative momentum P^i (working in the center-of-mass frame),

$$\frac{dP_i}{dt} = -\frac{\partial H_{\rm real}}{\partial X^i} + F_i, \tag{1.13}$$

with X^i being the relative position vector. The radiation-reaction force during the inspiral is known from post-Newtonian theory [17], and can be resummed using a Padé approximant to capture non-perturbative effects.[2] The binary's evolution is then computed by solving Hamilton's equations, and this is used with a resummed post-Newtonian waveform to obtain the inspiral-plus-plunge waveform [34]. A linear combination of quasinormal modes for the final Kerr black hole is then stitched on for the ringdown waveform.

A handful of adjustable parameters that represent unknown higher-order post-Newtonian effects can be introduced, such as in the effective background metric and the resummed inspiral-plus-plunge waveforms, and are fixed by calibrating the effective-one-body model with numerical relativity results. It has been shown that effective-one-body and numerical relativity waveforms can agree remarkably well for nonspinning black holes [35, 36]. In chapter 6, this analysis is extended to spinning, non-precessing black holes, using the numerical simulations of chapter 5. In the spin anti-aligned case, the difference in the dominant $(2,2)$-mode of the waveforms is slightly over the numerical errors, while in the spin aligned case

[2] Given a truncated Taylor expansion $T_{m+n}(x) = \sum_{l=0}^{m+n} c_l x^l$, the corresponding Padé approximant is $P^n_m(x) = \sum_{l=0}^{n} a_l x^l / \sum_{l=0}^{m} b_l x^l$ where a_i and b_i are such that when $P^n_m(x)$ is Taylor expanded, the result matches all the terms of $T_{m+n}(x)$.

the difference is within numerical errors during the inspiral. In both cases though, the faithfulness of the waveforms, calculating using the noise curves (see section 6.3.3 for references) of Enhanced LIGO and Advanced LIGO, is found to exceed the requirements for detection and measurement for binaries with a total mass of $30 - 200M_{\odot}$. My main contribution to this work was generating the necessary data from the numerical simulations, while Yi Pan and Alessandra Buonanno were chiefly responsible for the analysis of the effective-one-body waveforms. It should be noted that for the spin aligned case, only the inspiral waveforms were calibrated because the full numerical waveforms were only available at a later date.

1.4 Quasilocal black hole horizons

Numerical relativity has benefited from concepts in mathematical relativity, and one such example is the quasilocal characterization of black holes, which only requires information at points on a single spatial hypersurface. To track the motion of a black hole and calculate its properties during a simulation, one is immediately faced with the question of how to represent the black hole surface. The traditional notion of the event horizon is not feasible, since it requires a knowledge of the entire future history of the spacetime, and in practice can only be (approximately) located after the simulation has proceeded for a sufficiently long time. Instead, a quasilocal horizon known as a marginally outer trapped surface is used [37]. For typical spacetimes of interest in numerical relativity, a marginally outer trapped surface is either inside of or coincides with the event horizon [38]. The fact that a marginally outer trapped surface can be located also signals the presence of a spacetime singularity [39].

A marginally outer trapped surface is defined as a 2-surface in a spatial hypersurface, on which the expansion $\theta_{(l)}$ of its future-directed null normals l^{μ} vanishes,

$$\theta_{(l)} = \bar{q}^{\mu\nu}\nabla_{\mu}l_{\nu} = 0, \tag{1.14}$$

where $\bar{q}_{\mu\nu}$ is the induced metric on the 2-surface. The null normals l^{μ} form a congruence of geodesics, and the expansion $\theta_{(l)}$ can be interpreted as the fractional rate of change of the congruence's cross-sectional area [40]. Then $\theta_{(l)} < 0$ corresponds to future-directed null geodesics that are converging toward each other, and $\theta_{(l)} > 0$ to diverging ones. Intuition would reasonably suggest that a surface inside a black hole should be defined by the former condition, a surface outside by the latter condition, and so the surface of the black hole itself by Eq. (1.14).

Clearly, a better understanding of quasilocal horizons is useful in elucidating the be-

havior of black holes in numerical simulations, and there have been many related modern developments in mathematical relativity, such as existence theorems for marginally outer trapped surfaces [41, 42], and the isolated horizon [43, 44] and dynamical horizon [45, 46] frameworks that describe black holes in and out of equilibrium, respectively. These results have been fruitfully applied to extract physical information from numerical simulations [47, 37, 48]. Conversely, numerical simulations are capable of exploring the behavior of quasilocal horizons in highly dynamical situations involving strong gravity, that may not be readily amenable to mathematical analysis. Thus, the subject of quasilocal horizons serves as a valuable bridge between the numerical and mathematical relativity communities.

An example of how mathematical notions of quasilocal horizons can be combined with numerical relativity to yield insights into strong gravitational dynamics is presented in chapter 7. Initial data representing a rotating black hole with a pulse of ingoing gravitational radiation are constructed and evolved. For the largest distortion of the black hole considered, which more than doubles the black hole's mass, up to five marginally outer trapped surfaces are found at a single time. During the distortion, all the world tubes traced out by the marginally outer trapped surfaces are dynamical horizons, and together form a single dynamical horizon that weaves forwards and backwards in time. The rate of change of energy and angular momentum across the black hole is evaluated with the dynamical horizon flux law of Ashtekar and Krishan [45], and the angular momentum flux law of Gourgoulhon [49]. To my knowledge, this is the first application of the dynamical horizon flux law in a numerical relativity simulation that utilizes a proper rescaling of null vectors, and the first application of the angular momentum flux law in any numerical relativity simulation. The event horizon is also examined, and finally a simple illustration of the formation of multiple marginally outer trapped surfaces in the Vaidya spacetime is given. I am responsible for most of the work in this chapter, which was done under the guidance of Harald Pfeiffer. Michael Cohen found the event horizon described in section 7.6.3.

Bibliography

[1] M. Oda, Space Sci. Rev. **20**, 757 (1977).

[2] M. Miyoshi et al., Nature **373**, 127 (1995).

[3] D. Richstone et al., Nature **385**, A14 (1998).

[4] A. M. Ghez et al., Astrophys. J. Lett. **586**, L127 (2003).

[5] J. E. McClintock and R. A. Remillard, Black hole binaries, in *Compact Stellar X-ray Sources*, edited by W. H. G. Lewin and M. van der Klis, pages 157–213, Cambridge University Press, Cambridge, UK, 2006.

[6] A. S. Sengupta, J. Phys.: Conf. Ser. **228**, 012002 (2010).

[7] L. S. Finn, Phys. Rev. D **46**, 5236 (1992).

[8] P. C. Peters, Phys. Rev. **136**, B1224 (1964).

[9] J. W. York, Jr., Kinematics and dynamics of general relativity, in *Sources of Gravitational Radiation*, edited by L. L. Smarr, pages 83–126, Cambridge University Press, Cambridge, England, 1979.

[10] M. Shibata and T. Nakamura, Phys. Rev. D **52**, 5428 (1995).

[11] T. W. Baumgarte and S. L. Shapiro, Phys. Rev. D **59**, 024007 (1998), gr-qc/9810065.

[12] L. Lindblom, M. A. Scheel, L. E. Kidder, R. Owen, and O. Rinne, Class. Quantum Grav. **23**, S447 (2006).

[13] http://www.black-holes.org/SpEC.html.

[14] R. Arnowitt, S. Deser, and C. W. Misner, The dynamics of general relativity, in *Gravitation: An Introduction to Current Research*, edited by L. Witten, Wiley, New York, 1962.

[15] J.-M. Wang, Y.-M. Chen, L. C. Ho, and R. J. McLure, Astrophys. J. **642**, L111 (2006).

[16] J. E. McClintock et al., Astrophys. J. **652**, 518 (2006).

[17] L. Blanchet, Living Rev. Rel. **9** (2006).

[18] S. Nissanke, Phys. Rev. D **73**, 124002 (2006).

[19] N. K. Johnson-McDaniel, N. Yunes, W. Tichy, and B. J. Owen, Phys.Rev. **D80**, 124039 (2009).

[20] B. C. Mundim, B. J. Kelly, Y. Zlochower, H. Nakano, and M. Campanelli, Class. Quantum Grav. **28**, 134003 (2011).

[21] S. Chandrasekhar, *The mathematical theory of black holes*, Oxford University Press, New York, NY, 1983.

[22] F. Pretorius, Phys. Rev. Lett. **95**, 121101 (2005).

[23] J. P. Boyd, *Chebyshev and Fourier Spectral Methods*, Dover Publications, second edition, 1999.

[24] M. Hannam et al., Phys. Rev. D **79**, 084025 (2009).

[25] B. Aylott et al., Class. Quantum Grav. **26**, 165008 (2009).

[26] B. Aylott et al., Class. Quantum Grav. **26**, 114008 (2009).

[27] B. Szilagyi, L. Lindblom, and M. A. Scheel, Phys. Rev. D **80**, 124010 (2009).

[28] M. Boyle, A.H. Mroué , Phys. Rev. D **80**, 124045 (2009).

[29] The NINJA collaboration, www.ninja-project.org.

[30] A. Buonanno and T. Damour, Phys. Rev. D **59**, 084006 (1999).

[31] A. Buonanno and T. Damour, Phys. Rev. D **62**, 064015 (2000).

[32] Y. Pan et al., Phys. Rev. D **77**, 024014 (2008).

[33] A. Buonanno et al., Phys. Rev. D **76**, 104049 (2007).

[34] T. Damour, B. R. Iyer, and A. Nagar, Phys. Rev. D **79**, 064004 (2009).

[35] M. Boyle et al., Phys. Rev. D **78**, 104020 (2008).

[36] T. Damour and A. Nagar, Phys. Rev. D **79**, 081503 (2009).

[37] E. Schnetter, B. Krishnan, and F. Beyer, Phys. Rev. D **74**, 024028 (2006).

[38] S. W. Hawking and G. F. R. Ellis, *The large scale structure of space-time*, Cambridge University Press, Cambridge, England, 1973.

[39] R. Penrose, Phys. Rev. Lett. **14**, 57 (1965).

[40] E. Poisson, *A Relativist's Toolkit: The Mathematics of Black-Hole Mechanics*, Cambridge University Press, 2004.

[41] L. Andersson, M. Mars, and W. Simon, Phys. Rev. Lett. **95**, 11102 (2005).

[42] L. Andersson, M. Mars, J. Metzger, and W. Simon, Class. Quantum Grav. **26**, 085018 (2008).

[43] A. Ashtekar, C. Beetle, and S. Fairhurst, Class. Quantum Grav. **17**, 253 (2000).

[44] A. Ashtekar et al., Phys. Rev. Lett. **85**, 3564 (2000).

[45] A. Ashtekar and B. Krishnan, Phys. Rev. D **68**, 104030 (2003).

[46] A. Ashtekar and G. J. Galloway, Advances in Theoretical and Mathematical Physics **9**, 1 (2005).

[47] O. Dreyer, B. Krishnan, D. Shoemaker, and E. Schnetter, Phys. Rev. D **67**, 024018 (2003).

[48] B. Krishnan, Class. Quantum Grav. **25**, 114005 (2008).

[49] E. Gourgoulhon, Phys. Rev. D **72**, 104007 (2005).

Chapter 2

Binary-black-hole initial data with nearly extremal spins

There is a significant possibility that astrophysical black holes with nearly extremal spins exist. Numerical simulations of such systems require suitable initial data. In this chapter, we examine three methods of constructing binary-black-hole initial data, focusing on their ability to generate black holes with nearly extremal spins: (i) Bowen-York initial data, including standard puncture data (based on conformal flatness and Bowen-York extrinsic curvature), (ii) standard quasiequilibrium initial data (based on the extended-conformal-thin-sandwich equations, conformal flatness, and maximal slicing), and (iii) quasiequilibrium data based on the superposition of Kerr-Schild metrics. We find that the two conformally flat methods (i) and (ii) perform similarly, with spins up to about 0.99 obtainable at the *initial time*. However, *in an evolution*, we expect the spin to quickly relax to a significantly smaller value around 0.93 as the initial geometry relaxes. For quasiequilibrium superposed Kerr-Schild (SKS) data [method (iii)], we construct initial data with *initial* spins as large as 0.9997. We evolve SKS data sets with spins of 0.93 and 0.97 and find that the spin drops by only a few parts in 10^4 during the initial relaxation; therefore, we expect that SKS initial data will allow evolutions of binary black holes with relaxed spins above 0.99. Along the way to these conclusions, we also present several secondary results: the power law coefficients with which the spin of puncture initial data approaches its maximal possible value; approximate analytic solutions for large spin puncture data; embedding diagrams for single spinning black holes in methods (i) and (ii); nonunique solutions for method (ii). All of the initial data sets that we construct contain subextremal

black holes, and when we are able to push the spin of the excision boundary surface into the superextremal regime, the excision surface is always enclosed by a second, subextremal apparent horizon. The quasilocal spin is measured by using approximate rotational Killing vectors, and the spin is also inferred from the extrema of the intrinsic scalar curvature of the apparent horizon. Both approaches are found to give consistent results, with the approximate-Killing-vector spin showing least variation during the initial relaxation.

Originally published as G. Lovelace, R. Owen, H. P. Pfeiffer, and T. Chu, Phys. Rev. D **78**, 084017 (2008).

2.1 Introduction

There is a significant possibility that black holes with nearly extremal spins exist; by "nearly extremal", we mean that the spin S and mass M of the hole satisfy $0.95 \lesssim S/M^2 \lesssim 1$. Some models of black-hole accretion [1, 2, 3] predict that most black holes will have nearly extremal spins, and observational evidence for black holes with nearly extremal spins includes, e.g., estimates of black-hole spins in quasars [4] and estimates of the spin of a black hole in a certain binary X-ray source [5]. There is considerable uncertainty about whether black holes do in fact typically have nearly extremal spins; e.g., some models [6, 7, 8] of black-hole accretion do not lead to large spins. This uncertainty could be reduced by measuring the holes' spins directly using gravitational waves.

This prospect of detecting the gravitational waves emitted by colliding black holes, possibly with nearly extremal spins, motivates the goal of simulating these spacetimes numerically. Indeed, one focus of intense research has been spinning black hole binaries, including the discovery of dramatic kicks when two spinning black holes merge [9, 10, 11, 12, 13, 14, 15, 16, 17] as well as some initial exploration of the orbital dynamics of spinning binaries [18, 19, 20, 21, 22, 23]. All of these simulations start from puncture initial data as introduced by Brandt and Brügmann [24].

The simplifying assumptions employed in puncture initial data make it impossible to construct black holes with spins arbitrarily close to unity. The numerical value of the fastest obtainable spin depends on which dimensionless ratio is chosen to characterize "black hole spin." Often, dimensionless spin is defined based on quasilocal properties of the black hole,

$$\chi := \frac{S}{M^2}, \tag{2.1}$$

where S is taken to be nonnegative and is a suitable quasilocal spin (e.g., obtained using approximate rotational Killing vectors on the apparent horizon as described, for example, in Appendix 2.7) and M is a suitable quasilocal mass. The latter may be obtained from Christodoulou's formula relating spin, area and mass of a Kerr black hole,

$$M^2 := M_{\rm irr}^2 + \frac{S^2}{4M_{\rm irr}^2}, \tag{2.2}$$

where we define the irreducible mass in terms of the area A of the apparent horizon by $M_{\rm irr} := \sqrt{A/16\pi}$.

The quantity χ is not preserved during an evolution. Specifically, most black hole initial data are not exactly in equilibrium, which leads to transients and emission of an artificial pulse of gravitational radiation early in numerical simulations. The geometry in the vicinity of the black holes relaxes on a time scale $t_{\rm relax}$ (typically a few M), and during this relaxation, the spin changes by

$$\Delta\chi := \chi\left(t=0\right) - \chi\left(t_{\rm relax}\right). \tag{2.3}$$

When constructing a single spinning black hole with standard puncture data [24], for instance, $\chi(t=0) \lesssim 0.98$, which seems encouragingly large. However Dain *et al.* [25, 26] evolved standard puncture data with initial spin close to this limit, and they find that the spin rapidly drops to $\chi(t_{\rm relax}) \approx 0.93$, i.e., $\Delta\chi \approx 0.05$.

For single-black-hole spacetimes, another widely used dimensionless spin-measure is the ratio of total angular momentum[1] $J_{\rm ADM}$ and Arnowitt–Deser–Misner (ADM) energy $E_{\rm ADM}$,

$$\varepsilon_J := \frac{J_{\rm ADM}}{E_{\rm ADM}^2}. \tag{2.4}$$

Dain *et al.* noted that $\chi(t_{\rm relax})$ is close to ε_J and explained this result as follows: the spacetime is axisymmetric, which implies that the angular momentum $J_{\rm ADM}$ is conserved and that the black hole's spin equals $J_{\rm ADM}$. Moreover, so long as a negligible fraction of the spacetime's energy is carried off by the spurious radiation, the hole's quasi-local mass will relax to a value of $E_{\rm ADM}$, giving $\chi\left(t_{\rm relax}\right) \approx \varepsilon_J$. Thus conformally flat Bowen-York data cannot be used to simulate black holes with nearly extremal *equilibrium* spins, even though the *initial* spins can be made fairly close to $\chi = 1$.

This chapter examines three different approaches of constructing black hole initial data

[1] We define here $J_{\rm ADM}$ by an ADM–like surface integral at infinity; in axisymmetry this definition coincides with the standard Komar integral for angular momentum (see section 2.2.2 for details.)

with nearly extremal spin. First, we revisit puncture initial data and inversion-symmetric Bowen-York initial data. We show that for a single, spinning black hole at rest, both approaches are identical, and we determine spin limits based purely on initial data more accurately than before:

$$\varepsilon_J \leq 0.928200, \qquad \chi(t=0) \leq 0.9837. \tag{2.5}$$

We show that the limiting values of ε_J and $\chi(t=0)$ are approached as power laws of the spin parameter (curiously, with different powers). We furthermore give insight into the geometric structure of these high-spin Bowen-York initial data sets through numerical study and approximate analytical solutions and find that a cylindrical throat forms which lengthens logarithmically with the spin parameter.

Second, we investigate the high-spin limit of another popular approach to constructing initial data, the quasiequilibrium formalism [27, 28, 29, 30, 31] based on the conformal thin-sandwich equations [32, 33]. For the standard choices of conformal flatness and maximal slicing, we are able to construct initial data with spins somewhat *larger* than the standard Bowen-York limits given in Eq. (2.5):

$$\varepsilon_J \lesssim 0.94, \quad \chi(t=0) \lesssim 0.99. \tag{2.6}$$

Once again ε_J is much lower than $\chi(t=0)$, which suggests that these data sets lead to equilibrium spins of approximate magnitude $\chi \approx 0.94$. Interestingly, these families of initial data are found to exhibit nonunique solutions [34, 35, 36], and the largest spins are obtained along the upper branch.

The third approach also utilizes the quasiequilibrium formalism [27, 28, 29, 30, 31], but this time we make use of the freedom to choose arbitrary background data. Specifically, we choose background data as a superposition of two Kerr-Schild metrics. This approach is based on the original proposal of Matzner and collaborators [37, 38] and was first carried over into the conformal thin-sandwich equations in Ref. [39]; also, background data consisting of a single, nonspinning Kerr-Schild black hole was used to construct initial data for a black-hole–neutron-star binary in Ref. [40]. For single black holes, this data simply reduces to the analytical Kerr solution. For binary black holes, we construct initial data with spins as large as

$$\chi(t=0) = 0.9997. \tag{2.7}$$

We also present evolutions, demonstrating that our rapidly spinning initial data sets remain rapidly spinning after the numerical evolution relaxes. In particular, we evolve an orbiting binary with $\chi(t=0)=0.9275$ and a head-on merger with $\chi(t=0)=0.9701$. In both cases, $|\Delta\chi/\chi(t=0)|$ is significantly smaller than 10^{-3}. We conclude that the conformally curved superposed Kerr-Schild initial data we present in this chapter, in contrast with conformally flat Bowen-York data, is suitable for simulating binary black holes with nearly extremal spins.

We use two different techniques to measure the dimensionless spin of black holes, which are described in the appendices. The first (Appendix 2.7) technique uses the standard surface integral based on an approximate rotational Killing vector of the apparent horizon. We compute the approximate Killing vector with a variation of the technique introduced by Cook and Whiting [41], extended with new normalization conditions of the approximate Killing vector, and we denote the resulting spin "AKV spin," $\chi_{\rm AKV}$. The second approach (Appendix 2.8) is based on the shape of the horizon in the form of its scalar curvature; specifically, the spin magnitudes are inferred from the minimum and maximum of the intrinsic Ricci scalar curvature of the horizon. We call the spin inferred in this way the "scalar curvature spin," and we label the spin magnitudes inferred from the scalar curvature minimum and maximum as $\chi_{\rm SC}^{\rm min}$ and $\chi_{\rm SC}^{\rm max}$, respectively. Typically, binary-black-hole initial data produce holes that are initially *not* in equilibrium. Therefore, we use only the AKV spin to measure the *initial* black hole spin (sections 2.3–2.4). We use both the AKV and the scalar-curvature spin when we measure the spin after the holes have relaxed to equilibrium (section 2.5).

We also monitor whether any of the constructed initial data sets have superextremal spins, as this may shed light, for example, on the cosmic censorship conjecture. When using the Christodoulou formula [Eq. (2.2)] to define M, the quasilocal dimensionless spin χ is *by definition* bounded [42], $\chi \leq 1$. This can be seen most easily by introducing the parameter ζ, defined as

$$\zeta := \frac{S}{2M_{\rm irr}^2}, \tag{2.8}$$

and then rewriting χ as

$$\chi = 1 - \frac{(1-\zeta)^2}{1+\zeta^2}. \tag{2.9}$$

The ratio χ is therefore not useful to diagnose superextremal black holes. A more suitable diagnostic is found in the parameter ζ. For Kerr black holes, the second term on the right-hand side of Eq. (2.2) is always smaller or equal to the first, with equality only for extremal

spin; i.e., $\zeta \leq 1$, with equality for extremal spin. This motivates an alternative definition of extremality [42]: a black hole is said to be superextremal if the second term in Eq. (2.2) is larger than the first one, i.e., if $\zeta > 1$. In this chapter, we monitor ζ, which we call the spin-extremality parameter, along with the dimensionless spin χ. We find instances where ζ exceeds unity. Before this happens, however, a larger, subextremal ($\zeta < 1$) apparent horizon appears, enclosing the smaller, superextremal horizon (section 2.4.2, Fig. 2.12).

This chapter is organized as follows. Section 2.2 summarizes the various formalisms that we use to construct initial data. Section 2.3 investigates single black hole initial data, followed by the construction of binary-black-hole initial data in section 2.4. Section 2.5 presents binary-black-hole evolutions that show the good properties of superposed Kerr-Schild data, and the various spin diagnostics. We summarize and discuss our results in section 2.6. Finally, Appendix 2.7 and Appendix 2.8 present our techniques to define black hole spin.

2.2 Initial data formalism

Before constructing initial data for rapidly spinning single (section 2.3) and binary (section 2.4) black holes, we first summarize the initial data formalisms we will use. After laying some general groundwork in section 2.2.1, we describe Bowen-York initial data (including puncture initial data) in section 2.2.2 and quasiequilibrium extended-conformal-thin-sandwich data in section 2.2.3.

2.2.1 Extrinsic curvature decomposition

Initial data sets for Einstein's equations are given on a spatial hypersurface Σ and must satisfy the constraint equations

$$R + K^2 - K_{ij}K^{ij} = 0, \tag{2.10}$$

$$\nabla_j \left(K^{ij} - g^{ij}K \right) = 0. \tag{2.11}$$

Here, g_{ij} is the induced metric of the slice Σ, with covariant derivative ∇_i, $R := g^{ij}R_{ij}$ denotes the trace of the Ricci tensor R_{ij}, and K_{ij} denotes the extrinsic curvature of the slice Σ as embedded into the spacetime manifold $\mathcal{M}$.

The constraint equations (2.10) and (2.11) can be transformed into elliptic partial differential equations using a conformal transformation, e.g., [33]. One introduces a conformal

metric, $\tilde{g}_{ij}$ via

$$g_{ij} = \psi^4 \tilde{g}_{ij}, \tag{2.12}$$

with the strictly positive conformal factor $\psi > 0$. Substituting Eq. (2.12) into Eq. (2.10) yields an elliptic equation for ψ. One furthermore decomposes the extrinsic curvature into trace and tracefree part,

$$K^{ij} = A^{ij} + \frac{1}{3} g^{ij} K, \tag{2.13}$$

and splits off a longitudinal part from the tracefree extrinsic curvature,

$$A^{ij} = \frac{1}{\sigma} (\mathbb{L}V)^{ij} + M^{ij}. \tag{2.14}$$

In Eq. (2.14), σ is a strictly positive weight function, the longitudinal operator is defined as $(\mathbb{L}V)^{ij} = 2\nabla^{(i}V^{j)} - \frac{2}{3} g^{ij} \nabla_k V^k$, and M^{ij} is symmetric and tracefree.[2] Finally, one introduces the conformally scaled quantities $\sigma = \psi^6 \tilde{\sigma}$, $M^{ij} = \psi^{-10} \tilde{M}^{ij}$, which allows the momentum constraint [Eq. (2.11)] to be rewritten completely in terms of conformal quantities:

$$A^{ij} = \psi^{-10} \tilde{A}^{ij}, \tag{2.15}$$

$$\tilde{A}^{ij} = \frac{1}{\tilde{\sigma}} (\tilde{\mathbb{L}}V)^{ij} + \tilde{M}^{ij}. \tag{2.16}$$

The Hamiltonian and momentum constraints then become

$$\tilde{\nabla}^2 \psi - \frac{1}{8} \tilde{R} - \frac{1}{12} K^2 \psi^5 + \frac{1}{8} \tilde{A}_{ij} \tilde{A}^{ij} \psi^{-7} = 0, \tag{2.17}$$

$$\tilde{\nabla}_j \left(\frac{1}{\tilde{\sigma}} (\tilde{\mathbb{L}}V)^{ij} \right) - \frac{2}{3} \psi^6 \tilde{\nabla}^i K + \tilde{\nabla}_j \tilde{M}^{ij} = 0. \tag{2.18}$$

Given choices for $\tilde{M}^{ij}$, K, $\tilde{g}_{ij}$ and $\tilde{\sigma}$, *and also* boundary conditions, one can solve Eqs. (2.17) and (2.18) for ψ and V^i, and then assemble the (constraint-satisfying) initial data g_{ij} and K^{ij}.

Many important approaches to construct binary-black-hole initial data can be cast in this form. The various approaches differ in the choices for the freely specifiable parts and the boundary conditions. Some choices of free data aim for simplicity, such as Bowen-York initial data. Other approaches aim to preserve freedom, resulting in more complicated sets of equations but also more flexibility to control properties of the resulting initial data. The quasiequilibrium extended-conformal-thin-sandwich approach falls into this second category,

[2] It is also possible, but not necessary, to require that M^{ij} is divergence free.

and we will exploit precisely its inherent freedom in choosing the free data to construct black holes with nearly extremal spins.

2.2.2 Bowen-York initial data

In this section, we describe two approaches of constructing initial data based on the well-known Bowen-York extrinsic curvature. These two approaches, puncture data and inversion-symmetric data, differ in how they treat the coordinate singularity at $r = 0$; both can be obtained from the general procedure outlined in section 2.2.1 by setting $\tilde{\sigma} \equiv 1$, $K \equiv 0$, $\tilde{M}^{ij} \equiv 0$ and by using a conformally flat metric

$$\tilde{g}_{ij} = f_{ij}. \tag{2.19}$$

The momentum constraint [Eq. (2.18)] then reduces to $\tilde{\nabla}_j(\tilde{\mathbb{L}}V)^{ij} = 0$, which is solved by choosing the analytical Bowen-York solutions [43, 44].

The Bowen-York solutions can be written down most conveniently in Cartesian coordinates, $f_{ij} = \delta_{ij}$:

$$V_P^i = -\frac{1}{4r}\left[7P^i + n^i P^k n_k\right], \tag{2.20}$$

$$V_S^i = -\frac{1}{r^2}\epsilon^i{}_{lm} S^l n^m, \tag{2.21}$$

where $r = (x^i x^j \delta_{ij})^{1/2}$ is the coordinate distance to the origin and $n^i = x^i/r$ is the coordinate unit vector pointing from the origin to the point under consideration. The spatially constant vectors P^i and S^i parametrize the solutions[3]

$$\tilde{A}_P^{ij} = \frac{3}{2r^2}\left[2P^{(i}n^{j)} - \left(\delta^{ij} - n^i n^j\right) P_k n^k\right], \tag{2.22}$$

$$\tilde{A}_S^{ij} = \frac{6}{r^3} n_{(i}\epsilon_{j)kl} S^k n^l. \tag{2.23}$$

The conformal factor ψ is then determined by the Hamiltonian constraint [Eq. (2.17)], which simplifies to

$$\tilde{\nabla}^2\psi + \frac{1}{8}\psi^{-7}\tilde{A}^{ij}\tilde{A}_{ij} = 0. \tag{2.24}$$

We would like to recover an asymptotically flat space; this implies the boundary condition

[3] In Cartesian coordinates, upper and lower indices are equivalent, so index positioning in Eqs. (2.20)–(2.23) is unimportant. To find $\tilde{A}^{ij}_{P/S}$ in another coordinate system, first compute the Cartesian components Eqs. (2.20)–(2.23), and then apply the desired coordinate transformation.

$\psi \to 1$ as $r \to \infty$.

This boundary condition makes it possible to evaluate the linear ADM-momentum and ADM-like angular momentum of Bowen-York initial data *without* solving Eq. (2.24). These quantities are defined by surface integrals at infinity,

$$J_{(\xi)} = \frac{1}{8\pi} \oint_{\infty} (K_{ij} - g_{ij}K)\, \xi^i s^j \, dA, \tag{2.25}$$

where s^i is the outward-pointing unit normal to the integration sphere.[4] By letting $\psi \to 1$ in Eq. (2.15), one can replace K_{ij} by $\tilde{A}_{ij}$ and then evaluate the resulting integrals. The choice of vector ξ^i determines which quantity is computed: For instance, $\xi = \hat{e}_x$ corresponds to the x-component of the linear ADM-momentum, $\xi = \partial_\phi = -x\hat{e}_y + y\hat{e}_x$ yields the z-component of the ADM-like angular momentum.[5] For Eqs. (2.22) and (2.23), the results are $P^i_{\rm ADM} = P^i$ and $J^i_{\rm ADM} = S^i$, respectively.

The ADM energy is given by the expression

$$E_{\rm ADM} = \frac{1}{16\pi} \oint_{\infty} \nabla_j \left(\mathcal{G}_i{}^j - \delta_i{}^j \mathcal{G} \right) s^i \, dA, \tag{2.26}$$

where $\mathcal{G}_{ij} := g_{ij} - f_{ij}$, $\mathcal{G} := \mathcal{G}_{ij} g^{ij}$. For conformal flatness, Eq. (2.26) reduces to

$$E_{\rm ADM} = -\frac{1}{2\pi} \oint_{\infty} \partial_r \psi \, dA. \tag{2.27}$$

The derivative of the conformal factor is known only after Eq. (2.24) is solved; therefore, in contrast with the linear and angular momenta, $E_{\rm ADM}$ can be computed only after solving the Hamiltonian constraint.

We now turn our attention to inner boundary conditions. $\tilde{A}^{ij}_P$ and $\tilde{A}^{ij}_S$ are singular at $r = 0$. This singularity is interpreted as a second asymptotically flat universe; when solving Eq. (2.24), this can be incorporated in two ways:

- **Inversion Symmetry**: The demand that the solution be symmetric under inversion

[4] At infinity, the normal to the sphere s^i is identical to the coordinate radial unit vector n^i.

[5] As is common in the numerical relativity community, we introduce the phrase "ADM angular momentum" to refer to an angular momentum defined at spatial infinity in the manner of the other conserved ADM quantities of asymptotically flat spacetimes [45], despite the fact that (at least to our knowledge), no such quantity is widely agreed to rigorously exist in general, due to the supertranslation ambiguity that exists in four spacetime dimensions. For recent research on this issue see [46] and references therein. In the present work, this subtlety can be ignored, because we only compute this quantity in truly axisymmetric spacetimes, with $\vec{\xi}$ the global axisymmetry generator, so that $J_{\rm ADM}$ coincides with the standard Komar integral for angular momentum.

at a sphere with radius $R_{\rm inv}$ centered on the origin [44] results in a boundary condition for ψ at $r = R_{\rm inv}$, namely $\partial\psi/\partial r = -\psi/(2R_{\rm inv})$. The Hamiltonian constraint Eq. (2.24) is solved only in the exterior of the sphere, $r \geq R_{\rm inv}$, and the solution in the interior can be recovered from inversion symmetry [44], e.g.,

$$\psi\left(x^i\right) = \frac{R_{\rm inv}}{r}\psi\left(\frac{R_{\rm inv}^2}{r^2}x^i\right). \tag{2.28}$$

- **Puncture data**: One demands [24] the appropriate singular behavior of ψ for $r \to 0$ to ensure that the second asymptotically flat end is indeed flat. That is, ψ must behave as

$$\psi(x^i) = \frac{m_p}{2r} + 1 + u(x^i) \tag{2.29}$$

for some positive parameter m_p (the "puncture mass") and function $u(x^i)$ that is finite and continuous in $\mathbb{R}^3$ and approaches 0 as $r \to \infty$. Equation (2.24) then implies an equation for u that is finite everywhere and can be solved without any inner boundaries:

$$\tilde{\nabla}^2 u = -\frac{1}{8}\frac{\tilde{A}_{ij}\tilde{A}^{ij}\, r^7}{\left(r + \frac{m_p}{2} + ur\right)^7}. \tag{2.30}$$

The majority of binary black hole simulations use puncture data, see, e.g., Refs. [9-23].

Both approaches allow specification of multiple black holes at different locations, each with different spin and momentum parameters S^i and P^i. For puncture data this is almost trivial; this accounts for the popularity of puncture data as initial data for black hole simulations. In contrast, for inversion-symmetric data, one needs to employ a rather cumbersome imaging procedure[6] (see, e.g., [47] for details).

For a single spinning black hole at the origin, the extrinsic curvature $\tilde{A}_S^{ij}$ given by Eq. (2.23) is identical for inversion-symmetric and puncture data. For inversion-symmetric data, the conformal factor has the usual falloff at large radii,

$$\psi(x^i) = 1 + \frac{E_{\rm ADM}}{2r} + \mathcal{O}(r^{-2}), \quad \text{as } r \to \infty. \tag{2.31}$$

Using Eq. (2.28) we find the behavior of ψ as $r \to 0$:

$$\psi(x^i) = \frac{R_{\rm inv}}{r} + \frac{E_{\rm ADM}}{2R_{\rm inv}} + \mathcal{O}(r), \quad \text{as } r \to 0. \tag{2.32}$$

[6] Even for a single black hole with $P^k \neq 0$, Eq. (2.22) has to be augmented by additional terms of $\mathcal{O}(r^{-4})$ to preserve inversion symmetry [44].

Comparison with Eq. (2.29) shows that this is precisely the desired behavior for puncture data, if one identifies $R_{\rm inv} = m_p/2$ and $E/(2R_{\rm inv}) = 1 + u(0)$. Because puncture data has a unique solution, it follows that for single spinning black holes, puncture data and inversion-symmetric data are *identical*, provided $m_p = 2R_{\rm inv}$.

For inversion-symmetric initial data for a single, spinning black hole, it is well-known [48] that the apparent horizon coincides with the inversion sphere, $r_{\rm AH} = R_{\rm inv}$. Therefore, we conclude that for puncture data for a single, spinning black hole, the apparent horizon is an exact coordinate sphere with radius $r_{\rm AH} = m_p/2$, despite $\tilde{A}^{ij}_S$ and $u(x^i)$ not being spherically symmetric.

2.2.3 Quasi-equilibrium extended-conformal-thin-sandwich initial data

Another popular approach to constructing binary-black-hole initial data is the quasiequilibrium extended-conformal-thin-sandwich (QE-XCTS) formalism [29, 30, 31, 27, 28]. Instead of emphasizing the extrinsic curvature, the conformal thin-sandwich formalism [32] emphasizes the spatial metric g_{ij} and its *time derivative*. Nevertheless, it is equivalent [33] to the extrinsic curvature decomposition outlined in section 2.2.1. The vector V^i is identified with the shift β^i,

$$V^i \equiv \beta^i, \tag{2.33}$$

and the weight functions σ and $\tilde{\sigma}$ are identified (up to a factor 2) with the lapse and the conformal lapse, respectively,

$$\sigma \equiv 2\alpha, \qquad \tilde{\sigma} \equiv 2\tilde{\alpha}. \tag{2.34}$$

The tensor $\tilde{M}_{ij}$ is related to the time derivative of the spatial metric, $\tilde{u}_{ij} := \partial_t \tilde{g}_{ij}$ by

$$\tilde{M}_{ij} \equiv \frac{1}{2\tilde{\alpha}} \tilde{u}_{ij}. \tag{2.35}$$

Because M_{ij} is tracefree [Eqs. (2.13) and (2.15)–(2.16)], we require $\tilde{u}_{ij}$ to be tracefree.

The conformal thin-sandwich equations allow control of certain time derivatives in the subsequent evolution of the constructed initial data. If the lapse α and shift β^i from the initial data are used in the evolution, for instance, then the tracefree part of $\partial_t g_{ij}$ will be proportional to $\tilde{u}_{ij}$. Therefore (see Refs. [27, 29])

$$\tilde{u}_{ij} \equiv 0 \tag{2.36a}$$

is a preferred choice for initial data sets that begin nearly in equilibrium, such as binary black holes in quasicircular orbits.

The evolution equation for K can be used to derive an elliptic equation for the conformal lapse $\tilde{\alpha}$ (or, equivalently, for $\alpha\psi$). Upon specification of

$$\partial_t K \equiv 0, \tag{2.36b}$$

this fifth elliptic equation is to be solved for $\tilde{\alpha}$ simultaneously with Eqs. (2.17) and (2.18), cf. [27, 29].

Our numerical code uses the conformal factor ψ, the shift β^i, and the product of lapse and conformal factor $\alpha\psi = \tilde{\alpha}\psi^7$ as independent variables, in order to simplify the equation for $\partial_t K$. Thus, the actual equations being solved take the form

$$\begin{aligned}
0 &= \tilde{\nabla}^2\psi - \frac{1}{8}\tilde{R}\psi - \frac{1}{12}K^2\psi^5 + \frac{1}{8}\psi^{-7}\tilde{A}^{ij}\tilde{A}_{ij}, && \text{(2.37a)}\\
0 &= \tilde{\nabla}_j\Big(\frac{\psi^7}{2(\alpha\psi)}(\tilde{\mathbb{L}}\beta)^{ij}\Big) - \frac{2}{3}\psi^6\tilde{\nabla}^i K \\
&- \tilde{\nabla}_j\Big(\frac{\psi^7}{2(\alpha\psi)}\tilde{u}^{ij}\Big), && \text{(2.37b)}\\
0 &= \tilde{\nabla}^2(\alpha\psi) - (\alpha\psi)\left[\frac{\tilde{R}}{8} + \frac{5}{12}K^4\psi^4 + \frac{7}{8}\psi^{-8}\tilde{A}^{ij}\tilde{A}_{ij}\right] \\
&+ \psi^5(\partial_t K - \beta^k\partial_k K), && \text{(2.37c)}
\end{aligned}$$

with

$$\tilde{A}_{ij} = \frac{\psi^7}{2\alpha\psi}\left((\tilde{\mathbb{L}}\beta)_{ij} - \tilde{u}_{ij}\right). \tag{2.37d}$$

These equations can be solved only after

1. specifying the remaining free data: i.e., the conformal metric $\tilde{g}_{ij}$ and the trace of the extrinsic curvature K (we chose already $\tilde{u}_{ij} \equiv 0$ and $\partial_t K \equiv 0$),

2. choosing an inner boundary $\mathcal{S}$ which excises the black holes' singularities, and also an outer boundary $\mathcal{B}$, and

3. choosing boundary conditions for ψ, $\alpha\psi$, and β^i on $\mathcal{B}$ and $\mathcal{S}$.

The initial data is required to be asymptotically flat, and the outer boundary $\mathcal{B}$ is placed

at infinity.[7] If $\tilde{g}_{ij}$ is asymptotically flat, the outer boundary conditions are then

$$\begin{aligned} \psi &= 1 \text{ on } \mathcal{B}, && (2.38a) \\ \alpha\psi &= 1 \text{ on } \mathcal{B}, && (2.38b) \\ \beta^i &= (\mathbf{\Omega_0} \times \mathbf{r})^i + \dot{a}_0 r^i \text{ on } \mathcal{B}. && (2.38c) \end{aligned}$$

Here r^i is the coordinate position vector. The shift boundary condition consists of a rotation (parametrized by the orbital angular velocity $\mathbf{\Omega_0}$) and an expansion (parametrized by $\dot{a}_0$); the initial radial velocity is necessary for reducing orbital eccentricity in binary-black-hole initial data [49].

The inner boundary condition on the conformal factor ψ ensures that the excision surfaces $\mathcal{S}$ are apparent horizons [29]:

$$\begin{aligned} \tilde{s}^k \partial_k \psi &= -\frac{\psi^{-3}}{8\tilde{\alpha}} \tilde{s}^i \tilde{s}^j \left[(\tilde{\mathbb{L}}\beta)_{ij} - \tilde{u}_{ij} \right] \\ &\quad -\frac{\psi}{4} \tilde{h}^{ij} \tilde{\nabla}_i \tilde{s}_j + \frac{1}{6} K \psi^3 \text{ on } \mathcal{S}. \end{aligned} \tag{2.39}$$

Here $\tilde{s}^i := \psi^2 s^i$, s^i is unit vector normal to $\mathcal{S}$, and $\tilde{h}_{ij} := \tilde{g}_{ij} - \tilde{s}_i \tilde{s}_j$ is the induced conformal 2-metric on $\mathcal{S}$.

The inner boundary condition on the shift is

$$\beta^i = \alpha s^i - \Omega_r \xi^i \text{ on } \mathcal{S}, \tag{2.40}$$

where $\xi^i s_i = 0$. The first term on the right-hand side ensures that the apparent horizons are initially at rest; the tangential term determines the black hole's spin [29, 30, 31].

References [29, 30, 31] chose the sign of the last term in Eq. (2.40) such that positive values of Ω_r counteract the spin of the corotating holes that are obtained with $\Omega_r = 0$. Here, we are interested in large spins, and we reverse the sign of the last term in Eq. (2.40) so that positive, increasing Ω_r results in increasing spins.

Two sets of choices for $\tilde{g}_{ij}$, K, $\mathcal{S}$, and the boundary condition for $\alpha\psi$ on $\mathcal{S}$ are discussed in the next subsections. Each set of choices will be used to construct binary-black-hole initial data in section 2.4.

[7] In practice, $\mathcal{B}$ is a sphere with radius $\gtrsim 10^9$ times the coordinate radius of the black-hole horizons.

Conformal flatness and maximal slicing

The simplest choice for $\tilde{g}_{ij}$ is a flat metric,

$$\tilde{g}_{ij} \equiv f_{ij}. \tag{2.41}$$

This choice has been used almost exclusively in the previous formulations of binary-black-hole initial data.

The simplest choice for K, also commonly used in prior formulations of binary-black-hole initial data, is maximal slicing, i.e.,

$$K \equiv 0. \tag{2.42}$$

Also for simplicity, we choose to make the excision surface $\mathcal{S}$ consist of coordinate spheres:

$$\mathcal{S} = \bigcup_{a=1}^{n} \mathcal{S}_a, \tag{2.43}$$

where $\mathcal{S}_a$ are surfaces of constant Euclidean distance $r_{\rm exc}$ about the center of each excised hole, and $n = 1$ or 2 is the number of black holes present in the initial data.

The boundary condition for the lapse on $\mathcal{S}$ determines the temporal gauge; we adopt the condition given in Eq. (59a) of Ref. [30]:

$$\frac{\partial}{\partial r_a}(\alpha\psi) = 0 \text{ on } \mathcal{S}_a, \tag{2.44}$$

where r_a is the Euclidean distance from the center of hole a. This type of initial data is used in Refs. [50, 49, 51].

Superposed Kerr-Schild

Single black holes with angular [52, 53] or linear [54] momentum do not admit conformally flat spatial slicings; therefore, conformal flatness [Eq. (2.41)] is necessarily deficient. This has motivated investigations of binary-black-hole initial data whose free data have stronger physical motivation, e.g., Refs. [37, 38, 55, 56, 57, 58, 59, 60, 61].

In this subsection, we consider conformally curved data that are in the same spirit as the SKS data of Refs. [37, 38] although here (i) we apply the idea to the QE-XCTS formalism, and (ii) as discussed below, our free data is very nearly conformally flat and maximally sliced *everywhere except in the vicinity of the black holes.*

The choices we make here generalize the conformally curved data in chapter 6 of Ref. [39]

to nonzero spins. Specifically, the free data and lapse boundary condition will be chosen so that the conformal geometry near each hole's horizon is that of a boosted, spinning, Kerr-Schild black hole. The conformal metric $\tilde{g}_{ij}$ and the mean curvature K take the form

$$\tilde{g}_{ij} := f_{ij} + \sum_{a=1}^{n} e^{-r_a^2/w_a^2} \left(g^a_{ij} - f_{ij} \right), \tag{2.45}$$

$$K := \sum_{a=1}^{n} e^{-r_a^2/w_a^2} K_a. \tag{2.46}$$

Here g^a_{ij} and K_a are the spatial metric and mean curvature, respectively, of a boosted, spinning Kerr-Schild black hole with mass $\tilde{M}_a$, spin $\tilde{S}_a$, and speed $\tilde{v}_a$.

Far from each hole's horizon, the conformal metric is very nearly flat; this prevents the conformal factor from diverging on the outer boundary [39]. The parameter w_a is a weighting factor that determines how quickly the curved parts of the conformal data decay with Euclidean distance r_a ($a = 1, 2, ...$) from hole a; in this work, the weight factor w_a is chosen to be larger than the size scale of hole a but smaller than the distance d to the companion hole (if any): $M_a \lesssim w_a \lesssim d_a$. This is similar to the "attenuated" superposed-Kerr-Schild data of Refs. [38, 62], except that here the weighting functions are Gaussians which vanish far from the holes, while in Refs. [38, 62] the weighting functions go to unity far from the holes.

The excision surfaces $\mathcal{S}_a$ are not coordinate spheres unless $\tilde{S}_a = 0$ and $\tilde{v}_a = 0$. Instead they are deformed in two ways. (i) They are distorted so that they are surfaces of constant Kerr radius $r_{\rm Kerr}$, i.e.,

$$\frac{x^2 + y^2}{r_{\rm Kerr}^2 + \tilde{S}_a^{\,2}/\tilde{M}_a^{\,2}} + \frac{z^2}{r_{\rm Kerr}^2} = 1 \tag{2.47}$$

where x, y, and z are Cartesian coordinates on the $\mathcal{S}$. Then, (ii) the excision surfaces are Lorentz-contracted along the direction of the boost.

The boundary condition for the lapse α on $\mathcal{S}_a$ is a Dirichlet condition that causes α (and, consequently, the temporal gauge) in the vicinity of each hole to be nearly that of the corresponding Kerr-Schild spacetime, i.e.,

$$\alpha\psi = 1 + \sum_{a=1}^{n} e^{-r_a^2/w_a^2} (\alpha_a - 1) \text{ on } \mathcal{S}_a, \tag{2.48}$$

where α_a is the lapse corresponding to the Kerr-Schild spacetime a.

2.3 Single-black-hole initial data with nearly extremal spins

In this section, we examine to which extent the formalisms presented in section 2.2 can generate single black hole initial data with nearly extremal spin. We consider first Bowen-York initial data and then conformally flat quasiequilibrium data. Since superposed-Kerr-Schild data can represent single Kerr black holes exactly, there is no need to investigate single-hole superposed-Kerr-Schild data. In section 2.4, we will both consider conformally flat and superposed-Kerr-Schild data for binary black holes.

To orient the reader, the initial data sets constructed in this section, as well as the binary-black-hole data sets constructed in section 2.4, are summarized in Table 2.1.

Unless noted otherwise, all spins presented in this section are measured using the approximate-Killing-vector spin $\chi_{\rm AKV}$ described in Appendix 2.7. Therefore, the subscript "AKV" in $\chi_{\rm AKV}$ will be suppressed for simplicity.

2.3.1 Bowen-York (puncture) initial data

As discussed in section 2.2.2, for a single spinning black hole at rest, puncture initial data is *identical* to inversion-symmetric initial data. Such solutions have been examined in the past (e.g., [48, 63]), and additional results were obtained (partly in parallel to this work) in the study by Dain, Lousto, and Zlochower [25].

We revisit this topic here to determine the maximum possible spin of Bowen-York (BY) initial data more accurately than before, to establish the power law coefficients for the approach to these limits with increasing spin parameter S, and to present new results about the geometric structure of Bowen-York initial data with very large spin parameter.

We solve Eq. (2.30) with the pseudospectral elliptic solver described in Ref. [64]. The singular point of u at the origin is covered by a small rectangular block extending from $\pm 10^{-4} m_p$ along each coordinate axis. This block overlaps four concentric spherical shells with radii of the boundaries at $8 \cdot 10^{-5} m_p, 0.005 m_p, 0.3 m_p, 50 m_p$, and $10^9 m_p$. The equations are solved at several different resolutions, with the highest resolution using 20^3 basis functions in the cube, $L = 18$ in the spheres and 26 and 19 radial basis functions in the inner and outer two spherical shells, respectively.

Because of the axisymmetry of the data set, the rotational Killing vector of the apparent horizon is simply ∂_ϕ. The integral for the quasilocal spin, Eq. (2.78) turns out to be

Label	Section	Figures	n	d	Ω_0	$\dot{a}_0 \times 10^4$	Ω_r or S/m_p^2	$\tilde{S}$	$\lvert\chi_{\rm AKV}\rvert$	$M_{\rm irr}$	M	$E_{\rm ADM}$
BY-Single	2.3.1	2.1–2.5, 2.8, 2.19	1	-	-	-	$0.01 \leq S/m_p^2 \leq 10^4$	-				
CFMS-Single	2.3.2	2.6–2.8, 2.19	1	-	-	-	$0 \leq \Omega_r \leq 0.191$	-				
CFMS	2.4.1	2.9, 2.13	2	32	0.007985	0	$0 \leq \Omega_r \leq 0.1615$	-				
SKS-0.0	2.4.2	2.11, 2.13	2	32	0.006787	0	$0 \leq \Omega_r \leq 0.24$	0				
SKS-0.5	2.4.2	2.11, 2.13	2	32	0.006787	0	$0 \leq \Omega_r \leq 0.27$	0.5				
SKS-0.93	2.4.2	2.11–2.13	2	32	0.006787	0	$0 \leq \Omega_r \leq 0.35$	0.93				
SKS-0.99	2.4.2	2.10–2.13	2	32	0.007002	3.332	$0.28 \leq \Omega_r \leq 0.39$	0.99				
SKS-0.93-E0	2.5.2	2.14	2	32	0.006787	0	0.28	0.93	0.9278	0.9371	1.131	2.243
SKS-0.93-E1	2.5.2	2.14	2	32	0.007	0	0.28	0.93	0.9284	0.9375	1.132	2.247
SKS-0.93-E2	2.5.2	2.14	2	32	0.006977	3.084	0.28	0.93	0.9275	0.9395	1.134	2.249
SKS-0.93-E3	2.5.3	2.10–2.11, 2.13–2.16, 2.19	2	32	0.007002	3.332	0.28	0.93	0.9275	0.9397	1.134	2.250
SKS-HeadOn	2.5.4	2.10–2.11, 2.13, 2.17–2.19	2	100	0	0	0.3418	0.97	0.9701	0.8943	1.135	2.257

Table 2.1: Summary of the initial data sets constructed in this work. The first row represents Bowen-York initial data for single black holes of various spins. The next two rows are quasiequilibrium, conformally flat, maximally sliced initial data for single and binary spinning black holes, respectively. All other data sets employ superposed Kerr-Schild quasiequilibrium data with the second block of rows representing *families* of initial data sets for various spins and the last block of rows representing *individual* data sets to be evolved.

independent of ψ and can be evaluated analytically with a result equal to the spin parameter, S. Thus we can use this initial data set to check how well our spin diagnostics and our ADM angular momentum diagnostic work (recall that $J_{\rm ADM}$ is also equal to the spin parameter S). This comparison is performed in Fig. 2.1, which shows relative differences between the numerically extracted values for the approximate-Killing-vector (AKV) spin, the coordinate spin (defined with the AKV spin in Appendix 2.7), and the ADM angular momentum $J_{\rm ADM}$ relative to the expected answer, S. The figure also shows differences between neighboring resolutions for the two quantities of interest below, $S/M^2 = \chi$ and $S/E_{\rm ADM}^2 = J_{\rm ADM}/E_{\rm ADM}^2 = \varepsilon_J$.

Figure 2.1 seems to show exponential convergence with increased resolution N. Since puncture data is only C^2 at the puncture, one would rather expect polynomial convergence. The effect of the nonsmoothness at the puncture is mitigated by choosing a very high resolution close to the puncture (a small cube with sides $\pm 10^{-4} m_p$ with 20^3 basis functions). Therefore, for the resolutions considered in Fig. 2.1, the truncation error is dominated by the solution away from the puncture, and exponential convergence is visible. If we used infinite-precision arithmetic and were pushing toward higher resolution than shown in Fig. 2.1, then we would expect to eventually see polynomial convergence dominated by the cube covering the puncture.

Next, we construct a series of initial data sets with increasing spin parameter S, and compute χ, ε_J, and ζ for each initial data set. The results are plotted in Fig. 2.2 and confirm earlier results [63, 26]. In addition, the inset shows that the asymptotic values $\chi_{\rm max} = 0.9837$ and $\varepsilon_{u,{\rm max}} = 0.928200$ are approached as *power laws* in the spin parameter,

$$\chi_{\rm max} - \chi \propto \left(\frac{S}{m_p^2}\right)^{-0.75}, \tag{2.49}$$

$$\varepsilon_{J,{\rm max}} - \varepsilon_J \propto \left(\frac{S}{m_p^2}\right)^{-1.4}. \tag{2.50}$$

The exponents of these power laws are computed here for the first time.

To confirm that the apparent horizon is indeed at $r = R_{\rm inv}$, we ran our apparent horizon finder on the high-spin puncture initial data sets. The horizon finder had great difficulty converging, and the reason for this becomes clear from Fig. 2.3. The main panel of this figure shows the area of spheres with coordinate radius r. The area is minimal at $r = m_p/2$, as it must be, since $m_p/2 = R_{\rm inv}$ is the radius of the inversion sphere. However, the area is almost constant over a wide range in r—for $S/m_p^2 = 10000$ over about two decades in either direction: $0.01 \lesssim r/R_{\rm inv} \lesssim 100$. Thus, the Einstein-Rosen bridge (the throat) connecting

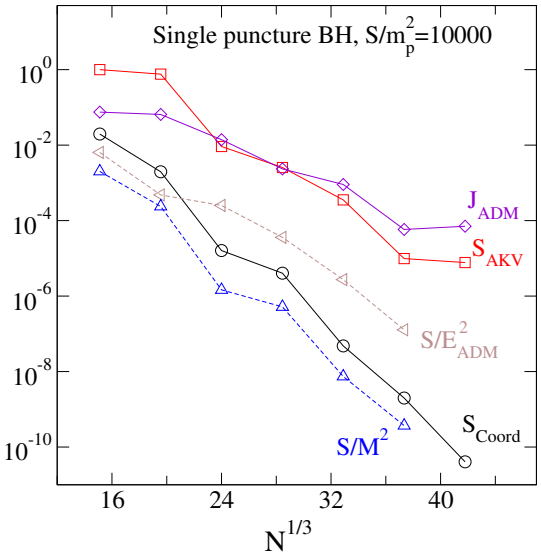

Figure 2.1: Convergence test for a single puncture black hole with a very large spin parameter $S/m_p^2 = 10000$. Plotted are results vs. resolution N, which is the total number of basis functions. The solid lines show the relative differences of three angular momentum measures to the analytically expected value 10000. The dashed lines show differences from the next-higher resolution of two dimensionless quantities for which no analytic answer is available.

the two asymptotically flat universes lengthens as the spin increases, giving rise to an ever-lengthening cylinder. If this were a perfect cylinder, then the expansion would be zero for any $r = \text{const}$ cross section. Because the geometry is not perfectly cylindrical, the expansion vanishes only for $r = m_p/2 = R_{\rm inv}$, but remains very small even a significant distance away from $r = m_p/2 = R_{\rm inv}$. This is shown in the inset, which plots the residual of the apparent horizon finder at different radii.

With the lengthening of the throat, the interval in r with small expansion lengthens, and the value of the expansion within this interval reduces. Both effects make it harder for the apparent horizon finder to converge. In Fig. 2.2, we have used our knowledge of the location of the apparent horizon to *set* $r_{\rm AH} = m_p/2$, rather than to find this surface numerically. Without this knowledge, which arises due to the identification of puncture data and inversion symmetric data, computation of Fig. 2.2 would have been significantly harder, perhaps impossible.

Let us assume for the moment that the solution $\psi(r) = \frac{m_p}{2r} + 1 + u(r)$ is spherically symmetric (we give numerical evidence below that this is indeed a good approximation).

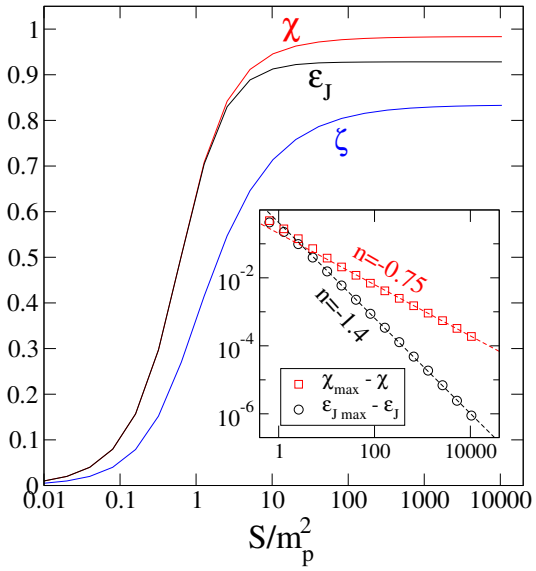

Figure 2.2: Properties of single, spinning puncture black holes with spin parameter S and puncture mass m_p. The dimensionless spin $\chi := S/M^2$, ADM angular momentum $\varepsilon_J := J_{\rm ADM}/E^2_{\rm ADM}$, and spin-extremality parameter $\zeta := S/\left(2M^2_{\rm irr}\right)$ are plotted against the spin parameter S/m_p^2. The horizon mass M is related to the spin S and irreducible mass $M_{\rm irr}$ in Eq. (2.2).

Because $g_{ij} = \psi^4 f_{ij}$, the area of coordinate spheres is then given by

$$A(r) = 4\pi\psi^4(r) r^2. \tag{2.51}$$

In the throat region, where $A(r) \approx$ const, the conformal factor must therefore behave like $1/\sqrt{r}$, as also argued independently by Dain, Lousto, and Zlochower [25].

To extend on Dain, Lousto, and Zlochower's analysis, let us substitute Eq. (2.23) into Eq. (2.24) to obtain the well-known equation

$$\tilde{\nabla}^2\psi = -\frac{9S^2\sin^2\theta}{4r^6}\psi^{-7}, \tag{2.52}$$

where θ is the angle between the spin direction and the point x^i. Continuing to assume that ψ is approximately spherically symmetric, we can replace the factor $\sin^2\theta$ by its angular average $(4\pi)^{-1}\int \sin^2\theta\, d\Omega = 2/3$, and obtain

$$\frac{d^2\bar{\psi}}{dr^2} + \frac{2}{r}\frac{d\bar{\psi}}{dr} = -\frac{3S^2}{2r^6}\bar{\psi}^{-7}. \tag{2.53}$$

Here, we introduced an overbar $\bar{\psi}$ to distinguish the spherically symmetric solution $\bar{\psi}(r)$

of Eq. (2.53) from the full solution $\psi(x^i)$ of puncture/inversion-symmetric initial data. Following Dain et *al.* [25] we assume that the conformal factor behaves as a power law ($\bar{\psi}(r) = Ar^\alpha$) and substitute this into Eq. (2.53). We find that Eq. (2.53) determines the power law exponent $\alpha = -1/2$ *and* the overall amplitude $A = (6S^2)^{1/8}$, so that

$$\bar{\psi}(r) = \frac{\left(6S^2\right)^{1/8}}{\sqrt{r}} = 96^{1/8} \left(\frac{S}{m_p^2}\right)^{1/4} \left(\frac{r}{R_{\rm inv}}\right)^{-1/2}. \tag{2.54}$$

In Eq. (2.54), we chose the scaling S/m_p^2 that is commonly used in the puncture-data literature, but kept $r/R_{\rm inv}$ to emphasize the inversion symmetry of the data in our figures (in a log-plot using $r/R_{\rm inv}$, the solution will appear symmetric, see e.g. Fig. 2.3). While $\bar{\psi}(r)$ solves the spherically symmetric Eq. (2.53) exactly, it must deviate from $\psi(x^i)$ for sufficiently large r because $\bar{\psi} \to 0$ as $r \to \infty$, whereas $\psi \to 1$. The deviation will become significant when $\bar{\psi} \sim 1$, i.e. at radius $r_x \sim \sqrt{S/m_p^2}$. Because of inversion symmetry, this implies a lower bound of validity at $1/r_x$, so that Eq. (2.54) holds for

$$\left(\frac{S}{m_p^2}\right)^{-1/2} \lesssim \frac{r}{R_{\rm inv}} \lesssim \left(\frac{S}{m_p^2}\right)^{1/2}. \tag{2.55}$$

The circumference of the cylindrical throat is

$$\mathcal{C} = 2\pi\bar{\psi}(r)^2 r = 2\pi 96^{1/4} \sqrt{\frac{S}{m_p^2}} R_{\rm inv}, \tag{2.56}$$

and its length is

$$\mathcal{L} = \int_{(S/m_p^2)^{-1/2}}^{(S/m_p^2)^{1/2}} \bar{\psi}^2(r)\, dr = 96^{1/4} \sqrt{\frac{S}{m_p^2}} \ln\left(\frac{S}{m_p^2}\right) R_{\rm inv}. \tag{2.57}$$

Therefore, the ratio of length to circumference,

$$\frac{\mathcal{L}}{\mathcal{C}} = \frac{1}{2\pi} \ln\left(\frac{S}{m_p^2}\right), \tag{2.58}$$

grows without bound as S/m_p^2 becomes large, albeit very slowly. The scaling with $(S/m_p^2)^{1/2}$ in Eqs. (2.55)–(2.57) might seem somewhat surprising. However, in the large spin limit, S/M^2 is just a constant close to unity (namely $\chi_{\rm max} = 0.9837$). Therefore, $S^{1/2} \approx M$, i.e., the scaling $S^{1/2}$ is effectively merely a scaling with mass.

Figure 2.4 shows the conformal factor ψ, the "puncture function" u, and the estimate $\bar{\psi}$ of Eq. (2.54) for three different values of S/m_p^2. There are several noteworthy features in

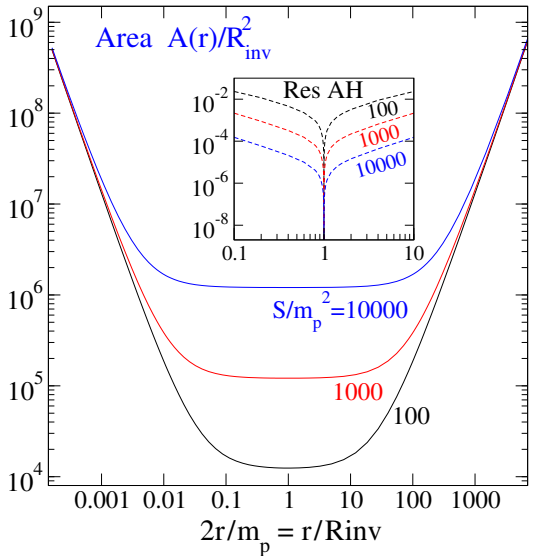

Figure 2.3: Properties of coordinate spheres with radius r for high-spin puncture initial data. *Main panel:* Area of these spheres. *Inset:* residual of the apparent horizon equation on these spheres. The area is almost constant over several orders of magnitude in r. The apparent-horizon-residual vanishes at $r = R_{\rm inv}$, but is very small over a wide range of r.

this figure. First, both ψ and u show clearly three different regimes:

- For large r, $\psi \approx 1$ and $u \propto 1/r$. This is the upper asymptotically flat end.
- For intermediate r, $\psi \propto 1/\sqrt{r}$ and $u \propto 1/\sqrt{r}$. This is the cylindrical geometry extending symmetrically around the throat. This region becomes more pronounced as S increases.
- For small r, $\psi \propto 1/r$ and $u \approx$ const. This is the lower asymptotically flat end.

Figure 2.4 also plots the approximate solution $\bar{\psi}$ [cf. Eq. (2.54)] for its range of validity [given by Eq. (2.55)]. Note that slope *and* amplitude of $\bar{\psi}$ fit very well the numerical solution ψ. In fact, the agreement is much better than with u.

One could also have started the calculation that led to Eq. (2.54) with Eq. (2.30). Assuming spherical symmetry, *and* assuming that $u \gg m_p/(2r) + 1$, we would have derived Eq. (2.53), but with $\bar{\psi}$ *replaced by* u. We would then have found the approximate behavior Eq. (2.54) *for* u. The disadvantage of this approach is the need for additional approximations, which reduce the accuracy of the result. From Fig. 2.4 we see that, in the throat region, the dotted lines representing $\bar{\psi}$ are close to the dashed lines of u. But the agreement between ψ and $\bar{\psi}$ is certainly better.

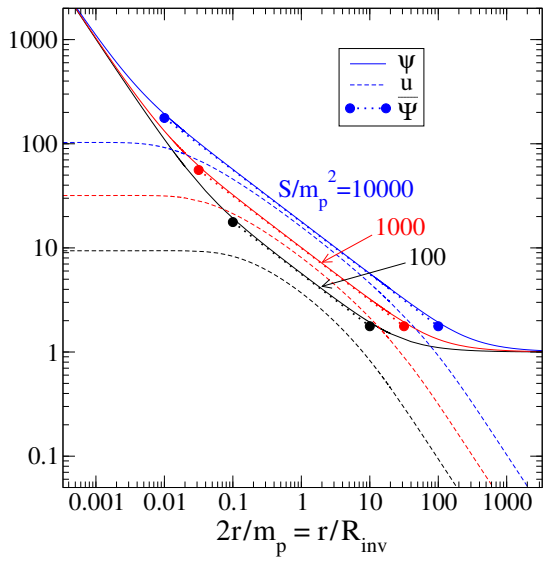

Figure 2.4: Solutions of high-spin puncture initial data. Plotted are the conformal factor ψ and puncture function u in the equatorial plane as a function of radius r. Furthermore, the approximate solution $\bar{\psi}$ is included, with solid circles denoting the range of validity of this approximation, cf. Eq. (2.55). Three curves each are plotted, corresponding from top to bottom to $S/m_p^2 = 10000, 1000, 100$.

Finally, we note that the limits of validity of $\bar{\psi}$ [Eq. (2.55)] match very nicely the points where the numerical ψ diverges from $\bar{\psi}$.

To close this section, we present numerical evidence that indeed ψ is approximately spherically symmetric, the assumption that entered into our derivation of Eq. (2.54). We decompose the conformal factor of the numerical puncture data solutions into spherical harmonics,

$$\psi(r,\theta,\phi) = \sum_{l=0}^{\infty} \sum_{m=-l}^{l} \psi_{lm}(r) Y_{lm}(\theta,\phi), \tag{2.59}$$

and plot in Fig. 2.5 the sizes of the $l \neq 0$ modes relative to the spherically symmetric mode ψ_{00}. Because of the symmetries of the problem, the only nonzero modes have $m = 0$ and even l. In the throat region, the largest nonspherically symmetric mode ψ_{20} is about a factor of 65 smaller than the spherically symmetric mode. With increasing l, ψ_{lm} decays very rapidly. Also, in both asymptotically flat ends, the nonspherically symmetric modes decay more rapidly than the $l = 0$ mode, as expected for asymptotically flat data. This figure again shows nicely the inversion symmetry of the data, under $r/R_{\rm inv} \to (r/R_{\rm inv})^{-1}$. Given the simple structure of the higher modes, it should be possible to extend the analytical analysis of the throat to include the nonspherical contributions. To do so, one would expand

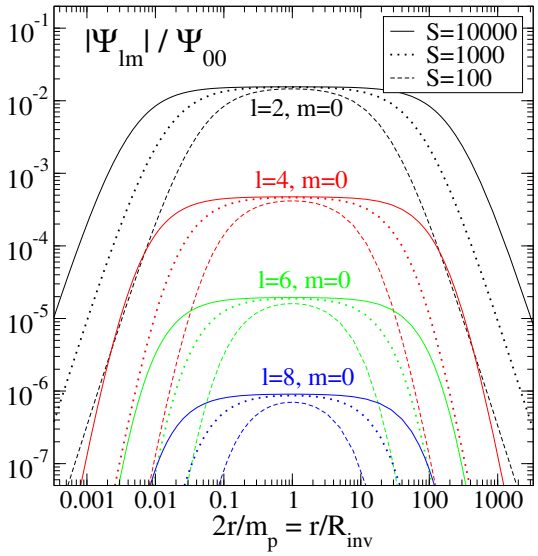

Figure 2.5: Angular decomposition of the conformal factor $\psi(r, \theta, \phi)$ for single black hole puncture data.

ψ as a series in Legendre polynomials in θ; the ψ^{-7}-term on the right-hand side of Eq. (2.52) would result in a set of ordinary differential equations for those coefficients. In the throat region, the radial behavior of each mode should be $\propto 1/\sqrt{r}$, and the ordinary differential equations should simplify to algebraic relations.

2.3.2 Quasi-equilibrium extended-conformal-thin-sandwich data

We have seen in section 2.3.1 that puncture initial data for single, spinning black holes can be constructed for holes with initial spins of $\chi \leq 0.9837$. In this section, we address the analogous question for excision black-hole initial data: how rapid can the initial spin be for a single, spinning black hole constructed using quasiequilibrium, extended-conformal-thin-sandwich (QE-XCTS) initial data?

As noted previously, if the free data $\tilde{g}_{ij}$ and K are chosen to agree with the analytic values for a Kerr black hole, $g_{ij}^{\rm Kerr}$ and $K^{\rm Kerr}$, then the QE-XCTS initial data can exactly represent a single Kerr black hole. In this case, $\chi = 1$ is obtained trivially by choosing $\tilde{S} = \tilde{M}^2 = 1$, where $\tilde{M}$ and $\tilde{S}$ are the mass and spin, respectively, of the Kerr black hole described by the conformal metric.

Setting aside this trivial solution, we construct conformally flat, maximally sliced (CFMS) data for a single, spinning hole. We construct a family of QE-XCTS initial data sets for single spinning black holes by numerically solving the XCTS equations [in the form stated

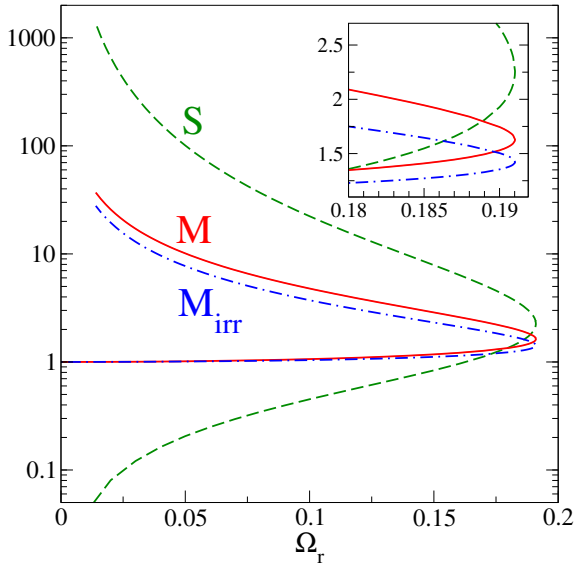

Figure 2.6: Conformally flat, maximally sliced, quasiequilibrium initial data sets with a single, spinning black hole. We plot the horizon mass M, irreducible mass $M_{\rm irr}$, and the (approximate-Killing-vector) spin S against the rotation parameter Ω_r [cf. Eq. (2.40)]. Only Ω_r is varied in this figure; all other parameters are held fixed. The upper and lower points with the same Ω_r are obtained numerically by choosing different initial guesses. The inset shows a close-up view of the turning point, which occurs at $\Omega_r \approx 0.191$.

in Eqs. (2.37a)–(2.37c)] using the same spectral elliptic solver [64] as in section 2.3.1. The free data are given by Eqs. (2.41)–(2.42) and by Eqs. (2.36a)–(2.36b).

On the outer boundary $\mathcal{B}$, we impose Eqs. (2.38a)–(2.38c). So that the coordinates are asymptotically inertial, we choose $\Omega_0 = \dot{a}_0 = 0$ in Eq. (2.38c).

We excise a coordinate sphere of radius $r_{\rm exc}$ about the origin, where

$$r_{\rm exc} = 0.85949977 \tag{2.60}$$

is chosen such that for zero spin $M = 1$. On this inner boundary $\mathcal{S}$, we impose Eqs. (2.39)–(2.40) and Eq. (2.44). The spin is determined by Eq. (2.40): first, the vector ξ^i is chosen to be the coordinate rotation vector ∂_ϕ, making the spin point along the positive z-axis; then, the rotation parameter Ω_r is varied while the other parameters are held fixed. The spin is measured on the apparent horizon using the approximate-Killing-vector spin (Appendix 2.7); because in this case the space is axisymmetric, the "approximate" Killing vector reduces to the corresponding exact rotational Killing vector.

Figure 2.6 shows how the mass M and AKV spin S depend on Ω_r. At $\Omega_r = 0$, we find the spherically symmetric solution with $S = 0$ and $M_{\rm irr} = M = 1$ (the mass is proportional

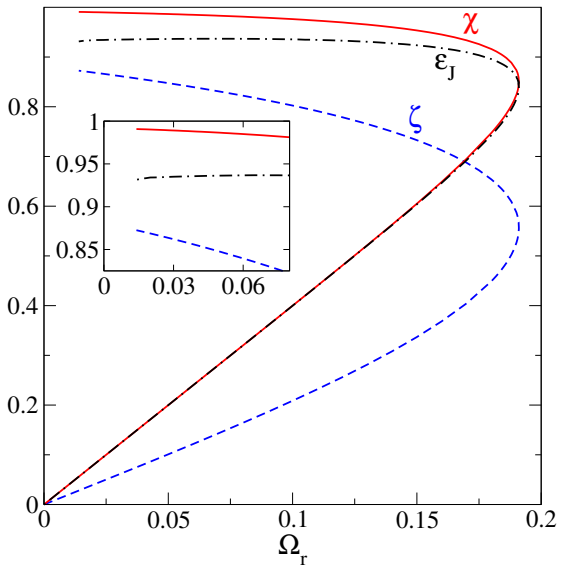

Figure 2.7: Conformally flat, maximally sliced quasiequilibrium initial data sets with a single spinning black hole: The dimensionless spin χ, dimensionless ADM angular momentum ε_J, and spin-extremality parameter ζ plotted against Ω_r [cf. Eq. (2.40)]. Only Ω_r is varied in this figure; all other parameters are held fixed. The inset enlarges the area in the upper left corner; we are able to generate data sets with $\chi > 0.99$, whereas the largest spin obtainable on the lower branch is $\chi \approx 0.85$.

to the excision radius, and Eq. (2.60) sets it to unity). Using this spherically symmetric solution as an initial guess for the elliptic solver, we find solutions for increasing Ω_r with spin increasing initially linearly with Ω_r and with approximately constant mass. Beyond some critical $\Omega_{\rm r,crit}$, the elliptic solver fails to converge, and close to this point, all quantities vary in proportion to $\sqrt{\Omega_{r,\rm crit} - \Omega_r}$. These symptoms indicate a critical point where the solutions "turn over" and continue towards smaller Ω_r. Analogous nonunique solutions of the XCTS equations have been discovered before in Ref. [34]. To construct solutions along the upper branch, one must choose a sufficiently close initial guess for the elliptic solver; we follow the steps outlined in Ref. [34] and are able to find solutions along the upper branch for a wide range of $\Omega_r < \Omega_{\rm r,crit}$. As Fig. 2.6 shows, the mass and spin of the horizon in solutions along the upper branch increase with decreasing Ω_r, analogous to the findings in [34, 35].

Figure 2.7 shows the dependence of $\chi = S/M^2$, $\varepsilon_J = J_{\rm ADM}/E^2_{\rm ADM}$, and $\zeta = S/\left(2M^2_{\rm irr}\right)$ on Ω_r. The curves reflect again the nonunique solutions. The dimensionless spin χ increases continuously along the lower branch, and reaches $\chi \approx 0.85$ at the critical point. As Ω_r is decreased along the upper branch, χ continues to increase, eventually reaching values larger

than 0.99. It appears χ continues to increase as $\Omega_r \to 0$. To find the limiting value, consider that the behavior of the extremality parameter ζ in the inset of Fig. 2.7. Assuming that ζ can be extrapolated to $\Omega_r \to 0$, we find a limiting value of $\zeta \approx 0.88$. By Eq. (2.9), this implies a maximal value of $\chi \approx 0.992$.

In Figs. 2.6–2.7, the data sets on the lower branch appear to be physically reasonable. For spins $\chi \lesssim 0.85$, the mass M is nearly constant, and the dimensionless spin χ increases linearly with Ω_r. Furthermore, as $\Omega_r \to 0$ the lower branch continuously approaches the exact Schwarzschild spacetime (see [30]). The upper branch appears to be physically less reasonable; for instance, the spin χ increases for *decreasing* horizon frequency Ω_r. Comparing Figs. 2.2 and 2.7, we see that the QE-XCTS data leads to somewhat larger values of χ and ε_J relative to puncture data. However, the values are not too different, and similar trends remain. For instance, χ is much closer to unity than ε_J.

To investigate differences or similarities between puncture data and QE-XCTS data further, we compute embedding diagrams of the equatorial planes of these data sets. The initial data for single black holes have rotational symmetry about the z-axis, so the metric (2.12) on the initial data hypersurface, when restricted to the equatorial plane, can be written as

$$ds^2 = \psi^4 \left(dr^2 + r^2 d\phi^2 \right), \tag{2.61}$$

where r and ϕ are the usual polar coordinates. This metric is now required to equal the induced metric on the 2-D surface given by $\mathrm{Z} = \mathrm{Z}(\mathrm{R})$ embedded in a 3-D Euclidean space with line element

$$ds^2_{\text{Euclidean}} = d\mathrm{R}^2 + \mathrm{R}^2 d\phi^2 + d\mathrm{Z}^2. \tag{2.62}$$

Setting $d\mathrm{Z} = \frac{d\mathrm{Z}}{d\mathrm{R}} d\mathrm{R}$, we obtain the induced metric on the $\mathrm{Z} = \mathrm{Z}(\mathrm{R})$ surface

$$ds^2 = \left[1 + \left(\frac{d\mathrm{Z}}{d\mathrm{R}} \right)^2 \right] d\mathrm{R}^2 + \mathrm{R}^2 d\phi^2. \tag{2.63}$$

Equating Eqs. (2.61) and (2.63), we find

$$\mathrm{R} = \psi^2 r \tag{2.64}$$

and

$$\left[1 + \left(\frac{d\mathrm{Z}}{d\mathrm{R}} \right)^2 \right] d\mathrm{R}^2 = \psi^4 dr^2. \tag{2.65}$$

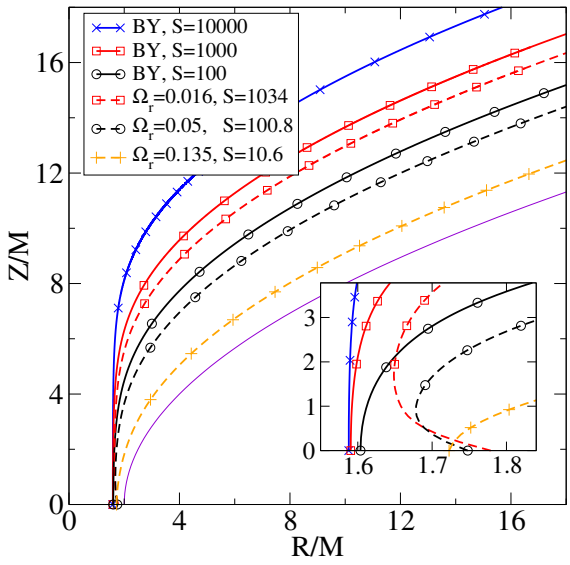

Figure 2.8: Embedding diagrams for puncture and quasiequilibrium initial data. Plotted is the embedding height Z as a function of the embedding radius R, both scaled by the mass M. For quasiequilibrium data (dashed lines), Z=0 at $r = r_{\rm exc}$; for puncture data (solid lines), Z=0 at $r = R_{\rm inv}$. The thin solid purple curve represents the embedding of a plane through a Schwarzschild black hole in Schwarzschild slicing.

Combining (2.65) and (2.64) results in

$$\left(\frac{d\mathrm{Z}}{dr}\right)^2 = -4r\psi^2\frac{d\psi}{dr}\left(\psi + r\frac{d\psi}{dr}\right). \tag{2.66}$$

Since the pseudospectral elliptic solver gives ψ as a function of r, Eqs. (2.64) and (2.66) allow us to solve for the embedding radius R and the embedding height Z in terms of r.

Figure 2.8 shows embedding diagrams for three sets of QE-XCTS and puncture data. We have set Z=0 at $r = r_{\rm exc}$ for QE-XCTS data and at $r = R_{\rm inv}$ for puncture data. This figure also contains the embedding of a plane through Schwarzschild in Schwarzschild coordinates (i.e. the $S = 0$ limit of BY puncture data), given by $R/M = Z^2/(8M^2) + 2$. Both puncture data and CFMS data exhibit a lengthening throat with increasing spin S/M^2. For puncture data, this lengthening can be deduced from the analytical results in section 2.3.1: as the spin parameter S of the puncture data increases by a factor of 10 while $m_p \equiv 1$ is held constant, we find from Eq. (2.57) that $\mathcal{L}/S^{1/2}$ should increase by

$$\Delta\mathcal{L}/S^{1/2} = \frac{96^{1/4}}{2}\ln 10 \approx 3.60, \tag{2.67}$$

where the factor 1/2 arises because $R_{\rm inv} = m_p/2 = 0.5$. The embedding diagram shows only the top half of the throat, and $S^{1/2} \approx M$ [cf. the discussion after Eq. (2.58)]. Therefore in Fig. 2.8 the $S = 100, 1000, 10000$ lines for BY (puncture) data should be spaced by $\Delta Z/M \approx 1.80$ for large R/M. This indeed is the case.

The CFMS data sets appear to scale proportionally to $\sqrt{S}$, which is similar to the puncture data's behavior. Furthermore, the CFMS initial data sets also develop a lengthening throat as S becomes large (the effect is not as pronounced as for puncture data, owing to the smaller maximal S we achieved.) Thus it appears that large spin CFMS data might be similar to large spin puncture data. However, the throats of the QE-XCTS data show a bulge near the bottom, because for these data sets R actually decreases with r in the immediate vicinity of $r_{\rm exc}$. This is unlike the puncture data, which very clearly exhibit cylindrical throats, consistent with the discussion leading to (2.58).

2.4 Binary-black-hole initial data with nearly extremal spins

In this section, we construct binary-black-hole initial data with rapid spins, confining our attention to the special case of spins aligned with the orbital angular momentum. In the limit of large separation, binary-black-hole puncture initial data will behave like two individual puncture initial data sets. Specifically, we expect that it should be possible to construct puncture binary-black-hole initial data with initial spins $\chi(t=0) \lesssim 0.98$, but the spins will rapidly drop to $\chi \lesssim 0.93$ as the black holes settle down. For this reason, and also because puncture data is not well suited to our pseudospectral evolution code, we will restrict our attention to binary black holes constructed with the QE-XCTS approach.

As laid out in Table 2.1, we first construct a family (labelled CFMS) of standard conformally flat initial data on maximal slices; then, we turn our attention to families (labelled SKS) of superposed Kerr-Schild initial data. Finally, we construct a few individual SKS initial-data sets which we evolve in section 2.5. All of the data sets represent equal-mass, equal-spin black holes with spins parallel to the orbital angular momentum.

In this section, unless otherwise indicated, all dimensionless spins are the approximate-Killing-vector spin $\chi_{\rm AKV}$ (Appendix 2.7), and the subscript "AKV" will be suppressed for simplicity.

2.4.1 Conformally flat, maximal slicing data

To construct conformally flat binary-black-hole data, we solve the same equations and boundary conditions as for the single-black-hole case, as described in section 2.3.2, with the main difference being that we excise *two* spheres with radius $r_{\rm exc}$ [cf. Eq. (2.60)] with centers on the x-axis at $x = \pm d/2$. The initial spins of the holes are set by adjusting Ω_r, just as in the single-hole case. The parameters $\mathbf{\Omega_0}$ and $\dot{a}_0$ in the outer boundary condition on the shift [Eq. 2.38c] determine the initial angular and radial motion of the holes, which in turn determine the initial eccentricity e of the orbit. We set $\mathbf{\Omega_0} = \Omega_0 \mathbf{e}_z$, where $\mathbf{e}_z$ is a unit vector that points along the positive z-axis. For the CFMS family of data sets considered here, we use values for Ω_0 and $\dot{a}_0$ that should result in closed, fairly circular orbits, since our choices of Ω_0 and $\dot{a}_0$ lead to data sets that approximately satisfy the Komar-mass condition $E_{\rm ADM} = M_K$ (cf. [31]). Specifically, on the lower branch of the resulting nonunique family of initial data,

$$\frac{|E_{\rm ADM} - M_K|}{E_{\rm ADM}} \lesssim 1\%, \tag{2.68}$$

where the Komar mass is defined by (e.g., Eq. (35) of Ref. [31])

$$M_K := \frac{1}{4\pi} \oint_\infty \left(\nabla_i \alpha - \beta^j K_{ij} \right) \, dA. \tag{2.69}$$

(On the upper branch, $E_{\rm ADM}$ and M_K differ by up to 3%.)

As the rotation parameter Ω_r is varied (with the coordinate separation d held fixed), we find that the CFMS-family of binary-black-hole initial data behaves qualitatively similarly to the analogous single-black-hole initial data discussed in section 2.3.2. There is a maximal $\Omega_{r,\rm crit}$ such that no solutions can be found for $\Omega_r > \Omega_{r,\rm crit}$; for values of Ω_r below $\Omega_{r,\rm crit}$, two solutions exist. Figure 2.9 plots the dimensionless spin χ and the spin-extremality parameter ζ against Ω_r for this family of initial data. We only show values for one of the holes, since the masses and spins are equal. Spins larger than $\chi \approx 0.85$ appear on the upper branch. The highest spin we have been able to construct is larger than $\chi = 0.97$.

2.4.2 Superposed-Kerr-Schild data

In this section, we solve the same equations and boundary conditions as in the conformally flat case, except that we use SKS free data instead of conformally flat free data. To construct the individual Kerr-Schild data, we need to choose for each black hole the coordinate location

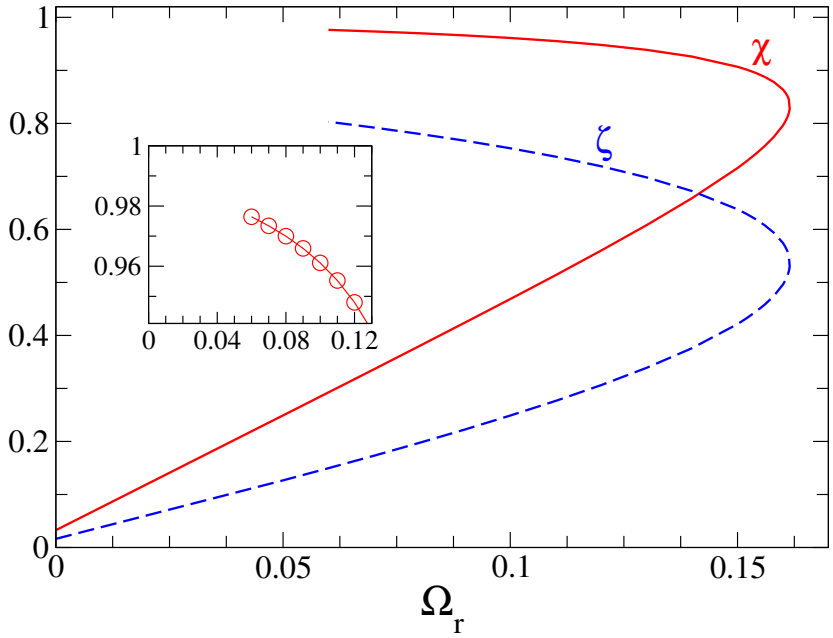

Figure 2.9: *Main panel:* Dimensionless spin χ [Eq. (2.1)] and spin-extremality parameter ζ [Eq. (2.8)] for the family CFMS of spinning binary-black-hole initial data. *Inset:* Enlargement of χ toward the end of the upper branch, with circles denoting the individual initial data sets that were constructed. Compare with Fig. 2.7.

of its center, its conformal mass $\tilde{M}$, conformal spin $\tilde{S}$, and its boost velocity. We center the black holes on the x-axis at $x = \pm d/2$, use the same mass $\tilde{M} = 1$ for both black holes, and set the boost velocity to $(0, \pm d\,\Omega_0/2, 0)$. The conformal spins are always equal and are aligned with the orbital angular momentum of the holes.

In contrast to the CFMS data, there are now *two* parameters that influence the black holes' spins: (i) the rotation parameter Ω_r in Eq. (2.40), and (ii) the conformal spin $\tilde{S}$. For concreteness, we choose to construct data for four different values of the conformal spin: $\tilde{S}/\tilde{M}^2 = 0, 0.5, 0.93$, and 0.99. For each choice, we construct a family of initial data sets for different values of Ω_r, which we label as SKS-0.0, SKS-0.5, SKS-0.93, and SKS-0.99 respectively.

Other choices that went into the construction of the SKS initial data sets are as follows:

- The excision boundaries are chosen to be the coordinate locations of the horizons of the individual Kerr-Schild metrics, i.e., they are surfaces of constant Kerr-radius

$$r_{\rm exc}^{\rm Kerr} = \tilde{r}_+ := \tilde{M} + \sqrt{\tilde{M}^2 - \tilde{S}^2}, \tag{2.70}$$

length contracted by the Lorentz-factor appropriate for the boost velocity of each black hole. This length contraction accounts for the tangential motion of the hole but neglects the much smaller radial motion.

- When superposing the individual Kerr-Schild metrics, we use a damping length scale $w = 10 r_{\rm exc}^{\rm Kerr}$ [cf. Eqs. (2.45) and (2.46)], except for the SKS-0.99 family, which uses $w = d/3$.

- The orbital frequency Ω_0 and radial expansion $\dot{a}_0$ are held fixed along each family. We expect that our choices for Ω_0 and $\dot{a}_0$ will lead to bounded, fairly circular orbits, since

$$\frac{|E_{\rm ADM} - M_K|}{E_{\rm ADM}} \lesssim 3\%. \tag{2.71}$$

  In section 2.5.2 we reduce the orbital eccentricity for one data set in the family SKS-0.93.

We again solve the XCTS equations using the spectral elliptic solver of Ref. [64]; the families of SKS initial data sets that we construct are summarized in Table 2.1. The elliptic solver needs some initial guess for the variables to be solved for; we superpose the respective single-black hole Kerr-Schild quantities, i.e.

$$\psi = 1, \tag{2.72a}$$

$$\alpha\psi = 1 + \sum_{a=1}^{n} e^{-r_a^2/w_a^2}(\alpha_a - 1), \tag{2.72b}$$

$$\beta^i = \sum_{a=1}^{n} e^{-r_a^2/w_a^2}\beta_a^i, \tag{2.72c}$$

where $n = 2$ and α_a and β_a^i are the lapse and shift corresponding to the boosted, spinning Kerr-Schild metrics g_{ij}^a used in the conformal metric $\tilde{g}_{ij}$. Convergence of the elliptic solver and spin are demonstrated in Fig. 2.10 by showing the decreasing constraint violation[8] and differences in spin with increasing resolution.

We now turn our attention to the physical properties of the SKS initial data sets. Figure 2.11 shows the horizon mass M and the dimensionless spin χ of either black hole for the four families of SKS initial data. As expected, we find that generally the spin χ increases

[8]The constraint violation is $\sqrt{\|\mathcal{C}\|_{L2}^2 + \|\mathcal{C}\|_{L2}^i \|\mathcal{C}\|_{L2}^j \delta_{ij}}$, where $\mathcal{C}$ and $\mathcal{C}^i$ are the residuals of Eqs. (2.10)–(2.11) and the L2 norm is given by Eq. (2.73).

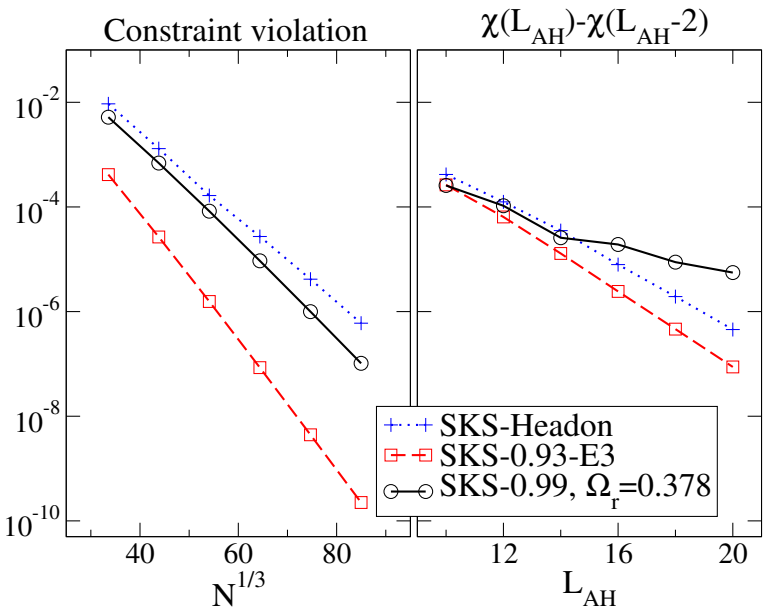

Figure 2.10: Convergence of the spectral elliptic solver. *Left panel*: The residual constraint violation as a function of the total number of grid points N. *Right panel:* Convergence of the black hole dimensionless spin χ [Eq. (2.1)] with increasing resolution $L_{\rm AH}$ of the apparent horizon finder, applied to the highest-resolution initial data set of the left panel.

with increasing Ω_r. For each of the SKS-families, we find that the elliptic solver fails to converge for sufficiently large Ω_r. We suspect that the SKS-families exhibit a turning point, similar to the CFMS-single and binary black hole initial data shown in Figs. 2.7 and 2.9. If this is the case, Fig. 2.11 only shows the lower branch of each family, and an additional branch of solutions will be present. Because we are satisfied with the spin magnitudes that are possible along the lower branch, we do not attempt to find the upper branch here.

In contrast to the CFMS data sets (where the lower branch only allowed spins as large as $\chi \lesssim 0.85$), the SKS initial data allows spins that are quite close to unity. For the different SKS families, we are able to construct initial data with spins as large as

- $\chi \approx 0.95$ for SKS-0,
- $\chi \approx 0.985$ for SKS-0.5,
- $\chi \approx 0.998$ for SKS-0.93,
- $\chi \approx 0.9997$ for SKS-0.99.

These spins are far closer to extremal than possible with Bowen-York initial data [$\chi \lesssim 0.984$ (Fig. 2.2)] or conformally flat, maximally sliced XCTS initial data [$\chi \lesssim 0.85$ or $\lesssim 0.99$ along the lower and upper branch, respectively (Fig. 2.7)].

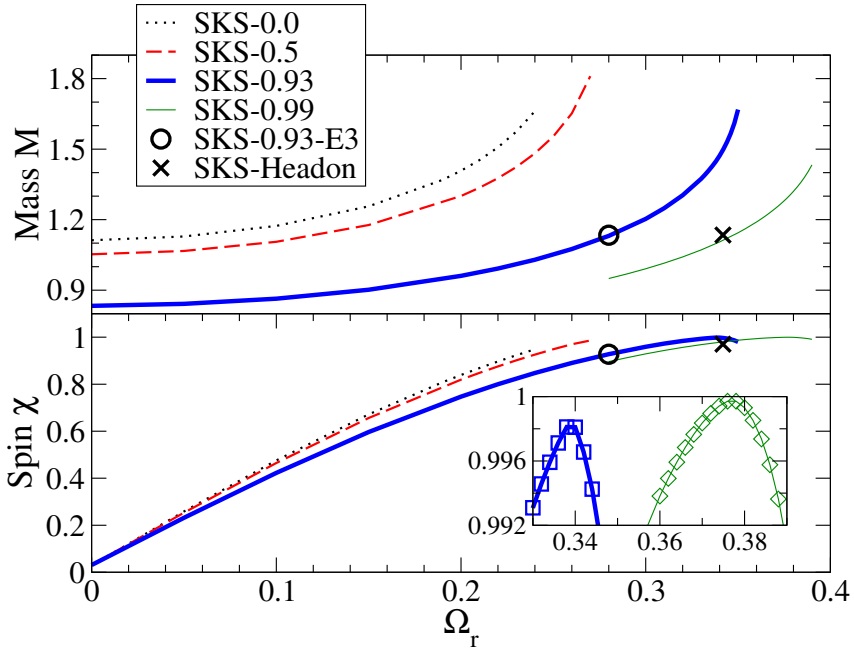

Figure 2.11: The mass M (*upper panel*) and dimensionless spin χ (*lower panel*) of one of the holes for superposed-Kerr-Schild (SKS) data sets, plotted against Ω_r. The *inset* in the lower panel shows a close-up of the spins as they approach unity, with symbols denoting the individual data sets.

We note that the spins in the SKS binary-black-hole initial data families are only weakly dependent on the orbital parameters Ω_0 and $\dot{a}_0$. This can be seen from the individual data-point labeled SKS-0.93-E3 shown in Fig. 2.11. This data set uses different values for Ω_0 and $\dot{a}_0$ but is nevertheless close to the family SKS-0.93. The initial data sets SKS-0.93-E3 and SKS-HeadOn will be discussed in detail in section 2.5.

The inset of Fig. 2.11 highlights a remarkable feature of the SKS-0.93 and SKS-0.99 families: with increasing Ω_r, the spin initially increases but eventually *decreases*. Figure 2.12 investigates this behavior in more detail, where this effect is more clearly visible in the lower two panels: both the spin χ and the extremality parameter ζ of the apparent horizon change direction and begin to decrease. For Ω_r smaller than this critical value, the apparent horizon finder always converges onto the excision surfaces, which by virtue of the boundary condition Eq. (2.39), are guaranteed to be marginally trapped surfaces. As Ω_r is increased through the critical value (at which χ and ζ change direction), a *second* marginally trapped surface (solid line) splits off from the excision surface (dashed line) and moves continuously outward. This can be seen in the upper panels of Fig. 2.12, which plot the minimal and maximal coordinate radius and the irreducible mass of both the excision surface and the

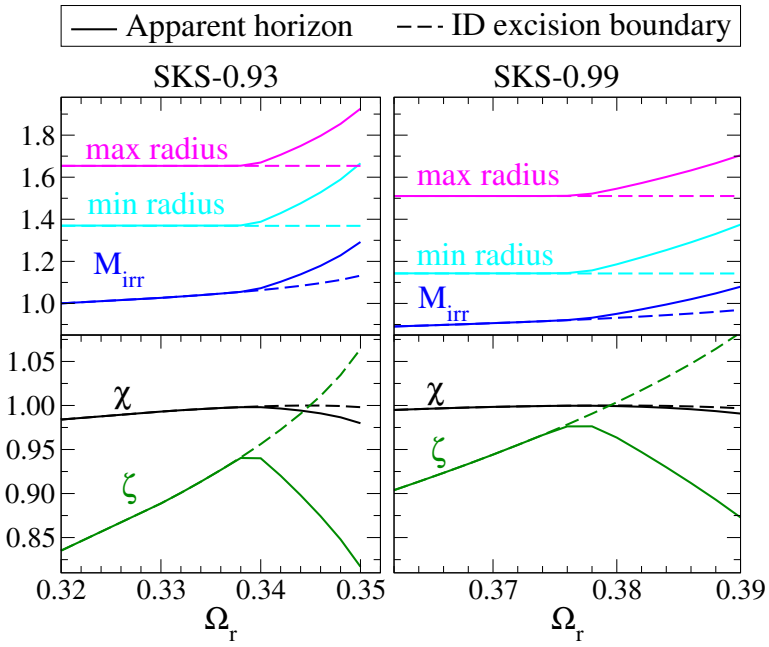

Figure 2.12: The irreducible mass $M_{\rm irr}$ and Euclidean coordinate radius r (*upper panels*) and dimensionless spin $\chi := S/M^2$ and spin-extremality parameter $\zeta := S/(2M_{\rm irr}^2)$ (*lower panels*) for one of the black holes in the SKS-0.93 (*left*) and SKS-0.99 (*right*) initial data families. These quantities are computed on two surfaces: (i) the apparent horizon (solid lines), and (ii) the excision boundary of the initial data (dashed lines).

outermost marginally trapped surface, which is by definition the apparent horizon.

But what about the excision surface? The boundary condition Eq. (2.39) forces the excision surface to be a marginally trapped surface, independent of the value of Ω_r. For sufficiently large Ω_r, however, the excision surface is surrounded by a larger marginally trapped surface and thus is *not* the apparent horizon. The dashed lines in Fig. 2.12 present data for the excision surface. These lines continue smoothly across the point where the second marginally trapped surface forms. The extremality parameter ζ for the excision surface continues to increase and eventually becomes larger than unity; the excision surface can then be thought of as having a superextremal spin. However, for the outer marginally trapped surface—the true apparent horizon—the extremality parameter always satisfies $\zeta < 1$. The irreducible mass $M_{\rm irr}$ of this surface increases faster than the spin, and therefore $\zeta = S/(2M_{\rm irr}^2)$ decreases with increasing Ω_r.

One might interpret these results as support of the cosmic censorship conjecture. The XCTS boundary conditions (2.39) and (2.40) control the location and the spin of the excision surface. By appropriate choices for the shift boundary condition (2.40), we can force the

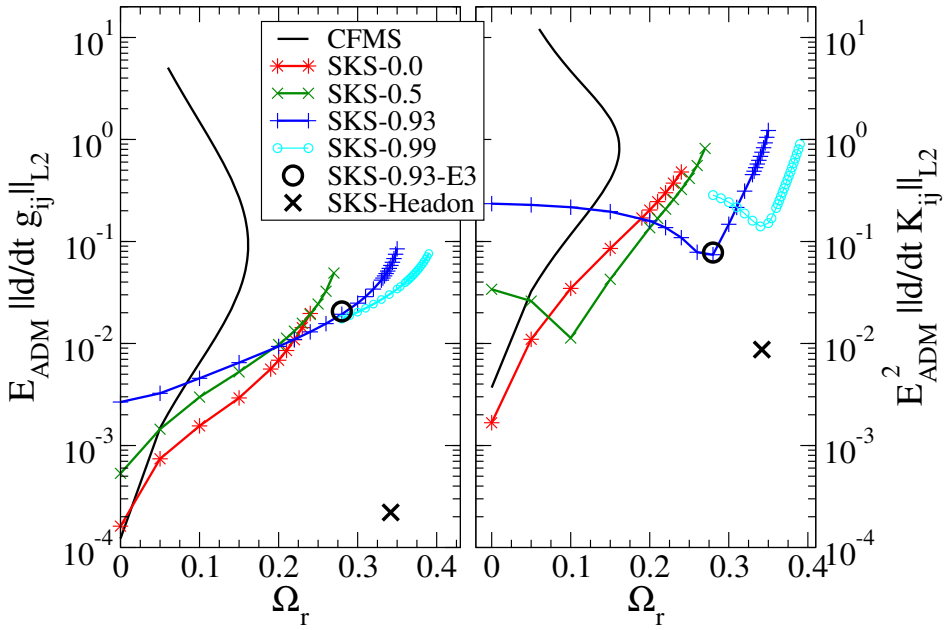

Figure 2.13: The time derivatives of the metric (*left panel*) and extrinsic curvature (*right panel*). In the superposed-Kerr-Schild (SKS) data sets, $\|\partial_t K_{ij}\|_{L2}$ has minima near values of Ω_r for which the dimensionless spin χ is approximately equal to the spin $\tilde{S}$ of the conformal metric (cf. Fig. 2.11). On the upper branch of the conformally flat, maximally sliced (CFMS) excision data, where the spin is $\chi > 0.83$ (Fig. 2.9), the time derivatives become much larger than the SKS time derivatives.

excision surface to become superextremal. However, before this can happen, a new horizon appears, surrounding the excision surface and hiding it from "our" asymptotically flat end of the spacetime. The newly formed outer horizon always remains subextremal.

2.4.3 Suitability for evolutions

In the previous sections, we have constructed a wide variety of binary-black-hole initial data sets. To get some indication about how suitable these are for evolutions, we consider the initial time derivatives of these data sets, $\partial_t g_{ij}$ and $\partial_t K_{ij}$. Recall that solutions of the XCTS equations give a preferred initial lapse and shift for the evolution of the initial data; hence, the time derivatives $\partial_t g_{ij}$ and $\partial_t K_{ij}$ can be computed by simply substituting the initial data into the ADM evolution equations. We expect initial data with smaller time derivatives to be closer to quasiequilibrium and to have less initial spurious radiation.

Figure 2.13 presents the L2 norms of the time derivatives, $\|\partial_t g_{ij}\|_{L2}$ and $\|\partial_t K_{ij}\|_{L2}$

where the L2 norm of a tensor $T_{ijk\cdots}(x)$ evaluated at N grid points x_i is defined as

$$\|T_{ijk\cdots}\|_{L2} := \sqrt{\frac{1}{N}\sum_{i=0}^{N}\bar{T}^2(x_i)}, \tag{2.73}$$

where

$$\bar{T} := \sqrt{T_{ijk\cdots}T_{i'j'k'\cdots}\delta^{ii'}\delta^{jj'}\delta^{kk'}\cdots}. \tag{2.74}$$

Figure 2.13 shows that generally $\partial_t K_{ij}$ is larger than $\partial_t g_{ij}$. This has also been found in previous work, e.g., [65], and is not surprising, because the XCTS formalism allows some control over the time derivative of the metric through the free data $\tilde{u}_{ij} = \partial_t \tilde{g}_{ij}$, whereas there is less control of $\partial_t K_{ij}$. We note that for CFMS data, the time derivatives are larger and grow more rapidly with χ than for SKS data; in particular, the time derivatives on the upper branch are $\sim$10 times larger than for SKS-initial data, suggesting that these data are much farther from equilibrium.

In the SKS case, the time derivatives of K_{ij} have local minima at particular values of Ω_r; comparison with Fig. 2.11 gives spins χ at these minima of $\|\partial_t K_{ij}\|_{L2}$ as follows:

- SKS-0.5: $\Omega_r \approx 0.1$, $\chi \approx 0.45$,
- SKS-0.93: $\Omega_r \approx 0.28$, $\chi \approx 0.93$,
- SKS-0.99: $\Omega_r \approx 0.34$, $\chi \approx 0.98$.

Note that these minima occur at values of Ω_r such that $\chi \approx \tilde{S}/\tilde{M}^2$; that is, transients in the initial data and presumably the spurious radiation are minimized when the conformal spin and AKV spin are consistent. For this reason, we conclude that SKS initial data with $\chi \approx \tilde{S}/\tilde{M}^2$ is preferable; this is the type of initial data we will evolve in the next section.

Also note that minimizing the spurious radiation has purely numerical advantages: the spurious radiation typically has finer structure (and thus requires higher resolution) than the physical radiation. If such radiation is minimized, the numerical evolutions may require less resolution and will be more efficient. Conformally-curved initial data has been found to reduce the amount of spurious radiation in Refs. [66, 39].

2.5 Exploratory evolutions of superposed Kerr-Schild initial data

So far, we have confined our discussion to black hole spins in the *initial data*. In this section, we compare the initial spin to the value to which the spin relaxes after the initial burst of spurious radiation, when the holes have settled down. Recall, for instance, that for Bowen-York puncture initial data with spins close to the maximal possible value [$\chi(t = 0) \approx 0.98$], the spins quickly relax by about $\Delta\chi \approx 0.05$ to a maximal possible relaxed value of $\chi(t_{\rm relax}) \approx 0.93$ (cf. [25]). While the SKS data presented in section 2.4.2 can achieve larger initial spins [$\chi(t = 0) = 0.9997$] than conformally flat puncture data, only evolutions can determine $\Delta\chi$ and $\chi(t_{\rm relax})$.

Therefore, in this section we perform brief, exploratory evolutions of some SKS initial data sets to determine $\Delta\chi$ for those data sets.[9] Besides determination of $\chi(t_{\rm relax})$, these evolutions will also allow us to demonstrate that the technique of eccentricity reduction developed in Ref. [49] is applicable to SKS initial data as well as to compare the spin measures defined in Appendices 2.7 and 2.8. The focus here lies on initial data, and we evolve only long enough for our purposes. Longer simulations that continue through merger and ringdown are the subject of ongoing research.

This section is organized as follows. In section 2.5.1, we summarize the evolution code that we will use. In section 2.5.2, we perform eccentricity reduction on one of the data sets in the SKS-0.93 family, which corresponds to an orbiting binary black hole with equal masses and equal spins (of magnitude $\chi \approx 0.93$) aligned with the orbital angular momentum. Then, in section 2.5.3, we evolve the resulting low-eccentricity data set (labeled SKS-0.93-E3). Finally, in section 2.5.4, we evolve a head-on plunge of SKS initial data (labeled SKS-Headon) representing two widely separated black holes with initial spins of magnitude $\chi = 0.970$ and direction normal to the equatorial plane.

2.5.1 Description of evolution code

The initial data are evolved using the Caltech-Cornell pseudospectral evolution code `SpEC` [50]. The details of the evolution methods, equations, and boundary conditions that we use are the same as those described in Ref. [67]. The singularities are excised, with the excision

[9] Note that there is no universal value of $\Delta\chi$—it will differ for different initial data sets, even within the same family of initial data.

surfaces chosen to lie slightly inside the black hole horizons. Note that whereas Ref. [67] excises coordinate spheres inside the black holes' apparent horizons, here we use Lorentz-contracted ellipsoidal excision boundaries which are adapted to the shape of the initial apparent horizons.

The highest-resolution initial data set (with $N \approx 85^3$ grid points) is interpolated onto evolution grids labelled $N1$, $N2$, and $N3$ with approximately 61^3, 67^3, and 74^3 grid points, respectively. The outer boundary is at a coordinate radius of $r = 32d$ for the orbiting simulation discussed in sections 2.5.2 and 2.5.3 and at $r = 14d$ for the head-on simulations discussed in section 2.5.4. This translates to about $r = 450E_{\rm ADM}$ and $r = 620E_{\rm ADM}$ for the orbiting and head-on simulations, respectively. As in earlier simulations [50, 49, 67], a small region of the evolution grid lies inside the horizon and is not covered by the initial data grid; we extrapolate ψ, $\alpha\psi$, and β^i into this region and then compute g_{ij} and K_{ij}.

2.5.2 Eccentricity removal

We obtain initial data with small orbital eccentricity using the iterative method of Ref. [49], as refined in Ref. [67], applied here for the first time to binary-black-hole data with rapid spin. In this method, the choice of Ω_0 and $\dot{a}_0$ for the next iteration are made so that if the orbit were Newtonian, the eccentricity would vanish. For the non-Newtonian orbit here, successive iterations succeed in reducing the orbital eccentricity.

This procedure is based on the proper separation s between the apparent horizons, measured along a coordinate line connecting the geometric centers of the apparent horizons. The time derivative ds/dt is fitted to a five-parameter curve that, together with the initial proper separation $s(t=0)$ is used to define the eccentricity e and to define improved values for Ω_0 and $\dot{a}_0$. Specifically,

$$\frac{ds}{dt} := A_0 + A_1 t + B\cos\left(\omega t + \varphi\right), \tag{2.75a}$$

$$e := \frac{B}{\omega s(t=0)}, \tag{2.75b}$$

$$\Omega_{0,\rm new} := \Omega_0 + \frac{B\sin\phi}{2\ s(t=0)}, \tag{2.75c}$$

$$\dot{a}_{0,\rm new} := \dot{a}_0 - \frac{B\cos\phi}{s(t=0)}. \tag{2.75d}$$

Heuristically, the eccentricity is embodied by the oscillating part of ds/dt.

Figure 2.14 illustrates the eccentricity reduction for one of the data sets in family SKS-0.93. Plotted are the proper separation s and its derivative ds/dt for evolutions of several

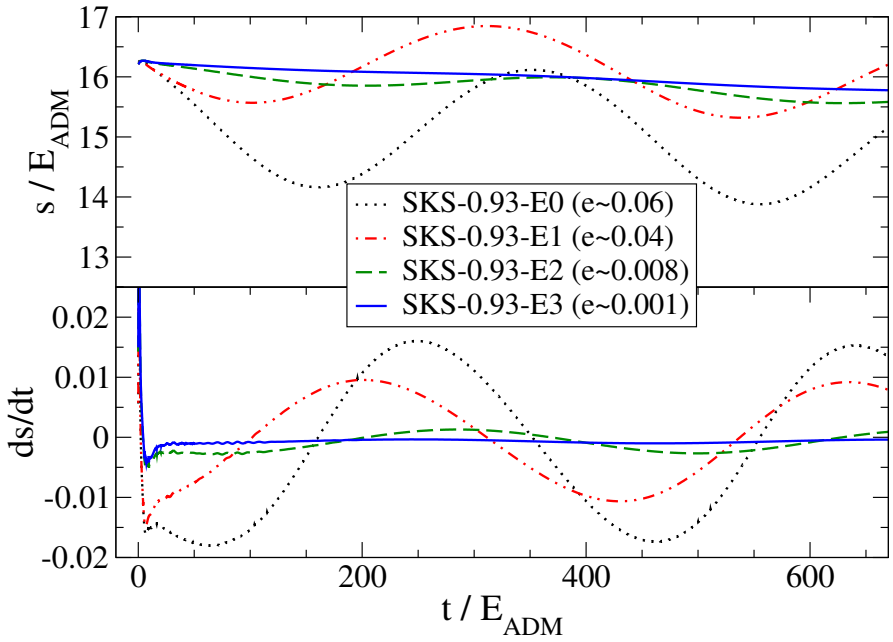

Figure 2.14: Eccentricity reduction for evolutions of superposed-Kerr-Schild binary-black-hole initial data. The proper separation s (*upper panel*) and its time derivative ds/dt (*lower panel*) are plotted for initial data sets SKS-0.93-E0, -E1, -E2, and -E3, which have successively smaller eccentricities e. All evolutions are performed at resolution $N1$.

initial data sets (summarized in Table 2.1):

- set SKS-0.93-E0, which is identical to the set in family SKS-0.93 with $\Omega_r = 0.28$ (Fig. 2.11);
- set SKS-0.93-E1, which is the same as SKS-0.93-E0 except that the orbital frequency Ω_0 is manually adjusted to lower the orbital eccentricity somewhat; and
- sets SKS-0.93-E2 and SKS-0.93-E3, which are successive iterations (starting from set SKS-0.93-E1) of the eccentricity-reduction scheme Eqs. (2.75).

The *ad hoc* adjustment of Ω_0 was somewhat effective, reducing e by about 50%. The subsequent iterations using Eqs. (2.75) reduced e by factors of about 5 and 8, respectively. Surprisingly, the lowest eccentricity, corresponding to a smooth inspiral trajectory is obtained with a positive $\dot{a}_0 = 3.332 \times 10^{-4}$. This is not due to insufficient resolution; for SKS-0.93-E3, we have verified that we obtain the same eccentricity $e \sim 0.001$ for all three numerical resolutions N1, N2, N3.

Note that we choose to stop the evolutions at about $t = 670 E_{\rm ADM}$, which corresponds to about 1.9 orbits; this is sufficient for reducing the eccentricity and for measuring $\Delta\chi$.

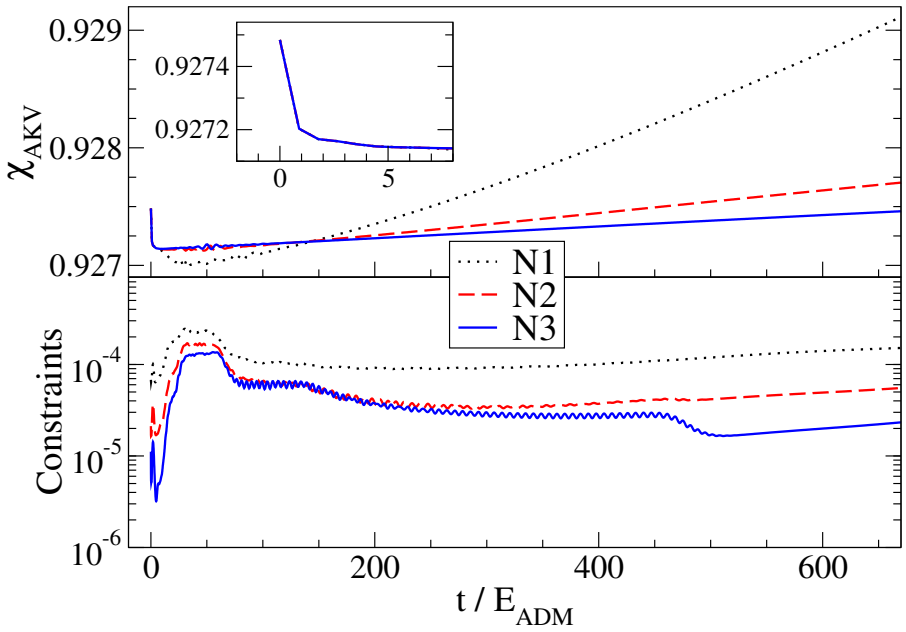

Figure 2.15: Convergence test of the evolution of the initial data set SKS-0.93-E3. Shown are evolutions on three different resolutions, $N1$, $N2$, and $N3$, with $N3$ being the highest resolution. The *top panel* shows the approximate-Killing-vector (AKV) spin of one of the holes as a function of time, with the *top inset* showing the spin's initial relaxation; the *bottom panel* shows the constraint violation as a function of time.

In the next subsection, we discuss the evolution of the low-eccentricity set SKS-0.93-E3 in detail, focusing on the relaxation of the spin χ.

2.5.3 Low-eccentricity inspiral with $\chi \approx 0.93$

We evolved the data set SKS-0.93-E3 at three different numerical resolutions for a duration of about $670E_{\rm ADM}$, corresponding to about 1.9 orbits. From post-Newtonian theory [68], we estimate that this simulation would proceed through about 20 orbits to merger.

Figure 2.15 presents a convergence test for this run. The lower panel of Fig. 2.15 shows the normalized constraint violation (see Eq. (71) of Ref. [69] for the precise definition.) While the constraints are small, the convergence seems poor until $t \approx 500E_{\rm ADM}$. For this time period the constraint violations at high resolution $N3$ are dominated by the outgoing pulse of spurious radiation—i.e., far away from the black holes—which we have not attempted to adequately resolve. At $t \approx 500E_{\rm ADM}$, the pulse of spurious radiation leaves the computational domain through the outer boundary; afterwards, the constraints decrease exponentially with increasing resolution, as expected.

The upper panel of Figure 2.15 shows the AKV spin $\chi_{\rm AKV} = S/M^2$ for the three runs with different resolutions $N1$, $N2$, and $N3$. Based on the difference between $N2$ and $N3$, the spin of the evolution $N3$ should be accurate to a few parts in 10^4. For the time-interval $5 < t/E_{\rm ADM} < 670$, the measured spin on resolution $N3$ is consistent with being constant within its estimated accuracy. Very early in the simulation, $t < 5E_{\rm ADM}$, the spin χ changes *convergently resolved* from its initial value $\chi(t=0) = 0.927\,48$ to a relaxed value $\chi(t_{\rm relax}) = 0.927\,14$ (see inset of Fig. 2.15). Therefore, for SKS-0.93-E3, we find $\Delta\chi = 0.000\,34$.

Contrast this result with the evolution of a binary black hole puncture initial data set with large spins, which is reported in Ref. [25]: for that particular evolution, $\chi(t=0) = 0.967$, $\chi(t_{\rm relax}) = 0.924$, i.e., $\Delta\chi = 0.043$, more than a factor 100 larger than for the evolution of SKS-0.93-E3 reported here. This comparison is somewhat biased against the puncture evolution in [25], which starts at a smaller separation possibly resulting in larger initial transients. However, even in the limit that the black holes are infinitely separated (i.e., in the single-black-hole limit), the spins in Bowen-York puncture data relax to values near $\varepsilon_J = J_{ADM}/E_{ADM}^2$; to achieve a final spin of $\chi(t_{\rm relax}) \approx 0.93$, the initial spin of Bowen-York data must be $\chi(t=0) \approx 0.98$ (cf. Fig. 2 of Ref. [25]). We conclude that the spin relaxes by a much smaller amount in the SKS case than in Bowen-York puncture or inversion symmetric data.

Figure 2.15 and the discussion in the previous paragraph only addresses the behavior of the AKV spin, where the approximate Killing vectors are computed from the minimization problem [cf. Eq. (2.87)]. We now compare the different spin definitions we present in Appendices 2.7 and 2.8. Figure 2.16 compares these different definitions of the black hole spin for the $N3$ evolution of initial data set SKS-0.93-E3. Shown are the AKV spin of one hole in the binary, the scalar curvature (SC) spins $\chi_{\rm SC}^{\rm min}$ and $\chi_{\rm SC}^{\rm max}$ of Appendix 2.8 [Eqs. (2.99a) and (2.99b)], and also the spin obtained by using Eq. 2.78 with a coordinate rotation vector instead of an approximate Killing vector (which we call the "coordinate spin" here). After the holes have relaxed, the SC spins track the AKV spin more closely than does the coordinate spin. However, during very early times, as the holes are relaxing and the horizon shape is very distorted, the SC spins show much larger variations. Consequently, the SC spin is a poorer measure of the spin at early times than even the coordinate spin.

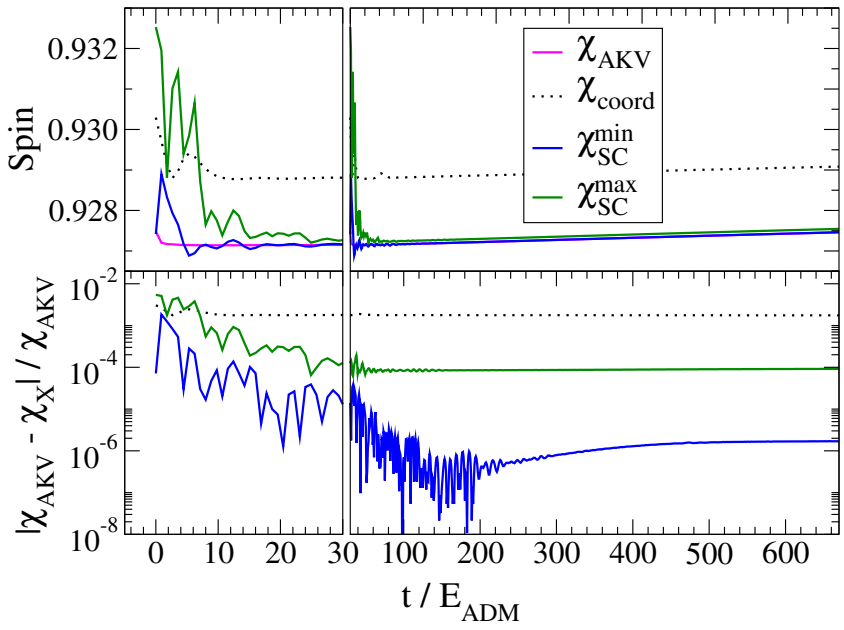

Figure 2.16: A comparison of different definitions of the spin. The *top panel* shows the spin as a function of time for several different measures of the spin; the *bottom panel* shows the fractional difference between $\chi_{\rm AKV}$ and alternative spin definitions. Note that for $t < 30E_{\rm ADM}$, the time-axis has a different scaling to make the initial transients visible.

2.5.4 Head-on plunge with $\chi \approx 0.97$

In the previous subsection, we have seen that for SKS binary-black hole-initial data with $\chi = 0.93$, the initial spins change by only a few parts in 10^4. A spin $\chi \approx 0.93$ is roughly the largest possible equilibrium spin that is obtainable using standard conformally flat, Bowen-York puncture data (cf. the discussion at the beginning of section 2.5). We now begin to explore binary-black-hole simulations with spin-magnitudes that are not obtainable with Bowen-York initial data methods.

We construct and evolve SKS binary-black-hole data for a head-on plunge of two equal mass black holes with spins of equal magnitude $\chi = 0.97$ and with the spins orthogonal to the line connecting the black holes. This data set, labelled SKS-Headon, is summarized in Table 2.1 and was briefly discussed in section 2.4.2, cf. Figs. 2.10, 2.11 and 2.13. As for the orbiting evolution SKS-0.93-E3, we adjust the rotation parameter Ω_r so that conformal spin $\tilde{S}/\tilde{M}^2$ and AKV spin χ are approximately equal. Starting such a simulation at close separation results in rapid coordinate motion of the apparent horizons during the first few $E_{\rm ADM}$ of the evolution. These motions are currently difficult to track with our excision code; therefore, we begin at a larger separation d than we used in the nearly circular data

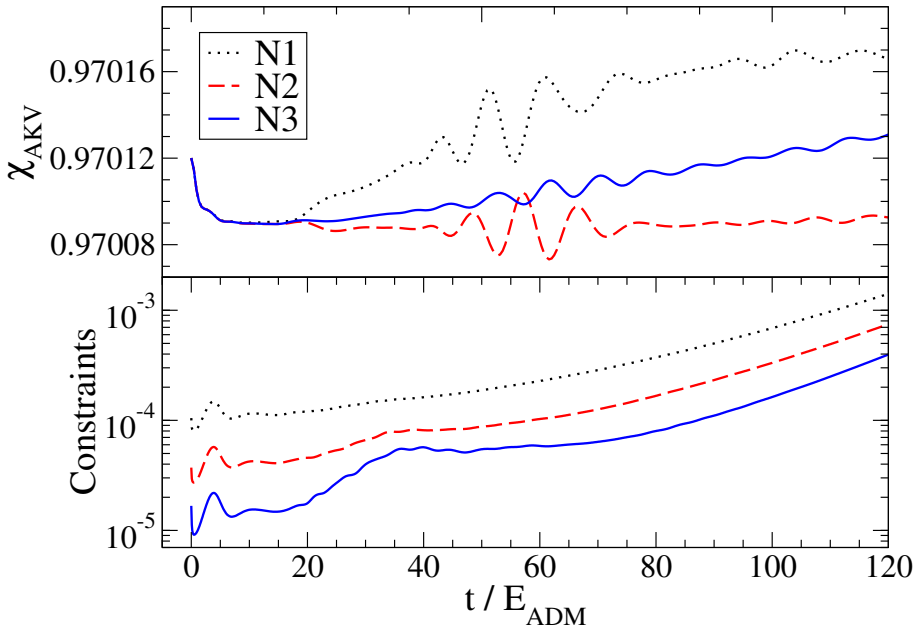

Figure 2.17: Convergence test of the head-on evolution SKS-HeadOn. Shown are evolutions at three different resolutions, $N1$, $N2$, and $N3$, with $N3$ being the highest-resolution. The *top panel* shows the approximate-Killing-vector (AKV) spin of one of the holes as a function of time; the *bottom panel* shows the constraint violations as a function of time.

sets described previously.

Figure 2.17 presents a convergence test of the constraints (lower panel) and the AKV spin $\chi_{\rm AKV}$ (upper panel) during the subsequent evolution. Again, we are interested in the initial relaxation of the spins; therefore, we choose to stop evolution at $t \approx 120 E_{\rm ADM}$. During this time, the black hole proper separation decreased from $s(t=0) = 47.6 E_{\rm ADM}$ to $s(t=120) = 44.1 E_{\rm ADM}$.

During the first $\sim 10 E_{\rm ADM}$, $\chi_{\rm AKV}$ shows (a numerically resolved) decrease of about 3×10^{-5}; this change arises due to initial transients as the black holes and the full geometry of the spacetime relax into an equilibrium configuration. Subsequently, the spin remains constant to within about 10^{-4}, where these variations are dominated by numerical truncation error.

Figure 2.18 compares our various spin measures for the head-on simulation. Interestingly, the spin $\chi_{\rm coord}$ computed from coordinate rotation vectors agrees much better with $\chi_{\rm AKV}$ than for the SKS-0.93-E3 evolution, perhaps because the black holes here are initially at rest. The scalar-curvature (SC) spins $\chi_{\rm SC}^{\rm min}$ and $\chi_{\rm SC}^{\rm max}$, derived from the scalar curvature of the apparent horizon [Eqs. (2.99a) and (2.99b)], show some oscillations at early times; after

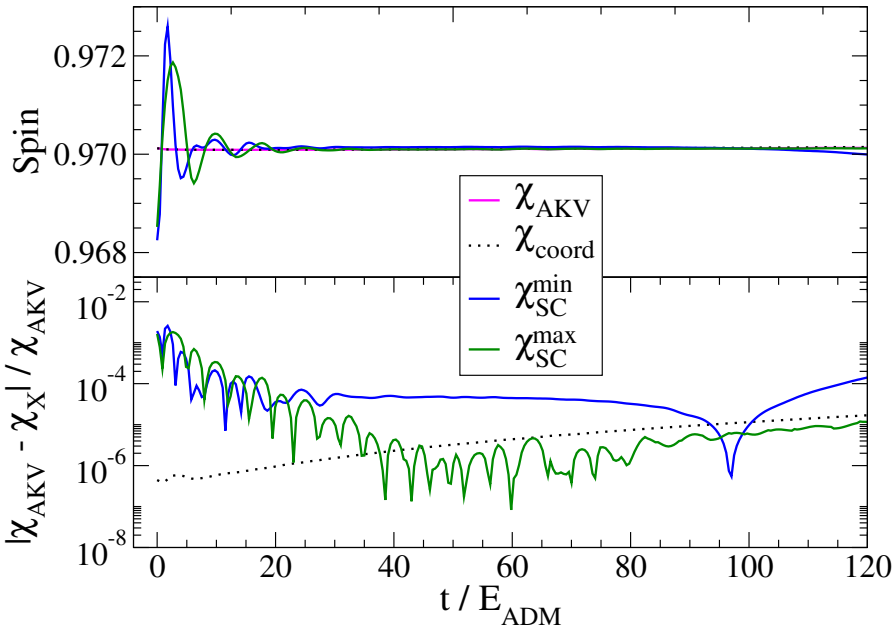

Figure 2.18: A comparison of various measures of the spin for the head-on evolution of data set SKS-Headon. The *top panel* shows various measures of the spin as a function of time, and the bottom panel shows the fractional difference between the approximate-Killing-vector (AKV) spin $\chi_{\rm AKV}$ and alternative spin definitions.

the initial relaxation, the SC spin agrees with the AKV spin to about 1 part in 10^4.

2.6 Discussion

2.6.1 Maximal possible spin

In this chapter, we have examined a variety of methods for constructing black hole initial data with a particular emphasis on the ability to construct black holes with nearly extremal spins. These are spins for which the dimensionless spin $\chi = S/M^2$ and spin-extremality parameter $\zeta = S/(2M_{\rm irr}^2)$ are close to unity.

When discussing black hole spin, one needs to distinguish between the *initial* black hole spin and the *relaxed* spin of the holes after they have settled down. Using conformally flat Bowen-York (BY) data (both puncture data or inversion symmetric data) for single black holes, the largest obtainable spins are $\chi \approx 0.984, \zeta \approx 0.833$ (cf. Ref. [63] and Fig. 2.2). With conformally flat, maximally sliced (CFMS), quasiequilibrium extended-conformal-thin-sandwich (QE-XCTS) data, we are able to obtain initial spins as large as $\chi \approx 0.99, \zeta \approx 0.87$ for single black holes (Fig. 2.7). The limitations of BY puncture data and

CFMS QE-XCTS data are already present when constructing highly spinning single black holes; therefore, we expect the methods to be able to construct binary-black-hole data with similar spins as for single holes—i.e., up to about 0.98. Construction of CFMS QE-XCTS binary-black-hole initial data confirms this conjecture (compare Fig. 2.9 with Fig. 2.7).

For superposed-Kerr-Schild (SKS) initial data, the situation is different. For single black holes, SKS data reduce to the analytical Kerr solution, without any limitations on the spin magnitude. Thus limitations of SKS data will only be visible for binary-black hole configurations. As Sections 2.4 and 2.5 show, however, those limitations are quite minor. SKS data can indeed achieve initial spins that are much closer to extremality than what is possible with BY data or CFMS QE-XCTS data; we have explicitly demonstrated this by constructing SKS data for binary black holes with $\chi \approx 0.9997, \zeta \approx 0.98$, as can be seen from Figs. 2.11 and 2.12.

As the black hole spacetimes settle into equilibrium and emits spurious gravitational radiation, the initial spin χ decreases to a smaller relaxed spin $\chi(t_{\rm relax})$. Thus an interesting quality factor for high-spin black hole initial data is $\Delta\chi = \chi(t=0) - \chi(t_{\rm relax})$ [Eq. (2.3)] considered as a function of the *relaxed* spin. The magnitude of $\Delta\chi$ is indicative of the amplitude of any initial transients, whereas the maximally achievable $\chi(t_{\rm relax})$ gives the largest possible spin which can be evolved with such initial data. Figure 2.19 presents this plot, with the circle and cross representing the two evolutions of SKS data which were described in section 2.5.

We have not evolved high-spin puncture data, nor high-spin CFMS-XCTS data; therefore, we do not know precisely $\Delta\chi$ for these initial data. We estimate $\Delta\chi$ for puncture data by noting that evolutions of single-hole, BY puncture data with large spins show [25] that the black hole spin $\chi := S/M^2$ relaxes approximately to the initial value of $\varepsilon_J := J_{\rm ADM}/E_{\rm ADM}^2$. Therefore, for BY puncture data, we approximate

$$\Delta\chi \approx \varepsilon_J - \chi(t=0), \tag{2.76}$$

$$\chi(t_{\rm relax}) \approx \varepsilon_J. \tag{2.77}$$

This curve is plotted in Fig. 2.19. Because high-spin single-black-hole, CFMS QE-XCTS initial data and BY puncture data have quite similar values of $\chi(t=0)$ and ε_J, as well as similar embedding diagrams (cf. Fig. 2.8), we conjecture that Eqs. (2.76)–(2.77) are also applicable to CFMS QE-XCTS data. This estimate is also included in Fig. 2.19. We see that both types of initial data result in a $\Delta\chi$ of similar magnitude which grows rapidly with

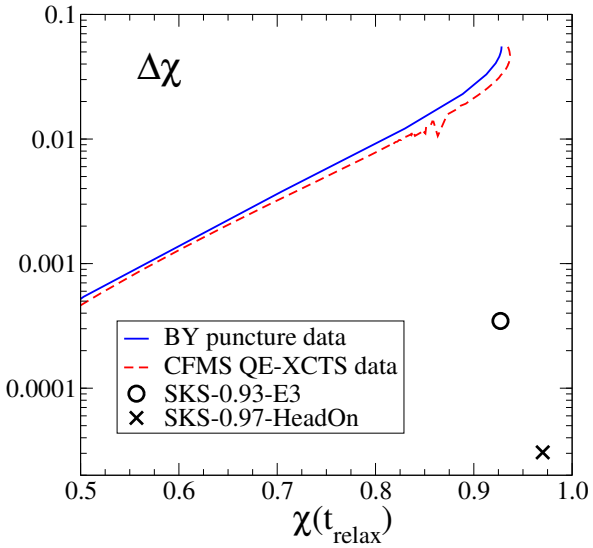

Figure 2.19: The change $\Delta\chi$ in black hole spin χ during the initial relaxation of black hole initial data plotted as a function of the black-hole spin *after* relaxation. The SKS initial data constructed in this work have smaller transients and allow for larger relaxed spins.

$\chi_{\rm relaxed}$.

Perhaps the most remarkable result of Fig. 2.19 is the extremely small change in black hole spin during the relaxation of SKS initial data, even at spins as large as $\chi = 0.97$. The small values of $\Delta\chi$ combined with the ability to construct initial data with initial spins $\chi(t = 0)$ as large as 0.9997 (cf. Fig. 2.11) makes it highly likely that SKS initial data are capable of constructing binary black holes with relaxed spins significantly closer to unity than 0.97. Evolutions of initial data with spins χ much closer to unity, i.e., farther into the regime that is inaccessible to conformally flat data, are a subject of our ongoing research.

2.6.2 Additional results

While working toward the main results discussed in the previous subsection, we have also established several additional interesting results. We have considered spinning, single-black-hole, puncture data which is identical to single-black-hole, spinning, inversion-symmetric data. Using this correspondence and our accurate spectral elliptic solver, we revisited the relation between black-hole spin χ, specific total angular momentum of the space-time ε_J, and the spin parameter S for BY puncture data, and established in Fig. 2.2 that both χ and ε_J approach their limits for $S \to \infty$ as *power laws*, cf. Eqs. (2.49) and (2.50). We have also extended the analytical analysis of Dain, Lousto, and Zlochower [25] of the throat

region of high-spin puncture data toward more quantitative results, including the precise amplitudes of the conformal factor, throat circumference and throat length, as well as their scaling with spin parameter S and puncture mass m_p [Eqs. (2.54)–(2.58)]. Furthermore, Ref. [25] implicitly assumed that the throat region is approximately spherically symmetric; our Fig. 2.5 presents explicit evidence in support of this assumption, but also shows that the throat is not precisely spherically symmetric.

We have also examined high-spin QE-XCTS initial data employing the common approximations of conformal flatness and maximal slicing (CFMS). With increasing angular frequency Ω_r of the horizon, we discover nonunique solutions. Thus, the nonuniqueness of the XCTS equations can not only be triggered by volume terms (as in [34]) but also through boundary conditions [in this case, by Eq. (2.40)]. Interestingly, CFMS QE-XCTS data appears to be very similar to BY puncture data, in regard to nearly extremal spins. Both data formalisms result in similar maximal values of $\chi(t = 0)$ and ε_J (Figs. 2.2, 2.7 and 2.19) and have embedding diagrams which develop a lengthening throat as the spin is increased (Fig. 2.8).

We also have found an interesting property of the horizon geometries for SKS data, which one might interpret as support of the cosmic censorship conjecture. Specifically, we find that by increasing Ω_r sufficiently, we can in fact force the excision boundaries of the initial data to be "horizons" (i.e., marginally trapped surfaces) with superextremal spin ($\zeta > 1$). However, these superextremal surfaces are always enclosed by a larger, subextremal ($\zeta < 1$) apparent horizon.

To measure black hole spins, we have employed and compared several different techniques to measure black hole spin. Primarily, we use a quasilocal spin definition based on (approximate) Killing vectors [Eq. (2.78)]. This formula requires the choice of an "approximate" Killing vector, and we have used both straightforward coordinate rotations to obtain $\chi_{\rm coord}$ and solved Killing's equation in a least-squares sense to obtain $\chi_{\rm AKV}$ (see Appendix 2.7 or details). Furthermore, we introduced a new technique to define black-hole spin which does not require choice of an approximate Killing vector and is invariant under spatial coordinate transformations and transformations associated with the boost gauge ambiguity of the dynamical horizon formalism. This new technique is based on the extrema of the scalar curvature of the apparent horizon. Figures 2.16 and 2.18 show that all four spin measures agree to good precision, but differences are noticeable. The spin measures based on the horizon curvature exhibit more pronounced variations during the initial transients, and the quasilocal spin based on coordinate rotations is off by several tenths of a

percent. The quasilocal spin based on approximate Killing vectors χ_{AKV} has the smallest initial variations.

2.7 Appendix A: Approximate-Killing-vector spin

It is standard in the numerical relativity community to compute the spin angular momentum of a black hole with the formula [70, 71, 72]

$$S = \frac{1}{8\pi} \oint_{\mathcal{H}} \phi^i s^j K_{ij} \, dA, \tag{2.78}$$

where s^i is the outgoing normal of $\mathcal{H}$ embedded in Σ and $\vec{\phi}$ is an "azimuthal" vector field, tangent to $\mathcal{H}$. The azimuthal vector field $\vec{\phi}$ carries information about the "axis" about which the spin is being computed. There are, however, far more vector fields on a two sphere than there are axes in conventional Euclidean space. We must find suitable criteria for fixing these azimuthal vector fields in numerical simulations, so that they reduce to the standard rotation generators when considered on a metric sphere.

Because angular momentum is generally thought of as a conserved charge associated with rotation symmetry—and indeed the quantity given in (2.78) can be shown to be conserved under time evolution [70, 72] when $\vec{\phi}$ is a Killing vector of the dynamical horizon worldtube—it makes sense to consider Killing's equation to be the essential feature of the azimuthal vector field. If a Killing vector on a dynamical horizon is tangent to each (2-dimensional) apparent horizon, then the vector field must be a Killing vector of each apparent horizon. However in a general spacetime, on an arbitrary apparent horizon, there is no reason to expect any Killing vectors to exist. So in the cases of most interest to numerical relativity, when there are no true rotation symmetries, we must relax the symmetry condition and find those vector fields that come "closest" to generating a symmetry of the apparent horizon. In other words, we seek optimal "approximate Killing vectors" of the apparent horizon. The method described here was developed by Owen [73]. Note that quantities relating to the geometry of the 2-dimensional apparent horizon surface $\mathcal{H}$ are denoted with a ring above them, to avoid confusion with the analogous quantities on the spatial slice, Σ.

2.7.1 Zero expansion, minimal shear

Killing's equation,

$$D_{(A}\phi_{B)} = 0, \tag{2.79}$$

has two independent parts: the condition that $\vec{\phi}$ be expansion free,

$$\Theta := \mathring{g}^{AB} D_A \phi_B = 0, \tag{2.80}$$

and the condition that it be shear free,

$$\sigma_{AB} := D_{(A}\phi_{B)} - \frac{1}{2}\mathring{g}_{AB}\Theta = 0, \tag{2.81}$$

where uppercase latin letters index the tangent bundle to the 2-dimensional surface, $\mathring{g}_{AB}$ is the metric on that surface, and D_A is the torsion-free covariant derivative compatible with that metric.

When constructing approximate Killing vectors, a question arises: which condition is more important, zero expansion or zero shear? Shear-free vector fields (conformal Killing vectors) are simply coordinate rotation generators in the common case of coordinate spheres in a conformally flat space. They are therefore readily available in that context. However, in the case of a general surface in a general spatial slice, the conformal Killing vectors are not known *a priori*, and they are more difficult to construct than expansion free vector fields. Expansion-free vector fields have the additional benefit of providing a gauge-invariant spin measure on a dynamical horizon [72], so we restrict attention to the expansion free case.

Any smooth, expansion free vector field tangent to a topological two-sphere can be written as

$$\phi^A = \epsilon^{AB} D_B z, \tag{2.82}$$

where ϵ^{AB} is the Levi-Civita tensor and z is some smooth potential function. We assume that the function z has one local maximum, one local minimum, and no other critical points. This is equivalent to the assumption that the orbits of $\vec{\phi}$ are simple closed loops. In order for $\phi^A\phi_A$ to have the proper dimensions, z must have dimensions of area. For the case of the standard rotation generators of the metric two-sphere, the three z functions are the three $\ell = 1$ spherical harmonics, multiplied by the square of the areal radius of the sphere.

Within this space of expansion free vector fields, we would now like to minimize the following positive-definite norm of the shear:

$$\|\sigma\|^2 := \oint_{\mathcal{H}} \sigma_{BC}\sigma^{BC}\, dA. \tag{2.83}$$

Substituting Eq. (2.82) for $\vec{\phi}$ in this expression and integrating twice by parts, $\|\sigma\|^2$ takes

the form of an expectation value:

$$\|\sigma\|^2 = \oint_{\mathcal{H}} zHz \, dA, \tag{2.84}$$

where H is the self-adjoint fourth-order differential operator defined by

$$Hz = D^4 z + \mathring{R} D^2 z + D^A \mathring{R} \, D_A z, \tag{2.85}$$

and D^2 is the Laplacian on the (not necessarily round) sphere, D^4 is its square, and $\mathring{R}$ is the Ricci scalar curvature of the sphere. In our sign convention, $\mathring{R} = 2$ on the unit sphere, so we can immediately see that $Hz = 0$ when z is an $\ell = 1$ spherical harmonic, and therefore that their associated vector fields are shear free.

Minimizing the functional $\|\sigma\|^2$ in (2.84) with respect to z will simply return the condition that z lie in the kernel of H. If there are no true Killing vectors, this will mean that z is a constant, and therefore that $\vec{\phi}$ vanishes. We need to restrict the minimization procedure to cases that satisfy some normalization condition. In this case, we require that the norm of the vector field,

$$\oint_{\mathcal{H}} \phi^A \phi_A \, dA, \tag{2.86}$$

take some given positive value. This restriction can be made with the use of a Lagrange multiplier. Specifically, the functional we wish to minimize is

$$I[z] := \oint_{\mathcal{H}} zHz \, dA + \lambda \left(\oint_{\mathcal{H}} D^A z \, D_A z \, dA - N \right) \tag{2.87}$$

for some yet undetermined positive parameter N. Note that λ is the Lagrange multiplier and we have made use of the fact that Eq. (2.82) implies that $\vec{\phi} \cdot \vec{\phi} = \vec{D}z \cdot \vec{D}z$. Minimizing the functional I with respect to z returns a generalized eigenvalue problem:

$$Hz = \lambda D^2 z. \tag{2.88}$$

The approach that we take to finding approximate Killing vectors begins with a spectral decomposition of Eq. (2.88). This problem provides as many eigenvectors as there are elements of the spectral decomposition. We restrict attention to the three eigenvectors with smallest eigenvalues (ignoring the vector corresponding to the constant eigenfunction, which is physically irrelevant and removed from discretization), as these are the ones corresponding to vector fields with the smallest shear, and at least for spheres that are only slightly

deformed, the orbits of these vector fields are smooth closed loops.

Only the eigenvector with the smallest eigenvalue corresponds to a vector field with strictly minimum shear: even locally, all other eigenvectors are saddle points of the minimization problem. The three of them taken together, however, provide a geometrically defined subspace of the vector space of expansion free vector fields, a natural generalization of the rotation generators on metric spheres. Using these three vector fields (normalized as described in the next subsection), one can define "components" of the spin angular momentum of a black hole, and from these components infer the spin around an arbitrary axis or even a spin "magnitude" using a metric on this three-dimensional space of generalized rotation generators. In practice, we have found no need to go quite so far. As mentioned in [41], the approximate Killing vectors generally adapt themselves so well to the horizon that one of the components is much larger than the other two, so this is considered the spin magnitude, and the associated approximate Killing vector is considered to define the spin axis.

2.7.2 Normalization

Solutions to the eigenproblem (2.88) can only determine the approximate Killing vectors up to a constant scaling. Fixing this scaling is equivalent to fixing the value of N in (2.87). The standard rotation generators of metric spheres are normalized such that, when considered as differential operators along their various orbits, they differentiate with respect to a parameter that changes by a value of 2π around each orbit. Naively one would like to fix the normalization of approximate Killing vectors in the same way, but a subtlety arises: we can only rescale the vector field by a fixed, constant value. Rescaling differently along different orbits would introduce extraneous shear and would remove the vector field from the pure eigenspace of (2.88) in which it initially resided. If an approximate Killing vector field has different parameter circumferences around different orbits, then it is impossible to rescale it such that the parameter distance is 2π around every orbit. The best one can ask is that 2π is the *average* of the distances around the various orbits.

To consider this in detail, introduce a coordinate system, topologically the same as the standard spherical coordinates on the metric sphere, but adapted to the potential function z so that the latitude lines are the level surfaces of z (and, in particular, the poles are at the two critical points we have assumed z to have). More precisely, choose z for the zenith coordinate on the sphere, and an arbitrary rotational coordinate—say, the azimuthal angle in the encompassing spatial slice, describing rotations about the axis connecting the critical

points of z—for the azimuthal coordinate φ on the sphere. If the parameter τ is defined such that $\vec{\phi} = (d/d\tau)_{z=\text{const.}}$, then in the basis related to these coordinates, the components of $\vec{\phi}$ are

$$\phi^z(z,\varphi) = \left(\frac{dz}{d\tau}\right)_{z=\text{const.}} = 0, \tag{2.89}$$

$$\phi^\varphi(z,\varphi) = \left(\frac{d\varphi}{d\tau}\right)_{z=\text{const.}}. \tag{2.90}$$

Around a closed orbit $\mathcal{C}(z)$, at fixed z, the parameter τ changes by a value of

$$\tau(z) = \int_{\mathcal{C}(z)} \frac{d\varphi}{\phi^\varphi(z,\varphi)} \tag{2.91}$$

$$= \int_{\mathcal{C}(z)} \frac{d\varphi}{\epsilon^{\varphi z}\partial_z z} \tag{2.92}$$

$$= \int_{\mathcal{C}(z)} \sqrt{\mathring{g}}\, d\varphi, \tag{2.93}$$

where $\mathring{g}$ is the determinant of the surface metric, evaluated in the (z,φ) coordinates. Note that Eq. (2.93) follows from Eq. (2.92) by the fact that the condition $\mathring{g}_{AB}\mathring{g}_{CD}\epsilon^{AC}\epsilon^{BD} = 2$ implies $\epsilon^{\varphi z} = 1/\sqrt{\mathring{g}}$. The average value of τ, over the various orbits, is:

$$\langle\tau\rangle = \frac{1}{z_{\max} - z_{\min}} \int_{z_{\min}}^{z_{\max}} \int_{\mathcal{C}(z)} \sqrt{\mathring{g}}\, d\varphi dz \tag{2.94}$$

$$= \frac{A}{z_{\max} - z_{\min}}, \tag{2.95}$$

where A is the surface area of the apparent horizon. Requiring this average to equal 2π, we arrive at the normalization condition:

$$2\pi(z_{\max} - z_{\min}) = A. \tag{2.96}$$

This normalization condition requires finding the minimum and maximum values of the function z, which is only computed on a discrete grid. In our spectral code, in particular, this numerical grid is quite coarse, so numerical interpolation is needed, in combination with an optimization routine. We have implemented such routines to search for $z_{\min}$ and $z_{\max}$, but a numerically cheaper normalization condition would be of interest. Such a condition arises when one assumes that the black hole under consideration is approximately Kerr. In the Kerr metric, for the function z generating the true rotation generator of the Kerr

horizon, the following identity holds:

$$\oint_{\mathcal{H}} \left(z - \langle\langle z \rangle\rangle\right)^2 \, dA = \frac{A^3}{48\pi^2}, \tag{2.97}$$

where $\langle\langle z \rangle\rangle$ is the average of z over the sphere. The existence of an identity of this form is somewhat nontrivial: the fact that the right side is given purely by the horizon area, and that it does not involve the spin of the Kerr hole, is what makes this identity useful as a normalization condition. This normalization is much easier to impose, and requires significantly less numerical effort.

2.8 Appendix B: Scalar-curvature spin

By assuming that the geometric properties of the horizon behave precisely as they do for a Kerr black hole, one can infer the hole's spin from those properties. For instance, it is common to measure polar and equatorial circumferences of the apparent horizon; the spin is then obtained by finding the Kerr spacetime with the same circumferences [74, 75, 76].

To avoid introducing coordinate dependence by defining "polar" and "equatorial" planes, we infer the spin from the horizon's intrinsic scalar curvature $\mathring{R}$. The horizon scalar curvature $\mathring{R}$ has previously been studied analytically for Kerr-Newman black holes [77] and for Kerr black holes perturbed by a distant moon [78]. Numerical studies of $\mathring{R}$ have focused attention on the quasinormal ringing of single, perturbed, black holes [74] as well as on the shape of the individual and common event horizons in Misner data [79]. To our knowledge, the scalar curvature $\mathring{R}$ has not been previously used to infer the horizon spin in numerical simulations.

At a given point on a Kerr black hole's horizon, the horizon scalar curvature $\mathring{R}$ depends only on the hole's mass M and spin S. The extrema of $\mathring{R}$ can be expressed in terms of the irreducible mass and dimensionless spin of the Kerr black hole via Eqs. (2.1)–(2.2) as

$$\min(\mathring{R}) = \frac{-1 + 2\sqrt{1-\chi^2}}{2M_{\rm irr}^2}, \tag{2.98a}$$

$$\max(\mathring{R}) = -\frac{2}{M_{\rm irr}^2 \chi^4}\left(-2 + \chi^2 + 2\sqrt{1-\chi^2}\right). \tag{2.98b}$$

Solving for χ and requiring it to be real yields χ as a function of $M_{\rm irr}$ and either $\min(\mathring{R})$ or $\max(\mathring{R})$. We take these functions as *definitions* of the spin, even when the space-time is

not precisely Kerr:

$$\left(\chi_{\rm SC}^{\rm min}\right)^2 := 1 - \left[\frac{1}{2} + M_{\rm irr}^2 \min(\mathring{R})\right]^2, \tag{2.99a}$$

$$\left(\chi_{\rm SC}^{\rm max}\right)^2 := \frac{-2 + 2\sqrt{2M_{\rm irr}^2 \max(\mathring{R})}}{M_{\rm irr}^2 \max(\mathring{R})}. \tag{2.99b}$$

The definitions of the spin given by Eqs. (2.99a)–(2.99b) are manifestly independent of spatial coordinates and are well-defined for black holes that are tidally deformed. Also, as they only involve the intrinsic 2-dimensional geometry of the apparent horizon, they are also manifestly independent of boost gauge, in the sense described in the previous appendix.

We expect $\chi_{\rm SC}^{\rm min}$ and $\chi_{\rm SC}^{\rm max}$ to be reasonable measures only if tidal forces can be neglected. Tidal forces scale with the cube of the separation of the holes; for binary with holes of equal mass M and separation d, tidal coupling is negligible when $\max(\mathring{R}) - \min(\mathring{R}) \gg M/d^3$.

We find it convenient to compute $\mathring{R}$ from (i) the scalar curvature R associated with the three-dimensional metric g_{ij} of the spatial slice Σ, and (ii) the outward-pointing unit-vector field s^i that is normal to $\mathcal{H}$. This can by done by means of Gauss's equation [e.g., Eq. (D.51) of Ref. [80] (note that the Riemann tensor in Ref. [80] disagrees with ours by an overall sign)]

$$\mathring{R} = R - 2R_{ij}s^i s^j - \mathring{K}^2 + \mathring{K}^{ij}\mathring{K}_{ij}, \tag{2.100}$$

where R_{ij} and R were defined after Eq. (2.11), and where $\mathring{K}_{ij}$ denotes the extrinsic curvature of the the apparent horizon $\mathcal{H}$ embedded in Σ (not to be confused with K_{ij}, the extrinsic curvature of the slice Σ embedded in $\mathcal{M}$). The horizon extrinsic curvature is given by

$$\mathring{K}_{ij} = \nabla_i s_j - s_i s^k \nabla_k s_j. \tag{2.101}$$

Inserting Eq. (2.101) into Eq. (2.100) shows that $\mathring{R}$ can be evaluated exclusively in terms of quantities defined on the three-dimensional spatial slice Σ.

Bibliography

[1] M. Volonteri, P. Madau, E. Quataert, and M. J. Rees, Astrophys. J. **620**, 69 (2005).

[2] C. F. Gammie, S. L. Shapiro, and J. C. McKinney, Astrophys. J. **602**, 312 (2004).

[3] S. L. Shapiro, Astrophys. J. **620**, 59 (2005).

[4] J.-M. Wang, Y.-M. Chen, L. C. Ho, and R. J. McLure, Astrophys. J. **642**, L111 (2006).

[5] J. E. McClintock et al., Astrophys. J. **652**, 518 (2006).

[6] A. R. King and J. E. Pringle, Monthly Notices of the Royal Astronomical Society: Letters **373**, L90 (2006).

[7] A. R. King, J. E. Pringle, and J. A. Hofmann, Monthly Notices of the Royal Astronomical Society **385**, 1621 (2008).

[8] E. Berti and M. Volonteri, Astrophys. J. **684**, 822 (2008).

[9] M. Koppitz et al., Phys. Rev. Lett. **99**, 041102 (2007).

[10] M. Campanelli, C. O. Lousto, Y. Zlochower, and D. Merritt, Phys. Rev. Lett. **98**, 231102 (2007).

[11] J. A. Gonzalez, M. D. Hannam, U. Sperhake, B. Brügmann, and S. Husa, Phys. Rev. Lett. **98**, 231101 (2007).

[12] F. Herrmann, I. Hinder, D. Shoemaker, P. Laguna, and R. A. Matzner, Astrophys. J. **661**, 430 (2007).

[13] D.-I. Choi et al., Phys. Rev. D **76**, 104026 (2007).

[14] M. Campanelli, C. O. Lousto, Y. Zlochower, and D. Merritt, Astrophys. J. Lett. **659**, L5 (2007).

[15] B. Brügmann, J. A. González, M. Hannam, S. Husa, and U. Sperhake, Phys. Rev. D **77**, 124047 (2008).

[16] J. G. Baker et al., Astrophys. J. **668**, 1140 (2007).

[17] J. D. Schnittman et al., Phys. Rev. D **77**, 044031 (2008).

[18] M. Campanelli, C. O. Lousto, Y. Zlochower, B. Krishnan, and D. Merritt, Phys. Rev. D **75**, 064030 (2007).

[19] M. Campanelli, C. O. Lousto, and Y. Zlochower, Phys. Rev. D **74**, 084023 (2006).

[20] M. Campanelli, C. O. Lousto, and Y. Zlochower, Phys. Rev. D **74**, 041501(R) (2006).

[21] F. Herrmann, I. Hinder, D. M. Shoemaker, P. Laguna, and R. A. Matzner, Phys. Rev. D **76**, 084032 (2007).

[22] P. Marronetti, W. Tichy, B. Brügmann, J. González, and U. Sperhake, Phys. Rev. D **77**, 064010 (2008).

[23] E. Berti, V. Cardoso, J. A. Gonzalez, U. Sperhake, and B. Brügmann, Class. Quantum Grav. **25**, 114035 (2008).

[24] S. Brandt and B. Brügmann, Phys. Rev. Lett. **78**, 3606 (1997).

[25] S. Dain, C. O. Lousto, and Y. Zlochower, Phys. Rev. D **78**, 024039 (2008).

[26] S. Dain, C. O. Lousto, and R. Takahashi, Phys. Rev. D **65**, 104038 (2002).

[27] E. Gourgoulhon, P. Grandclément, and S. Bonazzola, Phys. Rev. D **65**, 044020 (2002).

[28] P. Grandclément, E. Gourgoulhon, and S. Bonazzola, Phys. Rev. D **65**, 044021 (2002).

[29] G. B. Cook, Phys. Rev. D **65**, 084003 (2002).

[30] G. B. Cook and H. P. Pfeiffer, Phys. Rev. D **70**, 104016 (2004).

[31] M. Caudill, G. B. Cook, J. D. Grigsby, and H. P. Pfeiffer, Phys. Rev. D **74**, 064011 (2006).

[32] J. W. York, Phys. Rev. Lett. **82**, 1350 (1999).

[33] H. P. Pfeiffer and J. W. York, Phys. Rev. D **67**, 044022 (2003).

[34] H. P. Pfeiffer and J. W. York Jr., Phys. Rev. Lett. **95**, 091101 (2005).

[35] T. W. Baumgarte, N. O'Murchadha, and H. P. Pfeiffer, Phys. Rev. D **75**, 044009 (2007).

[36] D. M. Walsh, Class. Quantum Grav. **24**, 1911 (2007).

[37] R. A. Matzner, M. F. Huq, and D. Shoemaker, Phys. Rev. D **59**, 024015 (1998).

[38] P. Marronetti and R. A. Matzner, Phys. Rev. Lett. **85**, 5500 (2000).

[39] G. Lovelace, *Topics in Gravitational Wave Physics*, PhD thesis, California Institute of Technology, 2007.

[40] K. Taniguchi, T. W. Buamgarte, J. A. Faber, and S. L. Shapiro, Phys. Rev. D **74**, 041502(R) (2006).

[41] G. B. Cook and B. F. Whiting, Phys. Rev. D **76**, 041501(R) (2007).

[42] I. Booth and S. Fairhurst, Phys. Rev. D **77**, 084005 (2008).

[43] J. M. Bowen, Gen. Relativ. Gravit. **11**, 227 (1979).

[44] J. M. Bowen and J. W. York, Jr., Phys. Rev. D **21**, 2047 (1980).

[45] R. Arnowitt, S. Deser, and C. W. Misner, The dynamics of general relativity, in *Gravitation: An Introduction to Current Research*, edited by L. Witten, Wiley, New York, 1962.

[46] A. Ashtekar, J. Engle, and D. Sloan, Class. Quantum Grav. **25**, 095020 (2008).

[47] G. Cook, Living Rev. Rel. **3** (2000), 5.

[48] J. W. York, Jr. and T. Piran, The initial value problem and beyond, in *Spacetime and Geometry*, edited by R. A. Matzner and L. C. Shepley, pages 147–176, University of Texas, Austin, 1982.

[49] H. P. Pfeiffer et al., Class. Quantum Grav. **24**, S59 (2007).

[50] M. A. Scheel et al., Phys. Rev. D **74**, 104006 (2006).

[51] M. A. Scheel et al., Phys. Rev. D **79**, 024003 (2009).

[52] A. Garat and R. H. Price, Phys. Rev. D **61**, 124011 (2000).

[53] J. A. Valiente Kroon, Phys. Rev. Lett. **92**, 041101 (2004).

[54] J. W. York, Jr., Energy and momentum of the gravitational field, in *Essays in General Relativity*, edited by F. J. Tipler, pages 39–58, Academic, New York, 1980.

[55] H. P. Pfeiffer, G. B. Cook, and S. A. Teukolsky, Phys. Rev. D **66**, 024047 (2002).

[56] W. Tichy, B. Brügmann, M. Campanelli, and P. Diener, Phys. Rev. D **67**, 064008 (2003).

[57] S. Nissanke, Phys. Rev. D **73**, 124002 (2006).

[58] N. Yunes, W. Tichy, B. J. Owen, and B. Brügmann, Phys. Rev. D **74**, 104011 (2006).

[59] N. Yunes and W. Tichy, Phys. Rev. D **74**, 064013 (2006).

[60] M. Hannam, S. Husa, B. Brügmann, J. González, and U. Sperhake, Class. Quantum Grav. **24**, S15 (2007).

[61] B. J. Kelly, W. Tichy, M. Campanelli, and B. F. Whiting, Phys. Rev. D **76**, 024008 (2007).

[62] E. Bonning, P. Marronetti, D. Neilsen, and R. Matzner, Phys. Rev. D **68**, 044019 (2003).

[63] G. B. Cook and J. W. York, Jr., Phys. Rev. D **41**, 1077 (1990).

[64] H. P. Pfeiffer, L. E. Kidder, M. A. Scheel, and S. A. Teukolsky, Comput. Phys. Commun. **152**, 253 (2003).

[65] H. P. Pfeiffer, *Initial Data for Black Hole Evolutions*, PhD thesis, Cornell University, 2003.

[66] M. Hannam, S. Husa, B. Brügmann, J. A. Gonzalez, and U. Sperhake, Class. Quantum Grav. **24**, S15 (2007).

[67] M. Boyle et al., Phys. Rev. D **76**, 124038 (2007).

[68] L. E. Kidder, Phys. Rev. D **52**, 821 (1995).

[69] L. Lindblom, M. A. Scheel, L. E. Kidder, R. Owen, and O. Rinne, Class. Quantum Grav. **23**, S447 (2006).

[70] J. D. Brown and J. W. York, Phys. Rev. D **47**, 1407 (1993).

[71] A. Ashtekar, C. Beetle, and J. Lewandowski, Phys. Rev. D **64**, 044016 (2001).

[72] A. Ashtekar and B. Krishnan, Phys. Rev. D **68**, 104030 (2003).

[73] R. Owen, *Topics in Numerical Relativity: The periodic standing-wave approximation, the stability of constraints in free evolution, and the spin of dynamical black holes*, PhD thesis, California Institute of Technology, 2007.

[74] P. Anninos et al., Phys. Rev. D **50**, 3801 (1994).

[75] S. R. Brandt and E. Seidel, Phys. Rev. D **52**, 870 (1995).

[76] M. Alcubierre et al., Phys. Rev. D **72**, 044004 (2005).

[77] L. Smarr, Phys. Rev. D **7**, 289 (1973).

[78] J. B. Hartle, Phys. Rev. D **9**, 2749 (1974).

[79] J. Massó, E. Seidel, W.-M. Suen, and P. Walker, Phys. Rev. D **59**, 064015 (1999).

[80] S. Carroll, *Spacetime and Geometry: An Introduction to General Relativity*, Addison Wesley, New York, 2003.

Chapter 3

Including realistic tidal deformations in binary-black-hole initial data

A shortcoming of current binary-black-hole initial data is their contamination by spurious gravitational radiation that is not astrophysically realistic. This is a consequence of an oversimplified modeling of the binary's physics, and reduces the accuracy of the actual gravitational waveforms of interest that are computed from the evolutions. This chapter presents one step toward addressing this issue, by incorporating post-Newtonian results in the construction of constraint-satisfying binary-black-hole initial data, and builds on the simple method of superposing two black hole metrics to compute the conformal data. Here we focus on including realistic tidal deformations in the initial data, by superposing appropriate tidally perturbed black hole metrics. The properties of our initial data are presented, and directions for future improvements are discussed.

3.1 Introduction

A key objective of numerical relativity is to accurately model the inspiral and coalescence of black-hole binaries, which are important sources of gravitational waves that are expected to be observed by detectors such as LIGO [1] and VIRGO [2] in the near future. Any simulation of a black-hole binary must begin with the construction of suitable initial data, a solution to the Einstein constraint equations, which ideally captures as many relevant features of the physical system as possible. Presently though, the majority of initial data assumes that

the spatial metric is conformally flat, a choice dictated by convenience. It is known that conformal flatness is generally incompatible with desired black hole solutions. For instance, a Kerr black hole with nonzero spin does not admit a conformally flat slicing [3], and neither does a black-hole binary starting at $\mathcal{O}\left(v^4\right)$ in the post-Newtonian (PN) approximation [4], where v is the binary's orbital velocity (in units where $c = 1$ is the speed of light).

A side effect of conformally flat initial data for black-hole binaries is the generation of spurious gravitational radiation, so-called junk radiation, when they are evolved, leading to a contamination of the waveforms of interest. The presence of junk radiation reduces the accuracy of numerical waveforms, and interferes with their comparison to PN waveforms [5, 6]. Valuable computational resources are also wasted in waiting for the junk radiation to propagate off the computational domain, in order to extract reliable waveforms. Also, the high-frequency components of the junk radiation require a large increase in numerical resolution to fully resolve. Additionally, the initial properties of the black holes themselves are altered by the junk radiation, relaxing to slightly different values later on in the evolution.

Over the last several years, various efforts have been made to go beyond the assumption of conformal flatness, by using conformally curved initial data. A direct superposition of black holes metrics was introduced in [7, 8, 9] to specify the conformal metric, and a similar procedure was shown in [10] to reduce the junk radiation in the head-on collision of two black holes. Later on, a weighted superposition of black hole metrics was used in [11, 12], and was shown to reduce the junk radiation in the inspiral of two equal-mass, nonspinning black holes [12]. These superposed-black-hole initial data already provide a substantial improvement to conformally flat initial data, but they do not take advantage of all the available information to better represent the binary's physics, such as results from PN theory [13]. Including such information could prove to be very useful.

Initial data incorporating the PN approximation include that of [4], which has interaction terms between the black holes in the conformal metric, and that of [14], which contains the outgoing gravitational radiation of the binary in the conformal metric. The initial data in [14] was evolved in [15, 16], and was found to reduce the low-frequency components of the junk radiation. However, currently all such initial data have been restricted to nonspinning black holes. Furthermore, the regions near the holes are not adequately treated in the approaches above, because no attempt was made to account for the tidal deformations of the holes.

The latter issue was addressed in [17], by describing the vicinity of the black holes by tidally perturbed Schwarzschild metrics in horizon penetrating coordinates, which were

asymptotically matched to a PN metric to determine the tidal fields. This follows the earlier work of [18, 19], which used black hole metrics in coordinates that are not horizon penetrating, and were thus inconvenient for numerical implementation. The inclusion of tidal deformations is expected to reduce the high-frequency components of the junk radiation, which are typically attributed to physically unrealistic deformations of the holes in the initial data, which radiate away as the holes oscillate and relax in an evolution. It should also be mentioned that all the previous initial data sets using the PN approximation only approximately satisfy the Einstein constraint equations, and were not used to provide free data for a constraint solver.

The present work examines the effect of including realistic tidal deformations in the context of superposed-black-hole initial data, and represents a first step in using PN results to construct constraint-satisfying initial data that further efforts can build on. In particular, excision initial data for an equal-mass, nonspinning black-hole binary is constructed in the extended-conformal-thin-sandwich formalism using a similar method as in [11, 12], by superposing two tidally perturbed Schwarzschild metrics given in [17]. The Einstein constraint equations are then solved with the pseudospectral elliptic solver of [20]. Various properties of the resulting initial data are described, including the junk radiation, which can be compared to the conformally flat initial data and the superposed-boosted-Schwarzschild initial data of [12].

This chapter is organized as follows. Section 3.2 summarizes the extended-conformal-thin-sandwich formalism for constructing initial data, and details our choices for the freely specifiable data and boundary conditions. Section 3.3 presents a few properties of our initial data, such as the resulting tidal deformations of the black holes. In section 3.4, we evolve the initial data and describe some further properties as seen from the evolutions, including the junk radiation content. Finally, section 3.5 discusses directions for future improvements.

3.2 Initial data formalism

3.2.1 Extended-conformal-thin-sandwich equations

Initial data is constructed within the extended-conformal-thin-sandwich formalism [21, 22]. First, the spacetime metric is decomposed into $3+1$ form [23, 24]

$$ {}^{(4)}ds^2 = g_{\mu\nu}dx^\mu dx^\nu = -N^2dt^2 + g_{ij}\left(dx^i + \beta^i dt\right)\left(dx^j + \beta^j dt\right), \tag{3.1} $$

where g_{ij} is the spatial metric of a $t =$ constant hypersurface Σ_t, N is the lapse function, and β^i is the shift vector. (Here and throughout this chapter, Greek indices are spacetime indices running from 0 to 3, while Latin indices are spatial indices running from 1 to 3.) The Einstein equations then become a set of evolution equations,

$$(\partial_t - \mathcal{L}_\beta) g_{ij} = -2NK_{ij}, \tag{3.2}$$

$$(\partial_t - \mathcal{L}_\beta) K_{ij} = N\left(R_{ij} - 2K_{ik}K^k{}_j + KK_{ij}\right) - \nabla_i \nabla_j N, \tag{3.3}$$

and a set of constraint equations,

$$R + K^2 - K_{ij}K^{ij} = 0, \tag{3.4}$$

$$\nabla_j \left(K^{ij} - g^{ij}K\right) = 0. \tag{3.5}$$

Equation (3.4) is known as the Hamiltonian constraint, and Eq. (3.5) is the momentum constraint. In the above, all matter source terms have been neglected, since we will only be interested in vacuum spacetimes. Also, $\mathcal{L}$ is the Lie derivative, ∇_i is the covariant derivative compatible with g_{ij}, $R = g^{ij}R_{ij}$ is the trace of the Ricci tensor R_{ij} of g_{ij}, and $K = g^{ij}K_{ij}$ is the trace of the extrinsic curvature K_{ij} of Σ_t.

The spatial metric is decomposed in terms of a conformal metric $\tilde{g}_{ij}$ and a conformal factor ψ,

$$g_{ij} = \psi^4 \tilde{g}_{ij}. \tag{3.6}$$

The tracefree time derivative of the conformal metric is denoted by

$$\tilde{u}_{ij} = \partial_t \tilde{g}_{ij}, \tag{3.7}$$

and satisfies $\tilde{u}_{ij}\tilde{g}^{ij} = 0$. A conformal lapse is also defined by $\tilde{N} = \psi^{-6}N$. Equations (3.4), (3.5), and the trace of (3.3) can then be written as

$$\tilde{\nabla}^2\psi - \frac{1}{8}\psi\tilde{R} - \frac{1}{12}\psi^5 K^2 + \frac{1}{8}\psi^{-7}\tilde{A}_{ij}\tilde{A}^{ij} = 0, \tag{3.8}$$

$$\tilde{\nabla}_j\left(\frac{1}{2\tilde{N}}\left(\mathbb{L}\beta\right)^{ij}\right) - \tilde{\nabla}_j\left(\frac{1}{2\tilde{N}}\tilde{u}^{ij}\right) - \frac{2}{3}\psi^6\tilde{\nabla}^i K = 0, \tag{3.9}$$

$$\tilde{\nabla}^2\left(\tilde{N}\psi^7\right) - \left(\tilde{N}\psi^7\right)\left(\frac{1}{8}\tilde{R} + \frac{5}{12}\psi^4 K^2 + \frac{7}{8}\psi^{-8}\tilde{A}_{ij}\tilde{A}^{ij}\right) = -\psi^5\left(\partial_t K - \beta^k\partial_k K\right). \tag{3.10}$$

In the above, $\tilde{\nabla}_i$ is the covariant derivative compatible with $\tilde{g}_{ij}$, $\tilde{R} = \tilde{g}^{ij}\tilde{R}_{ij}$ is the trace of

the Ricci tensor $\tilde{R}_{ij}$ of $\tilde{g}_{ij}$, $\tilde{\mathbb{L}}$ is the longitudinal operator,

$$\left(\tilde{\mathbb{L}}\beta\right)^{ij} = \tilde{\nabla}^i\beta^j + \tilde{\nabla}^j\beta^i - \frac{2}{3}\tilde{g}^{ij}\tilde{\nabla}_k\beta^k, \tag{3.11}$$

and $\tilde{A}^{ij}$ is

$$\tilde{A}^{ij} = \frac{1}{2\tilde{N}}\left(\left(\tilde{\mathbb{L}}\beta\right)^{ij} - \tilde{u}^{ij}\right), \tag{3.12}$$

which is related to K_{ij} by

$$K_{ij} = \psi^{-10}\tilde{A}_{ij} + \frac{1}{3}g_{ij}K. \tag{3.13}$$

For freely specifiable $\tilde{g}_{ij}$, $\tilde{u}_{ij}$, K, and $\partial_t K$, Eqs. (3.8), (3.9), and (3.10) constitute a coupled set of elliptic equations, known as the extended-conformal-thin-sandwich equations, which can be solved for ψ, $\tilde{N}$, and β^i. From these solutions, the physical initial data g_{ij} and K_{ij} are obtained from (3.6) and (3.13), respectively.

3.2.2 Freely specifiable data

The freely speciable data consist of the conformal metric $\tilde{g}_{ij}$, its tracefree time derivative $\tilde{u}_{ij}$, the trace of the extrinsic curvature K, and its time derivative $\partial_t K$. The starting point for the construction of the conformal metric $\tilde{g}_{ij}$ is the tidally perturbed Schwarzschild metric of [17]. This metric describes one black hole in a binary, in Cook-Scheel harmonic coordinates $X^\mu = (T, X^i)$, comoving with and centered on that black hole. To facilitate our discussion of it, for all equations in this subsection that appear before Eq. (3.27), indices are raised and lowered with the flat spacetime metric $\eta_{\mu\nu}$. The tidally perturbed Schwarzschild metric is then given by

$$\begin{aligned}
h_{\mu\nu}dX^\mu dX^\nu = &-H_{T^2}dT^2 \\
&+ H_{RT}dRdT \\
&+ \frac{16}{3}\frac{M^2}{R}\left[1 + \frac{M}{R} - \frac{2}{3}\frac{M^3}{R^2(R+M)}\right]\dot{\mathcal{C}}_{klp}X^l X^p dX^k dT \\
&+ H^{[1]}_k dX^k\left[\left(1 - \frac{M^2}{R^2}dT\right) - 4\frac{M^2}{R^2}dR\right] \\
&+ H^{[2]}_k dX^k dR \\
&+ H_{R^2}dR^2 \\
&+ H_{\rm trc}dX_s dX^s + \mathcal{O}(R^4/\mathcal{R}^4),
\end{aligned} \tag{3.14}$$

where $R = \sqrt{X_i X^i}$, and the metric functions are

$$
\begin{aligned}
H_{T^2} &= \frac{R-M}{R+M} + \left[1-\frac{M}{R}\right]^2 \left[(\mathcal{E}_{kl} + T\dot{\mathcal{E}}_{kl})X^k X^l + \frac{1}{3}\mathcal{E}_{klp}X^k X^l X^p\right] \\
&\quad + \frac{4M^2}{(R+M)^2}\left[R - \frac{5}{3}\frac{M^2}{R}\right]\dot{\mathcal{E}}_{kl}X^k X^l, \\
H_{RT} &= \frac{8M^2}{(R+M)^2} + 8\frac{M^2}{R^2}\frac{R-M}{R+M}\left[(\mathcal{E}_{kl} + T\dot{\mathcal{E}}_{kl})X^k X^l + \frac{1}{3}\mathcal{E}_{klp}X^k X^l X^p\right] \\
&\quad - \left[\frac{4}{3}R + \frac{14}{3}M + \frac{8}{3}\frac{M^2}{R} - 2\frac{M^3}{R^2} - \frac{104}{3}\frac{M^4}{R^2(R+M)} + \frac{80}{3}\frac{M^5}{R^2(R+M)^2}\right. \\
&\quad \left. + \frac{32}{3}\frac{M^6}{R^2(R+M)^3}\right]\dot{\mathcal{E}}_{kl}X^k X^l, \\
H_k^{[1]} &= \frac{2}{3}\left[1+\frac{M}{R}\right]\left[2(\mathcal{C}_{klp} + T\dot{\mathcal{C}}_{klp})X^l X^p + \left(1 - \frac{1}{3}\frac{M}{R}\right)\mathcal{C}_{klps}X^l X^p X^s\right], \qquad (3.15) \\
H_k^{[2]} &= \left[\frac{R}{3} + 2M + \frac{16}{3}\frac{M^2}{R} + \frac{26}{3}\frac{M^3}{R^2} - 11\frac{M^4}{R^3} - \frac{32}{3}\frac{M^5}{R^3(R+M)} - \frac{64}{9}\frac{M^6}{R^3(R+M)^2}\right] \\
&\qquad \times \dot{\mathcal{C}}_{klp}X^l X^p, \\
H_{R^2} &= \sum_{n=1}^{3}\left(\frac{2M}{R+M}\right)^n - \frac{2M}{R} - \frac{M^2}{R^2} + \left[2\frac{M}{R} + 3\frac{M^2}{R^2} - \frac{M^4}{R^4} - \frac{16M^4}{R^2(R+M)^2}\right] \\
&\qquad \times (\mathcal{E}_{kl} + T\dot{\mathcal{E}}_{kl})X^k X^l, \\
&\quad + \left[\frac{1}{3}\frac{M}{R} + \frac{1}{3}\frac{M^2}{R^2} - \frac{2}{5}\frac{M^3}{R^3} - \frac{7}{15}\frac{M^4}{R^4} - \frac{1}{15}\frac{M^5}{R^5} - \frac{16}{3}\frac{M^4}{R^2(R+M)^2}\right]\mathcal{E}_{klp}X^k X^l X^p \\
&\quad + \left[\frac{16}{3}\frac{M^2}{R} + \frac{80}{3}\frac{M^3}{R^2} + 28\frac{M^4}{R^3} + \frac{40}{3}\frac{M^5}{R^4} - \frac{176}{3}\frac{M^6}{R^4(R+M)} + \frac{72M^7}{R^4(R+M)^2}\right. \\
&\quad \left. - \frac{32}{3}\frac{M^8}{R^4(R+M)^3} - \frac{32}{3}\frac{M^9}{R^4(R+M)^4}\right]\dot{\mathcal{E}}_{kl}X^k X^l, \\
H_{\rm trc} &= \left[1+\frac{M}{R}\right]^2\left[1 - \left(1 + 2\frac{M}{R} - \frac{M^2}{R^2}\right)(\mathcal{E}_{kl} + T\dot{\mathcal{E}}_{kl})X^k X^l\right. \\
&\quad \left. - \frac{1}{3}\left(1 + \frac{M}{R} - \frac{M^2}{R^2} - \frac{1}{5}\frac{M^3}{R^3}\right)\mathcal{E}_{klp}X^k X^l X^p - 4\frac{M^2}{R^2}\left(R + 2M - \frac{2}{3}\frac{M^2}{R+M}\right)\dot{\mathcal{E}}_{kl}X^k X^l\right],
\end{aligned}
$$

and $\mathcal{R}$ is the characteristic length scale of the perturbation. The electric tidal fields are denoted by $\mathcal{E}_{kl}$ and $\mathcal{E}_{klp}$, and the magnetic tidal fields by $\mathcal{B}_{kl}$ and $\mathcal{B}_{klp}$. The latter enter Eq. (3.14) through $\mathcal{C}_{klp} = \epsilon_{kls}\mathcal{B}^s_p$ and $\mathcal{C}_{klps} = \epsilon_{klu}\mathcal{B}^u_{ps}$, where ϵ_{ijk} is the spatial Levi-Civita symbol. The overdots on the tidal fields denote time derivatives. Note that $h_{\mu\nu}$ is formally only applicable for small R, since the metric functions in Eq. (3.15) contain terms that diverge as $R \to \infty$.

The tidal fields are determined by asymptotically matching the metric of Eq. (3.14) to an $\mathcal{O}\left(v^4\right)$ PN metric in barycentric harmonic coordinates $x^\mu = (t, x^i)$ and specialized to a circular orbit, which was performed in [17]. At $t = 0$, let one black hole ("hole 1") of mass

m_1 lie along the positive x-axis, and the other hole ("hole 2") of mass m_2 lie along the negative x-axis. Also, let $m = m_1 + m_2$, and b be the coordinate separation of the centers of the two holes (recall that in the PN approximation, the holes are treated as point particles). Then, to the order fixed by the matching, the tidal fields about hole 1 are

$$\mathcal{E}_{kl}(t) = \frac{m_2}{b^3}\left\{\left[1 - \frac{1}{2}\frac{m_2}{b}\right][\delta_{kl} - 3\hat{x}_k\hat{x}_l] + \frac{1}{2}\frac{m}{b}[4\hat{x}_k\hat{x}_l - 5\hat{y}_k\hat{y}_l + \hat{z}_k\hat{z}_l] - 6\sqrt{\frac{m}{b}}\frac{t}{b}\hat{x}_{(k}\hat{y}_{l)}\right\}, \tag{3.16}$$

$$\mathcal{B}_{kl}(t) = \frac{m_2}{b^3}\sqrt{\frac{m_2}{b}}\left\{\left[-6\sqrt{\frac{m}{m_2}} + \frac{m_2}{b}\left\{5\left(\frac{m}{m_2}\right)^{3/2} + 7\sqrt{\frac{m}{m_2}} - 3\sqrt{\frac{m_2}{m}}\right\}\right]\hat{x}_{(k}\hat{z}_{l)} - 6\frac{m}{m_2}\sqrt{\frac{m_2}{b}}\frac{t}{b}\hat{y}_{(k}\hat{z}_{l)}\right\}, \tag{3.17}$$

$$\mathcal{E}_{klp}(t) = \frac{m_2}{b^4}\left\{\left[1 - 3\frac{m_2}{b}\right][15\hat{x}_k\hat{x}_l\hat{x}_p - 9\delta_{(kl}\hat{x}_{p)}] - 3\frac{m}{b}[\hat{x}_k\hat{x}_l\hat{x}_p - 4\hat{y}_{(k}\hat{y}_l\hat{x}_{p)} + \hat{z}_{(k}\hat{z}_l\hat{x}_{p)}]\right\}, \tag{3.18}$$

$$\mathcal{B}_{klp}(t) = \frac{9}{2}\frac{m_2}{b^4}\sqrt{\frac{m}{b}}\left[5\hat{x}_{(k}\hat{x}_l\hat{z}_{p)} - \delta_{(kl}\hat{z}_{p)}\right], \tag{3.19}$$

where $\hat{x}^\mu, \hat{y}^\mu$, $\hat{z}^\mu$ (and $\hat{t}^\mu$ below) are Cartesian basis vectors in the coordinates x^μ, with indices raised and lowered with the flat spacetime metric $\eta_{\mu\nu}$. Still considering the region around hole 1, the characteristic length scale of the perturbation in Eq. (3.14) is $\mathcal{R} \sim \sqrt{b^3/m_2}$ [25]. The tidal fields about hole 2 are obtained by letting $m_2 \to m_1$, $\hat{x}_\mu \to -\hat{x}_\mu$, and $\hat{y}_\mu \to -\hat{y}_\mu$. Of course, these tidal fields are only valid for times $t \approx 0$.

To account for the orbital motion of the black holes, we transform $h_{\mu\nu}$ (appropriately modified for each hole) from Cook-Scheel harmonic coordinates X^μ to barycentric PN harmonic coordinates x^μ. Focusing on the region around hole 1, the coordinate transformation is

$$X^\alpha(x^\beta) = \sum_{j=0}^{5}\left(\frac{m_2}{b}\right)^{j/2}\left(X^\alpha\right)_j(x^\beta) + \mathcal{O}\left(v^6\right), \tag{3.20}$$

where

$$\left(X_\alpha\right)_0 = x_\alpha - \left(C_\alpha\right), \tag{3.21}$$

$$\left(X_\alpha\right)_1 = \left(F_{\beta\alpha}\right)_1\tilde{x}^\beta, \tag{3.22}$$

$$\left(X_\alpha\right)_2 = \left[1 - \frac{\tilde{x}}{b}\right]\Delta_{\alpha\beta}\tilde{x}^\beta + \frac{\Delta_{\beta\gamma}\tilde{x}^\beta\tilde{x}^\gamma}{2b}\hat{x}_\alpha - \frac{1}{2}\left(F_\alpha{}^\gamma\right)_1\left(F_{\beta\gamma}\right)_1\tilde{x}^\beta, \tag{3.23}$$

$$(X_\alpha)_3 = \sqrt{\frac{m}{m_2}}\left\{-\frac{yt}{b^2}\Delta_{\alpha\beta}\tilde{x}^\beta + \left[\frac{\tilde{x}_\mu\tilde{x}^\mu - 4\tilde{x}^2}{2b^2} + \left(2-\frac{m_2}{m}\right)\frac{\tilde{x}}{b} + \left(2+\frac{1}{2}\frac{m_2}{m}\right)\frac{m_2}{m}\right] y\hat{t}_\alpha \right.$$
$$\left. +2\left[1-\frac{m_2}{m}\right]\frac{yt}{b}\hat{x}_\alpha + \left[\frac{3\tilde{r}^2+t^2}{6b^2} + \left(\frac{m_2}{m}-2\right)\frac{\tilde{x}}{b} + \frac{1}{2}\left(\frac{m_2}{m}\right)^2 + 4\right] t\hat{y}_\alpha\right\}$$
$$+ \left(F_{\beta\alpha}\right)_3 \tilde{x}^\beta + \frac{1}{2b^3}\sqrt{\frac{m}{m_2}}\tilde{x}y\left(4\tilde{x}^2 - y^2 - z^2\right)\hat{t}_\alpha. \tag{3.24}$$

In the above, $\tilde{x}^\alpha = x^\alpha - (m_2/m)\, b\hat{x}^\alpha$, $\tilde{r} = \sqrt{\tilde{x}_k\tilde{x}^k}$, and

$$\left(F_{\alpha\beta}\right)_1 = 2\sqrt{\frac{m_2}{m}}\hat{t}_{[\alpha}\hat{y}_{\beta]}, \tag{3.25}$$

$$\left(F_{\alpha\beta}\right)_3 = \left[\left(\frac{m_2}{m}\right)^{3/2} + 3\sqrt{\frac{m_2}{m}} + 5\sqrt{\frac{m}{m_2}}\right]\hat{t}_{[\alpha}\hat{y}_{\beta]}, \tag{3.26}$$

encode the parts of the hole's Lorentz boost that are determined by the matching. In [17], the constant vector $(C_\alpha)_0$ in the zeroth order (in $\sqrt{m_2/b}$) piece of the transformation $(X_\alpha)_0$, is set to the give expected translation to the barycentric frame, i.e., $(C_\alpha)_0 = -(m_2/m)\, b\hat{x}_\alpha$. Here we also take $(C_\alpha)_0$ to have the same value, but this is fixed independently of b, so that b can be adjusted in the other pieces of the transformation to change the boost velocities of the holes for example, without any practical changes to the locations of their centers.

The fourth and fifth order pieces of the coordinate transformation, $(X_\alpha)_4$ and $(X_\alpha)_5$, are more complicated and are not displayed, but they have also been implemented. However, the lowest-order piece of the transformation between Cook-Scheel and PN harmonic coordinates for an unperturbed Schwarzschild black hole enters at fourth order, and we find that the constraint violations (before solving the constraints) are larger when including these higher-order pieces. This may be due in part to the fact that PN harmonic coordinates are not horizon penetrating, even though this transformation is only being applied perturbatively so that including these higher-order pieces still results in horizon penetrating coordinates. For now, we have decided to apply the coordinate transformation of Eq. (3.20) only through third order, since we are not yet including the PN metric in the conformal metric, and so are not too concerned with making the black hole metrics agree with the PN metric as close as possible.

The relationship between the mass M in the perturbed Schwarzschild metric $h_{\mu\nu}$ and the mass m_1 in the PN metric is also determined by the asymptotic matching, and they are identical to the highest order that the matching fixes them, $M = m_1 + \mathcal{O}\left(v^4\right)$. So far, the discussion of the coordinate transformation from Cook-Scheel to PN harmonic coordinates has been confined to the region around hole 1. The coordinate transformation

around hole 2 is obtained from the preceding results by making the substitutions $m_1 \to m_2$, $(t, x, y, z) \to (t, -x, -y, z)$, and $(T, X, Y, Z) \to (T, -X, -Y, Z)$.

Let the tidally perturbed metrics of holes 1 and 2, after transforming to PN harmonic coordinates, be called $g^1_{\mu\nu}$ and $g^2_{\mu\nu}$, respectively. Likewise, let the traces of their extrinsic curvatures (with respect to the transformed black hole metrics) be K_1 and K_2, respectively. Then the conformal metric $\tilde{g}_{ij}$ and the trace of the extrinsic curvature K of our initial data are constructed as

$$\tilde{g}_{ij} = \delta_{ij} + \sum_{A=1}^{2} e^{-r_A^2/w_A^2} \left(g^A_{ij} - \delta_{ij} \right), \tag{3.27}$$

$$K = \sum_{A=1}^{2} e^{-r_A^2/w_A^2} K_A, \tag{3.28}$$

where r_A is the Euclidean distance from the center of hole A in the coordinates of our initial data, and the weight factor w_A determines how quickly the conformal data approach that for a flat spacetime away from the holes. In the superposition, the Gaussian factors $e^{-r_A^2/w_A^2}$ will alter the original properties of the holes. For instance, the mass of each hole in the initial data is typically less than the corresponding value specified for M in the perturbed metric $h_{\mu\nu}$ of hole 1 or 2, and hence for m_1 or m_2 appearing in the tidal fields and coordinate transformation from Cook-Scheel to PN harmonic coordinates. Consequently, one may want to adjust the values of m_1 and m_2 in the coordinate transformation to accommodate these changes. Likewise, the parameter b in the tidal fields and coordinate transformation corresponds to the separation of the holes in PN harmonic coordinates, which are not exactly those of our initial data. So one may also want to adjust b to say, the proper separation between the holes' horizons as computed from the conformal data.

The remaining free data, $\tilde{u}_{ij}$ and $\partial_t K$, are simply set to zero in the *corotating* frame of the two black holes,

$$\tilde{u}_{ij} = 0, \tag{3.29}$$

$$\partial_t K = 0. \tag{3.30}$$

This reflects the assumption that the holes should be very nearly time independent, and that radiation reaction effects can be ignored to a good approximation. Of course other choices can be made, and should even be preferable when including the binary's outgoing gravitational radiation in the conformal data.

3.2.3 Boundary conditions

The singularities of the black holes are excised from our computational domain, so we must impose boundary conditions on the excision surfaces $\mathcal{S}$ when solving Eqs. (3.8), (3.9), and (3.10) for the conformal factor ψ, the lapse N, and the shift β^i. We choose to impose Dirichlet boundary conditions on $\mathcal{S}$, with values that are taken from the transformed (and superposed) tidally perturbed black hole metrics,

$$\psi = 1 \quad \text{on } \mathcal{S}, \tag{3.31}$$

$$N = 1 + \sum_{A=1}^{2} e^{-r_A^2/w_A^2}(N_A - 1) \quad \text{on } \mathcal{S}, \tag{3.32}$$

$$\beta^i = \sum_{A=1}^{2} e^{-r_A^2/w_A^2}\beta_A^i \quad \text{on } \mathcal{S}, \tag{3.33}$$

where N_A and β_A^i are the lapse and shift of hole A's transformed metric, respectively.

We point out that using the quasiequilibrium boundary conditions developed in [26] would not be appropriate here, since they were derived by requiring the excision surfaces to be marginally outer trapped surfaces [27] on which their outgoing null normals have vanishing shear. On the other hand, the marginally outer trapped surface of a tidally perturbed black hole does not satisfy the condition of vanishing shear. The quasiequilibrium boundary conditions could be generalized to dynamical horizons, but we have not yet attempted to do so. Imposing the Dirichlet boundary conditions above does have an advantage though, which is that the apparent horizons in our initial data lie outside the excision surfaces. This eliminates the need to extrapolate the initial data onto an evolution grid with smaller excision boundaries, which fills the interiors of the horizons with constraint-violating data.

Outer boundary conditions are imposed so that the initial data is asymptotically flat. The outer boundary $\mathcal{B}$ is not exactly at infinity, but can be treated as such for all practical purposes since it is taken to be a sphere with radius $\sim 10^9$ times the typical coordinate radius of an excision surface. The outer boundary conditions are

$$\psi = 1 \quad \text{on } \mathcal{B}, \tag{3.34}$$

$$N = 1 \quad \text{on } \mathcal{B}, \tag{3.35}$$

$$\beta^i = \left(\mathbf{\Omega_0} \times \mathbf{r}\right)^i + \dot{a}_0 r^i \quad \text{on } \mathcal{B}, \tag{3.36}$$

where $\mathbf{\Omega_0}$ is the orbital angular velocity, r^i is the coordinate position vector, and $\dot{a}_0$

Cook-Scheel mass	$M = 1$
PN mass of hole 1	$m_1 = 1$
PN mass of hole 2	$m_2 = 1$
PN separation parameter	$b = 30$
Orbital frequency	$\Omega_0 = 0.0078177$
Weight factors	$w_A = 12$
Radius of excision spheres	$r_{\rm exc} = 0.9$
Conformal data	
Black hole mass	$M_c = 0.99927$
Black hole spin	$S/M_c^2 = 1.17849 \times 10^{-6}$
Proper separation	$s_c/2M_c = 16.93365$
Initial Data	
Black hole mass	$M_i = 0.99206$
Black hole spin	$S/M_i^2 = 4.80788 \times 10^{-5}$
Proper separation	$s_i/2M_i = 17.81024$

Table 3.1: Various properties of the conformal data and initial data, constructed by superposing two tidally perturbed Schwarzschild black holes.

represents a possible radial velocity of the black holes. Because the tidally perturbed Schwarzschild metrics we use were derived under the assumption of vanishing radial velocities, we set $\dot{a}_0 = 0$ to be consistent. A downside to this is that the ability to reduce the eccentricity in our initial data is limited, and indicates the need for more general tidally perturbed black hole metrics. The outer boundary condition on β^i sets the coordinates of our initial data to be corotating with the holes.

3.3 Initial data

3.3.1 Parameters

The initial data set considered below describes two equal-mass, nonspinning black holes in a quasicircular orbit. The mass M in the tidally perturbed Schwarzschild metric $h_{\mu\nu}$ of Eq. (3.14) is set to $M = 1$ for both black holes 1 and 2. The center of hole 1 is fixed at $x = 15M$ to zeroth order in the transformation from Cook-Scheel to PN harmonic coordinates (i.e., $(C_\alpha)_0 = -15M\hat{x}_\alpha$), and that of hole 2 is fixed at $x = -15M$ to zeroth order. As a first illustration here, we also set the remaining parameters in the tidal fields and

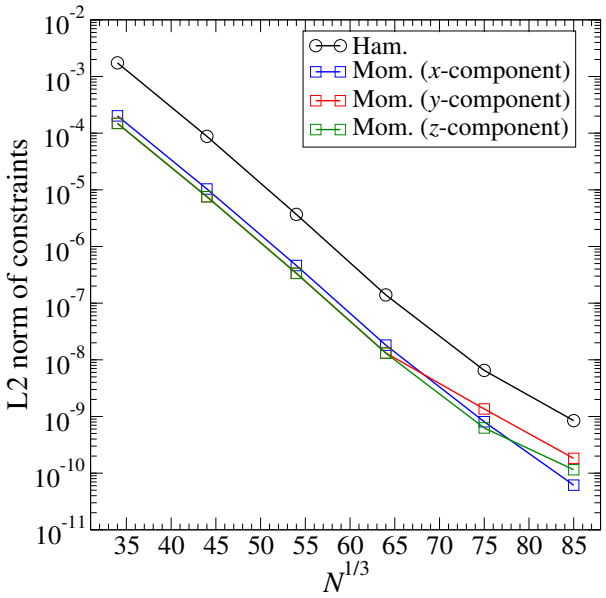

Figure 3.1: L2 norms of the Hamiltonian and momentum constraints, as a function of the total number of grid points N in the computational domain.

coordinate transformations to the most naive values possible without further adjustments, that is $m_1 = 1$, $m_2 = 1$, and $b = 30$. The orbital motion takes place in the xy-plane, and the orbital frequency that enters into the shift boundary condition of Eq. (3.36) is set to the value for a circular orbit as computed from the PN equations,

$$\Omega_0 = \sqrt{\frac{m}{b^3}}\left[1 + \frac{m}{2b}\left(\frac{m_1 m_2}{m^2} - 3\right) + \mathcal{O}\left(\frac{m^2}{b^2}\right)\right] = 0.0078177. \tag{3.37}$$

Various properties of the conformal data (without solving the constraints) and the initial data are summarized in Table 3.1. The spin S of each black holes is calculated using the method of approximate Killing vectors in [11]. The mass of a black hole in the conformal data and initial data (M_c and M_i in Table 3.1) is calculated from Christodoulou's formula

$$M_{\text{Ch.}} = \sqrt{M_{\text{irr}}^2 + \frac{S^2}{4M_{\text{irr}}^2}}, \tag{3.38}$$

where $M_{\text{irr}} = \sqrt{A/16\pi}$ is the irreducible mass and A is the area of the apparent horizon.

3.3.2 Constraints

The extended-conformal-thin-sandwich equations, Eqs. (3.8), (3.9), and (3.10), are solved with the pseudospectral elliptic solver of [20]. The computational domain consists of a

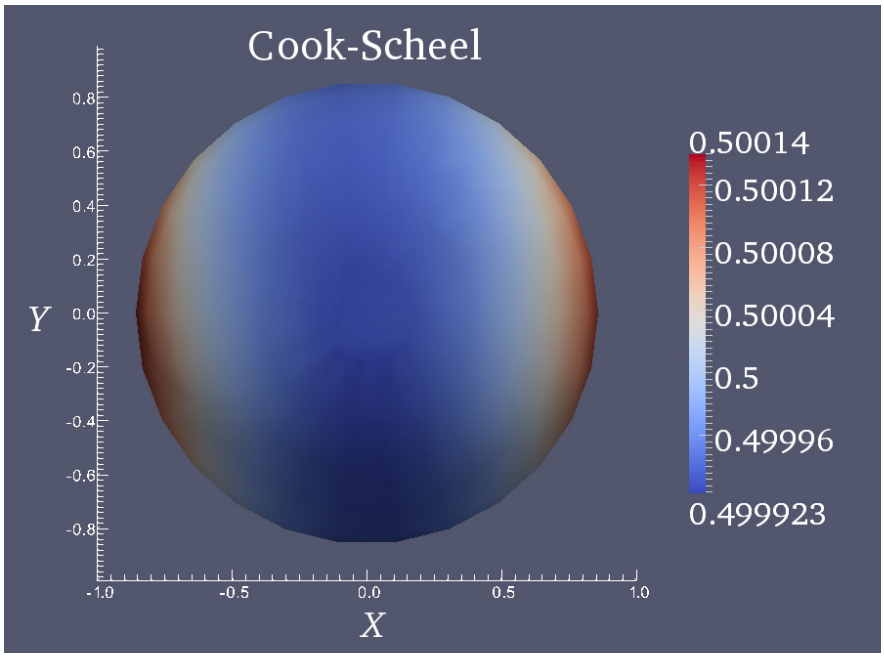

Figure 3.2: Intrinsic scalar curvature $M^2\mathring{R}$ of black hole 1's apparent horizon in Cook-Scheel harmonic coordinates X^μ (cf. Eq. (3.14)) centered on the hole at $T = 0$, without solving the constraints. The view is along the Z-axis, downwards onto the XY-plane.

spherical shell around each black hole, with the excision radius $r_{\rm exc} = 0.9$ of each shell slightly inside the hole's apparent horizon. These inner shells overlap a structure of touching cylinders and rectangular blocks, which is surrounded by a large spherical shell extending to $r = 10^9$. Figure 3.1 shows the L2 norms of the Hamiltonian and momentum constraints of Eqs. (3.4) and (3.5), as a function of numerical resolution. The constraints decrease exponentially as the total number of grid points N is increased.

3.3.3 Tidal deformations

We indicate the tidal deformations of a black hole by the intrinsic scalar curvature $\mathring{R}$ of its apparent horizon. This can be evaluated from the Ricci tensor R_{ij} of the spatial metric g_{ij}, its trace R, and the outward-directed spatial unit normal s^i to the apparent horizon [28],

$$\mathring{R} = R - 2R_{ij}s^i s^j - \mathring{K}^2 + \mathring{K}^{ij}\mathring{K}_{ij}, \tag{3.39}$$

where $\mathring{K}_{ij} = \nabla_i s_j - s_i s^k \nabla_k s_j$ is the extrinsic curvature of the apparent horizon as embedded in the spatial hypersurface Σ_t. Figure 3.2 shows $\mathring{R}$ of black hole 1, in Cook-Scheel harmonic coordinates X^μ centered on the hole at $T = 0$, before the constraints were solved. Figure 3.3

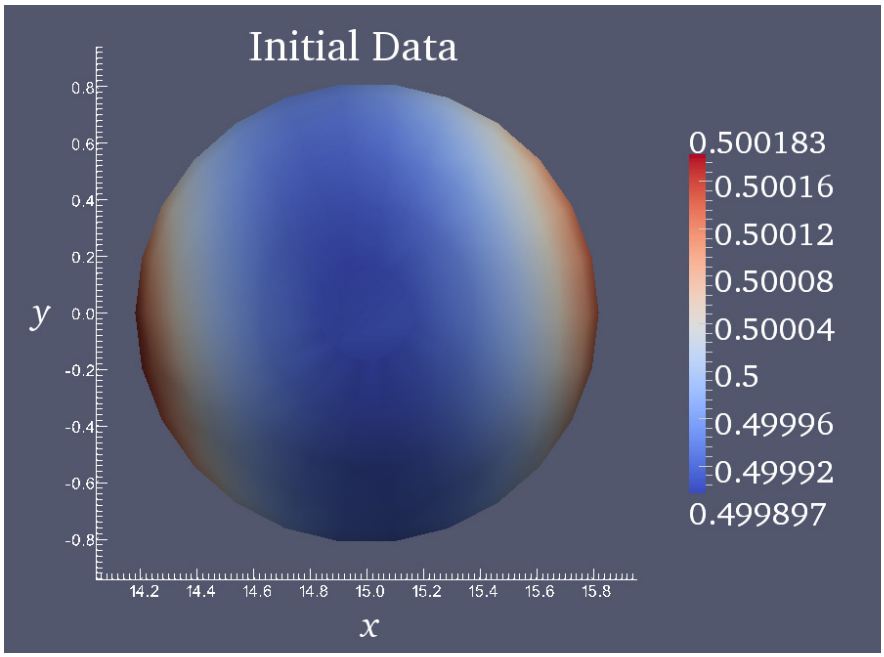

Figure 3.3: Intrinsic scalar curvature $M_i^2 \mathring{R}$ of black hole 1's apparent horizon in the initial data, after transforming to PN harmonic coordinates x^μ and solving the constraints. The view is along the z-axis, downwards onto the xy-plane. Black hole 2 (not shown) is to the left, along the negative x-axis.

shows $\mathring{R}$ of black hole 1 in the initial data, for which the hole has been transformed to PN harmonic coordinates $x^\mu$and the constraints have been solved. The qualitative features of the tidal deformations for the untransformed black hole are largely preserved in the initial data, and in both cases $\mathring{R}$ is greatest along the direction of hole 2.

3.4 Evolutions

The initial data are evolved with methods similar to that described in [29]. The main difference is our evolution domain, which is based on the "cubed-sphere" domain of [30] that has since been improved by Szilágyi. It consists of spherical shells centered on each black hole, which are surrounded by a set of filled cylinders and cylindrical shells to fill out the volume of a large sphere. This structure is in turn surrounded by a series of large spherical shells. The black hole interiors are partially excised from the domain, with the excision boundaries being the same as that of the initial data domain, at approximately $r_{\rm exc} = 0.9 M_i$. The outer boundary is located at approximately $960 M_i$. We perform evolutions at two different numerical resolutions, N1 with 51^3 grid points, and N2 with 57^3 grid points.

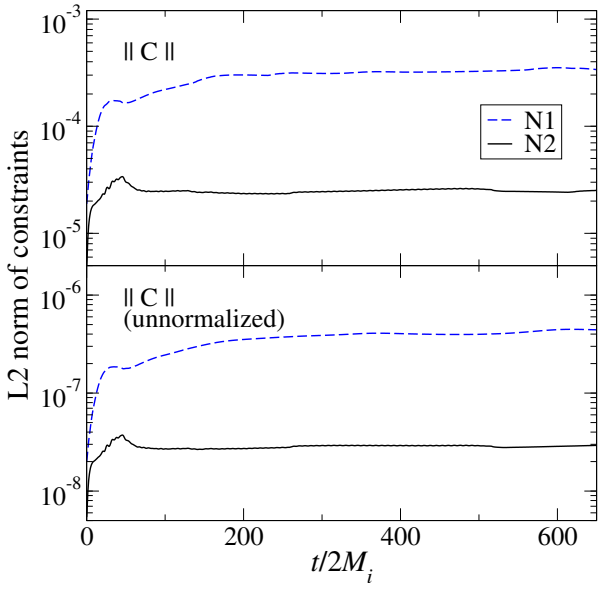

Figure 3.4: L2 norms of the Hamiltonian and momentum constraints, as a function of the total number of grid points N in the computational domain.

The Einstein evolution equations are solved with the pseudospectral evolution code described in Ref. [31], which uses a first-order representation of the generalized harmonic system [32]. The outer boundary conditions [32, 33, 34] are designed to prevent the influx of unphysical constraint violations [35, 36, 37, 38, 39, 40, 41] and undesired incoming gravitational radiation [42, 43], while allowing the outgoing gravitational radiation to pass freely through the boundary.

3.4.1 Constraints

The Einstein constraints or the secondary constraints of the first-order generalized harmonic evolution system are not explicitly enforced, so it is useful to monitor their values to obtain an indication of the accuracy of the evolutions. The constraints are shown in Fig. 3.4. The top panel shows the L^2 norm of all the constraint fields of the first-order generalized harmonic system, normalized by the L^2 norm of the spatial gradients of the dynamical fields (cf. Eq. (71) in [32]). The bottom panel shows the same quantity, but without the normalization factor. The L^2 norms are taken over the portion of the computational volume that lies outside the apparent horizons. Initially, there is a sharp increase in the constraints because the numerical resolution of the initial data domain is much higher than that of the evolution domains. The constraints then level off and stay fairly constant during the early inspiral.

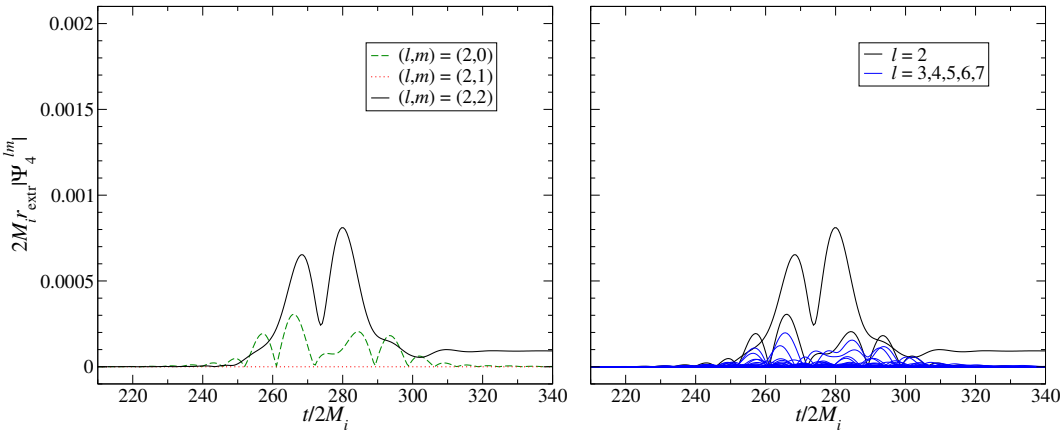

Figure 3.5: Junk radiation in the N2 evolution, as indicated by the values of $2M_i r_{\rm extr}\left|\Psi_4^{lm}\right|$ extracted at $r_{\rm extr}/2M_i = 265$. The left panel only shows the values for modes with $l = 2$ and $m \geq 0$. The right panel shows the values for modes with $2 \leq l \leq 7$ and $m \geq 0$.

3.4.2 Junk radiation

Gravitational waves are extracted from the simulation on different spheres of coordinate radius $r_{\rm extr}$, following the same procedure as in [5]. The Newman-Penrose scalar Ψ_4 is expanded in terms of spin-weighted spherical harmonics of weight -2,

$$\Psi_4\left(t,r,\theta,\phi\right) = \sum_{lm} \Psi_4^{lm}\left(t,r\right) {}_{-2}Y_{lm}\left(\theta,\phi\right), \tag{3.40}$$

with expansion coefficients Ψ_4^{lm}. The junk radiation is visible at early times in Ψ_4^{lm}. We shall consider the waveforms extracted at $r_{\rm extr}/2M_i = 265$, so that they may more easily be compared to the results for the superposed-boosted-Schwarzschild (SBS) initial data in [12], which do not include tidal deformations in the black hole metrics and are solved for with quasiequilibrium boundary conditions.

The left panel of Fig. 3.5 shows the components of the junk radiation with $l = 2$ and $m \geq 0$ in the N2 evolution, which are indicated by the appropriate values of $2M_i r_{\rm extr}\left|\Psi_4^{lm}\right|$ extracted at $r_{\rm extr}/2M_i = 265$ (the vertical scale is the same as the corresponding figures in [12]). It is interesting to observe that while the magnitudes of the $(2,0)$ and $(2,2)$ components are very similar for the SBS initial data of [12], here the $(2,0)$ component is noticeably smaller than the $(2,2)$ component. Not surprisingly, a relative reduction in the $(2,2)$ component of the junk is not seen for the tidally deformed initial data, but this situation is expected to improve once the binary's outgoing radiation is included. The right panel of Fig. 3.5 shows the components of the junk radiation with $2 \leq l \leq 7$ and $m \geq 0$.

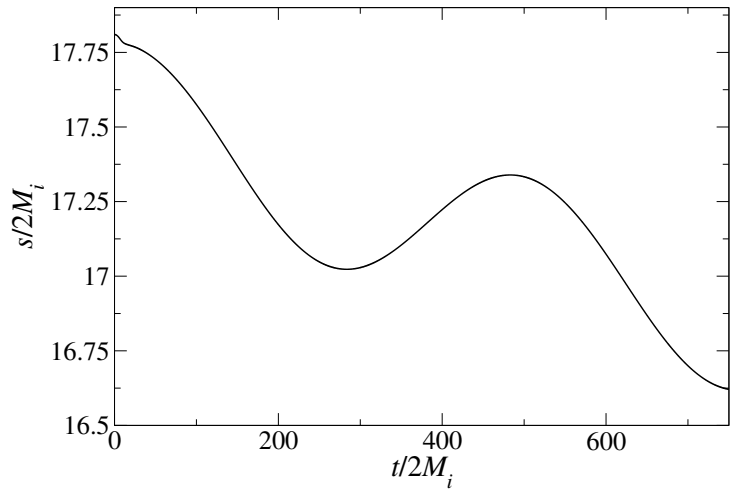

Figure 3.6: Proper separation s of the black holes during the early inspiral. The oscillatory behavior is due to the eccentricity, which has a value of $e \sim 0.01$.

The higher-frequency ($l \geq 3$) components of the junk radiation also appear to be slightly reduced relative to that of the SBS initial data, although an appreciable amount is still present.

3.4.3 Eccentricity

We have not attempted to reduce the eccentricity of our initial data, so that the eccentricity is currently quite large. This can be seen from the oscillatory behavior in the proper separation s of the black holes, as shown in Fig. 3.6. The eccentricity can be estimated according to the technique of [44], by fitting the time derivative of s to a function of the form

$$f(t) = A_0 + A_1 t + B\cos(\omega t + \varphi), \tag{3.41}$$

where A_0, A_1, B, and ω are constants. The eccentricity is then estimated by $e = B/\omega\bar{s}$, where $\bar{s}$ is the average value of s over the time interval of the fit. Carrying out the fitting in the time interval of Fig. 3.6, we estimate the eccentricity of our initial data to be $e \sim 0.01$.

3.5 Future work

We have presented a method for constructing binary-black-hole initial data that includes realistic tidal deformations of the holes as determined from the PN approximation, by building on the approach in [11] of superposing black hole metrics, and using the tidally

perturbed Schwarzschild metrics in [17]. Nevertheless, ample room remains for improving our initial data. The tidal fields may be more accurately represented by different choices of the separation parameter b and the mass parameters m_1 and m_2, as mentioned below Eq. (3.28). Since these parameters also affect the boost velocities of the holes, the orbital eccentricity could possibly be reduced in the process as well. The Gaussian factors that are used for the superposition may be replaced with suitable alternatives, such as functions that remain much closer to unity near the holes so that the properties of the black hole metrics in the conformal data are better preserved.[1] The simple assumption that the freely specifiable time derivatives should be zero in the corotating frame of the holes, $\tilde{u}_{ij} = \partial_t K = 0$, can also be suitably modified. Of course we can go on to include the PN metrics describing both the near zone in the vicinity of both holes, and the wave zone far away from the holes, which includes the outgoing gravitational radiation. These possibilities will be explored in future work.

[1] For instance, we have also used generalized Gaussians such as $e^{-r_A^4/w_A^4}$ and $e^{-r_A^6/w_A^6}$. In these particular cases though, we find that the much steeper falloffs of these factors away from the holes cause the constraints (especially the Hamiltonian constraint) of the initial data to decrease much slower with numerical resolution.

Bibliography

[1] B. A. et al., Phys. Rev. D **73**, 062001 (2006).

[2] L. di Fiore, Class. Quantum Grav. **19**, 1421 (2002).

[3] A. Garat and R. H. Price, Phys. Rev. D **61**, 124011 (2000).

[4] S. Nissanke, Phys. Rev. D **73**, 124002 (2006).

[5] M. Boyle et al., Phys. Rev. D **76**, 124038 (2007).

[6] M. Hannam, S. Husa, J. A. González, U. Sperhake, and B. Brügmann, Phys. Rev. D **77**, 044020 (2008).

[7] R. A. Matzner, M. F. Huq, and D. Shoemaker, Phys. Rev. D **59**, 024015 (1998).

[8] P. Marronetti and R. A. Matzner, Phys. Rev. Lett. **85**, 5500 (2000).

[9] P. Marronetti et al., Phys. Rev. D **62**, 024017 (2000).

[10] M. Hannam, S. Husa, B. Brügmann, J. A. Gonzalez, and U. Sperhake, Class. Quantum Grav. **24**, S15 (2007).

[11] G. Lovelace, R. Owen, H. P. Pfeiffer, and T. Chu, Phys. Rev. D **78**, 084017 (2008).

[12] G. Lovelace, Class. Quantum Grav. **26**, 114002 (2009).

[13] L. Blanchet, Living Rev. Rel. **9** (2006).

[14] B. J. Kelly, W. Tichy, M. Campanelli, and B. F. Whiting, Phys. Rev. D **76**, 024008 (2007).

[15] B. J. Kelly, W. Tichy, Y. Zlochower, M. Campanelli, and B. Whiting, Class. Quantum Grav. **27**, 114005 (2010).

[16] B. C. Mundim, B. J. Kelly, Y. Zlochower, H. Nakano, and M. Campanelli, Class. Quantum Grav. **28**, 134003 (2011).

[17] N. K. Johnson-McDaniel, N. Yunes, W. Tichy, and B. J. Owen, Phys.Rev. **D80**, 124039 (2009).

[18] N. Yunes, W. Tichy, B. J. Owen, and B. Brügmann, Phys. Rev. D **74**, 104011 (2006).

[19] N. Yunes and W. Tichy, Phys. Rev. D **74**, 064013 (2006).

[20] H. P. Pfeiffer, L. E. Kidder, M. A. Scheel, and S. A. Teukolsky, Comput. Phys. Commun. **152**, 253 (2003).

[21] J. W. York, Phys. Rev. Lett. **82**, 1350 (1999).

[22] H. P. Pfeiffer and J. W. York, Phys. Rev. D **67**, 044022 (2003).

[23] R. Arnowitt, S. Deser, and C. W. Misner, The dynamics of general relativity, in *Gravitation: An Introduction to Current Research*, edited by L. Witten, Wiley, New York, 1962.

[24] J. W. York, Jr., Kinematics and dynamics of general relativity, in *Sources of Gravitational Radiation*, edited by L. L. Smarr, pages 83–126, Cambridge University Press, Cambridge, England, 1979.

[25] K. S. Thorne and J. B. Hartle, Phys. Rev. D **31**, 1815 (1985).

[26] G. B. Cook and H. P. Pfeiffer, Phys. Rev. D **70**, 104016 (2004).

[27] E. Schnetter, B. Krishnan, and F. Beyer, Phys. Rev. D **74**, 024028 (2006).

[28] S. Carroll, *Spacetime and Geometry: An Introduction to General Relativity*, Addison Wesley, New York, 2003.

[29] M. Boyle et al., Phys. Rev. D **78**, 104020 (2008).

[30] B. Szilagyi, L. Lindblom, and M. A. Scheel, Phys. Rev. D **80**, 124010 (2009).

[31] M. A. Scheel et al., Phys. Rev. D **74**, 104006 (2006).

[32] L. Lindblom, M. A. Scheel, L. E. Kidder, R. Owen, and O. Rinne, Class. Quantum Grav. **23**, S447 (2006).

[33] O. Rinne, Class. Quantum Grav. **23**, 6275 (2006).

[34] O. Rinne, L. Lindblom, and M. A. Scheel, Class. Quantum Grav. **24**, 4053 (2007).

[35] J. M. Stewart, Class. Quantum Grav. **15**, 2865 (1998).

[36] H. Friedrich and G. Nagy, Commun. Math. Phys. **201**, 619 (1999).

[37] J. M. Bardeen and L. T. Buchman, Phys. Rev. D **65**, 064037 (2002).

[38] B. Szilágyi, B. Schmidt, and J. Winicour, Phys. Rev. D **65**, 064015 (2002).

[39] G. Calabrese, J. Pullin, O. Reula, O. Sarbach, and M. Tiglio, Commun. Math. Phys. **240**, 377 (2003).

[40] B. Szilágyi and J. Winicour, Phys. Rev. D **68**, 041501(R) (2003).

[41] L. E. Kidder, L. Lindblom, M. A. Scheel, L. T. Buchman, and H. P. Pfeiffer, Phys. Rev. D **71**, 064020 (2005).

[42] L. T. Buchman and O. C. A. Sarbach, Class. Quantum Grav. **23**, 6709 (2006).

[43] L. T. Buchman and O. C. A. Sarbach, Class. Quantum Grav. **24**, S307 (2007).

[44] H. P. Pfeiffer et al., Class. Quantum Grav. **24**, S59 (2007).

Chapter 4

High-accuracy waveforms for binary black hole inspiral, merger, and ringdown

The first spectral numerical simulations of 16 orbits, merger, and ringdown of an equal-mass nonspinning binary black hole system are presented. Gravitational waveforms from these simulations have accumulated numerical phase errors through ringdown of $\lesssim$0.1 radians when measured from the beginning of the simulation, and $\lesssim$0.02 radians when waveforms are time and phase shifted to agree at the peak amplitude. The waveform seen by an observer at infinity is determined from waveforms computed at finite radii by an extrapolation process accurate to $\lesssim$0.01 radians in phase. The phase difference between this waveform at infinity and the waveform measured at a finite radius of $r = 100M$ is about half a radian. The ratio of final mass to initial mass is $M_f/M = 0.95162 \pm 0.00002$, and the final black hole spin is $S_f/M_f^2 = 0.68646 \pm 0.00004$.

Originally published as M. A. Scheel, M. Boyle, T. Chu, L. E. Kidder, K. D. Matthews, and H. P. Pfeiffer, Phys. Rev. D **79**, 024003 (2009).

4.1 Introduction

Beginning with the groundbreaking binary black hole evolutions of Pretorius [1] and the development of the moving puncture method [2, 3], it has recently become possible to solve Einstein's equations numerically for the inspiral, merger, and ringdown of two black holes in a binary orbit. Already these simulations have provided tests of post-Newtonian approximations [4, 5, 6, 7, 8, 9, 10, 11, 12, 13, 14], have allowed initial exploration of the

orbital dynamics of spinning binaries [15, 16, 17, 18, 19, 20], have determined the recoil velocity of the final black hole when the masses are unequal [21, 22, 23, 24], and have led to the discovery of dramatically large recoil velocity from certain spin configurations [25, 26, 27, 28, 18, 29, 30, 31, 32, 33, 34, 35, 36, 37].

Waveforms from these numerical simulations are important for gravitational-wave detectors such as LIGO and LISA. This is not only because detected waveforms can be compared with numerical models to measure astrophysical properties of the sources of gravitational radiation, but also because the detection probability itself can be increased via the technique of matched filtering [38], in which noisy data are convolved with numerical templates to enhance the signal.

However, binary black hole simulations are time consuming: a single simulation following approximately 10 orbits, merger, and ringdown typically requires a few weeks of runtime on approximately 50 or 100 processors of a parallel supercomputer, and typically such a simulation produces waveforms of only modest accuracy. This large computational expense precludes, for example, producing a full template bank of numerical waveforms covering the entire parameter space of black hole masses and spins. Hence there has been much interest in construction of phenomenological analytical waveforms [39, 7, 40, 41] that can be computed quickly and are calibrated by a small number of numerical simulations. While the accuracy of typical simulations is sufficient for creating LIGO detection templates, it is most likely inadequate for LIGO parameter estimation and is far from what is required for LISA data analysis [42].

One approach to increasing the accuracy and efficiency of simulations is to adopt more efficient numerical methods. In particular, a class of numerical techniques known as spectral methods holds much promise. For smooth solutions, the errors produced by spectral methods decrease exponentially as computational resources are increased, whereas the errors of finite difference methods, the methods used by the majority of binary black hole simulations, decrease polynomially. Indeed, spectral methods have been used to produce very accurate initial data for binary black holes and neutron stars [43, 44, 45, 46, 47, 48, 49, 50, 51, 52, 53, 54, 55, 56], and they have been used to produce the longest and most accurate binary black hole inspiral simulation to date [57, 9].

However, a key difficulty with time-dependent spectral binary black hole simulations has been handling the merger of the two holes. For example, the spectral simulations described in [57, 9, 12] are very accurate and efficient, but they follow only the inspiral of the two black holes, and fail just before the holes merge. This is sufficient for some applications,

such as comparing post-Newtonian formulae with numerical results during the inspiral and finding accurate analytic templates that match the numerical inspiral waveforms [9, 12], but for most purposes the merger is the most crucial part of the process: for instance the gravitational-wave emission is the strongest during merger, and details of the merger determine the recoil velocity of the final black hole.

In this chapter, we present a spectral binary black hole simulation that follows sixteen orbits of the binary plus merger and ringdown of the merged black hole. In section 4.2 we describe the equations, gauge conditions, and numerical methods we use to solve Einstein's equations; in particular, sections 4.2.3 and 4.2.4 describe changes to our gauge conditions that allow simulation of the merger, and our method for extending the evolution through ringdown. In section 4.3 we discuss extraction of the gravitational waveform from the simulation, including the process of extrapolating the waveform to infinity. Section 4.3 also includes an estimate of the uncertainty in the waveform from several sources. Finally, in section 4.4 we discuss outstanding difficulties and future improvements.

4.2 Solution of Einstein's Equations

4.2.1 Initial data

The initial data describe two nonspinning black holes, each with Christodoulou mass $M/2$, in quasicircular orbit with low eccentricity. The initial data are exactly as described in Ref. [9]. Briefly, initial data are constructed within the conformal thin sandwich formalism [58, 59] using a pseudospectral elliptic solver [49]. We employ quasi-equilibrium boundary conditions [60, 50] on spherical excision boundaries, choose conformal flatness and maximal slicing, and use Eq. (33a) of Ref. [53] as the lapse boundary condition. The spins of the black holes are made very small ($\sim 10^{-7}$) via an appropriate choice of the tangential shift at the excision surfaces, as described in [53]. Finally, the initial orbital eccentricity is tuned to a very small value ($\sim 5\times 10^{-5}$) using the iterative procedure described in Ref. [9], which is an improved version of the procedure of Ref. [61].

4.2.2 Evolution of the inspiral phase

The evolution of the first $\sim$15 binary orbits is identical to the simulation presented in Ref. [9]. We describe it here briefly in order to facilitate the presentation of our method for continuing the evolution through merger and ringdown, which is described in sections 4.2.3

and 4.2.4.

The Einstein evolution equations are solved with the pseudospectral evolution code described in Ref. [57]. This code evolves a first-order representation [62] of the generalized harmonic system [63, 64, 65]. We handle the singularities by excising the black hole interiors from the computational domain. Our outer boundary conditions [62, 66, 67] are designed to prevent the influx of unphysical constraint violations [68, 69, 70, 71, 72, 73, 74] and undesired incoming gravitational radiation [75, 76], while allowing the outgoing gravitational radiation to pass freely through the boundary.

We employ the dual-frame method described in Ref. [57]: we solve the equations in an "inertial frame" that is asymptotically Minkowski, but our domain decomposition is fixed in a "comoving frame" that rotates with respect to the inertial frame and also shrinks with respect to the inertial frame as the holes approach each other. The positions of the holes are fixed in the comoving frame; we account for the motion of the holes by dynamically adjusting the coordinate mapping between the two frames. Note that the comoving frame is referenced only internally in the code as a means of treating moving holes with a fixed domain. Therefore all coordinate quantities (e.g., black hole trajectories, wave-extraction radii) mentioned in this work are inertial-frame values unless explicitly stated otherwise.

As described in [9], the mapping between inertial and comoving coordinates for the inspiral, expressed in polar coordinates relative to the center of mass of the system, is

$$r = \left[a(t) + (1 - a(t)) \frac{r'^2}{R_0'^2}\right] r', \tag{4.1}$$

$$\theta = \theta', \tag{4.2}$$

$$\phi = \phi' + b(t), \tag{4.3}$$

where $a(t)$ and $b(t)$ are functions of time, and R_0' is a constant usually chosen to be roughly the radius of the outer boundary in comoving coordinates. Here primes denote the comoving coordinates. For the choice $R_0' = \infty$, the mapping is simply a rotation by $b(t)$ plus an overall contraction given by $a(t)$. The functions $a(t)$ and $b(t)$ are determined by a dynamical control system as described in Ref. [57]. This control system dynamically adjusts $a(t)$ and $b(t)$ so that the centers of the apparent horizons remain stationary in the comoving frame. Note that the outer boundary of the computational domain is at a fixed comoving radius $R'_{\rm max}$, so the inertial-coordinate radius of the outer boundary $R_{\rm max}(t)$ is a function of time.

The gauge freedom in the generalized harmonic system is fixed via a freely specifiable

gauge source function H_a that satisfies the constraint

$$0 = \mathcal{C}_a \equiv \Gamma_{ab}{}^{b} + H_a, \tag{4.4}$$

where $\Gamma^{a}{}_{bc}$ are the spacetime Christoffel symbols. To choose this gauge source function, we first define a new quantity $\tilde{H}_a$ that has the following two properties: (i) $\tilde{H}_a$ transforms like a tensor, and (ii) in inertial coordinates $\tilde{H}_a = H_a$. We choose H_a so that the constraint equation (4.4) is satisfied initially, and we demand that $\tilde{H}_{a'}$ is constant in the moving frame, i.e., that $\partial_{t'}\tilde{H}_{a'} = 0$.

4.2.3 Extending inspiral runs through merger

If the inspiral runs described above are allowed to continue without any modification of the algorithm, then as the binary approaches merger, the horizons of the black holes become extremely distorted and the dynamical fields begin to develop sharp (but numerically convergent) features near each hole. These features grow rapidly in time, eventually halting the simulation before merger. This is due to a gauge effect: The gauge condition used during the inspiral, namely fixing H_a in time in the comoving frame, was chosen based on the idea that each black hole is in quasi-equilibrium in this frame. Once the black holes begin to interact strongly, this gauge condition no longer allows the coordinates to sufficiently react to the changing geometry, and coordinate singularities develop.

Therefore we must modify our gauge conditions in order to handle merger. Because the inspiral gauge works so well before merger, we choose to remain in that gauge until some time $t = t_g$, and then we change (smoothly) to a new gauge.

We have experimented with several gauge conditions [77], but so far the simplest gauge choice that works, and the one used in the simulations presented here, is based on the gauge treatment of Pretorius [65, 1, 78]: We promote the gauge source function H_a to an independent dynamical field that satisfies

$$\nabla^c\nabla_c H_a = Q_a(x, t, \psi_{ab}) + \xi_2 t^b \partial_b H_a, \tag{4.5}$$

where $\nabla^c\nabla_c$ is the curved space *scalar* wave operator (i.e. each component of H_a is evolved as a scalar), ψ_{ab} is the spacetime metric, and t^a is the timelike unit normal to the hyper-

surface. The driving function Q_a is

$$Q_t = f(x,t)\xi_1 \frac{1-N}{N^\eta}, \tag{4.6}$$

$$Q_i = g(x,t)\xi_3 \frac{N_i}{N^2}. \tag{4.7}$$

Here N and N^i are the lapse function and the shift vector, η, ξ_1, ξ_2, and ξ_3 are constants, and $f(x,t)$ and $g(x,t)$ are prescribed functions of the spacetime coordinates (we describe our choices for these objects below).

Equation (4.5) is a damped, driven wave equation with damping parameter ξ_2 and driving function Q_a. The driving term Q_t in Eq. (4.6) was introduced by Pretorius [1, 65] to drive the lapse function toward unity so as to prevent it from becoming small. The driving term Q_i is new; it drives the shift vector toward zero near the horizons. This causes the horizons to expand in coordinate space, and has the effect of smoothing out the dynamical fields near the horizon and preventing gauge singularities from developing. A different gauge choice that causes similar coordinate expansion of the horizons was introduced in Ref. [79]. Care must be taken so that the horizons do not expand too quickly relative to the excision boundaries; otherwise the characteristic fields will fail to be purely outgoing (into the holes) at the excision boundaries, and excision will fail. We find that with appropriate choices of ξ_1, ξ_3, $f(x,t)$, and $g(x,t)$ as described below, the horizons expand gradually and not too rapidly.

For the runs presented here we choose $\eta = 4$, $\xi_1 = 0.1$, $\xi_2 = 10$, and $\xi_3 = 0.4$. The functions $f(x,t)$ and $g(x,t)$ in Eqs. (4.6) and (4.7) are chosen based on two criteria: the first is that the driving terms Q_a are nonzero only near the black holes where they are needed; if these terms are nonzero in the wave-extraction zone they lead to complicated gauge dynamics in this region, making waveform extraction difficult. The second criterion is that the driving terms are turned on in a gradual manner so that the gauge does not change too rapidly. We choose

$$\begin{aligned} f(x,t) = g(x,t) &= (2 - e^{-(t-t_g)/\sigma_1}) \\ &\times (1 - e^{-(t-t_g)^2/\sigma_2^2}) e^{-r'^2/\sigma_3^2}, \end{aligned} \tag{4.8}$$

where r' is the coordinate radius in comoving coordinates, and the constants are $\sigma_1 \sim 17.5M$, $\sigma_2 \sim 15M$, and $\sigma_3 \sim 40M$. Here M is the sum of the initial Christodoulou masses of the two holes.

Equation (4.5) is a second-order hyperbolic equation, which we evolve in first-order form by defining new fields Π_a^H and Φ_{ia}^H, representing (up to the addition of constraints) the appropriate time and space derivatives of H_a, respectively:

$$\Pi_a^H = -t^b \partial_b H_a, \tag{4.9}$$

$$\Phi_{ia}^H = \partial_i H_a. \tag{4.10}$$

The representation of wave equations of this type in first-order form is well understood, see e.g., Refs. [80, 62]; the result for Eq. (4.5) is

$$\partial_t H_a = -N\Pi_a^H + N^k \Phi_{ka}^H, \tag{4.11}$$

$$\begin{aligned} \partial_t \Pi_a^H &= N^k \partial_k \Pi_a^H - N g^{ki} \partial_k \Phi_{ia}^H - \gamma_2^H N^k \partial_k H_a \\ &+ \gamma_2^H N^k \Phi_{ka}^H + N(\Gamma^{kj}{}_j - g^{kj}\partial_j N)\Phi_{ka}^H \\ &+ NK\Pi_a^H + Q_a, \end{aligned} \tag{4.12}$$

$$\begin{aligned} \partial_t \Phi_{ia}^H &= N^k \partial_k \Phi_{ia}^H - N\partial_i \Pi_a^H + \gamma_2^H N \partial_i H_a \\ &- \Pi_a^H \partial_i N + \Phi_{ka}^H \partial_i N^k - \gamma_2^H N \Phi_{ia}^H, \end{aligned} \tag{4.13}$$

where g_{ij} is the spatial metric and K is the trace of the extrinsic curvature. We choose the constraint-damping parameter γ_2^H to be $\gamma_2^H = 4/M$.

These equations are symmetric hyperbolic, and require boundary conditions on all incoming characteristic fields at all boundaries. The characteristic fields for Eqs. (4.11)–(4.13) in the direction of a unit spacelike covector n_i are

$$U_a^{H\pm} = \Pi_a^H \pm n^i \Phi_{ia}^H - \gamma_2^H H_a, \tag{4.14}$$

$$Z_a^{H1} = H_a, \tag{4.15}$$

$$Z_{ia}^{H2} = (\delta_i^k - n_i n^k)\Phi_{ka}^H. \tag{4.16}$$

The (coordinate) characteristic speeds for $U_a^{H\pm}$, Z_a^{H1}, and Z_{ia}^{H2} are $\pm N - n_i N^i$, 0, and $-n_i N^i$, respectively.

At the excision boundaries all characteristic fields are outgoing (i.e. into the holes) or nonpropagating, so no boundary conditions are necessary and none are imposed. At the

outer boundary, we must impose boundary conditions on U_a^{H-} and Z_{ia}^{H2}. Define

$$D_t(U_a^{H\pm}) \equiv \partial_t \Pi_a^H \pm n^i \partial_t \Phi_{ia}^H - \gamma_2^H \partial_t H_a, \tag{4.17}$$

$$D_t(Z_a^{H1}) \equiv \partial_t H_a, \tag{4.18}$$

$$D_t(Z_{ia}^{H2}) \equiv (\delta_i^k - n_i n^k)\partial_t \Phi_{ka}^H, \tag{4.19}$$

where the time derivatives on the right-hand side are evaluated using Eqs. (4.11)–(4.13). Then we impose the following boundary conditions:

$$\partial_t U_a^{H-} = -\gamma_2^H D_t(Z_a^{H1}), \tag{4.20}$$

$$\partial_t Z_{ia}^{H2} = D_t(Z_{ia}^{H2}) + 2 n_k N^k n^j \partial_{[i} \Phi_{j]a}^H. \tag{4.21}$$

Equation (4.20) is the outgoing-wave boundary condition described in detail in Ref. [80]. Equation (4.21) ensures that violations of the artificial constraint $C_{ia} \equiv \Phi_{ia}^H - \partial_i H_a = 0$ do not enter the domain through the boundary; it is the direct analogue of the constraint-preserving boundary condition we apply to the analogous variable in the generalized harmonic formulation of Einstein's equations, Eq. (65) of Ref. [62].

Note that Eqs. (4.11)–(4.13) involve only first derivatives of the spacetime metric, and similarly, the generalized harmonic Einstein equations involve only first derivatives of H_a. Therefore, adding Eqs. (4.11)–(4.13) to the system does not change the hyperbolicity or characteristic fields of the generalized harmonic Einstein equations, so we can impose the same boundary conditions on the generalized harmonic variables as we do during the inspiral, as described in Refs. [57, 66].

Equations (4.11)–(4.13) require as initial data the values of H_a and Π_a^H at $t = t_g$. These quantities can be computed from the gauge choice used during the inspiral for $t \leq t_g$, so we choose them to be continuous at $t = t_g$.

Note that Eqs. (4.11)–(4.13) and the boundary conditions (4.20) and (4.21) are written in the inertial coordinate system. The equations are actually solved in the comoving coordinate system using the dual-frame method described in Ref. [57].

With the modifications to the gauge conditions described here, the evolution of the binary can be tracked up until (and shortly after) the formation of a common horizon that encompasses both black holes. Because of the more rapid dynamics and the distortions of the horizons during the merger, we typically increase the numerical resolution slightly when we make these changes to the gauge conditions (this is the difference between the first

and second entry in the $N_{\rm pts}$ column in Table 4.1). After the common horizon forms, the problem reduces to evolving a single highly distorted dynamical black hole, rather than two separate black holes. We change the algorithm to take advantage of this, as described in the next section.

4.2.4 Evolution from merger through ringdown

We make three main changes to our evolution algorithm once we detect a common apparent horizon. First, because there is now only one black hole and not two, we interpolate all variables onto a new computational domain that contains only a single excised region. Second, we choose a new comoving coordinate system (and a corresponding mapping to inertial coordinates) so that the new excision boundary tracks the shape of the (distorted, rotating, pulsating) apparent horizon in the inertial frame, and so that the outer boundary behaves smoothly in time. Third, we modify the gauge conditions so that the shift vector is no longer driven toward zero, allowing the solution to eventually relax to a time-independent state. We now discuss these three changes in detail.

Our new computational domain contains only a single excised region, and is much simpler than the one used until merger. It consists only of nested spherical-shell subdomains that extend from a new excision boundary $R''_{\rm min}$, chosen to be slightly inside the common apparent horizon, to an outer boundary $R''_{\rm max}$ that coincides with the outer boundary of the old domain.

To understand how we choose our new comoving frame, first recall that in the dual-frame technique [57], the comoving frame is the one in which the computational domain is fixed, the inertial frame is the one in which the coordinates are Minkowski-like at infinity, and the two frames are related by a mapping that is chosen so that the computational domain tracks the motion of the black holes. Let x^a represent the inertial coordinates (which are the same before and after merger), let x'^a represent the old comoving coordinates, and let x''^a represent the new comoving coordinates. The mapping between x'^a and x^a is given by Eqs. (4.1)–(4.3). The mapping between x''^a and x^a is chosen to be

$$\begin{aligned} r &= \tilde{r}\Bigg[1+\sin^2(\pi\tilde{r}/2R''_{\rm max}) \\ &\quad \times\left(A(t)\frac{R'_{max}}{R''_{\rm max}}+(1-A(t))\frac{R'^3_{max}}{R''_{\rm max}R'^2_0}-1\right)\Bigg], \end{aligned} \tag{4.22}$$

$$\tilde{r} = r'' - q(r'') \sum_{\ell=0}^{\ell_{\max}} \sum_{m=-\ell}^{\ell} \lambda_{\ell m}(t) Y_{\ell m}(\theta'', \phi''), \tag{4.23}$$

$$\theta = \theta'', \tag{4.24}$$

$$\phi = \phi'' + B(t), \tag{4.25}$$

where R'_{max} is the outer boundary of the premerger computational domain in the old comoving coordinates, and $q(r'')$, $A(t)$, $B(t)$, and $\lambda_{\ell m}(t)$ are functions we will now discuss.

First we describe the angular map: The function $B(t)$ is chosen so that the new comoving frame initially rotates with respect to the inertial frame, but this rotation slows to a halt after a short time. In particular,

$$B(t) = B_0 + (B_1 + B_2(t - t_m))e^{-(t-t_m)/\tau_B}, \tag{4.26}$$

where the constants B_0, B_1, and B_2 are chosen so that $B(t)$ matches smoothly onto $b(t)$ from Eq. (4.3): $B(t_m) = b(t_m)$, $\dot{B}(t_m) = \dot{b}(t_m)$, and $\ddot{B}(t_m) = \ddot{b}(t_m)$. Here t_m is the time at which we transition to the new domain decomposition. The constant τ_B is chosen to be on the order of $20M$.

The radial map is a composition of two individual maps: Eqs. (4.22) and (4.23). The purpose of Eq. (4.22) is to match the outer boundary of the new domain smoothly onto that of the old domain, while far from the outer boundary Eq. (4.22) approaches the identity. We have found that without the use of Eq. (4.22), the (inertial-coordinate) location of the boundary changes nonsmoothly at $t = t_m$, thereby generating a spurious ingoing gauge pulse that spoils waveform extraction. The function $A(t)$ is

$$A(t) = A_0 + (A_1 + A_2(t - t_m))e^{-(t-t_m)/\tau_A}, \tag{4.27}$$

where the constants A_0, A_1, and A_2 are chosen so that $A(t)$ matches smoothly onto $a(t)$ from Eq. (4.1): $A(t_m) = a(t_m)$, $\dot{A}(t_m) = \dot{a}(t_m)$, and $\ddot{A}(t_m) = \ddot{a}(t_m)$. The constant τ_A is chosen to be on the order of $5M$.

The other piece of the radial map, Eq. (4.23), is chosen so that the apparent horizon is nearly spherical in the new comoving coordinates x''^a. The function $q(r'')$ is

$$q(r'') = e^{-(r''-R''_{\rm AH})^3/\sigma_q^3}, \tag{4.28}$$

where $R''_{\rm AH}$ is the radius of the apparent horizon in comoving coordinates, and σ_q is a

constant of order $20M$. This function $q(r'')$ ensures that the piece of the radial map represented by Eq. (4.23) acts only in the vicinity of the merged hole and not in the exterior wave-extraction region.

We now discuss the choice of the functions $\lambda_{\ell m}(t)$ that appear in Eq. (4.23). Given the known location of the apparent horizon in inertial coordinates, the $\lambda_{\ell m}(t)$ determine the shape of the apparent horizon in comoving coordinates. At $t = t_m$, we choose these quantities so that the apparent horizon is spherical (up to spherical harmonic component $\ell = \ell_{\rm max}$) in comoving coordinates: that is, if the comoving-coordinate radius of the apparent horizon as a function of angles is written as

$$r''_{\rm AH}(\theta'', \phi'') \equiv \sum_{\ell=0}^{\ell_{\rm max}} \sum_{m=-\ell}^{\ell} Q_{\ell m}(t) Y_{\ell m}(\theta'', \phi''), \tag{4.29}$$

then for $1 \leq \ell \leq \ell_{\rm max}$ we choose $\lambda_{\ell m}(t_m)$ so that $Q_{\ell m}(t_m) = 0$. In addition, we choose $\lambda_{00}(t_m) = 0$; this determines $R''_{\rm AH}$. For $t > t_m$, $\lambda_{\ell m}(t)$ are determined by a dynamical feedback control system identical to the one described in Ref. [57], which adjusts these functions so that the apparent horizon is driven to a sphere (up to spherical harmonic component $\ell = \ell_{\rm max}$) in comoving coordinates. This dynamical feedback control allows us to freely choose the first and second time derivatives of $\lambda_{\ell m}$ at $t = t_m$. Simply choosing these to be zero causes the control system to oscillate wildly before settling down, and unless the time step is very small, these oscillations are large enough that the excision boundary crosses the horizon and our excision algorithm fails. So instead, we obtain the time derivatives of $\lambda_{\ell m}$ by finding the apparent horizon at several times surrounding $t = t_m$, computing $\lambda_{\ell m}$ at these times, and finite-differencing in time. For the equal-mass zero-spin merger presented here, in Eq. (4.23) it suffices to sum only over even ℓ and m and to choose $\ell_{\rm max} = 6$.

The last change we make before continuing the simulation past merger is to modify the functions $f(x,t)$ and $g(x,t)$, which before merger were given by Eq. (4.8), to

$$\begin{aligned} f(x,t) &= (2 - e^{-(t-t_g)/\sigma_1}) \\ &\times (1 - e^{-(t-t_g)^2/\sigma_2^2}) e^{-r''^2/\sigma_3^2}, \end{aligned} \tag{4.30}$$

$$g(x,t) = f(x,t) e^{-(t-t_m)^2/\sigma_4^2}, \tag{4.31}$$

where $\sigma_4 = 7M$. The modification of $g(x,t)$ turns off the term in the gauge evolution equations that drives the shift to zero near the holes. Before merger, it is advantageous to have the shift driven to zero so that the horizons expand in coordinate space and so

Run	$R'_{\rm max}$	$R''_{\rm max}$	R'_0	$N_{\rm pts}$	CPU-h	CPU-h/T
30c1/N4	462	462	698	$(57^3, 59^3, 57^3)$	8,800	2.0
30c1/N5	462	462	698	$(62^3, 66^3, 63^3)$	15,000	3.4
30c1/N6	462	462	698	$(67^3, 73^3, 70^3)$	23,000	5.3
30c2/N6	722	96	∞	$(71^3, 76^3, 63^3)$	25,000	5.7

Table 4.1: Outer boundary parameters, collocation points, and CPU usage for several zero-spin binary black hole evolutions. The first column identifies the inspiral run in the nomenclature of Ref. [9]. $N_{\rm pts}$ is the approximate number of collocation points used to cover the entire computational domain. The three values for $N_{\rm pts}$ are those for the inspiral, merger, and ringdown portions of the simulation, which are described in sections 4.2.2, 4.2.3, and 4.2.4, respectively. The outer boundary parameters $R'_{\rm max}$, $R''_{\rm max}$ and R'_0, as well as run times T, are in units of the initial Christodoulou mass M of the system, which provides a natural time and length scale.

that growing gauge modes remain inside the common horizon. After merger, however, it is no longer desirable for the horizon to expand, since this would prevent the solution from eventually settling down to a time-independent state in which the horizon is stationary with respect to the coordinates.

To summarize, the steps involved in the transition from evolving a binary black hole spacetime to evolving a merged single black hole spacetime are as follows: (i) Find the common apparent horizon in the inertial frame at several times near $t = t_m$. (ii) Solve for the $\lambda_{\ell m}(t_m)$ that make the horizon spherical in the comoving frame, and simultaneously solve for $R''_{\rm AH}$. (iii) Choose the inner boundary of the new computational domain $R''_{\rm min}$ to be slightly less than $R''_{\rm AH}$, and choose the outer boundary $R''_{\rm max}$ [for sufficiently small $a(t_m)$ it is necessary to choose $R''_{\rm max} < R'_{\rm max}$ so that the mapping (4.22) is invertible]. At this point the computational domain and the mapping (4.22)– (4.25) have been determined. (iv) Interpolate all dynamical variables from the old computational domain onto the new one. This interpolation is done via the spectral expansion in the old domain, so it introduces no additional error. (v) Modify the gauge source evolution equations so that the shift is no longer driven to zero. (vi) Continue the evolution on the new computational domain. All of these steps can be automated.

4.2.5 Properties of the numerical solution

In Table 4.1 we list outer boundary parameters, resolutions, and run times of several runs we have done using the algorithm described above. Three of these runs are identical except for numerical resolution, and the fourth is performed on a different domain with a different

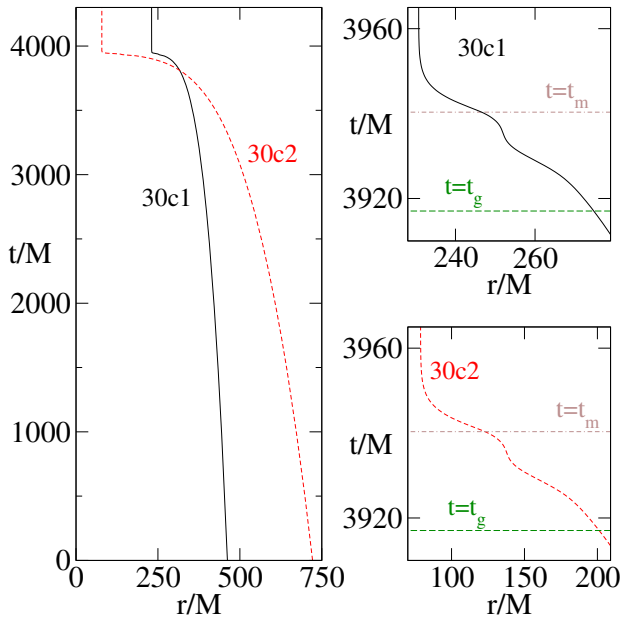

Figure 4.1: Spacetime diagram showing the spacetime volume simulated by the numerical evolutions listed in Table 4.1. Each curve represents the worldline of the outer boundary for a particular simulation. The magnified views on the right show that the outer boundary moves smoothly near merger. The transition times $t_g = 3917M$ and $t_m = 3940M$ are indicated on the right panels.

outer boundary location. As discussed above, the outer boundary of our simulation varies in time because of the dual-frame approach we use to follow the black holes. Figure 4.1 is a spacetime diagram illustrating the region of spacetime being evolved in our simulation.

We do not explicitly enforce either the Einstein constraints or the secondary constraints that arise from writing the system in first-order form. Therefore, examining how well these constraints are satisfied provides a useful consistency check. Figure 4.2 shows the constraint violations for run 30c1. The top panel shows the L^2 norm of all the constraint fields of our first-order generalized harmonic system, normalized by the L^2 norm of the spatial gradients of the dynamical fields (see Eq. (71) of Ref. [62]). The bottom panel shows the same quantity, but without the normalization factor (i.e., just the numerator of Eq. (71) of Ref. [62]). The L^2 norms are taken over the portion of the computational volume that lies outside apparent horizons. At early times, $t < 500M$, the constraints converge rather slowly with resolution because the junk radiation contains high frequencies. Convergence is more rapid during the smooth inspiral phase, after the junk radiation has exited through the outer boundary.

The constraints increase as the holes approach each other and the solution becomes increasingly distorted. At $t = 3917M$ ($t = 3927M$ for resolution N4), the gauge conditions

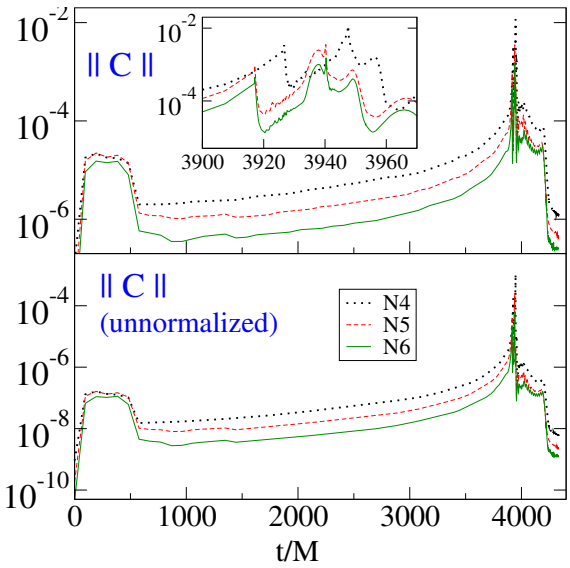

Figure 4.2: Constraint violations of run 30c1. The top panel shows the L^2 norm of all constraints, normalized by the L^2 norm of the spatial gradients of all dynamical fields. The bottom panel shows the same data, but without the normalization factor. The L^2 norms are taken over the portion of the computational volume that lies outside apparent horizons.

are changed (cf. section 4.2.3) and the resolution is increased slightly (compare the first and second entry in the $N_{\rm pts}$ column in Table 4.1). Because of the change of resolution, the constraints drop rapidly by almost two orders of magnitude, but then they begin to grow again. The transition to a single-hole evolution (cf. section 4.2.4) occurs at $t = 3940M$ ($t = 3948M$ for resolution N4). At this time the constraint norm drops by about an order of magnitude because the region in which the largest constraint violations occur—the interior of the common horizon—is newly excised.

After the binary proceeds through inspiral, merger, and ringdown, it settles down to a final stationary black hole. In our simulation this final state is not expressed in any standard coordinate system used to describe Kerr spacetime, but nevertheless the final mass and spin of the hole can be determined. The area A of the apparent horizon provides the irreducible mass of the final black hole,

$$M_{\rm irr} = \sqrt{A/16\pi}, \tag{4.32}$$

which we find to be $M_{\rm irr}/M = 0.88433 \pm 0.00001$, where M is the sum of the initial irreducible masses of the black holes. The uncertainty in $M_{\rm irr}/M$ is determined from the difference between runs 30c1/N6, 30c1/N5, and 30c2/N6, so it includes only uncertainties due to numerical resolution and outer boundary location. We have verified that the uncertainty due to the finite resolution of our apparent horizon finder is negligible.

Initial orbital eccentricity:	e	$\sim$	5×10^{-5}
Initial spin of each hole:	S_i/M^2	$\lesssim$	10^{-7}
Time of evolution:	T/M	$=$	4330
Final Christodoulou mass:	M_f/M	$=$	0.95162 ± 0.00002
Final spin:	S_f/M_f^2	$=$	0.68646 ± 0.00004

Table 4.2: Physical parameters describing the equal-mass nonspinning binary black hole evolutions presented here. The dimensionful quantity M is the initial sum of the Christodoulou masses of the black holes. Uncertainty estimates include numerical uncertainties and the effects of varying the outer boundary location.

The final spin S_f of the black hole can be computed by integrating a quasilocal angular momentum density over the final apparent horizon [81, 82]. Our implementation of this method is described in detail in Appendix A of [55]. Furthermore, an alternative method of computing the final spin, which is based on evaluating the extremal values of the 2-dimensional scalar curvature on the apparent horizon and comparing these values to those obtained analytically for a Kerr black hole, is also described in [55]. Using these measures, we determine the dimensionless spin of the final black hole to be $S_f/M_f^2 = 0.68646 \pm 0.00004$, where the uncertainty is dominated by the difference between runs 30c1/N6 and 30c1/N5 rather than by the differences between different methods of measuring the spin. Here M_f is the Christodoulou mass of the final black hole,

$$M_f^2 = M_{\rm irr}^2 + \frac{S_f^2}{4M_{\rm irr}^2}. \tag{4.33}$$

We find that the ratio of the final to initial black hole mass is $M_f/M = 0.95162 \pm 0.00002$. The mass and spin of the final hole are consistent with those found by other groups [2, 83, 84, 85, 4]. Physical parameters describing the evolutions are summarized in Table 4.2.

4.3 Computation of the waveform

The numerical solution of Einstein's equations obtained using the methods described above yields the spacetime metric and its first derivatives at all points in the computational domain. In this section we describe how this solution is used to compute the key quantity relevant for gravitational-wave observations: the gravitational waveform as seen by an observer infinitely far from the source.

4.3.1 Waveform extraction

Gravitational waves are extracted from the simulation on a sphere of coordinate radius r using the Newman-Penrose scalar Ψ_4, following the same procedure as in Refs. [61, 86]. To summarize, we compute

$$\Psi_4 = -C_{\alpha\mu\beta\nu}\ell^\mu\ell^\nu\bar{m}^\alpha\bar{m}^\beta, \tag{4.34}$$

where

$$\ell^\mu = \frac{1}{\sqrt{2}}(t^\mu - r^\mu), \tag{4.35a}$$

$$m^\mu = \frac{1}{\sqrt{2}r}\left(\frac{\partial}{\partial\theta} + i\frac{1}{\sin\theta}\frac{\partial}{\partial\phi}\right)^\mu. \tag{4.35b}$$

Here (r, θ, ϕ) denote the standard spherical coordinates in the inertial frame, t^μ is the timelike unit normal to the spatial hypersurface, and r^μ is the outward-pointing unit normal to the extraction sphere. We then expand Ψ_4 in terms of spin-weighted spherical harmonics of weight -2:

$$\Psi_4(t, r, \theta, \phi) = \sum_{lm} \Psi_4^{lm}(t, r)\, {}_{-2}Y_{lm}(\theta, \phi), \tag{4.36}$$

where the Ψ_4^{lm} are expansion coefficients defined by this equation.

Note that our choice of m^μ is not exactly null nor exactly of unit magnitude at finite r, as is required by the standard definition. The resulting Ψ_4^{lm} computed at finite r will therefore disagree with the waveforms observed at infinity. Our definition does, however, agree with the standard definition of Ψ_4^{lm} as $r \to \infty$. Because we extrapolate the extracted waves to find the asymptotic radiation field (see section 4.3.3), these tetrad effects should not play a role: Relative errors in Ψ_4^{lm} introduced by using the simple coordinate tetrad fall off like powers of M/r, and thus should vanish after extrapolating to obtain the asymptotic behavior. More careful treatment of the extraction method—such as those discussed in Refs. [87, 88, 89]—may improve the quality of extrapolation and would be interesting to explore in the future.

In this work, we focus on the dominant $(l, m) = (2, 2)$ mode. Following common practice (see e.g. [84, 85]), we split the extracted waveform into real phase ϕ and real amplitude A, defined by

$$\Psi_4^{22}(r, t) = A(r, t)e^{-i\phi(r,t)}. \tag{4.37}$$

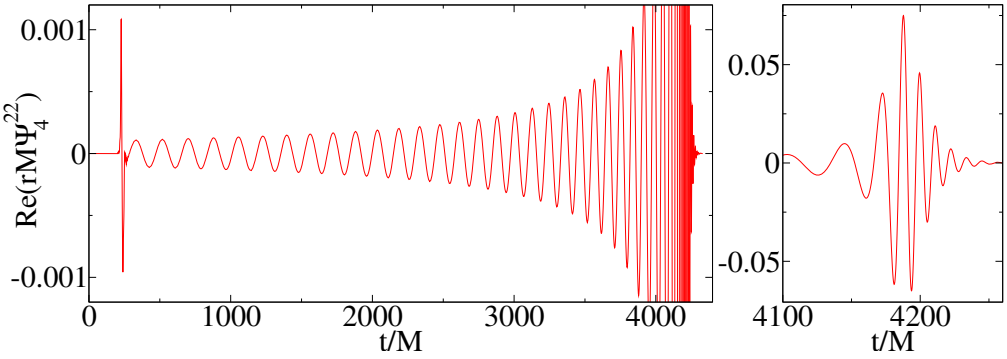

Figure 4.3: Gravitational waveform extracted at finite radius $r = 225M$, for the case 30c1/N6 in Table 4.1. The left panel zooms in on the inspiral waveform, and the right panel zooms in on the merger and ringdown.

The gravitational-wave frequency is given by

$$\omega = \frac{d\phi}{dt}. \tag{4.38}$$

The minus sign in Eq. (4.37) is chosen so that the phase increases in time and ω is positive.

The $(l, m) = (2, 2)$ waveform, extracted at a single radius for run 30c1/N6, is shown in Fig. 4.3. The short pulse at $t \sim 200M$ is caused by imperfect initial data that are not precisely in equilibrium; this pulse is usually referred to as "junk radiation."

4.3.2 Convergence of extracted waveforms

In this section we examine the convergence of the gravitational waveforms extracted at fixed radius, without extrapolation to infinity. This allows us to study the behavior of our code without the complications of extrapolation. The extrapolation process and the resulting extrapolated waveforms are discussed in section 4.3.3.

Figure 4.4 shows the convergence of the gravitational-wave phase ϕ and amplitude A with numerical resolution. For this plot, the waveform was extracted at a fixed inertial-coordinate radius of $r = 60M$. This fairly small extraction radius was chosen to allow a comparison of the simulations 30c1 and 30c2. Each solid line in the top panel shows the absolute difference between ϕ computed at some particular resolution and ϕ computed from our highest-resolution run, labeled 30c1/N6 in Table 4.1. The solid curves in the bottom panel similarly show the *relative* amplitude differences. When subtracting results at different resolutions, no time or phase adjustment has been performed. The noise at early times is due to "junk radiation" generated near $t = 0$. While most of this radiation

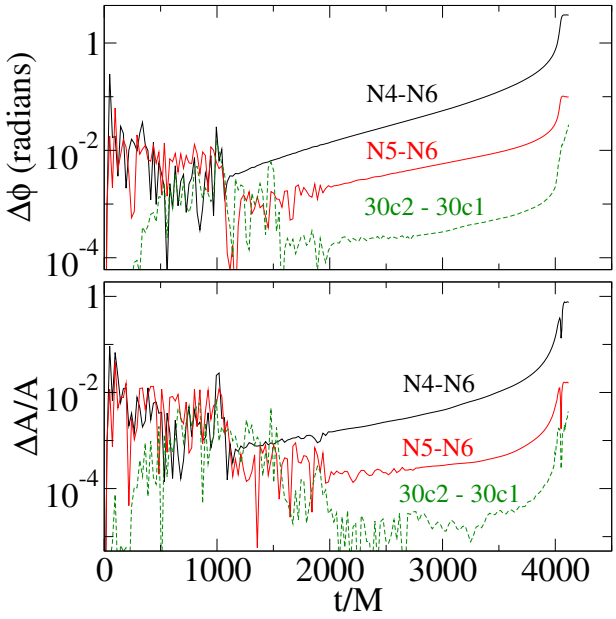

Figure 4.4: Convergence of waveforms with numerical resolution and outer boundary location. Shown are phase and amplitude differences between numerical waveforms Ψ_4^{22} computed using different numerical resolutions. Shown also is the difference between our highest-resolution waveforms using two different outer boundary locations. All waveforms are extracted at $r = 60M$, and no time shifting or phase shifting is done to align waveforms.

leaves through the outer boundary after one crossing time, some remains visible for a few crossing times.[1] The plots show that the phase difference accumulated over 16 orbits plus merger and ringdown is less than 0.1 radians for our medium resolution, and the relative amplitude differences are less than 0.015; these numbers can be taken as an estimate of the numerical truncation error of our *medium* resolution run.

Also shown as a dotted curve in each panel of Fig. 4.4 is the difference between our highest-resolution run, 30c1/N6, and a similar run but with a different outer boundary location, 30c2/N6. The 30c2 run initially has a more distant outer boundary than 30c1, but during the inspiral the outer boundary moves rapidly inward, as seen in Fig. 4.1, so that extraction of the full waveform is possible only for extraction radii $r \lesssim 75M$. Comparing runs 30c1 and 30c2 provides an estimate of the uncertainty in the waveform due to outer boundary effects such as imperfect boundary conditions that might reflect outgoing waves. From Fig. 4.4 we estimate this uncertainty to be 0.03 radians in phase and half a percent in amplitude (when no time shift is applied).

[1] The junk radiation at early times is discussed in more detail in Ref. [9] (specifically, just before Eq. (9) and in the third paragraph of section II E), which presents the exact same waveform as shown here but without merger and ringdown.

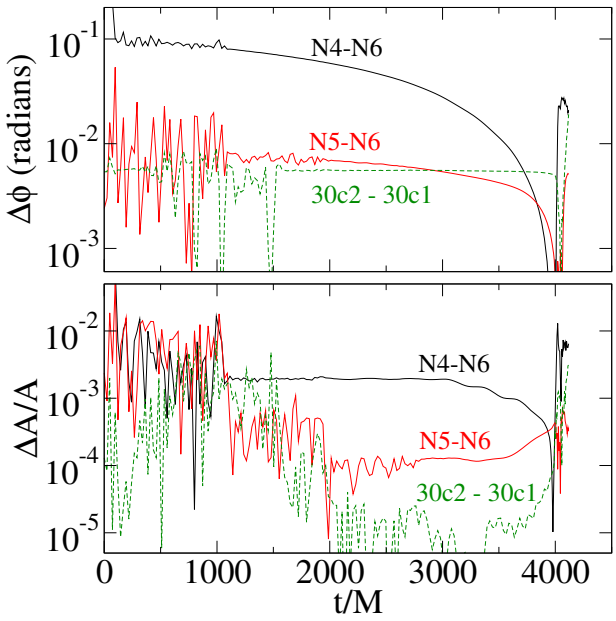

Figure 4.5: Convergence of waveforms with numerical resolution and outer boundary location. Same as Fig. 4.4 except waveforms are time shifted and phase shifted so that the maximum amplitude occurs at the same time and phase.

Figure 4.5 is the same as Fig. 4.4 except each waveform is time shifted and phase shifted so that the maximum amplitude of the wave occurs at the same time and phase. This type of comparison is relevant for analysis of data from gravitational-wave detectors: when comparing experimental data with numerical detection templates, the template will be shifted in both time and phase to best match the data. For this type of comparison, Fig. 4.5 shows that the numerical truncation error of our medium resolution run is less than 0.01 radians in phase and 0.1 percent in amplitude for $t > 1000M$. At earlier times, the errors are somewhat larger and are dominated by residual junk radiation. Our uncertainty due to outer boundary effects is similar to that in Fig. 4.4: about 0.02 radians in phase and half a percent in amplitude. Boundary effects are most prominent during the ringdown.

4.3.3 Extrapolation of waveforms to infinity

Our numerical simulations cover only a finite spacetime volume, as shown in Fig. 4.1, so it is necessary to extract our numerical waveforms at a finite distance from the source. However, gravitational-wave detectors measure waveforms as seen by an observer infinitely far from the source. Accordingly, after extracting waveforms at multiple finite radii, we extrapolate these waveforms to infinite radius using a procedure similar to that described in [9]. This

extrapolation procedure is intended to remove not only near-field effects that are absent at infinity, but also gauge effects that can be caused by the time dependence of the lapse function or the nonoptimal choice of tetrad for computing Ψ_4.

The extraction procedure described in section 4.3.1 yields a set of waveforms $\Psi_4^{22}(t,r)$, with each waveform extracted at a different radius. To extrapolate to infinite radius we must compare waveforms at different radii, but these waveforms must be offset in time by the light-travel time between adjacent radii. To account for this time shift, for each extraction radius we compute $\Psi_4^{22}(u,r)$, where u is the retarded time at that radius. Assuming for simplicity that the background spacetime is nearly Schwarzschild, we compute the retarded time u using

$$u \equiv t_s - r^*, \tag{4.39}$$

where t_s is some approximation of Schwarzschild time, and the tortoise-coordinate radius [90] is

$$r^* = r_{\rm areal} + 2E_{\rm ADM} \ln\left(\frac{r_{\rm areal}}{2E_{\rm ADM}} - 1\right). \tag{4.40}$$

Here $E_{\rm ADM}$ is the ADM mass of the initial data, and $r_{\rm areal} = \sqrt{A/4\pi}$, where A is the measured (time-dependent) area of the extraction sphere. If we were to choose t_s to be simply the coordinate time t, then the retarded time coordinate u would fail to be null, largely because the lapse function in our simulation is time dependent and differs from the Schwarzschild value. We attempt to account for this by assuming that our background spacetime coordinates are Schwarzschild, but with g_{tt} replaced by $-N_{\rm avg}^2$, where $N_{\rm avg}$ is the (time-dependent) average value of the lapse function measured on the extraction sphere. Under these assumptions, it can be shown that the one-form

$$\frac{N_{\rm avg}}{\sqrt{1-2E_{\rm ADM}/r_{\rm areal}}}dt - dr^* \tag{4.41}$$

is null, so we equate this one-form with du and thus define

$$t_s = \int_0^t \frac{N_{\rm avg}}{\sqrt{1-2E_{\rm ADM}/r_{\rm areal}}}dt. \tag{4.42}$$

We show below (cf. Fig. 4.9) that choosing Eq. (4.42) instead of $t_s = t$ significantly increases the accuracy of our extrapolation procedure during merger and ringdown.

Having computed the retarded time at each extraction radius, we now consider the extracted waveforms as functions of retarded time u and extraction radius $r_{\rm areal}$, i.e.,

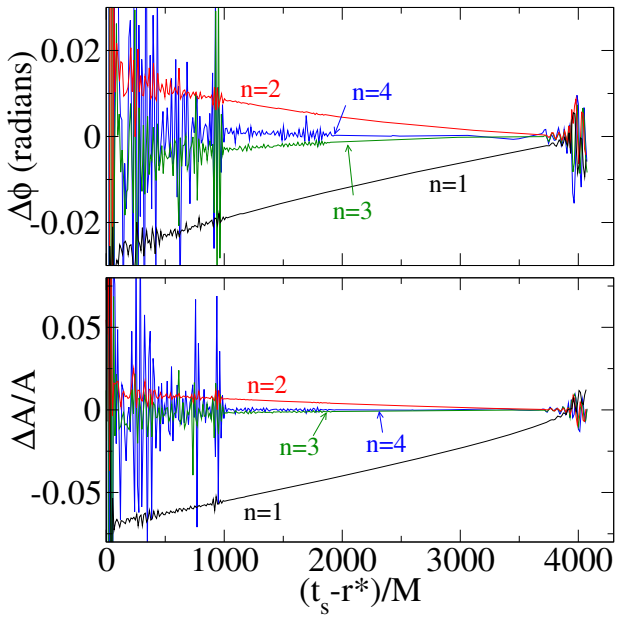

Figure 4.6: Convergence of extrapolation to infinity for extrapolation of order n. For each n, plotted is the extrapolated waveform from run 30c1/N6 using order $n+1$ minus the extrapolated waveform using order n. The top panel shows phase differences, the bottom panel shows amplitude differences. No shifting in time or phase has been done for this comparison. Increasing n increases accuracy in smooth regions but also amplifies noise.

$\Psi_4^{22}(u, r_{\rm areal})$. At each value of u, we have the phase and amplitude of Ψ_4^{22} at several extraction radii $r_{\rm areal}$. Therefore at each value of u, we fit phase and amplitude separately to a polynomial in $1/r_{\rm areal}$:

$$\phi(u, r_{\rm areal}) = \phi_{(0)}(u) + \sum_{k=1}^{n} \frac{\phi_{(k)}(u)}{r_{\rm areal}^k}, \tag{4.43}$$

$$r_{\rm areal}\, A(u, r) = A_{(0)}(u) + \sum_{k=1}^{n} \frac{A_{(k)}(u)}{r_{\rm areal}^k}. \tag{4.44}$$

The phase and amplitude of the desired asymptotic waveform are thus given by the leading-order term of the appropriate polynomial, as a function of retarded time:

$$\phi(u) = \phi_{(0)}(u), \tag{4.45}$$

$$r_{\rm areal}\, A(u) = A_{(0)}(u). \tag{4.46}$$

Figure 4.6 shows phase and amplitude differences between extrapolated waveforms that are computed using different values of polynomial order n in Eqs. (4.43) and (4.44). For

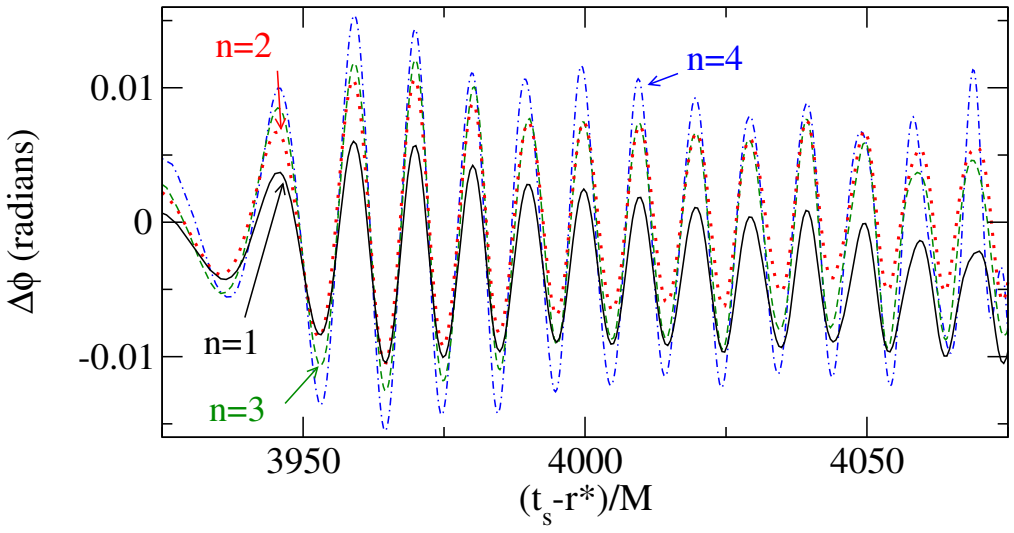

Figure 4.7: Late-time phase convergence of extrapolation to infinity. Same as the top panel of Fig. 4.6, except zoomed to late times. The peak amplitude of the waveform occurs at $t_s - r^* = 3954M$.

the extrapolation we use waveforms extracted at radii $75M$, $85M$, $100M$, $110M$, $130M$, $140M$, $150M$, $160M$, $170M$, $180M$, $190M$, $200M$, $210M$, and $225M$. From Fig. 4.6 it is clear that increasing n increases the accuracy of the extrapolation in smooth regions, but also amplifies any noise present in the waveform. Our preferred choice, $n = 3$, gives a phase error of 0.005 radians and a relative amplitude error of 0.003 during most of the inspiral, and a phase error of 0.01 radians and a relative amplitude error of 0.01 in the ringdown. The junk radiation epoch $t_s - r^* \lesssim 1000M$ has moderately larger errors than the ringdown. If we were to choose instead $n = 4$, we would gain higher accuracy in the smooth regions at the expense of increased noise in the junk radiation epoch and slightly larger errors during the merger and ringdown.

Figure 4.7 is the same as the top panel of Fig. 4.6, except zoomed to late times. Note that during merger and ringdown, the extrapolation procedure does not converge with increasing extrapolation order n: the phase differences are slightly larger for larger n. This lack of convergence suggests that the nonextrapolated numerical waveform contains some small contamination that does not obey the fitting formulae, Eqs. (4.43) and (4.44). Figure 4.8 shows the n=1 and n=2 convergence curves from Fig. 4.7, but computed for two different numerical resolutions, 30c1/N5 and 30c1/N6. The N5 and N6 lines are very close to each other in this figure, indicating that the lack of convergence with extrapolation order n is not dominated by insufficient numerical resolution. We suspect that the main contribution

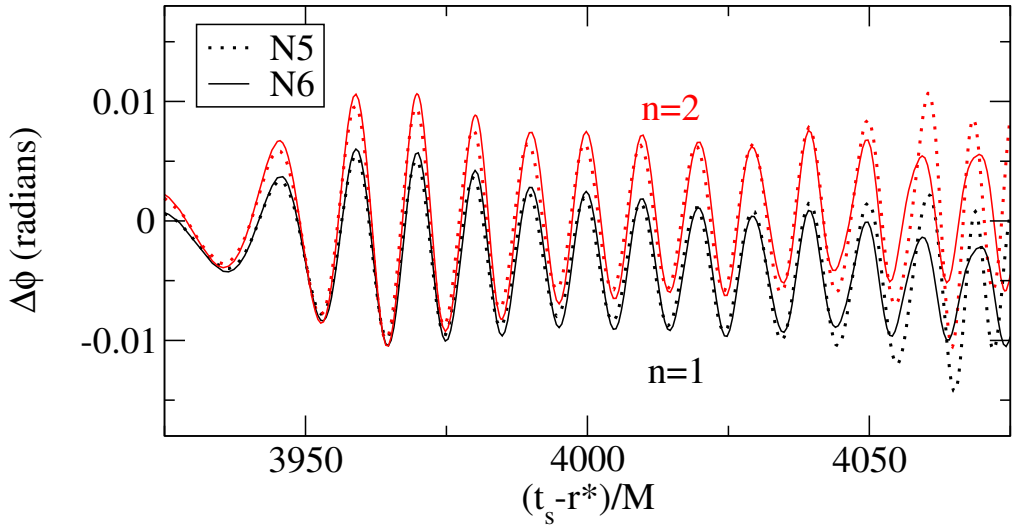

Figure 4.8: Effect of numerical resolution on extrapolation to infinity. The solid curves are identical to the "n=1" and "n=2" curves from Fig. 4.7. The dotted curves are the same quantities computed using the lower resolution run 30c1/N5.

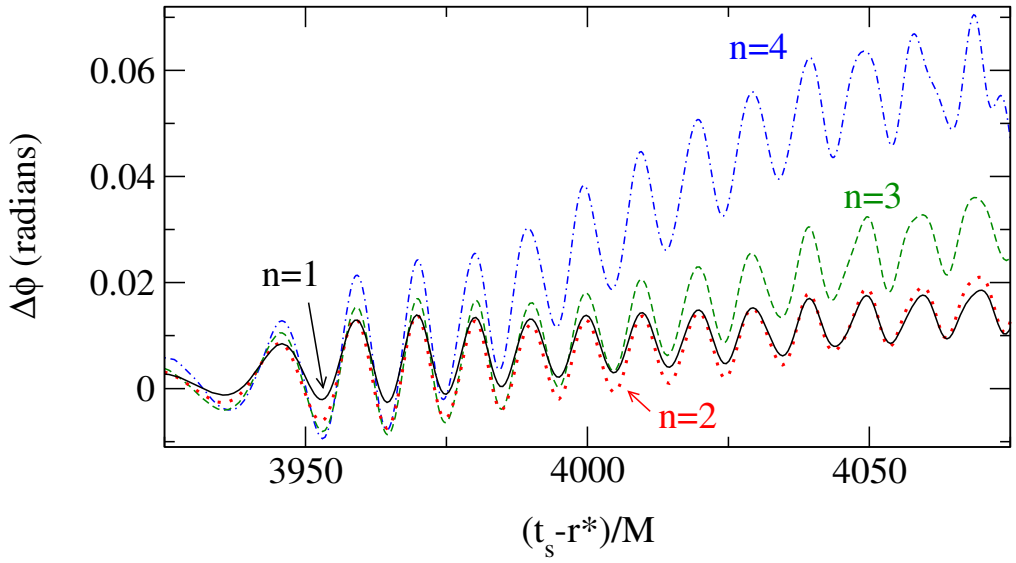

Figure 4.9: Effect of t_s on extrapolation to infinity. Same as Fig. 4.7, except the quantity t_s that appears in the retarded time, Eq. (4.39), is chosen to be coordinate time t rather than the integral in Eq. (4.42). Note the difference in vertical scale between this figure and Fig. 4.7.

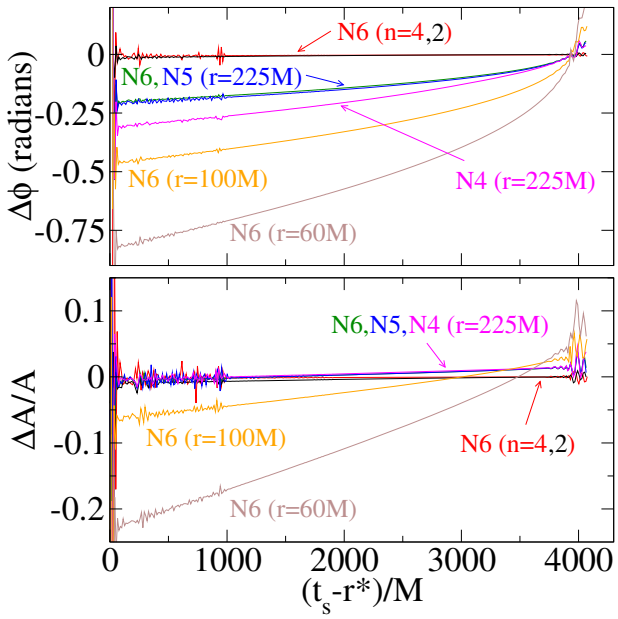

Figure 4.10: Comparison of extrapolated and nonextrapolated waveforms. Plotted are differences between selected waveforms and the 30c1/N6 waveform extrapolated to infinity using $n = 3$. Each selected waveform is labeled by the numerical resolution (N4, N5, or N6), and either the extraction radius (for nonextrapolated waveforms) or the extrapolation order (for extrapolated waveforms). Each waveform has been shifted in time and phase so as to minimize the least-squares difference from the N6, $n = 3$ waveform. The top panel shows phase differences, the bottom panel shows amplitude differences. Differences between extrapolated and nonextrapolated waveforms are much larger than differences between different extrapolation orders. Phase differences between resolutions N5 and N6, and amplitude differences between all three resolutions, are indistinguishable on the plot.

is instead due to gauge effects. Such gauge effects might be reduced by improving the gauge conditions in the numerical simulation or by adopting more sophisticated wave extraction and extrapolation algorithms that better compensate for dynamically varying gauge fields.

Indeed, we have already made a first attempt at correcting for a time-dependent lapse function by using t_s from Eq. (4.42) to compute the retarded time. Figure 4.9 illustrates the importance of this correction. Figures 4.7 and 4.9 differ only in the choice of t_s used to compute the retarded time: In Fig. 4.7, t_s is obtained from Eq. (4.42), and in Fig. 4.9, t_s is simply the coordinate time t. Using the naive choice $t_s = t$ clearly results in much larger phase differences that diverge with increasing n and grow in time.

In Fig. 4.10 we examine the difference between extrapolated waveforms and waveforms that have been extracted at a finite radius. We compare our preferred waveform, 30c1/N6 extrapolated to infinity using $n = 3$, vs. nonextrapolated waveforms and vs. extrapolated waveforms with different values of n. Because the extrapolated and nonextrapolated wave-

forms differ by overall time and phase offsets which are irrelevant for many purposes, each waveform in Fig. 4.10 has been shifted in time and phase so as to best match with the $n = 3$ extrapolated waveform. This best match is determined by a simple least-squares procedure: we minimize the function

$$f(t_0, \phi_0) = \sum_i \Big(A_1(t_i) e^{i\phi_1(t_i)} - A_2(t_i + t_0) e^{i(\phi_2(t_i+t_0)+\phi_0)} \Big)^2, \tag{4.47}$$

by varying t_0 and ϕ_0. Here A_1, ϕ_1, A_2, and ϕ_2 are the amplitudes and phases of the two waveforms being matched, and the sum goes over all times t_i at which waveform 1 is sampled.

We find from Fig. 4.10 that extrapolation to infinity has a large effect on the phase of the final waveform and a much smaller effect on the amplitude, when comparing to data extracted at our outermost extraction radius, $r = 225M$. The $r = 225M$ waveforms have an accumulated phase difference of 0.2 radians relative to the extrapolated waveform, much larger than the difference between different extrapolation orders or different numerical resolutions. For extraction at smaller radii, the differences are larger still, the $r = 60M$ waveform having a phase difference of 0.8 radians and amplitude difference of 20 percent compared to the extrapolated waveform. We find that the phase differences between extrapolated and nonextrapolated waveforms scale quite accuratly like $1/r$, and the amplitude differences scale roughly like $1/r^{2.5}$, where r is the extraction radius. These scalings seem to be related to near-field effects, for which one expects scalings like $1/r$ in phase and $1/r^2$ in amplitude [86].

Figure 4.11 presents the final waveform after extrapolation to infinite radius. There are 33 gravitational-wave cycles before the maximum of $|\Psi_4|$. The simulation is further able to resolve 10 gravitational-wave cycles during ringdown, during which the amplitude $|\Psi_4|$ drops by four orders of magnitude.

4.4 Discussion

We have presented the first spectral computation of a binary black hole inspiral, merger, and ringdown, and we have extracted accurate gravitational waveforms from our simulation. A key ingredient in handling the merger phase is a choice of gauge that causes the individual holes to expand in coordinate size. This eliminates the coordinate singularities that prevented our earlier simulations from continuing through merger. The largest downside to

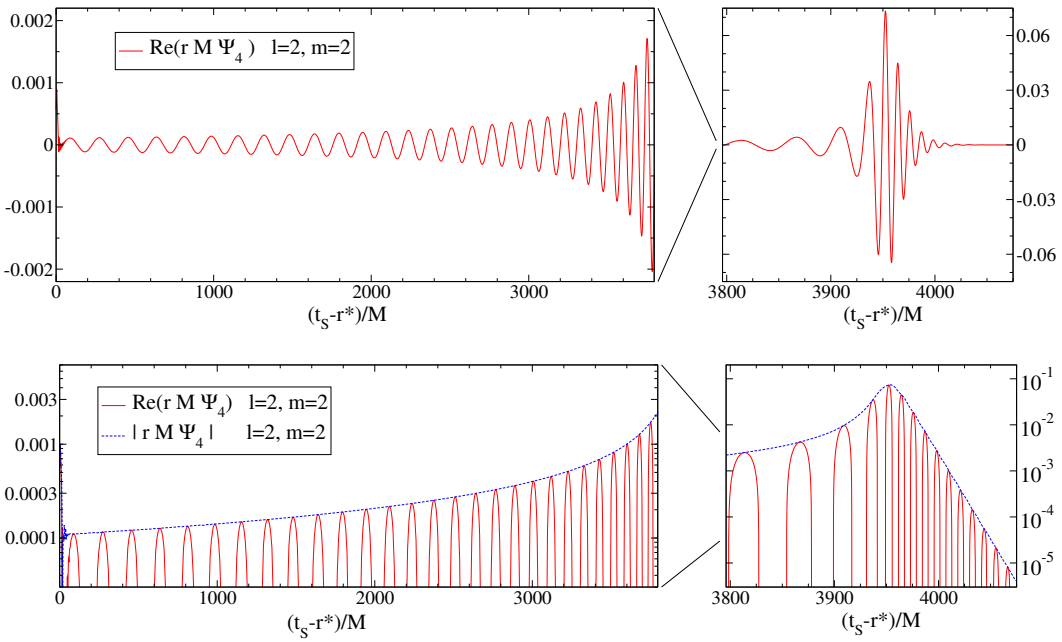

Figure 4.11: Final waveform, extrapolated to infinity. The top panels show the real part of Ψ_4^{22} with a linear y-axis, the bottom panels with a logarithmic y-axis. The right panels show an enlargement of merger and ringdown.

the gauge used here is that the success of the method depends sensitively on some of the gauge parameters, namely σ_1 and σ_2 in Eq. (4.8), and ξ_1 and ξ_3 in Eqs. (4.6) and (4.7). If these parameters are chosen poorly, the characteristic fields at the excision boundaries fail to be purely outgoing (i.e., into the holes) at some instant in time, causing the code to terminate due to lack of a proper boundary condition at an excision boundary. An alternative approach to gauge conditions for the generalized harmonic system [77] is in progress, and promises to be more robust.

We compute the spin of the final black hole with three distinct diagnostics, one based on approximate rotational Killing vectors, the others based on the minimum and maximum of the scalar curvature of the apparent horizon ($\chi_{\rm AKV}$, $\chi_{\rm SC}^{\rm min}$, and $\chi_{\rm SC}^{\rm max}$ in the language of Appendices A and B of [55]). We find that these diagnostics agree to an exquisite degree. Since these diagnostics coincide exactly for a Kerr black hole, this suggests that the final state is indeed a Kerr black hole. The uncertainty of the final spin quoted in section 4.2.5 is due to numerical truncation error, (i.e., differences between resolutions 30c1/N5 and 30c1/N6), rather than due to differences between spin diagnostics, and we find $S_f/M_f^2 = 0.68646 \pm 0.00004$, and $M_f = (0.95162 \pm 0.00002)M$.

The physical waveform at infinity produced by any numerical relativity code should of course be independent of the coordinates used during the simulation. However, in practice it is difficult to remove coordinate effects from the waveform for several reasons. First, waveforms are typically extracted on coordinate spheres (not geometric spheres) of finite radius as functions of coordinate time (which may not agree with proper time at infinity). Second, the extracted waveform on a given sphere is typically expanded in spin-weighted spherical harmonics ${}_sY_{\ell m}(\theta,\phi)$ using the θ and ϕ coordinates from the simulation rather than some geometrically defined θ and ϕ coordinates. Finally, standard formulae equating Ψ_4 with the asymptotic radiation field assume that Ψ_4 is computed at infinity. Such gauge ambiguities can be significant for the accuracy of waveforms from numerical simulations [87, 88, 89]. Indeed, if we choose a deliberately "bad" gauge just after merger by omitting the factor $e^{-r''^2/\sigma_3^2}$ in the function $f(x,t)$ [cf. Equation (4.30)], we find that the lapse function oscillates in time even at large distances, and that the resulting waveform extracted at a finite radius differs by more than a radian in phase from the waveform presented here. We defer further discussion of gauge effects on the waveform to future work.

We have also shown that extrapolation of waveforms to infinity is crucial: waveforms extracted at a finite radius differ (particularly in phase) from waveforms extrapolated to infinity by far more than the numerical errors, as shown in Fig. 4.10. Although it is likely that the need for extrapolation may be somewhat reduced by more sophisticated algorithms for wave extraction at finite radius, it appears that most of the difference between waveforms that have and have not been extrapolated to infinity is due to physics (in the form of near-zone effects) rather than to gauge and tetrad ambiguities [86].

We are currently extending our methods to binary black holes with unequal masses and nontrivial spins. Inspiral simulations for these more generic systems have already been computed by our code; it remains to be seen whether mergers of more generic black hole systems can be simulated with the methods described here, or whether alternative gauge conditions, such as those described in Ref. [77], will be necessary.

It would be interesting to compare the waveforms presented here with those from other groups computing binary black hole mergers, particularly since other groups use different numerical methods, different formulations of the equations, and different gauge conditions than our group. Several such comparisons are presently under way.

Waveforms are available at http://www.black-holes.org/Waveforms.html.

4.5 Appendix: Estimating the gauge error of numerical waveforms

In our attempts to successfully simulate binary black hole mergers using spectral methods, the choice of gauge conditions has proven to be an important factor. For instance, undesirable gauge conditions can cause slice stretching, or drive the motion of the horizons too quickly relative to the excision boundaries and give rise to ingoing characteristic fields, all of which can prevent the simulation from proceeding long enough to form a common horizon. Although the physical gravitational waves calculated at future null infinity should be independent of the gauge conditions used, in practice the extraction of waveforms at finite radii can still lead to lingering gauge effects in the final extrapolated waveforms. Here we estimate the gauge error in our waveforms at late times by repeating the merger and ringdown portions of the above simulation with the damped harmonic gauge of [91] and comparing the resulting waveforms with the previous results. We find that for waveforms extracted at a finite radius, the gauge error can become larger than the numerical error. For waveforms extrapolated to infinity on the other hand, the gauge error is of the same order or smaller than the numerical error, which demonstrates the necessity and effectiveness of our waveform extrapolation.

4.5.1 Damped harmonic gauge evolutions

The damped harmonic gauge [91] aims to reduce unwanted dynamics in the spatial coordinates by setting the spatial components of the gauge source function H^i equal to a damping term with coefficient μ_S,

$$H^i \equiv \nabla^c \nabla_c x^i = \mu_S t^i = -\mu_S N^i / N. \tag{4.48}$$

Motivated by the observation of a rapid growth in $g = \det g_{ij}$ near the horizons in failed merger simulations, and that $t^a H_a$ can be written as

$$t^a H_a = t^a \partial_a \log\left(\frac{\sqrt{g}}{N}\right) - N^{-1} \partial_k N^k, \tag{4.49}$$

the damped harmonic gauge also sets

$$t^a H_a = -\mu_L \log\left(\frac{\sqrt{g}}{N}\right), \tag{4.50}$$

which leads to a damped wave equation for N that also suppresses the growth in $\sqrt{g}/N$. These conditions can be combined into the equation

$$H_a = \mu_L \log\left(\frac{\sqrt{g}}{N}\right) t_a - \mu_S N^{-1} g_{ai} N^i, \tag{4.51}$$

where the damping factors are set to $\mu_S = \mu_L = \mu_0 \left[\log\left(\frac{\sqrt{g}}{N}\right)\right]^2$, and μ_0 is a specifiable function of time.

We continue the inspirals of runs 30c1/N5 and 30c1/N6 with the damped harmonic gauge, and we shall refer to the resulting runs as 30d1/N5 and 30d1/N6. The inspiral gauge transitions smoothly to the damped harmonic gauge at $t = t_g = 3850M$, by choosing

$$H_a(t) = \tilde{H}_a(t) e^{(t-t_g)^4/\sigma_g^4} + \mu_L \log\left(\frac{\sqrt{g}}{N}\right) t_a - \mu_S N^{-1} g_{ai} N^i, \tag{4.52}$$

where $\tilde{H}_a(t)$ is the value of $H_a(t)$ during the inspiral and $\sigma_g = 20M$. In μ_L and μ_S, we also set

$$\mu_0 = \begin{cases} 0, & t < t_g \\ 1 - e^{(t-t_g)^2/\sigma_d^2}, & t > t_g \end{cases} \tag{4.53}$$

where $\sigma_d = 50M$.

During the merger portions, the runs 30d1/N5 and 30d1/N6 are continued on the improved grid structure utilizing cubed-spheres introduced in [91]. However, the number of collocation points used in the computational domain is chosen to be nearly the same as before. The merger portion of 30d1/N5 is continued on a domain with $N_{\rm pts} = 66$, and that of 30d1/N6 is continued on a domain with $N_{\rm pts} = 72$. The ringdown portions use the same computational domain as before.

4.5.2 Gauge and numerical errors

For the purposes of this appendix, we introduce a definition of the error in our waveforms that is convenient to evaluate. Given two waveforms Ψ_4 and Ψ_4', we can express their difference in terms of Ψ_4^{lm} and $\Psi_4'^{lm}$, the coefficients in their expansions using spin-weighted spherical harmonics of weight -2 given in Eq. (4.36), by integrating the quantity $|\Psi_4 - \Psi_4'|^2$ over the unit sphere,

$$\int_S |\Psi_4 - \Psi_4'|^2 \, d\Omega = \sum_{lm} \left|\Psi_4^{lm} - \Psi_4'^{lm}\right|^2. \tag{4.54}$$

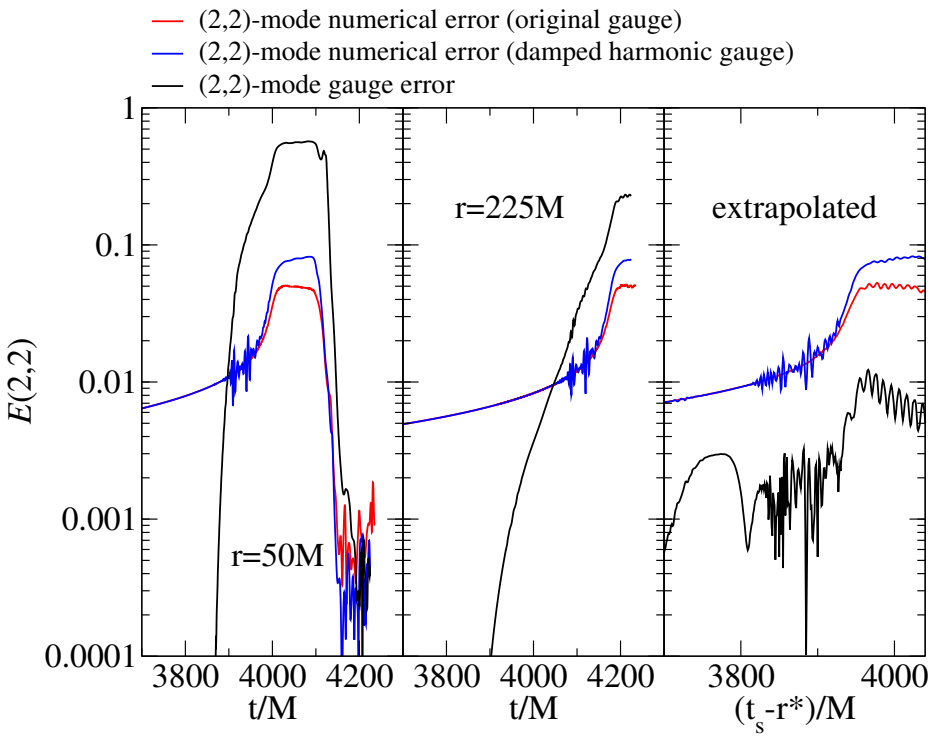

Figure 4.12: The left and middle panel show the numerical and gauge errors of Ψ_4^{22}, extracted at $r = 50M$ and $225M$, respectively. The right panel shows the same quantities for Ψ_4^{22} extrapolated to infinity. The gauge error becomes larger than the numerical errors for both extraction radii, but is always smaller than the numerical errors for the extrapolated waveforms.

For a particular set of (l, m)-modes, we then define the error of $\Psi_4'^{lm}$ relative to Ψ_4^{lm} according to

$$E(l,m) = \sqrt{\sum_{lm} \left|\Psi_4^{lm} - \Psi_4'^{lm}\right|^2} \Big/ \sqrt{\sum_{\text{all } lm} \left(\left|\Psi_4^{lm}\right| + \left|\Psi_4'^{lm}\right|\right)^2}. \tag{4.55}$$

The denominator is a normalization factor, with the sum over "all lm" being taken over all the (l, m)-modes of interest. This definition of the error avoids the need to split up each Ψ_4^{lm} into a phase and amplitude, and is useful when dealing with the ringdown waveforms for which the amplitudes decrease exponentially. In this situation, the phase is no longer well-defined and does not vary smoothly. When Ψ_4^{lm} is nonoscillatory, its representation by a phase and amplitude would also be problematic.

We shall only consider the seven largest modes $(l, m) = (2, 2), (3, 2), (4, 2), (4, 4), (5, 4), (6, 6), (8, 8)$, which are also used to evaluate the denominator in Eq. (4.55). The *numerical error* is calculated by taking both Ψ_4 and Ψ_4' from the same simulation, but at two different resolutions (30c1/N5 and 30c1/N6, or 30d1/N5 and 30d1/N6). The *gauge error* is estimated

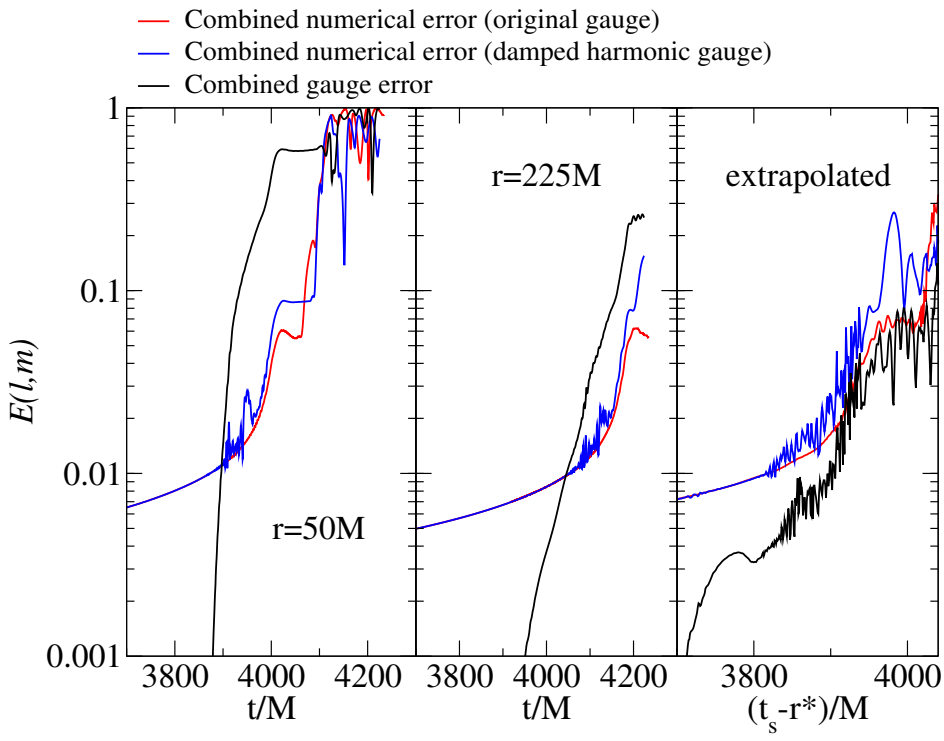

Figure 4.13: The left and middle panel show the numerical and gauge errors for the seven largest (l, m)-modes, extracted at $r = 50M$ and $225M$, respectively. The right panel shows the same quantities for the (l, m)-modes extrapolated to infinity. The gauge error becomes larger than the numerical errors for both extraction radii, but is smaller than or comparable to the numerical errors for the extrapolated waveforms.

by taking Ψ_4 from the simulation presented in the main text using the "original gauge," and Ψ_4' from the simulation using the damped harmonic gauge, at comparable resolutions (30c1/N6 and 30d1/N6). These errors are shown in Fig. 4.12 for the dominant $(2, 2)$-mode extracted at $r = 50M, 225M$, and extrapolated to infinity. Only late times are shown, since the different simulations only differ in gauge conditions after the inspiral. It is evident that gauge effects are prominent for a finite extraction radius, and the gauge error grows to become larger than the numerical errors. However, after the waveforms are extrapolated, the gauge error remains much smaller than the numerical errors. Figure 4.13 shows the errors for the seven largest modes combined. Both the numerical and gauge errors increase rapidly at late times for $r = 50M$, and the gauge error again becomes larger than the numerical errors at finite extraction radii. However, for the extrapolated waves, the gauge error is comparable to or smaller than the numerical errors.

Bibliography

[1] F. Pretorius, Phys. Rev. Lett. **95**, 121101 (2005).

[2] M. Campanelli, C. O. Lousto, P. Marronetti, and Y. Zlochower, Phys. Rev. Lett. **96**, 111101 (2006).

[3] J. G. Baker, J. Centrella, D.-I. Choi, M. Koppitz, and J. van Meter, Phys. Rev. Lett. **96**, 111102 (2006).

[4] A. Buonanno, G. B. Cook, and F. Pretorius, Phys. Rev. D **75**, 124018 (2007).

[5] J. G. Baker, J. R. van Meter, S. T. McWilliams, J. Centrella, and B. J. Kelly, Phys. Rev. Lett. **99**, 181101 (2007).

[6] Y. Pan et al., Phys. Rev. D **77**, 024014 (2008).

[7] A. Buonanno et al., Phys. Rev. D **76**, 104049 (2007).

[8] M. Hannam, S. Husa, J. A. González, U. Sperhake, and B. Brügmann, Phys. Rev. D **77**, 044020 (2008).

[9] M. Boyle et al., Phys. Rev. D **76**, 124038 (2007).

[10] A. Gopakumar, M. Hannam, S. Husa, and B. Brügmann, Phys. Rev. D **78**, 064026 (2008).

[11] M. Hannam, S. Husa, B. Brügmann, and A. Gopakumar, Phys. Rev. D **78**, 104007 (2008).

[12] M. Boyle et al., Phys. Rev. D **78**, 104020 (2008).

[13] A. H. Mroué, L. E. Kidder, and S. A. Teukolsky, Phys. Rev. D **78**, 044004 (2008).

[14] I. Hinder, F. Herrmann, P. Laguna, and D. Shoemaker, Comparisons of eccentric binary black hole simulations with post-Newtonian models, arXiv:0806.1037 (gr-qc), 2008.

[15] M. Campanelli, C. O. Lousto, and Y. Zlochower, Phys. Rev. D **74**, 041501(R) (2006).

[16] M. Campanelli, C. O. Lousto, and Y. Zlochower, Phys. Rev. D **74**, 084023 (2006).

[17] M. Campanelli, C. O. Lousto, Y. Zlochower, B. Krishnan, and D. Merritt, Phys. Rev. D **75**, 064030 (2007).

[18] F. Herrmann, I. Hinder, D. M. Shoemaker, P. Laguna, and R. A. Matzner, Phys. Rev. D **76**, 084032 (2007).

[19] P. Marronetti, W. Tichy, B. Brügmann, J. González, and U. Sperhake, Phys. Rev. D **77**, 064010 (2008).

[20] E. Berti, V. Cardoso, J. A. Gonzalez, U. Sperhake, and B. Brügmann, Class. Quantum Grav. **25**, 114035 (2008).

[21] M. Campanelli, Class. Quantum Grav. **22**, S387 (2005).

[22] F. Herrmann, I. Hinder, D. Shoemaker, and P. Laguna, Class. Quantum Grav. **24**, S33 (2007).

[23] J. G. Baker et al., Astrophys. J. **653**, L93 (2006).

[24] J. A. González, U. Sperhake, B. Brügmann, M. Hannam, and S. Husa, Phys. Rev. Lett. **98**, 091101 (2007).

[25] M. Campanelli, C. O. Lousto, Y. Zlochower, and D. Merritt, Phys. Rev. Lett. **98**, 231102 (2007).

[26] J. A. Gonzalez, M. D. Hannam, U. Sperhake, B. Brügmann, and S. Husa, Phys. Rev. Lett. **98**, 231101 (2007).

[27] B. Brügmann, J. A. González, M. Hannam, S. Husa, and U. Sperhake, Phys. Rev. D **77**, 124047 (2008).

[28] F. Herrmann, I. Hinder, D. Shoemaker, P. Laguna, and R. A. Matzner, Astrophys. J. **661**, 430 (2007).

[29] D.-I. Choi et al., Phys. Rev. D **76**, 104026 (2007).

[30] J. G. Baker et al., Astrophys. J. **668**, 1140 (2007).

[31] W. Tichy and P. Marronetti, Phys. Rev. **D76**, 061502(R) (2007).

[32] J. D. Schnittman et al., Phys. Rev. D **77**, 044031 (2008).

[33] M. Campanelli, C. O. Lousto, Y. Zlochower, and D. Merritt, Astrophys. J. Lett. **659**, L5 (2007).

[34] M. Koppitz et al., Phys. Rev. Lett. **99**, 041102 (2007).

[35] S. H. Miller and R. Matzner, Gen. Rel. Grav. **41**, 525 (2009).

[36] J. G. Baker et al., Astrophys. J. **682**, L29 (2008).

[37] J. Healy et al., Phys. Rev. Lett. **102**, 041101 (2009).

[38] L. S. Finn, Phys. Rev. D **46**, 5236 (1992).

[39] P. Ajith et al., Class. Quantum Grav. **24**, S689 (2007).

[40] T. Damour and A. Nagar, Phys. Rev. D **77**, 024043 (2008).

[41] T. Damour, A. Nagar, M. Hannam, S. Husa, and B. Brügmann, Phys. Rev. D **78**, 044039 (2008).

[42] L. Lindblom, B. J. Owen, and D. A. Brown, Phys. Rev. D **78**, 124020 (2008).

[43] S. Bonazzola, J. Frieben, E. Gourgoulhon, and J.-A. Marck, Spectral methods in general relativity – toward the simulation of 3D-gravitational collapse of neutron stars, in *ICOSAHOM'95, Proceedings of the Third International Conference on Spectral and High Order Methods*, edited by A. V. Ilin and L. R. Scott, pages 3–19, Houston, 1996, Houston Journal of Mathematics.

[44] S. Bonazzola, E. Gourgoulhon, and J.-A. Marck, Phys. Rev. Lett. **82**, 892 (1999).

[45] P. Grandclément, S. Bonazzola, E. Gourgoulhon, and J.-A. Marck, J. Comp. Phys. **170**, 231 (2001).

[46] E. Gourgoulhon, P. Grandclément, and S. Bonazzola, Phys. Rev. D **65**, 044020 (2002).

[47] P. Grandclément, E. Gourgoulhon, and S. Bonazzola, Phys. Rev. D **65**, 044021 (2002).

[48] H. P. Pfeiffer, G. B. Cook, and S. A. Teukolsky, Phys. Rev. D **66**, 024047 (2002).

[49] H. P. Pfeiffer, L. E. Kidder, M. A. Scheel, and S. A. Teukolsky, Comput. Phys. Commun. **152**, 253 (2003).

[50] G. B. Cook and H. P. Pfeiffer, Phys. Rev. D **70**, 104016 (2004).

[51] M. Ansorg, B. Brügmann, and W. Tichy, Phys. Rev. D **70**, 064011 (2004).

[52] M. Ansorg, Phys. Rev. D **72**, 024018 (2005).

[53] M. Caudill, G. B. Cook, J. D. Grigsby, and H. P. Pfeiffer, Phys. Rev. D **74**, 064011 (2006).

[54] P. Grandclément, Phys. Rev. D **74**, 124002 (2006).

[55] G. Lovelace, R. Owen, H. P. Pfeiffer, and T. Chu, Phys. Rev. D **78**, 084017 (2008).

[56] F. Foucart, L. E. Kidder, H. P. Pfeiffer, and S. A. Teukolsky, Phys. Rev. D **77**, 124051 (2008).

[57] M. A. Scheel et al., Phys. Rev. D **74**, 104006 (2006).

[58] J. W. York, Phys. Rev. Lett. **82**, 1350 (1999).

[59] H. P. Pfeiffer and J. W. York, Phys. Rev. D **67**, 044022 (2003).

[60] G. B. Cook, Phys. Rev. D **65**, 084003 (2002).

[61] H. P. Pfeiffer et al., Class. Quantum Grav. **24**, S59 (2007).

[62] L. Lindblom, M. A. Scheel, L. E. Kidder, R. Owen, and O. Rinne, Class. Quantum Grav. **23**, S447 (2006).

[63] H. Friedrich, Commun. Math. Phys. **100**, 525 (1985).

[64] D. Garfinkle, Phys. Rev. D **65**, 044029 (2002).

[65] F. Pretorius, Class. Quantum Grav. **22**, 425 (2005).

[66] O. Rinne, Class. Quantum Grav. **23**, 6275 (2006).

[67] O. Rinne, L. Lindblom, and M. A. Scheel, Class. Quantum Grav. **24**, 4053 (2007).

[68] J. M. Stewart, Class. Quantum Grav. **15**, 2865 (1998).

[69] H. Friedrich and G. Nagy, Commun. Math. Phys. **201**, 619 (1999).

[70] J. M. Bardeen and L. T. Buchman, Phys. Rev. D **65**, 064037 (2002).

[71] B. Szilágyi, B. Schmidt, and J. Winicour, Phys. Rev. D **65**, 064015 (2002).

[72] G. Calabrese, J. Pullin, O. Reula, O. Sarbach, and M. Tiglio, Commun. Math. Phys. **240**, 377 (2003).

[73] B. Szilágyi and J. Winicour, Phys. Rev. D **68**, 041501(R) (2003).

[74] L. E. Kidder, L. Lindblom, M. A. Scheel, L. T. Buchman, and H. P. Pfeiffer, Phys. Rev. D **71**, 064020 (2005).

[75] L. T. Buchman and O. C. A. Sarbach, Class. Quantum Grav. **23**, 6709 (2006).

[76] L. T. Buchman and O. C. A. Sarbach, Class. Quantum Grav. **24**, S307 (2007).

[77] L. Lindblom, K. D. Matthews, O. Rinne, and M. A. Scheel, Phys. Rev. D **77**, 084001 (2008).

[78] F. Pretorius, Class. Quantum Grav. **23**, S529 (2006).

[79] B. Szilágyi, D. Pollney, L. Rezzolla, J. Thornburg, and J. Winicour, Class. Quantum Grav. **24**, S275 (2007).

[80] M. Holst et al., Phys. Rev. D **70**, 084017 (2004).

[81] G. B. Cook and B. F. Whiting, Phys. Rev. D **76**, 041501(R) (2007).

[82] R. Owen, *Topics in Numerical Relativity: The periodic standing-wave approximation, the stability of constraints in free evolution, and the spin of dynamical black holes*, PhD thesis, California Institute of Technology, 2007.

[83] M. Campanelli, C. O. Lousto, and Y. Zlochower, Phys. Rev. D **73**, 061501(R) (2006).

[84] J. G. Baker, J. Centrella, D.-I. Choi, M. Koppitz, and J. van Meter, Phys. Rev. D **73**, 104002 (2006).

[85] B. Brügmann et al., Phys. Rev. D **77**, 024027 (2008).

[86] M. Boyle and A. H. Mroué, Extrapolating gravitational-wave data from numerical simulations, arXiv:0905.3177 (gr-qc), 2009.

[87] A. Nerozzi, M. Bruni, L. M. Burko, and V. Re, Towards a novel wave-extraction method for numerical relativity, in *Proceedings of the Albert Einstein Century International Conference, Paris, France*, pages 702–707, 2005, [AIP Conf. Proc. 861, 702 (2006)].

[88] E. Pazos et al., Class. Quantum Grav. **24**, S341 (2007).

[89] L. Lehner and O. M. Moreschi, Phys. Rev. D **76**, 124040 (2007).

[90] D. R. Fiske, J. G. Baker, J. R. van Meter, D.-I. Choi, and J. M. Centrella, Phys. Rev. D **71**, 104036 (2005).

[91] B. Szilagyi, L. Lindblom, and M. A. Scheel, Phys. Rev. D **80**, 124010 (2009).

Chapter 5

High-accuracy simulations of black-hole binaries: spins anti-aligned with the orbital angular momentum

High-accuracy binary black hole simulations are presented for black holes with spins anti-aligned with the orbital angular momentum. The particular case studied represents an equal-mass binary with spins of equal magnitude $S/m^2 = 0.43757 \pm 0.00001$. The system has initial orbital eccentricity $\sim 4 \times 10^{-5}$, and is evolved through 10.6 orbits plus merger and ringdown. The remnant mass and spin are $M_f = (0.961109 \pm 0.000003)M$ and ${S_f}/{M_f}^2 = 0.54781 \pm 0.00001$, respectively, where M is the mass during early inspiral. The gravitational waveforms have accumulated numerical phase errors of $\lesssim 0.1$ radians without any time or phase shifts, and $\lesssim 0.01$ radians when the waveforms are aligned with suitable time and phase shifts. The waveform is extrapolated to infinity using a procedure accurate to $\lesssim 0.01$ radians in phase, and the extrapolated waveform differs by up to 0.13 radians in phase and about one percent in amplitude from the waveform extracted at finite radius $r = 350M$. The simulations employ different choices for the constraint damping parameters in the wave zone; this greatly reduces the effects of junk radiation, allowing the extraction of a clean gravitational wave signal even very early in the simulation.

Originally published as T. Chu, H. P. Pfeiffer, and M. A. Scheel, Phys. Rev. D **80**, 124051 (2009).

5.1 Introduction

Much progress has been made in recent years in the numerical solution of Einstein's equations for the inspiral, merger, and ringdown of binary black hole systems. Since the work of Pretorius [1] and the development of the moving puncture method [2, 3], numerical simulations have been used to analyze post-Newtonian approximations [4, 5, 6, 7, 8, 9, 10, 11, 12, 13, 14, 15, 16, 17, 18, 19], to investigate the recoil velocity of the final black hole [20, 21, 22, 23, 24, 25, 26, 27, 28, 29, 30, 31, 32, 33, 34, 35, 36, 37, 38], and to explore the the orbital dynamics of spinning binaries [39, 40, 41, 28, 42, 43].

Numerical simulations can provide an accurate knowledge of gravitational waveforms, which is needed to make full use of the information obtained from gravitational-wave detectors such as LIGO and LISA. Not only can detected gravitational waveforms be compared with numerical results to measure astrophysical properties of the sources of gravitational radiation, but the detection probability itself can be increased via the technique of matched filtering [44], in which noisy data are convolved with numerical templates to enhance the signal.

The production of accurate numerical waveforms is computationally expensive, making it challenging to construct an adequate waveform template bank covering a sufficiently large region of the parameter space of black hole masses and spins. One way of increasing efficiency is to adopt techniques known as spectral methods. For smooth solutions, spatial discretization errors of spectral methods decrease exponentially with increasing numerical resolution. In contrast, errors decrease polynomially for the finite difference methods used in most black-hole binary simulations. Not only have spectral methods been used to prepare very accurate initial data [45, 46, 47, 48, 49, 50, 51, 52, 53, 54, 55, 56, 57, 58, 59], but they have been used to generate the longest and most accurate black-hole binary simulation to date [60].

Following the previous work of [60], this chapter presents the first spectral simulation of an orbiting and merging binary with spinning black holes: an equal mass system with spins of the black holes anti-aligned with the orbital angular momentum. Simulations of binaries with spins parallel to the orbital momentum are certainly not new, e.g., [39, 28, 34, 61, 42, 38, 11]. Our goal here is to show that such systems can be simulated with spectral methods, and that the high accuracies achieved for the nonspinning case carry over into this more general regime.

The spin of each black hole is $S/m^2 = 0.43757 \pm 0.00001$. The determination of this

quantity, as well as other spin measures, is explained in more detail in section 5.4.2. The evolution consists of 10.6 orbits of inspiral with an orbital eccentricity of $e \sim 4 \times 10^{-5}$, followed by the merger and ringdown. We find that this simulation has accuracy comparable to that of the simulation presented in [60]. We also present different choices for the constraint damping parameters in the wave zone; these choices cause the initial noise ("junk radiation") to damp more rapidly, resulting in a useable, almost noise-free waveform much earlier in the simulation.

This chapter is organized as follows: In section 5.2, we discuss the construction of our initial data. In section 5.3, we describe the equations, gauge conditions, and numerical methods used to solve Einstein's equations. In section 5.4, we present several properties of our simulations, including constraints, and the spins and masses of the black holes. In section 5.5, we explain the extraction of gravitational waveforms from the simulation, and the extrapolation of the waveforms to infinity. Finally, in section 5.6, we discuss outstanding difficulties and directions for future work.

5.2 Initial Data

The initial data are almost identical to those used in the simulation of an equal-mass, nonspinning black hole binary presented in Refs. [9, 60]. We use quasi-equilibrium initial data [62, 52, 55] (see also [48, 49]), built using the conformal thin sandwich formalism [63, 64], and employing the simplifying choices of conformal flatness and maximal slicing. Quasi-equilibrium boundary conditions are imposed on spherical excision boundaries for each black hole, with the lapse boundary condition given by Eq. (33a) of Ref. [55]. The excision spheres are centered at Cartesian coordinates $C_1^i = (d/2, 0, 0)$ and $C_2^i = (-d/2, 0, 0)$, where we choose the same coordinate distance d and the same excision radii as in [9].

Within this formalism, the spin of each black hole is determined by a parameter Ω_r and a conformal Killing vector ξ^i (tangential to the excision sphere); these enter into the boundary condition for the shift β^i at an excision surface [52]. We will use the sign convention of Eq. (40) in Ref. [57], so that positive Ω_r corresponds to corotating black holes. The same value of Ω_r is chosen at both excision surfaces, resulting in black holes with equal spins. In Refs. [9, 60], Ω_r was chosen to ensure that the black hole spins vanish [55]. In this work, we instead fix Ω_r at some negative value, resulting in moderately spinning black holes that counterrotate with the orbital motion.

Two more parameters need to be chosen before initial data can be constructed: The

Initial data	
Coordinate separation	$d/M_{\rm ID} = 13.354418$
Radius of excision spheres	$r_{\rm exc}/M_{\rm ID} = 0.382604$
Orbital frequency	$\Omega_0 M_{\rm ID} = 0.0187862$
Radial velocity	$v_r = -7.4710123 \times 10^{-4}$
Orbital frequency of horizons	$\Omega_r M_{\rm ID} = -0.242296$
Black hole spins	$\chi_{\rm ID} = 0.43785$
ADM energy	$M_{\rm ADM}/M_{\rm ID} = 0.992351$
Total angular momentum	$J_{\rm ADM}/M_{\rm ID}^2 = 0.86501$
Initial proper separation	$s_0/M_{\rm ID} = 16.408569$
Evolution	
Initial orbital eccentricity	$e \approx 4 \times 10^{-5}$
Mass after relaxation	$M = (1.000273 \pm 0.000001) M_{\rm ID}$
Spins after relaxation	$\chi = 0.43757 \pm 0.00001$
Time of merger (common AH)	$t_{\rm CAH} = 2399.38M$
Final mass	$M_f = (0.961109 \pm 0.000003) M$
Final spin	$\chi_f = 0.54781 \pm 0.00001$

Table 5.1: Summary of the simulation with anti-aligned spins presented in this work. The first block lists properties of the initial data, the second block lists properties of the evolution.

orbital angular frequency Ω_0 and the radial velocity v_r of each black hole. These parameters are determined by an iterative procedure that minimizes the orbital eccentricity during the subsequent evolution of the binary: We start by setting Ω_0 and v_r to their values in the nonspinning evolution of Ref. [65], we solve the initial value equations a pseudospectral elliptic solver [51], and we evolve for about 1 to 2 orbits using the techniques described in section 5.3. Analysis of this short evolution yields an estimate for the orbital eccentricity, and improved parameters Ω_0 and v_r that result in a smaller orbital eccentricity. This procedure is identical to Ref. [9], except that we include a term quadratic in t for the function used to fit the radial velocity (ds/dt), to obtain better fits. We repeat this procedure until the eccentricity of the black hole binary is reduced to $e \sim 4 \times 10^{-5}$. Properties of this low-eccentricity initial data set are summarized in the top portion of Table 5.1.

The data in the upper part of Table 5.1 are given in units of $M_{\rm ID}$, the sum of the black hole masses in the initial data. For any black hole (initial data, during the evolution, the

remnant black hole after merger), we define its mass using Christodoulou's formula,

$$m^2 = m_{\rm irr}^2 + \frac{S^2}{4m_{\rm irr}^2}. \tag{5.1}$$

We use the apparent horizon area $A_{\rm AH}$ to define the irreducible mass $m_{\rm irr} = \sqrt{A_{\rm AH}/(16\pi)}$. The *nonnegative* spin S of each black hole is computed with the spin diagnostics described in [57]. Unless noted otherwise, we compute the spin from an angular momentum surface integral [66, 67] using approximate Killing vectors of the apparent horizons, as described in [68, 57] (see also [69, 70]). We define the dimensionless spin by

$$\chi = \frac{S}{m^2}. \tag{5.2}$$

5.3 Evolutions

5.3.1 Overview

The Einstein evolution equations are solved with the pseudospectral evolution code described in Ref. [60]. This code evolves a first-order representation [71] of the generalized harmonic system [72, 73, 74] and includes terms that damp away small constraint violations [75, 74, 71]. The computational domain extends from excision boundaries located just inside each apparent horizon to some large radius, and is divided into subdomains with simple shapes (e.g., spherical shells, cubes, cylinders). No boundary conditions are needed or imposed at the excision boundaries, because all characteristic fields of the system are outgoing (into the black hole) there. The boundary conditions on the outer boundary [71, 76, 77] are designed to prevent the influx of unphysical constraint violations [78, 79, 80, 81, 82, 83, 84] and undesired incoming gravitational radiation [85, 86], while allowing the outgoing gravitational radiation to pass freely through the boundary. Interdomain boundary conditions are enforced with a penalty method [87, 88].

The gauge freedom in the generalized harmonic formulation of Einstein's equations is fixed via a freely specifiable gauge source function H_a that satisfies the constraint

$$0 = \mathcal{C}_a \equiv \Gamma_{ab}{}^{b} + H_a, \tag{5.3}$$

where $\Gamma^{a}{}_{bc}$ are the spacetime Christoffel symbols. We choose H_a differently during the inspiral, plunge and ringdown, as described in detail in Sections 5.3.3, 5.3.4, and 5.3.5.

Run	N_{pts}	CPU-h	CPU-h/T
N1	$(64^3, 65^3, 65^3)$	9,930	3.4
N2	$(70^3, 72^3, 72^3)$	16,195	5.6
N3	$(76^3, 78^3, 80^3)$	28,017	9.7
N4	$(82^3, 84^3, 87^3)$	44,954	15.5

Table 5.2: Approximate number of collocation points and CPU usage for the evolutions with anti-aligned spins. The first column indicates the name of the run. N_{pts} is the approximate number of collocation points used to cover the entire computational domain. The three values for N_{pts} are those for the inspiral, plunge, and ringdown portions of the simulation, which are described in Sections 5.3.3, 5.3.4 and 5.3.5, respectively. The total run times T are in units of the total Christodoulou mass M [cf. Eq. (5.1)] of the binary.

In order to treat moving holes using a fixed grid, we employ multiple coordinate frames [89]: The equations are solved in an "inertial frame" that is asymptotically Minkowski, but the grid is fixed in a "comoving frame" in which the black holes do not move. The motion of the holes is accounted for by dynamically adjusting the coordinate mapping between the two frames.[1] This coordinate mapping is chosen differently at different stages of the evolution, as described in Sections 5.3.3, 5.3.4, and 5.3.5.

The simulations are performed at four different resolutions, N1 to N4. The approximate number of collocation points and CPU usage for these resolutions are given in Table 5.2.

5.3.2 Relaxation of Initial Data

The initial data do not precisely correspond to two black holes in equilibrium, e.g., because tidal deformations are not incorporated correctly, and because of the simplifying choice of conformal flatness. Therefore, early in the evolution the system relaxes and settles down into a new steady-state configuration. Figure 5.1 shows the change in irreducible mass and spin relative to the initial data during the evolution. During the first $\sim 10M$ of the evolution, $M_{\rm irr}$ increases by about 3 parts in 10^4 while the spin decreases by about 1 part in 10^4. These changes are resolved by all four numerical resolutions, labeled N1 (lowest) to N4 (highest), and converge with increasing resolution. After the initial relaxation, for $10M \lesssim t \lesssim 2350M$, the mass is constant to about 1 part in 10^6, as can be seen from the convergence of the different resolutions in the upper panel of Fig. 5.1. In the last $\sim 50M$ before merger, the mass increases slightly (seen as a vertical feature at the right edge of the

[1] All coordinate quantities (e.g., trajectories, waveform extraction radii) in this work are given with respect to the inertial frame unless noted otherwise.

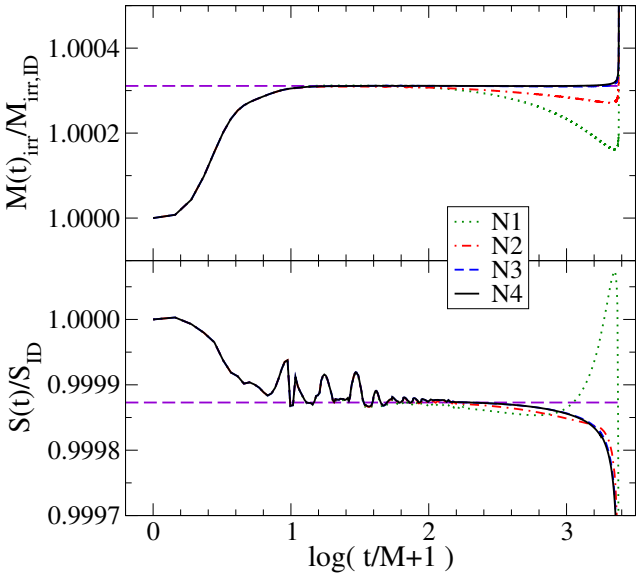

Figure 5.1: Irreducible mass (top panel) and spin (bottom panel) of the black holes during the relaxation of the initial data to the equilibriun (steady-state) inspiral configuration. Shown are four different numerical resolutions, N1 (lowest) to N4 (highest), cf. Table 5.2. Up to $t \sim 10M$, both mass and spin change by a few parts in 10^4, then they remain approximately constant (as indicated by the dashed horizontal lines) until shortly before merger. These steady-state values are used to define M and χ.

plot), an effect we will discuss in more detail in the context of Fig. 5.5. The spin is likewise almost constant for $10 \lesssim t/M \lesssim 1000$, although some noise is visible for $t \lesssim 100M$.

We shall take the steady-state masses and spins evaluated at $t \sim 200M$ as the physical parameters of the binary being studied. Specifically, all dimensionful quantities will henceforth be expressed in terms of the mass scale M, which we define as the total mass *after* relaxation.

The relaxation of the black holes in the first $\sim 10M$ of the evolution is also accompanied by the emission of a pulse of unphysical "junk radiation." This pulse passes through the computational domain, and leaves through the outer boundary after one light crossing time. The junk radiation contains short wavelength features, which are not resolved in the wave zone. It turns out that the *constraint damping parameters* γ_0 and γ_2 (see [71]) influence how the unresolved junk radiation interacts with the numerical grid. Large constraint damping parameters enhance the conversion of the outgoing junk radiation (at the truncation error level) into incoming modes. This incoming radiation then lingers for several light-crossing times within the computational domain, imprinting noise into the extracted gravitational radiation. For small constraint damping parameters, this conversion is greatly suppressed,

and numerical noise due to junk radiation diminishes much more rapidly. The simulations presented here use $\gamma_0 = \gamma_2 \sim 0.00225/M$ in the wave zone; these values are smaller by a factor 100 than those used in [9, 60]. (Even smaller constraint damping parameters fail to suppress constraint violations. Note that constraint damping parameters are much larger, $\gamma_0 = \gamma_2 \sim 3.56/M$, in the vicinity of the black holes.) The waveforms presented here show consequently reduced contaminations in the early part of the evolution will be discussed in section 5.6, cf. Fig. 5.15.

5.3.3 Inspiral

During the inspiral, the mapping between the comoving and inertial frames is chosen in the same way as in Refs. [9, 60] and is denoted by $\mathcal{M}_{\rm I} : x'^i \to x^i$, where primed coordinates denote the comoving frame and unprimed coordinates denote the inertial frame. Explicitly, this map is

$$r = \left[a(t) + (1 - a(t)) \frac{r'^2}{R_0'^2}\right] r', \tag{5.4}$$

$$\theta = \theta', \tag{5.5}$$

$$\phi = \phi' + b(t), \tag{5.6}$$

where (r, θ, ϕ) and (r', θ', ϕ') denote spherical polar coordinates relative to the center of mass of the system in inertial and comoving coordinates, respectively. We choose $R_0' = 467M$. The functions $a(t)$ and $b(t)$ are determined by a dynamical control system as described in Ref. [89]. This control system adjusts $a(t)$ and $b(t)$ so that the centers of the apparent horizons remain stationary in the comoving frame.

While each hole is roughly in equilibrium during inspiral, we choose the gauge source function H_a in the same way as in Refs. [9, 60]: A new quantity $\tilde{H}_a$ is defined that has the following two properties: (i) $\tilde{H}_a$ transforms like a tensor, and (ii) in inertial coordinates $\tilde{H}_a = H_a$. H_a is chosen so that the constraint Eq. (5.3) is satisfied initially, and $\tilde{H}_{a'}$ is kept constant in the comoving frame, i.e.,

$$\partial_{t'} \tilde{H}_{a'} = 0. \tag{5.7}$$

Here primes refer to comoving frame coordinates. This is essentially an equilibrium condition.

5.3.4 Plunge

We make two key modifications to our algorithm to allow evolution through merger. The first is a change in gauge conditions, as in Ref. [60]. The second is a change in coordinate mappings that allows the excision boundaries to more closely track the horizons. We describe both of these changes here.

Following Ref. [60], at some time $t = t_g$ (where g stands for "gauge") we promote the gauge source function H_a to an independent dynamical field that satisfies

$$\nabla^c \nabla_c H_a = Q_a(x, t, \psi_{ab}) + \xi_2 t^b \partial_b H_a. \tag{5.8}$$

Here $\nabla^c \nabla_c$ is the curved space *scalar* wave operator (i.e., each component of H_a is evolved as a scalar), ψ_{ab} is the spacetime metric, and t^a is the timelike unit normal to the hypersurface. The driving functions Q_a are

$$Q_t = f(x,t)\xi_1 \frac{1-N}{N^\eta}, \tag{5.9}$$

$$Q_i = g(x,t)\xi_3 \frac{\beta_i}{N^2}, \tag{5.10}$$

where N and β^i are the lapse function and the shift vector, η, ξ_1, ξ_2, and ξ_3 are constants, and $f(x,t)$, and $g(x,t)$ are prescribed functions of the spacetime coordinates. Eq. (5.8) is evolved in first-order form, as described in Ref. [60]. Eq. (5.8) requires values of H_a and its time derivative as initial data; these are chosen so that H_a and $\partial_t H_a$ are continuous at $t = t_g$.

This gauge is identical to the one used in Ref. [60], except that the parameters and functions that go into Eq. (5.8) are chosen slightly differently: We set $\eta = 4$, $\xi_1 = 0.1$, $\xi_2 = 6.5$, $\xi_3 = 0.01$, and

$$\begin{aligned} f(x,t) &= (2 - e^{-(t-t_g)/\sigma_1}) \\ &\times (1 - e^{-(t-t_g)^2/\sigma_2^2}) e^{-r'^2/\sigma_3^2}, \end{aligned} \tag{5.11}$$

$$\begin{aligned} g(x,t) &= (1 - e^{-(t-t_g)/\sigma_4}) \\ &\times (1 - e^{-(t-t_g)^2/\sigma_5^2})(t - t_g) e^{-r'^2/\sigma_3^2}, \end{aligned} \tag{5.12}$$

where r' is the coordinate radius in comoving coordinates, and the constants are $\sigma_1 \sim 62M$, $\sigma_2 \sim 44.5M$, $\sigma_3 \sim 35M$, $\sigma_4 \sim 4.5M$, and $\sigma_5 \sim 3M$. The function $g(x,t)$ in Q_i, which drives the shift toward zero near the black holes, has a factor $(t - t_g)$ that is absent in Ref. [60].

Prescribing $g(x,t)$ in this way drives the shift toward zero more strongly at late times, which for this case is more effective in preventing gauge singularities from developing.

The second change we make at $t = t_g$ is to control the shape of each excision boundary so that it matches the shape of the corresponding apparent horizon. In the comoving frame, where the excision boundaries are spherical by construction, this means adjusting the coordinate mapping between the two frames such that the apparent horizons are also spherical. Without this "shape control," the horizons become sufficiently distorted with respect to the excision boundaries that the excision boundaries fail to remain outflow surfaces and our excision algorithm fails. For the nonspinning black hole binary in Ref. [60], shape control was not necessary before merger. To control the shape of black hole 1, we define the map $\mathcal{M}_{\rm AH\,1} : x'^i \to \tilde{x}^i$,

$$\tilde{\theta} = \theta', \tag{5.13}$$

$$\tilde{\phi} = \phi', \tag{5.14}$$

$$\tilde{r} \equiv r' - q_1(r') \sum_{\ell=0}^{\ell_{\rm max}} \sum_{m=-\ell}^{\ell} \lambda^1_{\ell m}(t) Y_{\ell m}(\theta', \phi'), \tag{5.15}$$

where

$$q_1(r') = e^{-(r'-r'_0(t))^3/\sigma_q^3}, \tag{5.16}$$

and (r', θ', ϕ') are spherical polar coordinates centered at the (fixed) comoving-coordinate location of black hole 1. The function $q_1(r')$ limits the action of the map to the vicinity of hole 1. The constant σ_q is chosen to be $\sim 4.5M$, and $r'_0(t) = r'_0 + \nu_1 (t - t_g)^{2.1}$ is a function of time that approximately follows the radius of the black hole, with constants $r'_0 \sim 1.2M$ and $\nu_1 \sim 0.00046M$. Similarly, we define the map $\mathcal{M}_{\rm AH\,2}$ for black hole 2. Then the full map $\mathcal{M}_{\rm m} : x'^i \to x^i$ from the comoving coordinates x'^i to the inertial coordinates x^i is given by

$$\mathcal{M}_{\rm m} := \mathcal{M}_{\rm I} \circ \mathcal{M}_{\rm AH\,2} \circ \mathcal{M}_{\rm AH\,1}. \tag{5.17}$$

The functions $\lambda^1_{\ell m}(t)$ and $\lambda^2_{\ell m}(t)$ are determined by dynamical control systems as described in Refs. [89, 60], so that the apparent horizons are driven to spheres (up to spherical harmonic component $l = l_{\rm max}$) in comoving coordinates. Note that $\mathcal{M}_{\rm AH\,1} : x'^i \to \tilde{x}^i$ is essentially the same map that we use to control the shape of the merged horizon during ringdown, and the control system for that map (and for the map $\mathcal{M}_{\rm AH\,2}$) is the same as the one described in Ref. [60] for controlling the shape of the merged horizon.

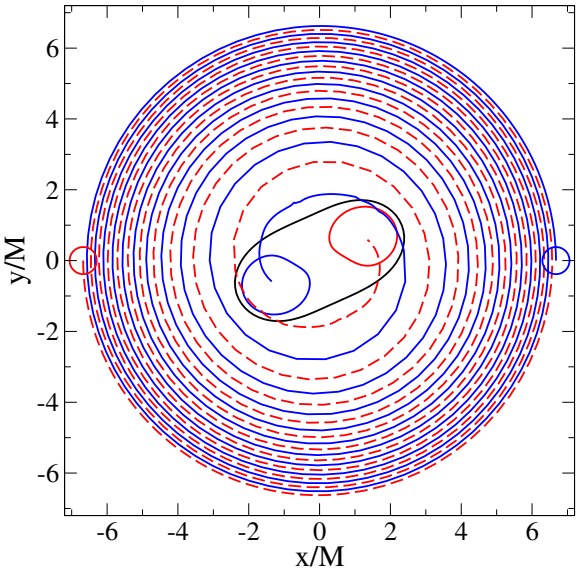

Figure 5.2: Coordinate trajectories of the centers of the apparent horizons represented by the blue and red curves, up until the formation of a common horizon. The closed curves show the coordinate shapes of the corresponding apparent horizons.

In addition to the modifications to the gauge conditions and coordinate map described above, the numerical resolution is also increased slightly around the two black holes during this more dynamical phase, and the evolution is continued until time t_m, shortly after the formation of a common horizon. The coordinate trajectories of the apparent horizon centers are shown in Fig. 5.2 up until t_m, at which point the binary has gone through 10.6 orbits.

5.3.5 Ringdown

Our methods for continuing the evolution once a common horizon has formed are the same as in Ref. [60]. After a common apparent horizon is found, all variables are interpolated onto a new computational domain that has only a single excised region. Then, a new comoving coordinate system (and a corresponding mapping to inertial coordinates) is chosen so that the new excision boundary tracks the shape of the apparent horizon in the inertial frame, and also ensures that the outer boundary behaves smoothly in time. The gauge conditions are modified as well: the shift vector is no longer driven to zero, so that the solution can relax to a time-independent state. This is done by allowing the gauge function $g(x,t)$ that appears in Eq. (5.10) to gradually approach zero; the gauge source function H_a still obeys Eqs. (5.8)–(5.10) as during the plunge. Specifically, we change the functions $f(x,t)$ and

$g(x,t)$ from Eqs. (5.11) and (5.12) to

$$\begin{aligned} f(x,t) &= (2 - e^{-(t-t_g)/\sigma_1}) \\ &\times (1 - e^{-(t-t_g)^2/\sigma_2^2}) e^{-r''^2/\sigma_3^2}, \end{aligned} \tag{5.18}$$

$$\begin{aligned} g(x,t) &= (1 - e^{-(t-t_g)/\sigma_4}) \\ &\times (1 - e^{-(t-t_g)^2/\sigma_5^2})(t - t_g) e^{-r''^2/\sigma_3^2} \\ &\times e^{-(t-t_m)/\sigma_6^2}, \end{aligned} \tag{5.19}$$

where r'' is the coordinate radius in the new comoving coordinates, $\sigma_6 \sim 3.1M$, and t_m (here m stands for "merger") is the time we transition to the new domain decomposition.

5.4 Properties of the numerical solutions

5.4.1 Constraints

We do not explicitly enforce either the Einstein constraints or the secondary constraints that arise from writing the system in first-order form. Therefore, examining how well these constraints are satisfied provides a useful consistency check. Figure 5.3 shows the contraint violations for the evolutions at different resolutions. The top panel shows the L^2 norm of all the constraint fields of our first-order generalized harmonic system, normalized by the L^2 norm of the spatial gradients of the dynamical fields (see Eq. (71) of Ref.[71]). The bottom panel shows the same quantity, but without the normalization factor (i.e., just the numerator of Eq. (71) of Ref.[71]). The L^2 norms are taken over the portion of the computational volume that lies outside the apparent horizons.

The constraints increase as the black holes approach each other and become increasingly distorted. At $t_g = 2372.05M$ for N4 ($t_g = 2372.05M$ for N3, $t_g = 2376.5M$ for N2, $t_g = 2376.5M$), the gauge conditions are changed (cf. 5.3.4) and the resolution around the holes is increased slightly. Because of the change in resolution, the constraints drop by more than an order of magnitude. Close to merger, the constraints grow larger again. The transition to a single-hole evolution (cf. 5.3.5) occurs at $t_m = 2399.64M$ for N4 ($t_m = 2399.66M$ for N3, $t_m = 2401.27M$ for N2, $t_m = 2404.23M$ for N1). Shortly after this time, the constraints drop by about two orders of magnitude. This is because the largest constraint violations occur near and between the individual apparent horizons, and this region is newly excised from the computational domain at $t = t_m$.

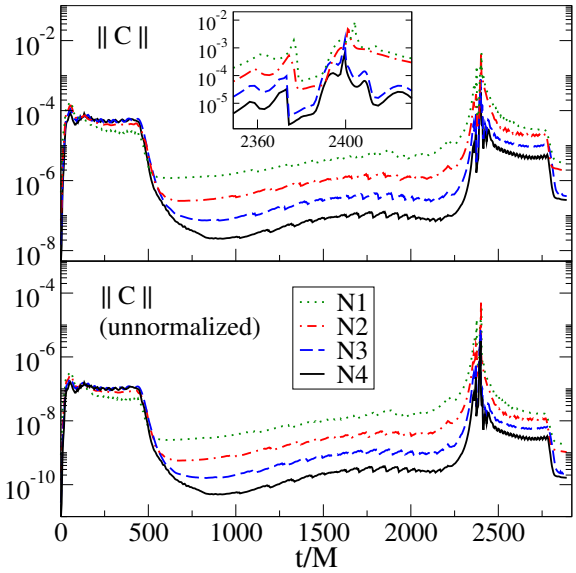

Figure 5.3: Constraint violations of runs on different resolutions. The top panel shows the L^2 norm of all constraints, normalized by the L^2 norm of the spatial gradients of all dynamical fields. The bottom panel shows the same data, but without the normalization factor. The L^2 norms are taken over the portion of the computational volume that lies outside apparent horizons. Note that the time when we change the gauge before merger, $t_g \sim 2370M$, and the time when we regrid onto a new single-hole domain after merger, $t_m \sim 2400M$, are slightly different for different resolutions.

5.4.2 Black hole spins and masses

There are different ways to compute the spin $\chi(t)$ of a black hole. The approach we prefer computes the spin from an angular momentum surface integral [66, 67] using approximate Killing vectors of the apparent horizons, as described in [68, 57] (see also [69, 70]). We shall denote the resulting spin by $\chi_{\rm AKV}(t)$. Another less sophisticated method simply uses coordinate rotation vectors, and we denote the resulting spin by $\chi_{\rm Coord}(t)$. We also use two more spin diagnostics that are based on the minimium and maximum of the instrinsic scalar curvature of the apparent horizon for a Kerr black hole [57]; we call these $\chi_{\rm SC}^{\rm min}(t)$ and $\chi_{\rm SC}^{\rm max}(t)$. These last two measures of spin are expected to give reasonable results when the black holes are sufficiently far apart and close to equilibrium, and after the final black hole has settled down to a time-independent state. However, they are expected to be less accurate near merger and at the start of the evolution.

Figure 5.4 shows these four spin measures for black hole 1 in the N4 evolution during inspiral and plunge. From the lower left panel we see that $\chi_{\rm SC}^{\rm min}(t)$ and $\chi_{\rm SC}^{\rm max}(t)$ differ from $\chi_{\rm Coord}(t)$ and $\chi_{\rm AKV}(t)$ by more than a factor of two at $t = 0$. This indicates that the

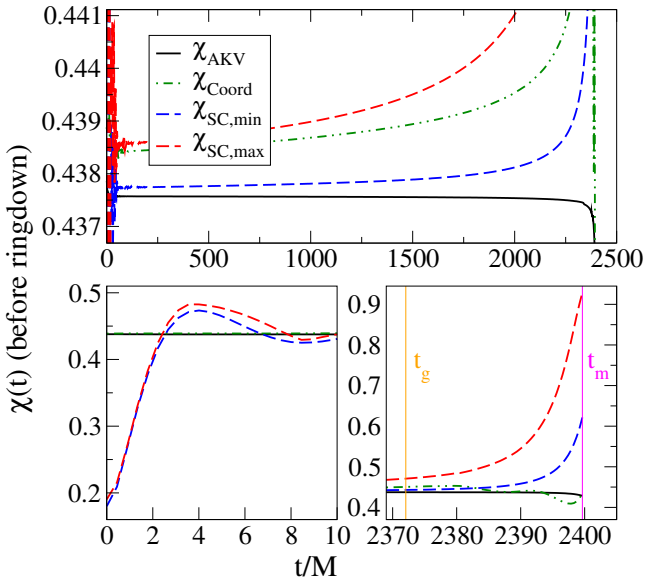

Figure 5.4: Dimensionless spins χ of one black hole in the N4 evolution, evaluated using an approximate Killing vector, a coordinate rotation vector $-\partial_\phi$, or the extrema of the instrinsic scalar curvature on the apparent horizon. Bottom panels show detail at early and late times. Also shown are the time of gauge change t_g before merger, and the time t_m that we transition to a single-hole evolution just after merger.

initial black holes do not have the appropriate shape for the Kerr solution; i.e., they are distorted because of the way the initial data is constructed. As the black holes relax, $\chi_{\rm SC}^{\rm min}(t)$ and $\chi_{\rm SC}^{\rm max}(t)$ approach the other two spin measures. The relaxed spin at $t \sim 200M$ is $\chi = 0.43757 \pm 0.00001$, where the uncertainty is based on the variation in $\chi_{\rm AKV}$ between $t = 100M$ and $t = 1000M$. During the inspiral, $\chi_{\rm AKV}(t)$ decreases slowly and monotonically, dropping by 10^{-4} at $90M$ before merger, and dropping by 0.01 at the time of merger. Tidal dissipation should *slow down* the black holes, so this decrease is physically sensible. In contrast, the other three spin diagnostics show a mild *increase* in spin, suggesting that they are less reliable. Close to merger, $\chi_{\rm SC}^{\rm min}(t)$ and $\chi_{\rm SC}^{\rm max}(t)$ increase dramatically, with $\chi_{\rm SC}^{\rm max}(t)$ growing as large as 0.92. In this regime, the shapes of the individual black holes are dominated by tidal distortion, and are therefore useless for measuring the spin.

The Christodoulou mass m of one black hole, as defined in Eq. (5.1), depends on the spin. We take $\chi_{\rm AKV}(t)$ as the preferred spin measure, and use it to compute the total Christodoulou mass $M(t)$ during the inspiral and plunge. This is shown in the top panel of Fig. 5.5. The Christodoulou mass settles down to $M(t)/M = 1.000000$ after $t = 150M$ (this defines M), and increases to $M(t)/M = 1.00114$ at the time of merger. Most of the increase in mass occurs very close to merger, as can be seen from the inset of Fig. 5.5. Until

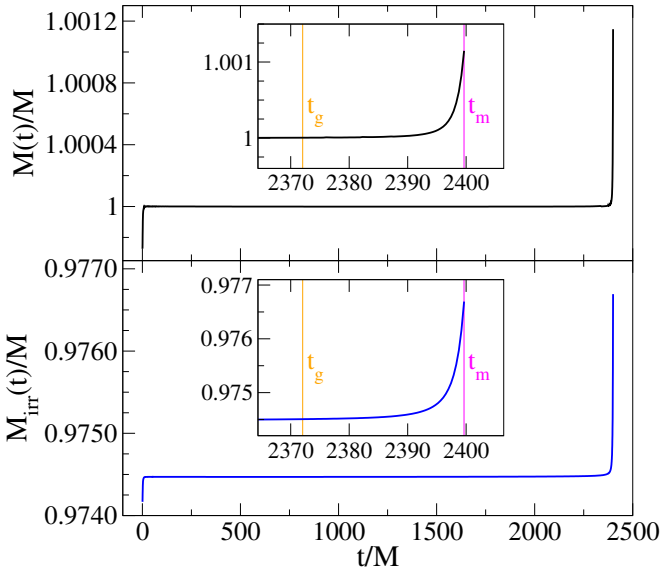

Figure 5.5: Sum of Christodoulou masses $M(t)$ and sum of irreducible masses $M_{\rm irr}(t)$ of the two black holes during inspiral. The data is from the N4 evolution, and uses $\chi_{\rm AKV}$ when computing $M(t)$. Insets show detail at late times, and indicate the transition times t_g and t_m.

about $30M$ before merger (i.e., $t = 2370M$), the mass is constant to a few parts in 10^6. For comparison, in the bottom panel we also display $M_{\rm irr}(t)$, the sum of the irreducible masses, which does not depend on the spin. This quantity settles down to $M_{\rm irr}(t)/M = 0.974508$ at $t = 200M$, and increases to $M_{\rm irr}(t)/M = 0.97668$ at $t = 2400M$. Again, almost all of this increase happens shortly before merger. During the inspiral up to $30M$ before merger, $M_{\rm irr}(t)/M$ increases by only 6×10^{-5}, but in the last $30M$ the increase is $\sim$0.002.

The merger results in one highly distorted black hole, which subsequently rings down into a stationary Kerr black hole. Figure 5.6 shows our four spin diagnostics during the ringdown. The spin measures $\chi_{\rm SC}^{\rm min}(t)$ and $\chi_{\rm SC}^{\rm max}(t)$ assume a Kerr black hole. Just after merger, the horizon is highly distorted, so these two spin diagnostics are not valid there. However, as the remnant black hole rings down to Kerr, $\chi_{\rm SC}^{\rm max}(t)$ and $\chi_{\rm SC}^{\rm min}(t)$ approach the quasi-local AKV spin to better than 1 part in 10^5 (see the inset of Fig. 5.6). The quasi-local spin based on coordinate rotation vectors, $\chi_{\rm Coord}(t)$, also agrees with the other spin measures to a similar level at late times. The spin of the final black hole points in the direction of the initial orbital angular momentum.

The Christodoulou mass $M_f(t)$ of the final black hole in the N4 evolution, again evaluated using $\chi_{\rm AKV}(t)$, is shown in the top panel of Fig. 5.7. The mass settles down to a final value of $M_f/M = 0.961109 \pm 0.000003$. The bottom panel shows the irreducible mass $M_{\rm irr,f}(t)$ of

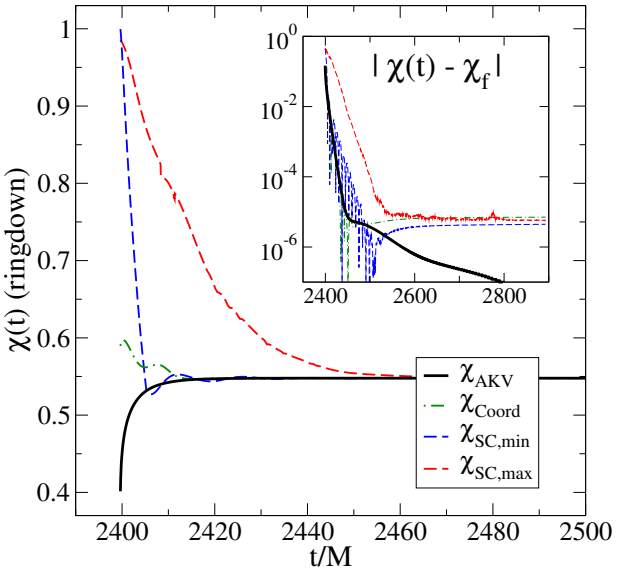

Figure 5.6: Dimensionless spins $\chi(t)$ of the final black hole in the N4 evolution. The (most reliable) spin diagnostic $\chi_{\rm AKV}$ starts at $\sim$0.4 and increases to its final value $\chi_f = 0.54781 \pm 0.00001$. The other spin diagnostics are unreliable for the highly distorted black hole shortly after merger, but subsequently approach $\chi_{\rm AKV}$.

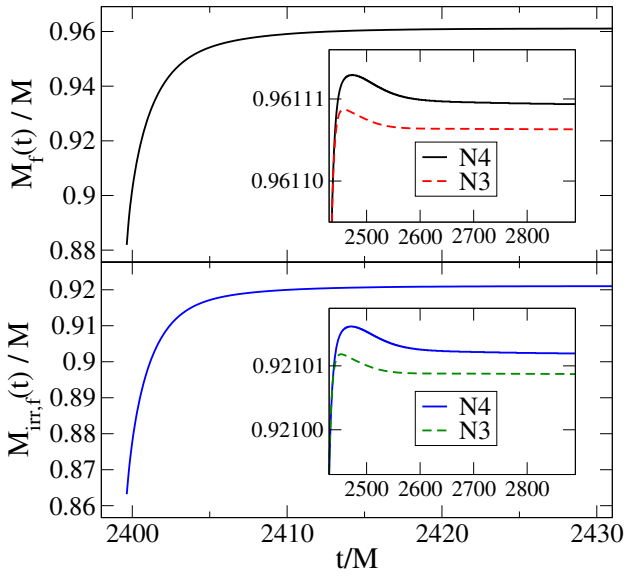

Figure 5.7: The top panel shows the Christodoulou mass $M_f(t)$ of the final black hole in the N4 and N3 runs, computed using $\chi_{\rm AKV}(t)$. The bottom panel shows the irreducible mass $M_{\rm irr,f}(t)$.

the final black hole, which settles down to a final value of $M_{\rm irr,f} = 0.921012 \pm 0.000003$. The uncertainties are determined from the difference between runs N4 and N3, so they include

only numerical truncation error and not any systematic effects. The uncertainty in the mass is visible in the insets of Fig. 5.7.

5.5 Computation of the waveform

5.5.1 Waveform extraction

Gravitational waves are extracted from the simulation on spheres of different values of the coordinate radius r, following the same procedure as in Refs. [65, 9, 60]. The Newman-Penrose scalar Ψ_4 is expanded in terms of spin-weighted spherical harmonics of weight -2:

$$\Psi_4\left(t,r,\theta,\phi\right) = \sum_{lm} \Psi_4^{lm}\left(t,r\right) {}_{-2}Y_{lm}\left(\theta,\phi\right), \tag{5.20}$$

where the Ψ_4^{lm} are expansion coefficients defined by this equation. Here we also focus on the dominant $(l,m) = (2,2)$ mode, and split the extracted waveform into real phase ϕ and real amplitude A, defined by (see e.g., [3, 90])

$$\Psi_4^{22}(r,t) = A(r,t)e^{-i\phi(r,t)}. \tag{5.21}$$

The gravitational-wave frequency is given by

$$\omega = \frac{d\phi}{dt}. \tag{5.22}$$

The minus sign in Eq. (5.21) is chosen so that the phase increases in time and ω is positive.

The coordinate radius of our outer boundary is located at $R_{\rm max} = 427M$ at $t = 0$ and $R_{\rm max} = 365M$ at $t > 2500M$; it shrinks slightly during the evolution because of the mappings (cf. Eq. (5.4)) used in our dual frame approach. The $(l,m) = (2,2)$ waveform, extracted at a single coordinate radius $r = 350M$ for the N4 evolution, is shown in Fig 5.8. The short pulse at $t \sim 360M$ is due to junk radiation. The magnitude of this pulse is about twice as large as for nonspinning black holes, cf. Ref. [9, 60].

5.5.2 Convergence of extracted waveforms

In this section we examine the convergence of the gravitational waveforms extracted at fixed radius, without extrapolation to infinity. This allows us to study the behavior of our code without the complications of extrapolation. The extrapolation process and the resulting

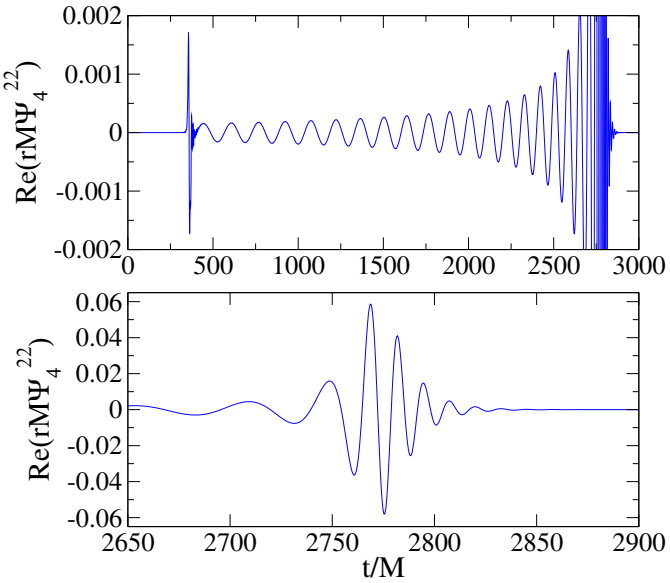

Figure 5.8: Gravitational waveform extracted at finite radius $r = 350M$ for the N4 evolution. The top panel zooms in on the inspiral waveform, and the bottom panel zooms in on the merger and ringdown.

extrapolated waveforms are discussed in section 5.5.3.

Figure 5.9 shows the convergence of the gravitational-wave phase ϕ and amplitude A with numerical resolution. For this plot, the waveform was extracted at a fixed inertial-coordinate radius of $r = 350M$. Each line in the top panel shows the absolute difference between ϕ computed at some particular resolution and ϕ computed from our highest resolution N4 run. The curves in the bottom panel similarly show the *relative* amplitude differences. When subtracting results at different resolutions, no time or phase adjustment has been performed. The noise at early times is due to junk radiation generated near $t = 0$. Most of this junk radiation leaves through the outer boundary after one crossing time. The plots show that the phase difference accumulated over 10.6 orbits plus merger and ringdown—in total 31 gravitational wave cycles—is less than 0.1 radians, and the relative amplitude differences are less than 0.017. These numbers can be taken as an estimate of the numerical truncation error of our N3 run. Because of the rapid convergence of the code, we expect that the errors of the N4 run are significantly smaller.

Figure 5.10 is the same as Fig. 5.9 after the N1, N2, N3 waveforms have been time shifted and phase shifted to best match the waveform of the N4 evolution. This best match

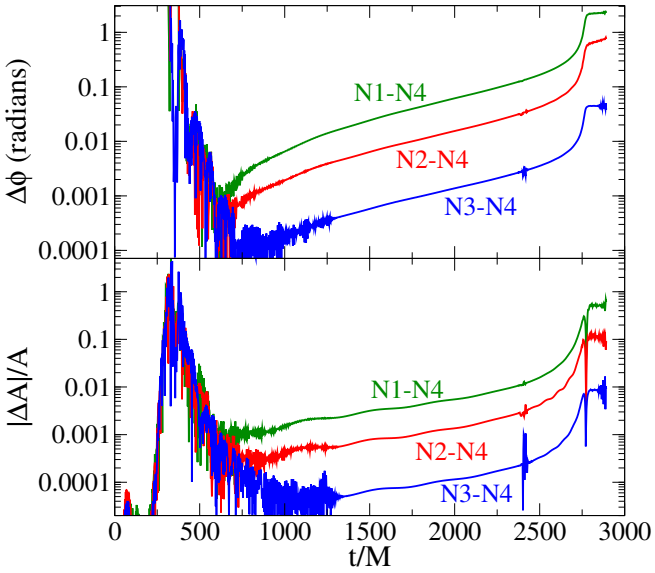

Figure 5.9: Convergence of gravitational waveforms with numerical resolution. Shown are phase and amplitude differences between numerical waveforms Ψ_4^{22} computed using different numerical resolutions. All waveforms are extracted at $r = 350M$, and no time shifting or phase shifting is done to align waveforms.

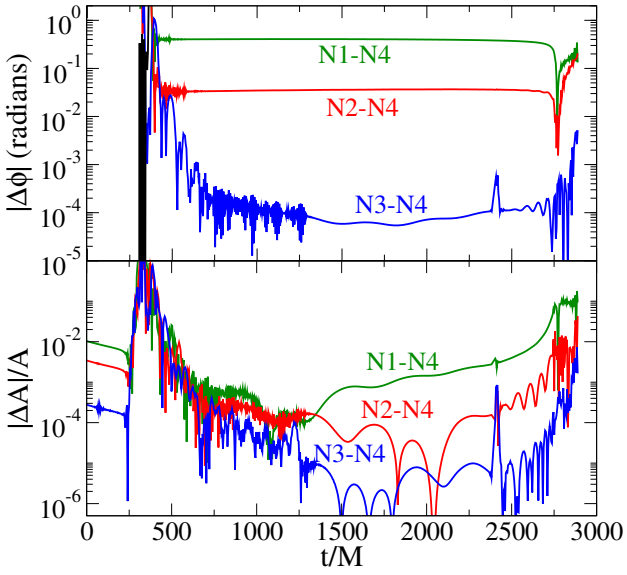

Figure 5.10: Convergence of gravitational waveforms with numerical resolution. Same as Fig. 5.9 except all other waveforms are time shifted and phase shifted to best match the waveform of the N4 run.

is determined by a simple least-squares procedure: we minimize the function

$$\sum_i \left(A_1(t_i) e^{i\phi_1(t_i)} - A_2(t_i + t_0) e^{i(\phi_2(t_i+t_0)+\phi_0)} \right)^2, \tag{5.23}$$

by varying t_0 and ϕ_0. Here A_1, ϕ_1, A_2, and ϕ_2 are the amplitudes and phases of the two waveforms being matched, and the sum goes over all times t_i at which waveform 1 is sampled. This type of comparison is relevant for analysis of data from gravitational-wave detectors: when comparing experimental data with numerical detection templates, the template will be shifted in both time and phase to best match the data. For this type of comparison, Fig. 5.10 shows that the numerical truncation error of our N3 run is less than 0.01 radians in phase and 0.1 percent in amplitude for $t > 550M$. At earlier times, the errors are somewhat larger and are dominated by residual junk radiation.

5.5.3 Extrapolation of waveforms to infinity

Gravitational-wave detectors measure waveforms as seen by an observer effectively infinitely far from the source. Since our numerical simulations cover only a finite spacetime volume, after extracting waveforms at multiple finite radii, we extrapolate these waveforms to infinite radius using the procedure described in [60] (see also [91] for more details). This is intended to reduce near-field effects as well as gauge effects that can be caused by the time dependence of the lapse function or the nonoptimal choice of tetrad for computing Ψ_4.

The extrapolation of the extracted waveforms involves first computing each extracted waveform as a function of retarded time $u = t_s - r^*$ and extraction radius $r_{\rm areal}$ (see [60] for precise definitions). Then at each value of u, the phase and amplitude are fitted to polynomials in $1/r_{\rm areal}$:

$$\phi(u, r_{\rm areal}) = \phi_{(0)}(u) + \sum_{k=1}^{n} \frac{\phi_{(k)}(u)}{r_{\rm areal}^k}, \tag{5.24}$$

$$r_{\rm areal} A(u, r_{\rm areal}) = A_{(0)}(u) + \sum_{k=1}^{n} \frac{A_{(k)}(u)}{r_{\rm areal}^k}. \tag{5.25}$$

The phase and amplitude of the desired asymptotic waveform are thus given by the leading-order term of the corresponding polynomial, as a function of retarded time:

$$\phi(u) = \phi_{(0)}(u), \tag{5.26}$$

$$r_{\rm areal} A(u) = A_{(0)}(u). \tag{5.27}$$

Figure 5.11 shows phase and amplitude differences between extrapolated waveforms that are computed using different values of polynomial order n in Eqs. (5.24) and (5.25). The extrapolation is based on waveforms extracted at 20 different radii between $75M$ and $350M$.

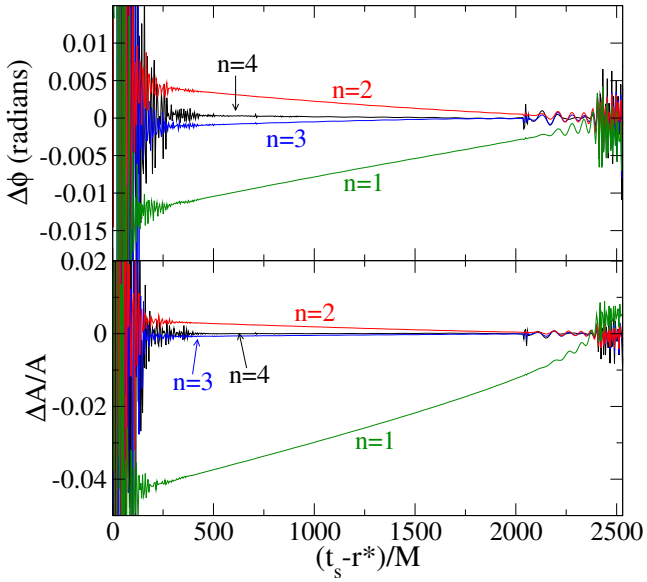

Figure 5.11: Convergence of extrapolation to infinity for extrapolation of order n. For each n, plotted is the extrapolated waveform from N4 using order $n+1$ minus the extrapolated waveform using order n. The top panel shows phase differences, the bottom panel shows amplitude differences. No shifting in time or phase has been done for this comparison.

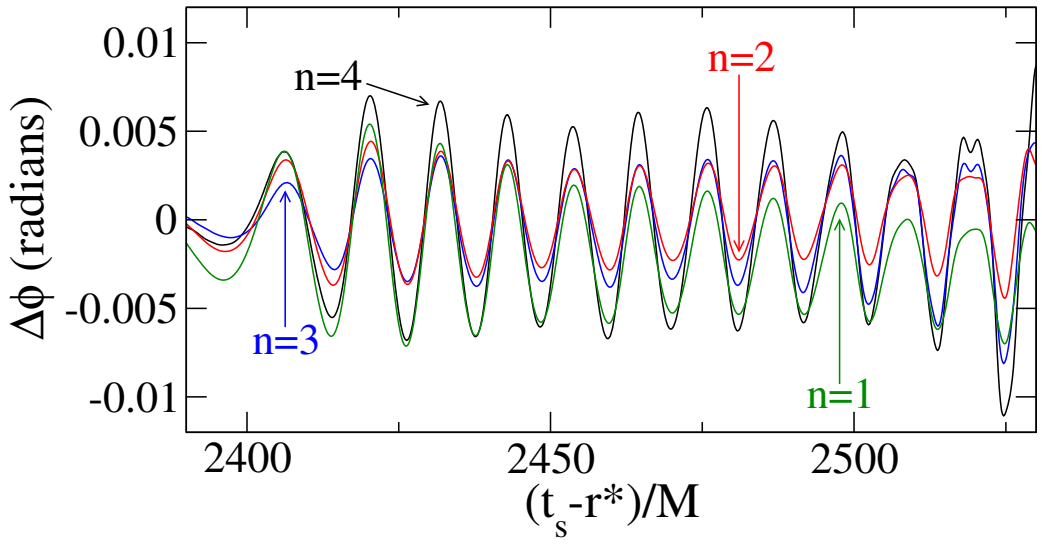

Figure 5.12: Late-time phase convergence of extrapolation to infinity. Same as the top panel of Fig. 5.11, except zoomed to late times. The peak amplitude of the waveform occurs at $t_s - r^* = 2410.6M$.

As in [60], our preferred extrapolation order is $n = 3$, which gives a phase error of less than 0.004 radians and a relative amplitude error of less than 0.006 during most of the inspiral,

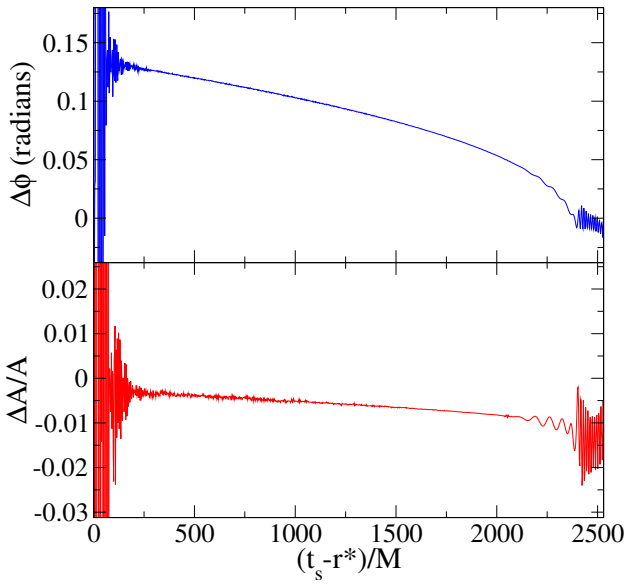

Figure 5.13: Phase and relative amplitude differences between extrapolated and extracted waveforms for N4. The extracted waveform is extracted at coordinate radius $r = 350M$. The waveforms are time shifted and phase shifted to produce the best least-squares match.

and a phase error of less than 0.01 radians and a relative amplitude error of 0.006 in the ringdown.

Figure 5.12 is the same as the top panel of Fig. 5.11, except zoomed to late times. During merger and ringdown, the extrapolation procedure does not converge with increasing extrapolation order n: the phase differences are slightly larger for larger n. This was also seen for the extrapolated waveforms of our equal-mass nonspinning black hole binary [60], and is possibly due to gauge effects that do not obey the fitting formulae, Eqs. (5.24) and (5.25).

Figure 5.13 shows the phase and amplitude differences between our preferred extrapolated waveform using $n = 3$ and the waveform extrapolated at coordinate radius $r = 350M$, both for the N4 run. The extrapolated waveform has been shifted in time and phase so as to best match the $n = 3$ extrapolated waveform, using the least-squares fit of Eq. (5.23). The phase difference between extrapolated waveform and waveform extracted at $r = 350M$ becomes as large as 0.13 radians, and the amplitude differenceis on the order of 1 percent.

Figure 5.14 presents the final waveform after extrapolation to infinite radius. There are 22 gravitational-wave cycles before the maximum of $|\Psi_4|$, and 9 gravitational-wave cycles during ringdown, over which the amplitude of $|\Psi_4|$ drops by four orders of magnitude.

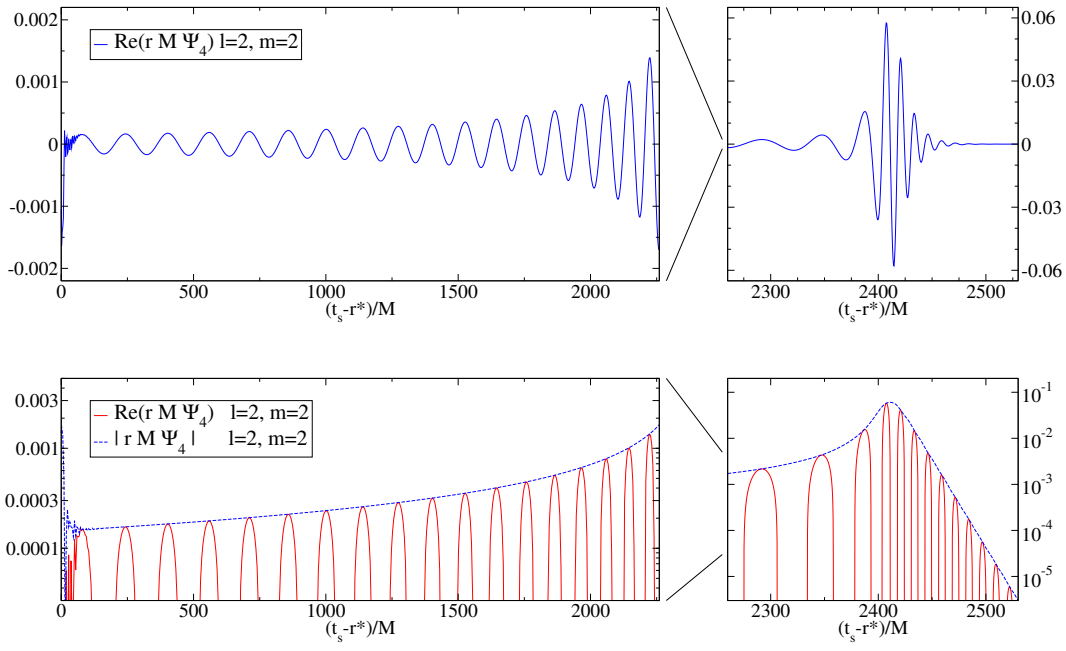

Figure 5.14: Final waveform, extrapolated to infinity. The top panels show the real part of Ψ_4^{22} with a linear y-axis, the bottom panels with a logarithmic y-axis. The right panels show an enlargement of merger and ringdown.

5.6 Discussion

We have presented the first spectral computation of a binary black hole inspiral, merger, and ringdown with spinning black holes, and find that we can achieve similar accuracy for the final mass, final spin, and gravitational waveforms as in the nonspinning case [60]. For initial spins of $\chi = 0.43757 \pm 0.00001$, the mass and spin of the final hole are $M_f/M = 0.961109 \pm 0.000003$ and $\chi_f = 0.54781 \pm 0.00001$. The uncertainties are based on comparing runs at our highest two resolutions, and do not take into account systematic errors (e.g., the presence of a finite outer boundary or gauge effects). Note that for the nonspinning case [60], we found that changing the outer boundary location produced a smaller effect on the final mass and spin than changing the resolution, and that the outer boundary for the evolutions presented here is more distant (at late times, when most of the radiation passes through the boundary) than it was in Ref. [60]. The uncertainties in the gravitational waveforms are $\lesssim$0.01 radians in phase and $\lesssim$0.6 percent in amplitude (when waveforms are time and phase shifted). These uncertainties are based on comparisons between our two highest resolution runs and comparisons between different methods of extrapolating

waveforms to infinite extraction radius.

The methods used here to simulate plunge and ringdown are similar to those in Ref. [60]. The primary disadvantage of these methods is that they require fine tuning during the plunge (section 5.3.4). For example, the function $g(x,t)$ defined in Eq. (5.12) must be chosen carefully or else the simulation fails shortly (a few M) before a common horizon forms. There are at least two reasons that fine tuning is currently necessary. First, the gauge conditions must be chosen so that no coordinate singularities occur before merger. Second, the excision boundaries do not coincide with the apparent horizons, but instead they lie somewhat inside the horizons. If the excision boundaries exactly followed the horizons, then the characteristic fields of the system would be guaranteed to be outflowing (into the holes) at the excision boundaries, so that no boundary condition is required there. But for excision boundaries inside the horizons, the outflow condition depends on the location of the excision boundary, its motion with respect to the horizon, and the gauge. Indeed, the most common mode of failure for improperly tuned gauge parameters is that the outflow condition fails at some point on one of the excision boundaries. We have been working on improved gauge conditions [92] and on improved algorithms for allowing the excision boundary to more closely track the apparent horizon. These and other improvements greatly reduce the amount of necessary fine tuning and allow mergers in generic configurations, and will be described in detail elsewhere [93].

Another quite important improvement lies in the choice of constraint damping parameters. To illustrate this effect, Fig. 5.15 compares the gravitational wave phase extrapolation for the simulation presented here with the similar plot for an earlier run [9] with different constraint damping parameters. As can be seen in Fig. 5.15, the improved constraint damping parameters result in significantly reduced noise. For the earlier simulation, the waveform was unusable for $t-r^* < 1000M$, and was still noticeably noisy at $1000M < t-r^* < 2000M$. For the new simulation, the smaller constraint damping parameters result in clean waveforms as early as $t - r^* \sim 250M$, despite the observation that the spinning black holes result in a pulse of junk radiation of about twice the amplitude of the earlier run. The new simulation also shows smaller extrapolation errors, presumably because the new simulation uses larger extraction radii (up to $r = 350M$, whereas Ref. [9] uses a largest extraction radius of $r = 240M$).

We employ four techniques to measure black hole spin: Two of these are based on the surface integral for quasi-local linear momentum, and utilize either simple coordinate rotation vectors $\chi_{\rm Coord}(t)$ or approximate Killing vectors, $\chi_{\rm AKV}(t)$; the other two are based

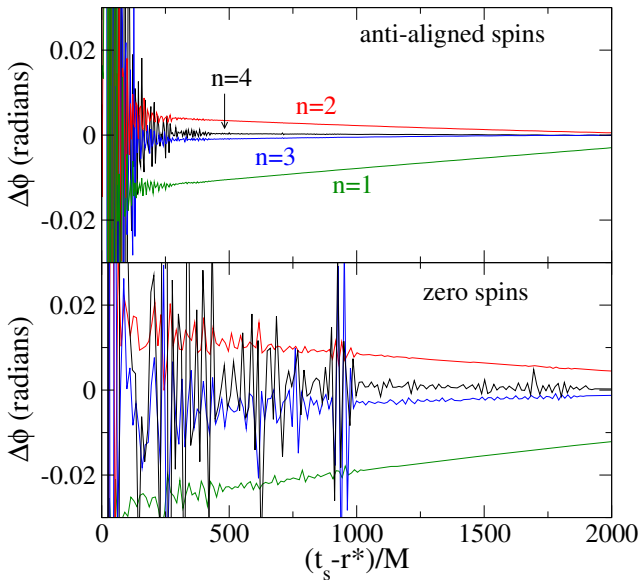

Figure 5.15: Comparison of waveform extrapolation between the current simulation of counter-rotating black holes (top panel), and the earlier simulation of nonspinning black holes [9, 60]. The noise is significantly reduced in the newer simulation, due to smaller constraint damping parameters in the wave zone.

on the shape of the apparent horizon, and infer the spin from the extrema of the scalar curvature ($\chi_{\rm SC}^{\rm min}(t)$, $\chi_{\rm SC}^{\rm max}(t)$). The four spin measures agree to better than 1 per cent during the inspiral. The AKV spin $\chi_{\rm AKV}(t)$ shows the least variations during the simulation, and is the only spin diagnostic that results in a monotonically decreasing spin during the inspiral, as expected from the effects of tidal friction. These results may be compared with those that can be found from tidal multipole moments (e.g., [99, 100, 101]), which we defer to future work. The other three spin measures ($\chi_{\rm coord}(t)$, $\chi_{\rm SC}^{\rm max}(t)$, $\chi_{\rm SC}^{\rm min}(t)$) show various undesired and physically unreasonable behaviors: All three result in *increasing* spin during the inspiral, inconsistent with tidal friction (cf. Fig. 5.4). $\chi_{\rm SC}^{\rm min}(t)$ and $\chi_{\rm SC}^{\rm max}(t)$, furthermore show very strong variations during the initial transients, just before merger, and just after the common horizon forms. This is expected, as in those regions of the evolution, the black holes can not be approximated as isolated Kerr black holes. The behavior of $\chi_{\rm SC}^{\rm min}(t)$ and $\chi_{\rm SC}^{\rm max}(t)$ contain information about the deformation of the black holes. The final state of the simulation is expected to be a single, stationary Kerr black hole, for which $\chi_{\rm SC}^{\rm min}(t)$ and $\chi_{\rm SC}^{\rm max}(t)$ should result in the correct spin. Indeed, all four spin diagnostics agree at very late time to five significant digits (cf. Fig. 5.6). The accuracy of our simulation places new constraints on analytic formulae that predict the final black hole spin from the initial spins and masses of a black hole binary. Table 5.3 lists some of these predictions.

Prediction Formula	χ_f	M_f/M
Kesden [94]	0.521153	0.97039
Buonanno, Kidder & Lehner [95]	0.505148	1.0
Tichy & Marronetti [96]	0.548602	0.962877
Boyle & Kesden [97]	0.547562	0.964034
Barausse & Rezzolla [98]	0.546787	1.0
Numerical result (this work)	0.54781	0.961109

Table 5.3: Predictions of final black hole spin and mass from analytical formulae in the literature, applied to the simulation considered here. Refs. [95, 98] do not predict the final mass, but instead assume zero mass loss.

5.7 Appendix: Spins aligned with the orbital angular momentum

The corresponding simulations in which both spins are aligned with the orbital angular momentum were completed after the publication of the work in the main text. Their properties and main results are given here. Since the techniques involved were very similar to the anti-aligned case, with the exception of the plunge evolutions, only this part of the simulations will be described in more detail. Some properties of the initial data and evolution are summarized in Table 5.4. The simulations are performed at three different resolutions, N2 to N4. The approximate number of collocation points and CPU usage for these simulations are given in Table 5.5. Key results are presented in the subsections below.

5.7.1 Plunge evolutions

During the plunge, we follow the procedure described in [93]. At some time $t = t_g$ after the inspiral, we switch to a grid structure of nonoverlapping subdomains, consisting of spherical shells around each hole that are surrounded by rectangular blocks and cubed-spheres. This new grid structure is found to remove numerical instabilities. At the same time, we transition smoothly to the damped harmonic gauge condition, by setting

$$H_a(t) = \tilde{H}_a(t) e^{-(t-t_g)^4/\sigma_g^4} + \mu_L \log\left(\frac{\sqrt{g}}{N}\right) t_a - \mu_S N^{-1} g_{ai} N^i, \tag{5.28}$$

Initial data	
Coordinate separation	$d/M_{\rm ID} = 13.365688$
Radius of excision spheres	$r_{\rm exc}/M_{\rm ID} = 0.382927$
Orbital frequency	$\Omega_0 M_{\rm ID} = 0.0185056$
Radial velocity	$v_r = -3.3287494 \times 10^{-4}$
Orbital frequency of horizons	$\Omega_r M_{\rm ID} = 0.207068$
Black hole spins	$\chi_{\rm ID} = 0.436823$
ADM energy	$M_{\rm ADM}/M_{\rm ID} = 0.992040$
Total angular momentum	$J_{\rm ADM}/M_{\rm ID}^2 = 1.25728$
Initial proper separation	$s_0/M_{\rm ID} = 16.361686$
Evolution	
Initial orbital eccentricity	$e \approx 2 \times 10^{-5}$
Mass after relaxation	$M = (1.000270 \pm 0.000001) M_{\rm ID}$
Spins after relaxation	$\chi = 0.43655 \pm 0.00001$
Time of merger (common AH)	$t_{\rm CAH} = 3360.18M$
Final mass	$M_f = (0.9358 \pm 0.0002)M$
Final spin	$\chi_f = 0.814 \pm 0.001$

Table 5.4: Summary of the simulation with aligned spins presented in this work. The first block lists properties of the initial data, the second block lists properties of the evolution.

Run	N_{pts}	CPU-h	CPU-h/T
N2	$(70^3, 77^3, 61^3)$	19,609	7.8
N3	$(76^3, 84^3, 69^3)$	33,417	14.4
N4	$(82^3, 90^3, 77^3)$	58,379	23.3

Table 5.5: Approximate number of collocation points and CPU usage for the evolutions with aligned spins. The first column indicates the name of the run. N_{pts} is the approximate number of collocation points used to cover the entire computational domain. The three values for N_{pts} are those for the inspiral, plunge, and ringdown portions of the simulation. The total run times T are in units of the total Christodoulou mass M of the binary.

where $\tilde{H}_a(t)$ is the value of the gauge source function during the inspiral and $\sigma_g = 50M$. The damping parameters are chosen to be $\mu_L = \mu_S = \mu_0 \left[\log\left(\frac{\sqrt{g}}{N}\right)\right]^2$, where

$$\mu_0 = \begin{cases} 0, & t < t_g \\ \left[1 - e^{(t-t_g)^2/\sigma_d^2}\right] e^{-r^4/\sigma_w^4}, & t > t_g \end{cases} \tag{5.29}$$

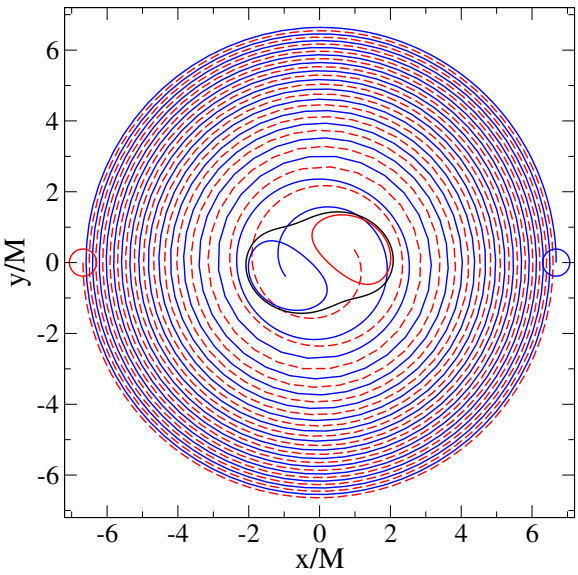

Figure 5.16: Coordinate trajectories of the centers of the apparent horizons represented by the blue and red curves, up until the formation of a common horizon. The closed curves show the coordinate shapes of the corresponding apparent horizons.

with $\sigma_d = 125M$ and $\sigma_w = 60M$. For all resolutions, $t_g = 3256M$.

The coordinate trajectories of the apparent horizon centers are shown in Fig. 5.16, up until the formation of a common horizon at time $t_{\rm CAH} = 3360.18M$. The coordinate shapes of the horizons are also shown at $t = 0$ and $t = t_{\rm CAH}$. The binary goes through 15.6 orbits before merger.

5.7.2 Constraints

The constraints are shown in Fig. 5.17 for the evolutions at different resolutions. The top panel shows the L^2 norm of all the constraint fields of our first-order generalized harmonic system, normalized by the L^2 norm of the spatial griadients of the dynamical fields. The bottom panel shows the same quantity, but without the normalization factor. The L^2 norms are taken over the computational volume that lies outside the apparent horizons. The transition to a single-hole evolution occurs at $t_m = 3360.39M$ for N4 ($t_m = 3360.90M$ for N3, $t_m = 3361.43M$ for N2), at which point the interior of the common horizon is excised, causing the constraints to drop steeply.

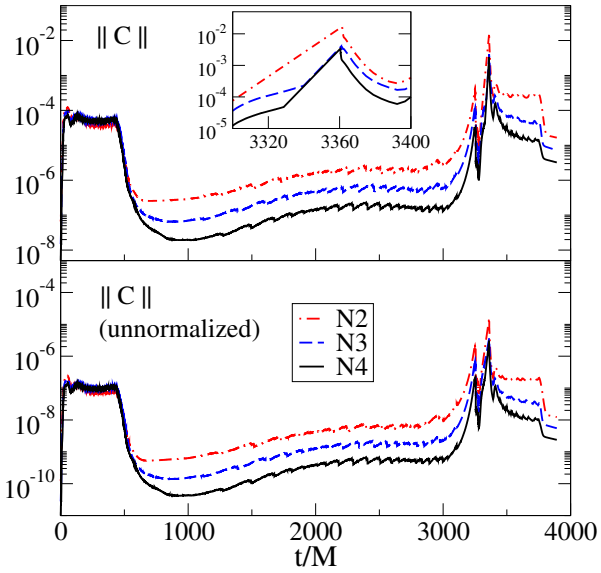

Figure 5.17: Constraint violations of runs on different resolutions. The top panel shows the L^2 norm of all constraints, normalized by the L^2 norm of the spatial gradients of all dynamical fields. The bottom panel shows the same data, but without the normalization factor. The L^2 norms are taken over the portion of the computational volume that lies outside apparent horizons.

5.7.3 Black hole spins

The spin of one black hole in the N4 run during the inspiral and plunge are shown in Fig. 5.18, using the spin measures of section 5.4.2. The initial scalar curvature spins $\chi_{\rm SC}^{\rm min}(t)$ and $\chi_{\rm SC}^{\rm max}(t)$ are substantially different from the spin determined with approximate Killing vectors $\chi_{\rm AKV}(t)$, indicating the black hole's distortion relative to a Kerr black hole. After the black hole has relaxed in the evolution, all spin measures show reasonable agreement. Near merger, the black hole becomes highly distorted, resulting in unreliable values for $\chi_{\rm SC}^{\rm min}(t)$ and $\chi_{\rm SC}^{\rm max}(t)$. The black hole's spin should also decrease, and this behavior is consistently seen throughout the evolution only for $\chi_{\rm AKV}(t)$.

The spin of the merged black hole during the ringdown is shown in Fig. 5.19. Just after merger, the black hole is highly distorted so that $\chi_{\rm SC}^{\rm min}(t)$ and $\chi_{\rm SC}^{\rm max}(t)$ are not applicable. As the black hole settles down, all spin measures agree to about 1 part in 10^5. It should be noted though, that the uncertainty in the final spin χ_f as given in Table 5.4 is much larger than for the anti-aligned case given in Table 5.1. This uncertainty is not dominated by the difference in spin measures, but the difference in values between the N3 and N4 runs. This is likely due to the lower resolutions used in the ringdown evolutions (cf. Table 5.5)

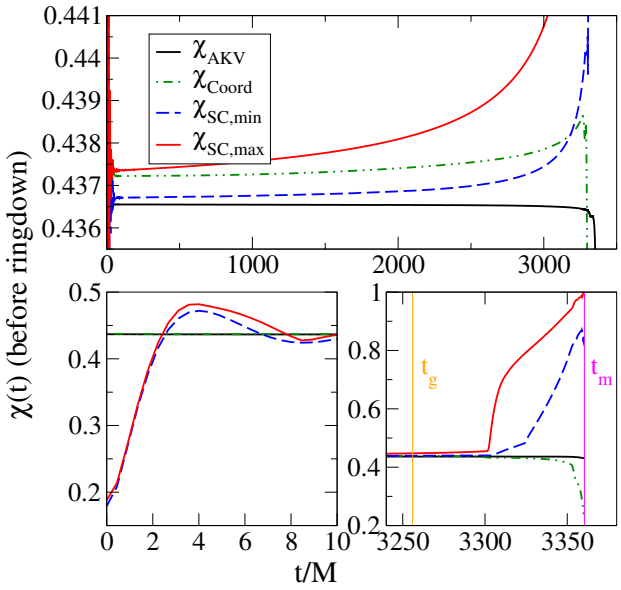

Figure 5.18: Dimensionless spins χ of one black hole in the N4 evolution, evaluated using an approximate Killing vector, a coordinate rotation vector ∂_ϕ, or the extrema of the instrinsic scalar curvature on the apparent horizon. Bottom panels show detail at early and late times. Also shown are the time of gauge change t_g before merger, and the time t_m that we transition to a single-hole evolution just after merger.

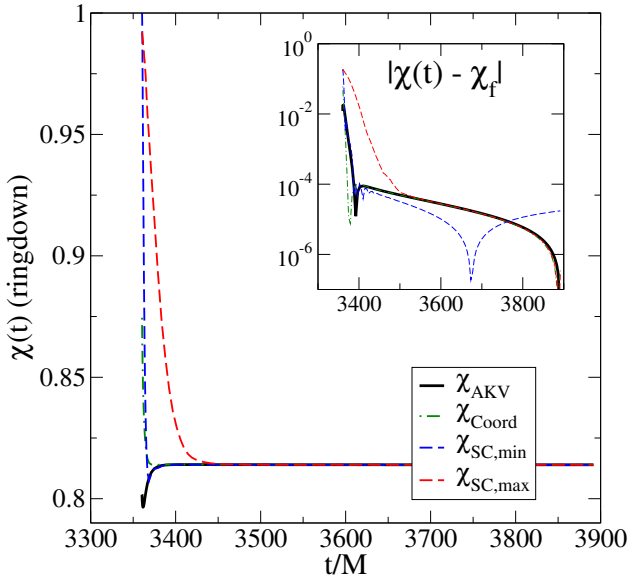

Figure 5.19: Dimensionless spins $\chi(t)$ of the final black hole in the N4 evolution. The (most reliable) spin diagnostic $\chi_{\rm AKV}$ starts at ~ 0.8 and increases to its final value $\chi_f = 0.814 \pm 0.001$. The other spin diagnostics are unreliable for the highly distorted black hole shortly after merger, but subsequently approach $\chi_{\rm AKV}$.

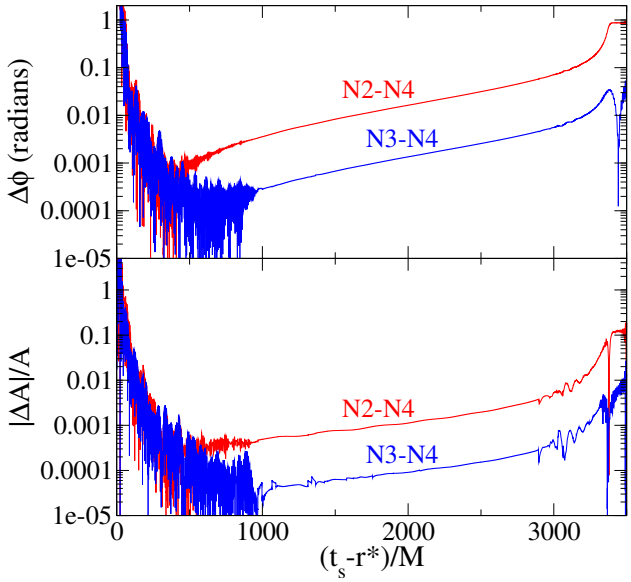

Figure 5.20: Convergence of gravitational waveforms with numerical resolution. Shown are phase and amplitude differences between numerical waveforms Ψ_4^{22} computed using different numerical resolutions. All waveforms are extrapolated to infinity with extrapolation order $n = 3$, and no time shifting or phase shifting is done to align waveforms.

relative to the anti-aligned case (cf. Table 5.2). The uncertainty in the final mass M_f is also dominated by the difference in values between the N3 and N4 runs.

5.7.4 Extrapolated waveforms

The waveforms from these simulations were extrapolated to infinity. The results here focus on the $(l, m) = (2, 2)$ mode. Figure 5.20 shows the convergence of the gravitational-wave phase ϕ and amplitude A with numerical resolution, for extrapolated waveforms using our preferred extrapolation polynomial of order $n = 3$. The top panel shows the absolute phase differences between the highest-resolution run N4 and the lower-resolutions runs, and similarly the bottom panel shows the relative amplitude differences. Also, no time shifting or phase shifting has been done to align waveforms. For the N3 run, the phase difference accumulated over 15.6 orbits is less than 0.1 radians, and the relative amplitude difference is less than 0.013. The numerical truncation errors of the N4 run are expected to be much smaller.

Figure 5.21 presents the final extrapolated waveform. There are 32 gravitational-wave cycles before the maximum of $|\Psi_4|$, and 12 gravitational-wave cycles during ringdown, over which the amplitude of $|\Psi_4|$ drops by four orders of magnitude.

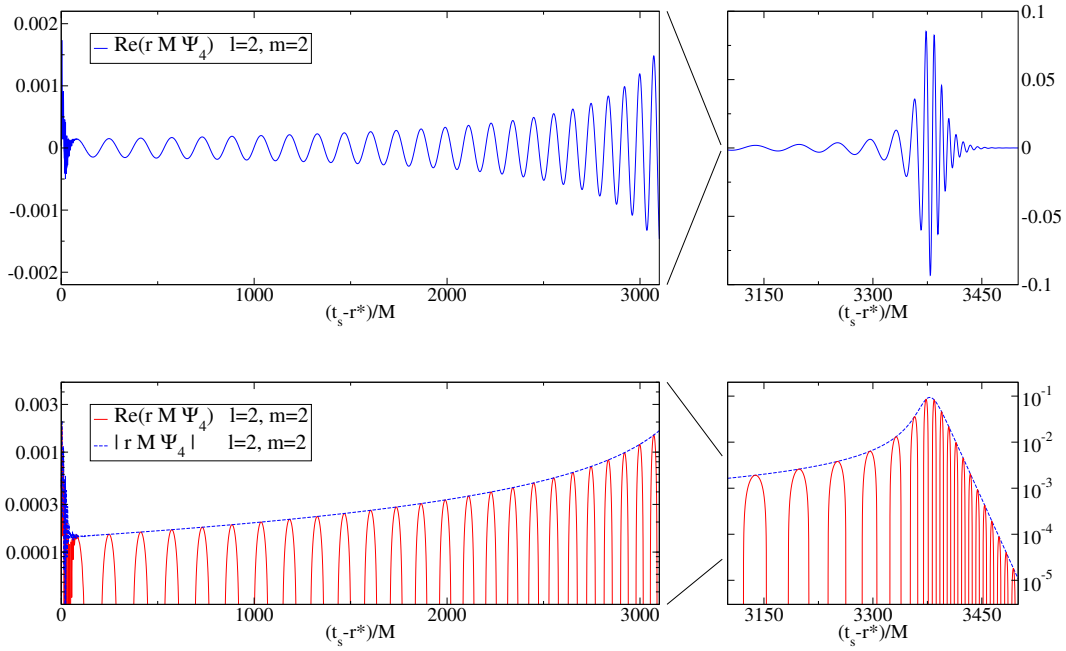

Figure 5.21: Final waveform, extrapolated to infinity. The top panels show the real part of Ψ_4^{22} with a linear y-axis, the bottom panels with a logarithmic y-axis. The right panels show an enlargement of merger and ringdown.

Bibliography

[1] F. Pretorius, Phys. Rev. Lett. **95**, 121101 (2005).

[2] M. Campanelli, C. O. Lousto, P. Marronetti, and Y. Zlochower, Phys. Rev. Lett. **96**, 111101 (2006).

[3] J. G. Baker, J. Centrella, D.-I. Choi, M. Koppitz, and J. van Meter, Phys. Rev. Lett. **96**, 111102 (2006).

[4] A. Buonanno, G. B. Cook, and F. Pretorius, Phys. Rev. D **75**, 124018 (2007).

[5] J. G. Baker, J. R. van Meter, S. T. McWilliams, J. Centrella, and B. J. Kelly, Phys. Rev. Lett. **99**, 181101 (2007).

[6] Y. Pan et al., Phys. Rev. D **77**, 024014 (2008).

[7] A. Buonanno et al., Phys. Rev. D **76**, 104049 (2007).

[8] M. Hannam, S. Husa, J. A. González, U. Sperhake, and B. Brügmann, Phys. Rev. D **77**, 044020 (2008).

[9] M. Boyle et al., Phys. Rev. D **76**, 124038 (2007).

[10] A. Gopakumar, M. Hannam, S. Husa, and B. Brügmann, Phys. Rev. D **78**, 064026 (2008).

[11] M. Hannam, S. Husa, B. Brügmann, and A. Gopakumar, Phys. Rev. D **78**, 104007 (2008).

[12] T. Damour, A. Nagar, E. N. Dorband, D. Pollney, and L. Rezzolla, Phys. Rev. D **77**, 084017 (2008).

[13] T. Damour and A. Nagar, Phys. Rev. D **77**, 024043 (2008).

[14] M. Boyle et al., Phys. Rev. D **78**, 104020 (2008).

[15] A. H. Mroué, L. E. Kidder, and S. A. Teukolsky, Phys. Rev. D **78**, 044004 (2008).

[16] I. Hinder, F. Herrmann, P. Laguna, and D. Shoemaker, Comparisons of eccentric binary black hole simulations with post-Newtonian models, arXiv:0806.1037 (gr-qc), 2008.

[17] T. Damour, A. Nagar, M. Hannam, S. Husa, and B. Brügmann, Phys. Rev. D **78**, 044039 (2008).

[18] T. Damour and A. Nagar, Phys. Rev. D **79**, 081503 (2009).

[19] A. Buonanno et al., Phys. Rev. D **79**, 124028 (2009).

[20] M. Campanelli, Class. Quantum Grav. **22**, S387 (2005).

[21] F. Herrmann, I. Hinder, D. Shoemaker, and P. Laguna, Class. Quantum Grav. **24**, S33 (2007).

[22] J. G. Baker et al., Astrophys. J. **653**, L93 (2006).

[23] J. A. González, U. Sperhake, B. Brügmann, M. Hannam, and S. Husa, Phys. Rev. Lett. **98**, 091101 (2007).

[24] M. Campanelli, C. O. Lousto, Y. Zlochower, and D. Merritt, Phys. Rev. Lett. **98**, 231102 (2007).

[25] J. A. Gonzalez, M. D. Hannam, U. Sperhake, B. Brügmann, and S. Husa, Phys. Rev. Lett. **98**, 231101 (2007).

[26] B. Brügmann, J. A. González, M. Hannam, S. Husa, and U. Sperhake, Phys. Rev. D **77**, 124047 (2008).

[27] F. Herrmann, I. Hinder, D. Shoemaker, P. Laguna, and R. A. Matzner, Astrophys. J. **661**, 430 (2007).

[28] F. Herrmann, I. Hinder, D. M. Shoemaker, P. Laguna, and R. A. Matzner, Phys. Rev. D **76**, 084032 (2007).

[29] D.-I. Choi et al., Phys. Rev. D **76**, 104026 (2007).

[30] J. G. Baker et al., Astrophys. J. **668**, 1140 (2007).

[31] W. Tichy and P. Marronetti, Phys. Rev. **D76**, 061502(R) (2007).

[32] J. D. Schnittman et al., Phys. Rev. D **77**, 044031 (2008).

[33] M. Campanelli, C. O. Lousto, Y. Zlochower, and D. Merritt, Astrophys. J. Lett. **659**, L5 (2007).

[34] M. Koppitz et al., Phys. Rev. Lett. **99**, 041102 (2007).

[35] S. H. Miller and R. Matzner, Gen. Rel. Grav. **41**, 525 (2009).

[36] J. G. Baker et al., Astrophys. J. **682**, L29 (2008).

[37] J. Healy et al., Phys. Rev. Lett. **102**, 041101 (2009).

[38] L. Rezzolla et al., Astrophys. J. **679**, 1422 (2008).

[39] M. Campanelli, C. O. Lousto, and Y. Zlochower, Phys. Rev. D **74**, 041501(R) (2006).

[40] M. Campanelli, C. O. Lousto, and Y. Zlochower, Phys. Rev. D **74**, 084023 (2006).

[41] M. Campanelli, C. O. Lousto, Y. Zlochower, B. Krishnan, and D. Merritt, Phys. Rev. D **75**, 064030 (2007).

[42] P. Marronetti, W. Tichy, B. Brügmann, J. González, and U. Sperhake, Phys. Rev. D **77**, 064010 (2008).

[43] E. Berti, V. Cardoso, J. A. Gonzalez, U. Sperhake, and B. Brügmann, Class. Quantum Grav. **25**, 114035 (2008).

[44] L. S. Finn, Phys. Rev. D **46**, 5236 (1992).

[45] S. Bonazzola, J. Frieben, E. Gourgoulhon, and J.-A. Marck, Spectral methods in general relativity – toward the simulation of 3D-gravitational collapse of neutron stars, in *ICOSAHOM'95, Proceedings of the Third International Conference on Spectral and High Order Methods*, edited by A. V. Ilin and L. R. Scott, pages 3–19, Houston, 1996, Houston Journal of Mathematics.

[46] S. Bonazzola, E. Gourgoulhon, and J.-A. Marck, Phys. Rev. Lett. **82**, 892 (1999).

[47] P. Grandclément, S. Bonazzola, E. Gourgoulhon, and J.-A. Marck, J. Comp. Phys. **170**, 231 (2001).

[48] E. Gourgoulhon, P. Grandclément, and S. Bonazzola, Phys. Rev. D **65**, 044020 (2002).

[49] P. Grandclément, E. Gourgoulhon, and S. Bonazzola, Phys. Rev. D **65**, 044021 (2002).

[50] H. P. Pfeiffer, G. B. Cook, and S. A. Teukolsky, Phys. Rev. D **66**, 024047 (2002).

[51] H. P. Pfeiffer, L. E. Kidder, M. A. Scheel, and S. A. Teukolsky, Comput. Phys. Commun. **152**, 253 (2003).

[52] G. B. Cook and H. P. Pfeiffer, Phys. Rev. D **70**, 104016 (2004).

[53] M. Ansorg, B. Brügmann, and W. Tichy, Phys. Rev. D **70**, 064011 (2004).

[54] M. Ansorg, Phys. Rev. D **72**, 024018 (2005).

[55] M. Caudill, G. B. Cook, J. D. Grigsby, and H. P. Pfeiffer, Phys. Rev. D **74**, 064011 (2006).

[56] P. Grandclément, Phys. Rev. D **74**, 124002 (2006).

[57] G. Lovelace, R. Owen, H. P. Pfeiffer, and T. Chu, Phys. Rev. D **78**, 084017 (2008).

[58] F. Foucart, L. E. Kidder, H. P. Pfeiffer, and S. A. Teukolsky, Phys. Rev. D **77**, 124051 (2008).

[59] L. T. Buchman, H. P. Pfeiffer, and J. M. Bardeen, Phys. Rev. D **80**, 084024 (2009).

[60] M. Scheel, M. Boyle, T. Chu, L. Kidder, K. Matthews and H. Pfeiffer, Phys. Rev. D **79**, 024003 (2009).

[61] D. Pollney et al., Phys. Rev. **D76**, 124002 (2007).

[62] G. B. Cook, Phys. Rev. D **65**, 084003 (2002).

[63] J. W. York, Phys. Rev. Lett. **82**, 1350 (1999).

[64] H. P. Pfeiffer and J. W. York, Phys. Rev. D **67**, 044022 (2003).

[65] H. P. Pfeiffer et al., Class. Quantum Grav. **24**, S59 (2007).

[66] J. D. Brown and J. W. York, Phys. Rev. D **47**, 1407 (1993).

[67] A. Ashtekar and B. Krishnan, Living Rev. Rel. **7** (2004), 10.

[68] R. Owen, *Topics in Numerical Relativity: The periodic standing-wave approximation, the stability of constraints in free evolution, and the spin of dynamical black holes*, PhD thesis, California Institute of Technology, 2007.

[69] O. Dreyer, B. Krishnan, D. Shoemaker, and E. Schnetter, Phys. Rev. D **67**, 024018 (2003).

[70] G. B. Cook and B. F. Whiting, Phys. Rev. D **76**, 041501(R) (2007).

[71] L. Lindblom, M. A. Scheel, L. E. Kidder, R. Owen, and O. Rinne, Class. Quantum Grav. **23**, S447 (2006).

[72] H. Friedrich, Commun. Math. Phys. **100**, 525 (1985).

[73] D. Garfinkle, Phys. Rev. D **65**, 044029 (2002).

[74] F. Pretorius, Class. Quantum Grav. **22**, 425 (2005).

[75] C. Gundlach, J. M. Martin-Garcia, G. Calabrese, and I. Hinder, Class. Quantum Grav. **22**, 3767 (2005).

[76] O. Rinne, Class. Quantum Grav. **23**, 6275 (2006).

[77] O. Rinne, L. Lindblom, and M. A. Scheel, Class. Quantum Grav. **24**, 4053 (2007).

[78] J. M. Stewart, Class. Quantum Grav. **15**, 2865 (1998).

[79] H. Friedrich and G. Nagy, Commun. Math. Phys. **201**, 619 (1999).

[80] J. M. Bardeen and L. T. Buchman, Phys. Rev. D **65**, 064037 (2002).

[81] B. Szilágyi, B. Schmidt, and J. Winicour, Phys. Rev. D **65**, 064015 (2002).

[82] G. Calabrese, J. Pullin, O. Reula, O. Sarbach, and M. Tiglio, Commun. Math. Phys. **240**, 377 (2003).

[83] B. Szilágyi and J. Winicour, Phys. Rev. D **68**, 041501(R) (2003).

[84] L. E. Kidder, L. Lindblom, M. A. Scheel, L. T. Buchman, and H. P. Pfeiffer, Phys. Rev. D **71**, 064020 (2005).

[85] L. T. Buchman and O. C. A. Sarbach, Class. Quantum Grav. **23**, 6709 (2006).

[86] L. T. Buchman and O. C. A. Sarbach, Class. Quantum Grav. **24**, S307 (2007).

[87] D. Gottlieb and J. S. Hesthaven, J. Comput. Appl. Math. **128**, 83 (2001).

[88] J. S. Hesthaven, Appl. Num. Math. **33**, 23 (2000).

[89] M. A. Scheel et al., Phys. Rev. D **74**, 104006 (2006).

[90] B. Brügmann et al., Phys. Rev. D **77**, 024027 (2008).

[91] M. Boyle, A.H. Mroué , Phys. Rev. D **80**, 124045 (2009).

[92] L. Lindblom and B. Szilágyi, Phys. Rev. D **80**, 084019 (2009).

[93] B. Szilagyi, L. Lindblom, and M. A. Scheel, Phys. Rev. D **80**, 124010 (2009).

[94] M. Kesden, Phys. Rev. D **78**, 084030 (2008).

[95] A. Buonanno, L. E. Kidder, and L. Lehner, Phys. Rev. D **77**, 026004 (2008).

[96] W. Tichy and P. Marronetti, Phys. Rev. D **78**, 081501(R) (2008).

[97] L. Boyle and M. Kesden, Phys. Rev. D **78**, 024017 (2008), arXiv:0712.2819 [astro-ph].

[98] E. Barausse and L. Rezzolla, Astrophys. J. Lett. **704**, L40 (2009).

[99] E. Poisson, Phys. Rev. D **70**, 084044 (2004).

[100] E. Poisson and I. Vlasov, (2009).

[101] N. Yunes and J. Gonzalez, Phys. Rev. D **73**, 024010 (2006).

Chapter 6

Effective-one-body waveforms calibrated to numerical relativity simulations: coalescence of nonprecessing, spinning, equal-mass black holes

We present the first attempt at calibrating the effective-one-body (EOB) model to accurate numerical-relativity simulations of spinning, nonprecessing black-hole binaries. Aligning the EOB and numerical waveforms at low frequency over a time interval of $1000M$, we first estimate the phase and amplitude errors in the numerical waveforms and then minimize the difference between numerical and EOB waveforms by calibrating a handful of EOB-adjustable parameters. In the equal-mass, spin aligned case, we find that phase and fractional amplitude differences between the numerical and EOB (2,2) mode can be reduced to 0.01 radians and 1%, respectively, over the entire inspiral waveforms. In the equal-mass, spin anti-aligned case, these differences can be reduced to 0.13 radians and 1% during inspiral and plunge, and to 0.4 radians and 10% during merger and ringdown. The waveform agreement is within numerical errors in the spin aligned case while slightly over numerical errors in the spin anti-aligned case. Using Enhanced LIGO and Advanced LIGO noise curves, we find that the overlap between the EOB and the numerical (2,2) mode, maximized over the initial phase and time of arrival, is larger than 0.999 for binaries with total mass 30–$200M_{\odot}$. In addition to the leading (2,2) mode, we compare four subleading modes. We find good amplitude and frequency agreements between the EOB and numerical modes for both spin configurations considered, except for the (3,2) mode

in the spin anti-aligned case. We believe that the larger difference in the (3,2) mode is due to the lack of knowledge of post-Newtonian spin effects in the higher modes.

Originally published as Y. Pan, A. Buonanno, L. T. Buchman, T. Chu, L. E. Kidder, H. P. Pfeiffer, and M. A. Scheel, Phys. Rev. D **81**, 084041 (2010).

6.1 Introduction

Coalescing black-hole binaries are among the most promising sources for the current and future laser-interferometer gravitational-wave detectors such as LIGO/Virgo [1, 2, 3] and LISA [4].

In general relativity, black holes are defined by their masses and spins alone; restricting ourselves to circular orbits [5], a black-hole binary depends on a total of eight parameters $(m_1, \boldsymbol{S}_1, m_2, \boldsymbol{S}_2)$. Hence, when black holes carry spins, it is expected that tens of thousands of waveform templates may be needed in order to extract the gravitational-wave signal from the noise using matched-filtering techniques. Considering the high computational cost of running numerical-relativity simulations of spinning binary black holes (tens of thousands of CPU hours for moderate spins and mild mass ratios) and the large binary parameter space, it will be impractical for numerical relativity alone to provide data analysts with a template bank. The work at the interface between analytical and numerical relativity [6, 7, 8, 9, 10, 11, 12, 13, 14, 15, 16, 17] has demonstrated the possibility of modeling analytically the dynamics and the gravitational-wave emission of coalescing *nonspinning* black holes, thus providing data analysts with preliminary analytical template families to be used for the searches. The next important step is to extend those studies to *spinning, precessing* black holes. This chapter represents the first attempt in this direction, although limited to *nonprecessing* waveforms, within the effective-one-body (EOB) formalism [18, 19, 20] of spinning black holes [21, 22]. Recently, Ref. [23] constructed a template family of spinning, nonprecessing black-hole binaries using a phenomenological approach, where the numerical-relativity waveforms are fitted to templates which resemble the post-Newtonian (PN) expansion [24, 25], but in which the coefficients predicted by PN theory are replaced by many arbitrary coefficients calibrated to numerical simulations.

The first EOB Hamiltonian that included spin effects was worked out in Ref. [21]. In Ref. [26], the authors used the nonspinning EOB Hamiltonian augmented with PN spin terms to carry out the first exploratory study of the dynamics and gravitational radiation of spinning black-hole binaries during inspiral, merger and ringdown. Subsequently, Ref. [22]

extended the EOB Hamiltonian of Ref. [21] to include next-to-leading-order spin-orbit couplings. In those descriptions, the effective particle is endowed not only with a mass μ, but also with a spin $\boldsymbol{\sigma}$. As a consequence, the effective particle interacts with the effective Kerr background (having spin $\boldsymbol{S}_{\rm Kerr}$) both via a geodesic-type interaction and via an additional spin-dependent interaction proportional to its spin $\boldsymbol{\sigma}$. The EOB Hamiltonian developed in Refs. [21, 22] (with nonspinning PN couplings through 3PN order) clarified several features of spinning two-body dynamics. However, as we shall discuss below, it is not straightforward to extend this Hamiltonian to include higher-order nonspinning PN couplings, such as the 4PN or 5PN adjustable parameters recently calibrated to numerical-relativity simulations [15, 16]. Moreover, the EOB Hamiltonian of Ref. [22], based on an *ad hoc* test-particle limit, does not reduce to the Hamiltonian of a spinning test particle in Kerr spacetime. More recently, Ref. [27] derived the canonical Hamiltonian of a spinning test particle in a generic curved spacetime at linear order in the particle spin. The construction of an improved EOB Hamiltonian based on the results of Ref. [27] is currently under development. Despite the limitations mentioned above, the EOB Hamiltonian of Ref. [22] is an excellent starting point for exploring the calibration of numerical-relativity waveforms of spinning black holes within the EOB formalism. Thus, we have used it in this first exploratory study, augmenting it with a few *adjustable* parameters that we shall calibrate to two numerical-relativity simulations. For the EOB nonconservative dynamics, we use the gravitational-wave energy flux which includes spin effects and which has been computed using the factorized multipolar waveforms of Refs. [28, 29].

The two numerical-relativity simulations we shall use describe the evolution of equal-mass, equal-spin, nonprecessing black-hole binaries. They are produced by the pseudospectral code SpEC of the Caltech-Cornell-CITA collaboration. In these two configurations, the spins are either aligned ("up-up" or UU) or anti-aligned ("down-down" or DD) with the orbital angular momentum, and have dimensionless magnitude $\chi_1 = \chi_2 = 0.43655$ for the UU configuration, and 0.43757 for the DD configuration. The UU simulation lasts for about 28 gravitational-wave cycles or until $t = 3250M$, and stops about three gravitational-wave cycles before merger. The DD simulation lasts for about 22 gravitational-wave cycles or until $t = 2500M$, and contains the full inspiral, merger, and ringdown waveform. Detailed information on the numerical simulation of the DD configuration can be found in Ref. [30].

For zero spin, the EOB-model considered here agrees with the waveform of the equal-mass nonspinning binary black hole [31] to a similar degree as the model constructed in our earlier work [16]. It differs from the model presented in [16] by its modeling of the energy

flux of gravitational-wave radiation.

This chapter is organized as follows. In section 6.2, we describe the spin EOB model adopted in this work, including its adjustable parameters. In section 6.3, we calibrate the spin EOB model to the numerical simulations, and discuss the impact of our results on data analysis. Finally, section 6.4 summarizes our main conclusions.

6.2 EOB model for spinning black-hole binaries

In this section, we describe the spin EOB model adopted in our study and its adjustable parameters. Henceforth we use natural units $G = c = 1$. We use m_i, $\boldsymbol{X}_i$, $\boldsymbol{P}_i$, and $\boldsymbol{S}_i$ to denote the mass, the position vector, the linear momentum vector, and the spin vector of the ith body. We work in the center-of-mass frame defined by $\boldsymbol{P}_1 + \boldsymbol{P}_2 = 0$. The two body system is described by the relative position $\boldsymbol{R} \equiv \boldsymbol{X} = \boldsymbol{X}_1 - \boldsymbol{X}_2$ and the relative linear momentum $\boldsymbol{P} \equiv \boldsymbol{P}_1 = -\boldsymbol{P}_2$. For convenience, we define reduced variables

$$\boldsymbol{r} \equiv \frac{\boldsymbol{R}}{M} \qquad \boldsymbol{p} \equiv \frac{\boldsymbol{P}}{\mu}\,, \tag{6.1}$$

where $M \equiv m_1 + m_2$ and $\mu \equiv m_1 m_2/(m_1 + m_2)$.

6.2.1 EOB conservative dynamics

Following Refs. [21, 22], we assume that the effective particle in the EOB description is endowed not only with a mass μ, but also with a spin $\boldsymbol{\sigma}$. As a consequence, the effective particle interacts with the effective Kerr background (having spin $\boldsymbol{S}_{\rm Kerr}$ and mass M) both via a geodesic-type interaction and via an additional spin-dependent interaction proportional to its spin $\boldsymbol{\sigma}$. We define the Kerr-like parameter a as $a \equiv S_{\rm Kerr}/M$, where $S_{\rm Kerr}$ denotes the modulus of the deformed-Kerr spin vector $\boldsymbol{S}_{\rm Kerr}$. Following Ref. [21], we write the effective Kerr contravariant metric components in a fixed Cartesian-like coordinate system. This is done by introducing

$$\begin{aligned} n^i \equiv \frac{X^i}{R}, \quad s^i \equiv \frac{S^i_{\rm Kerr}}{S_{\rm Kerr}}, \quad \cos\theta \equiv n^i s^j \delta_{ij}, \\ \rho \equiv \sqrt{R^2 + a^2\cos^2\theta}, \end{aligned} \tag{6.2}$$

and

$$\alpha \equiv (-g^{00}_{\rm eff})^{-1/2}, \quad \beta^i \equiv \frac{g^{0i}_{\rm eff}}{g^{00}_{\rm eff}}, \quad \gamma^{ij} \equiv g^{ij}_{\rm eff} - \frac{g^{0i}_{\rm eff}\, g^{0j}_{\rm eff}}{g^{00}_{\rm eff}}, \tag{6.3}$$

and writing the contravariant metric components as

$$g^{00}_{\rm eff} = -\frac{(R^2+a^2)^2 - a^2\,\Delta_t(R)\,\sin^2\theta}{\rho^2\,\Delta_t(R)}, \tag{6.4a}$$

$$g^{0i}_{\rm eff} = -\frac{a\,(R^2+a^2-\Delta_t(R))}{\rho^2\,\Delta_t(R)}(\boldsymbol{s}\times\boldsymbol{R})^i, \tag{6.4b}$$

$$g^{ij}_{\rm eff} = \frac{1}{\rho^2}\Big[\Delta_R(R)\,n^i\,n^j + R^2\,(\delta^{ij}-n^i n^j)\Big] - \frac{a^2}{\rho^2\,\Delta_t(R)}(\boldsymbol{s}\times\boldsymbol{R})^i(\boldsymbol{s}\times\boldsymbol{R})^j, \tag{6.4c}$$

where [1]

$$\Delta_t(R) = R^2\,P^n_m\left[A(R)+\frac{a^2}{R^2}\right], \tag{6.5a}$$

$$\Delta_R(R) = \frac{\Delta_t(R)}{D(R)}. \tag{6.5b}$$

The Taylor approximants to the coefficients $A(R)$ and $D(R)$ can be written as

$$A_k(r) = \sum_{i=0}^{k+1}\frac{a_i(\nu)}{r^i}, \tag{6.6a}$$

$$D_k(r) = \sum_{i=0}^{k}\frac{d_i(\nu)}{r^i}. \tag{6.6b}$$

The functions $A_k(r)$ and $D_k(r)$ all depend on the symmetric mass ratio $\nu\equiv\mu/M$ through the ν–dependent coefficients $a_i(\nu)$ and $d_i(\nu)$. These coefficients are currently known through 3PN order (i.e., up to $k=4$) and can be read off from Eqs. (47) and (48) in Ref. [14]. It is worth noticing that although through 3PN order the Padé approximant to the function $\Delta_t(R)$ of Eq. (6.5a) does not pose any problem [22], when including 4PN- and 5PN-order coefficients, the Padé approximant develops poles for several spin values a. In particular, poles are present at large separation when $a>0.7M$ and the 4PN- and 5PN-order coefficient a_5 and a_6 are included. [2] Those poles could be regularized by adding in $A_k(r)$ higher-order spin terms $a^2\,\tilde{a}_3(\nu)/r^5$, $a^2\,\tilde{a}_4(\nu)/r^6$ and choosing for the coefficients $\tilde{a}_3(1/4)$ and $\tilde{a}_4(1/4)$ large negative values (around -100). Since in this first exploratory study we investigate only numerical simulations of moderate spins, we do not include any regularization of the poles, and consider only the 4PN-order coefficient a_5. In the nonspinning case [10, 11, 15, 16], the coefficient a_5 plays an important role in improving the agreement between the EOB and

[1] We denote with P^n_m the operation of taking the (n,m)-Padé approximant.

[2] Poles also develop when only the 4PN-order coefficient a_5 is included and $a>0.96M$.

numerical waveforms. Here, we choose for a_5 the value obtained by taking the nonspinning limit of the spin EOB model and calibrating it to the equal-mass black-hole waveform of [31], following [16]. In this way, we obtain $a_5(1/4) = 1.775$; thus, a_5 is no longer an adjustable parameter in the spin EOB model.

In Eq. (6.5a), we choose $m = 1$ and $n = 4$ so that $\Delta_t(R)/R^2$ in the limit of $a \to 0$ reduces to the nonspinning $A(R)$ used in Refs. [10, 11, 15, 16], and we choose the same 3PN $D(R)$ function used in those references. Therefore, in the spin EOB model, we have

$$\frac{\Delta_t(R)}{R^2} = \frac{\mathrm{Num}(\Delta_t)}{\mathrm{Den}(\Delta_t)}\,, \tag{6.7}$$

$$D(r) = \frac{r^3}{r^3 + 6\,\nu r + 2\,\nu(26 - 3\,\nu)}\,, \tag{6.8}$$

with

$$\begin{aligned}\mathrm{Num}(\Delta_t) &= r^3\left[32 - 24\nu - 4a_4(\nu) - a_5(\nu) - (32 - 4\nu)\chi^2 + 6\chi^4\right] \\ &\quad + r^4[a_4(\nu) - 16 + 8\nu + 12\chi^2 - \chi^4]\,,\end{aligned} \tag{6.9}$$

and

$$\begin{aligned}\mathrm{Den}(\Delta_t) &= -a_4^2(\nu) - 8a_5(\nu) - 8a_4(\nu)\nu + 2a_5(\nu)\nu - 16\nu^2 + (4a_5(\nu) - 8a_4(\nu) - 8\nu^2)\chi^2 \\ &\quad + (2a_4(\nu) - 12\nu)\chi^4 - \chi^8 + r\left[-8a_4(\nu) - 4a_5(\nu) - 2a_4(\nu)\nu - 16\nu^2\right. \\ &\quad \left. + (a_5(\nu) - 16\nu)\chi^2 - 2\nu\chi^4 - 2\chi^6\right] + r^2\left[-4a_4(\nu) - 2a_5(\nu) - 16\nu\right. \\ &\quad \left. - a_4(\nu)\chi^2 - 4\chi^4 + \chi^6\right] + r^3\left[-2a_4(\nu) - a_5(\nu) - 8\nu - (8 - 4\nu)\chi^2 + 4\chi^4\right] \\ &\quad + r^4\left[-16 + a_4(\nu) + 8\nu + 12\chi^2 - \chi^4\right]\,,\end{aligned} \tag{6.10}$$

where $\chi \equiv a/M$ and $a_4(\nu) = \left(94/3 - 41/32\pi^2\right)\,\nu$. Making use of Eqs. (6.3) and (6.4), we can derive

$$\alpha = \rho\sqrt{\frac{\Delta_t(R)}{(R^2 + a^2)^2 - a^2\,\Delta_t(R)\,\sin^2\theta}}, \tag{6.11a}$$

$$\beta^i = \frac{a\,(R^2 + a^2 - \Delta_t(R))}{(R^2 + a^2)^2 - a^2\,\Delta_t(R)\,\sin^2\theta}(\boldsymbol{s} \times \boldsymbol{R})^i, \tag{6.11b}$$

$$\gamma^{ij} = g_{\mathrm{eff}}^{ij} + \frac{\beta^i\,\beta^j}{\alpha^2}. \tag{6.11c}$$

The EOB effective Hamiltonian reads [21, 22]

$$H_{\rm eff}(\boldsymbol{R},\boldsymbol{P},\boldsymbol{S}_1,\boldsymbol{S}_2) \quad = \quad H_{\rm eff\,Kerr}(\boldsymbol{R},\boldsymbol{P},\boldsymbol{S}_{\rm Kerr}) + H_{\rm eff\,part}(\boldsymbol{R},\boldsymbol{P},\boldsymbol{\sigma}), \tag{6.12}$$

and

$$\begin{aligned} H_{\rm eff\,Kerr}(\boldsymbol{R},\boldsymbol{P},\boldsymbol{S}_{\rm Kerr}) &= \beta^i P_i + \alpha\sqrt{\mu^2+\gamma^{ij}P_iP_j+Q_4}\,, \\ H_{\rm eff\,part}(\boldsymbol{R},\boldsymbol{P},\boldsymbol{\sigma}) &= \frac{R^2+a^2-\Delta_t(R)}{(R^2+a^2)^2-a^2\,\Delta_t(R)\,\sin^2\theta}\,\boldsymbol{L}\cdot\boldsymbol{\sigma}, \end{aligned} \tag{6.13}$$

where $Q_4(P_i)$ is a quartic-momentum term at 3PN order independent of spins [20] and $\boldsymbol{L}\equiv\boldsymbol{R}\times\boldsymbol{P}$ is the orbital angular momentum. In this work, as a first attempt, we use the same spin coupling for the spin $\boldsymbol{\sigma}$ suggested in Ref. [22], even though it does not reduce to the spinning test-particle limit [27] at PN orders higher than 2.5PN.

In order for $H_{\rm eff}$ to match the PN-expanded spin-orbit Hamiltonian through 2.5PN order, we need to require that the sum of the spin-orbit couplings of $H_{\rm eff\,Kerr}$ and $H_{\rm eff\,part}$ gives

$$[H_{\rm eff\,Kerr}+H_{\rm eff\,part}]_{\rm SO} \simeq \frac{2}{R^3}\mathbf{L}\cdot\Big(\frac{1}{2}g_S^{\rm eff}\boldsymbol{S}+\frac{1}{2}g_{S^*}^{\rm eff}\boldsymbol{S}^*\Big), \tag{6.14}$$

where

$$\boldsymbol{S} \equiv \mathbf{S}_1+\mathbf{S}_2\,, \tag{6.15a}$$

$$\boldsymbol{S}_* \equiv \frac{m_2}{m_1}\mathbf{S}_1+\frac{m_1}{m_2}\mathbf{S}_2\,, \tag{6.15b}$$

and where the two effective gyro-gravitomagnetic ratios $g_S^{\rm eff}$ and $g_{S^*}^{\rm eff}$ read [22]

$$g_S^{\rm eff} \equiv 2+\left[\frac{3}{8}\nu+a(\nu)\right]\mathbf{p}^2-\left[\frac{9}{2}\nu+3a(\nu)\right](\mathbf{n}\cdot\mathbf{p})^2-[\nu+a(\nu)]\,\frac{1}{r}, \tag{6.16a}$$

$$g_{S^*}^{\rm eff} \equiv \frac{3}{2}+\left[-\frac{5}{8}+\frac{1}{2}\nu+b(\nu)\right]\mathbf{p}^2-\left[\frac{15}{4}\nu+3b(\nu)\right](\mathbf{n}\cdot\mathbf{p})^2-\left[\frac{1}{2}+\frac{5}{4}\nu+b(\nu)\right]\frac{1}{r}. \tag{6.16b}$$

Here $a(\nu)$ and $b(\nu)$ are two *gauge* parameters related to the freedom of applying a canonical transformation involving spin variables. If we knew the exact Hamiltonian, the choice of these parameters should not affect the physics of the EOB model. However, since we start with an approximate Hamiltonian that reproduces the spin-orbit couplings only through 2.5PN order, we expect the EOB model to depend on the choice of $a(\nu)$ and $b(\nu)$. Con-

sidering the structure of the gyro-gravitomagnetic ratios, such dependence should start at 3.5PN order as a spin-orbit coupling term. Because of this dependence, $a(\nu)$ and $b(\nu)$ can be used as adjustable parameters.

Moreover, in order for $H_{\rm eff}$ to match the PN-expanded spin-spin Hamiltonian through 2PN order, the simplest choice is to require that the Kerr spin [22]

$$\boldsymbol{S}_{\rm Kerr} = \boldsymbol{S} + \boldsymbol{S}_* \,. \tag{6.17}$$

As a consequence, Eq. (6.14) implies

$$\sigma = \frac{1}{2}(g_S^{\rm eff} - 2)\boldsymbol{S} + \frac{1}{2}(g_{S^*}^{\rm eff} - 2)\boldsymbol{S}^* \,. \tag{6.18}$$

To include higher-order spin-spin contributions in the EOB effective Hamiltonian, we introduce a 3PN spin-spin term whose coefficient $a_{\rm SS}^{\rm 3PN}$ is currently unknown and can be used as an adjustable parameter

$$\begin{aligned} H_{\rm eff}(\boldsymbol{R},\boldsymbol{P},\boldsymbol{S}_1,\boldsymbol{S}_2) &= H_{\rm eff\,Kerr}(\boldsymbol{R},\boldsymbol{P},\boldsymbol{S}_{\rm Kerr}) \\ &+ H_{\rm eff\,part}(\boldsymbol{R},\boldsymbol{P},\boldsymbol{\sigma}) \\ &+ a_{\rm SS}^{\rm 3PN}\nu\,\frac{\boldsymbol{S}_{\rm Kerr}\cdot\boldsymbol{S}^*}{R^4} \,. \end{aligned} \tag{6.19}$$

Finally, the EOB Hamiltonian is

$$H_{\rm real} = Mc^2\sqrt{1 + 2\nu\Big(\frac{H_{\rm eff}}{\mu c^2} - 1\Big)}. \tag{6.20}$$

In summary, in this first exploratory study, we choose to employ only two adjustable parameters:[3] $b(\nu)$ which introduces a spin-orbit term at 3.5PN order, and $a_{\rm SS}^{\rm 3PN}$ which introduces a 3PN spin-spin term. As we shall see, these two adjustable parameters are sufficient to reduce the phase and amplitude differences between EOB and numerical waveforms of the UU and DD configurations to (almost) the numerical error. The remaining flexibility of the spin EOB model can be exploited in the future when numerical relativity simulations of other spin configurations will become available. Thus, for the rest of the chapter, we set $a(\nu)$ in Eq. (6.16a) to zero.

Within the Hamiltonian approach, radiation-reaction effects can be incorporated into

[3] We find that $b(\nu)$ is strongly degenerate with $a(\nu)$.

the dynamics in the following way [19, 26]:

$$\frac{dX^i}{dt} = \{X^i, H_{\rm real}\} = \frac{\partial H_{\rm real}}{\partial P_i}\,, \tag{6.21}$$

$$\frac{dP_i}{dt} = \{P_i, H_{\rm real}\} + F_i = -\frac{\partial H_{\rm real}}{\partial X^i} + F_i\,. \tag{6.22}$$

Here, F_i denotes the nonconservative force, which is added to the evolution equation of the (relative) momentum to take into account radiation-reaction effects. Following Ref. [26], we use[4]

$$F_i = \frac{1}{\Omega\,|\boldsymbol{L}|}\,\frac{dE}{dt}\,P_i\,, \tag{6.23}$$

where Ω is the orbital frequency and $\boldsymbol{L}$ is the orbital angular momentum. The gravitational-wave energy flux dE/dt is obtained by summing over the gravitational-wave modes (l, m) as

$$\frac{dE}{dt} = \frac{1}{16\pi}\sum_{\ell=2}^{8}\sum_{m=-\ell}^{\ell}\left|\dot{h}_{\ell m}\right|^2\,, \tag{6.24}$$

which reduces to the following expression for circular equatorial orbits in the adiabatic approximation:

$$\frac{dE}{dt} = \frac{1}{16\pi}\sum_{\ell=2}^{8}\sum_{m=-\ell}^{\ell}(m\,\hat{\Omega})^2\,|h_{\ell m}|^2\,, \tag{6.25}$$

where $\hat{\Omega}$ is the reduced orbital frequency $\hat{\Omega} \equiv M\Omega$. We shall define the EOB waveforms $h_{\ell m}$ in section 6.2.3. The equations of motion for the spins are simply obtained through the equations

$$\frac{d}{dt}\boldsymbol{S}_1 = \{\boldsymbol{S}_1, H_{\rm real}\} = \frac{\partial H_{\rm real}}{\partial \boldsymbol{S}_1}\times\boldsymbol{S}_1\,, \tag{6.26}$$

$$\frac{d}{dt}\boldsymbol{S}_2 = \{\boldsymbol{S}_2, H_{\rm real}\} = \frac{\partial H_{\rm real}}{\partial \boldsymbol{S}_2}\times\boldsymbol{S}_2\,. \tag{6.27}$$

In the nonspinning case, it is useful [32, 16] to replace the radial momentum P_R with P_{R^*}, the conjugate momentum of the EOB *tortoise* radial coordinate R^*: $dR^*/dR = \sqrt{D}/A$. This replacement improves the numerical stability of the EOB equations of motion because P_R diverges when approaching the zero of $A(r)$ (the EOB event horizon) but P_{R^*} does not. Therefore, in the spinning EOB Hamiltonian, we similarly choose to use the conjugate

[4] We notice that this choice of the radiation-reaction force introduces a radial component of the force $\boldsymbol{R}\cdot\boldsymbol{F} \propto \boldsymbol{R}\cdot\boldsymbol{P} = R\,P_R$. In the nonspinning EOB models, this component is usually ignored [15, 16].

momentum to the tortoise radial coordinate of the ν-deformed Kerr geometry:

$$\frac{dR^*}{dR} = \frac{R^2 + a^2}{\sqrt{\Delta_t \, \Delta_R}} \equiv \frac{1}{\xi_a(R)} \, . \tag{6.28}$$

In the limit $a \to 0$, Eq. (6.28) reduces to the nonspinning EOB tortoise coordinate defined above. In the limit $\nu \to 0$, Eq. (6.28) reduces to the tortoise coordinate of the Kerr geometry: $dR^*/dR = (R^2 + a^2)/\Delta$. Since the EOB Hamiltonian and Hamilton equations are written in Cartesian coordinates, some algebra is needed to rewrite them to include this transform of the radial coordinate. In the appendix, we write down explicitly the transformed EOB Hamiltonian and Hamilton equations in Cartesian coordinates. In particular, Eqs. (6.21) and (6.22) should be replaced by Eqs. (6.40) and (6.41).

Initial conditions for the Hamilton equations are constructed following the prescription of Ref. [26], which provided postcircular initial data for quasi-spherical orbits when neglecting spin-spin and next-to-leading order spin-orbit effects. Note that exact circular orbits cease to exist in the conservative dynamics when spin-spin and next-to-leading order spin-orbit effects are present, except for special configurations in which the spins are aligned or antialigned with the orbital angular momentum. We start each evolution at a large initial separation of $50M$. The EOB trajectory is sufficiently circularized when reaching a separation of $\sim 16M$, where numerical waveforms start. In this way, we remove the residual eccentricity in the EOB trajectory due to imperfect initial conditions, while physical eccentricity due to spin effects is preserved.

As a final remark, the spin variable in the EOB model is the *constant* spin variable, i.e., its magnitude does not change during precession [33]. We identify it with the spin variable in the numerical simulation, which also remains constant during the evolution [30].

6.2.2 Characteristics of EOB orbits for spinning, nonprecessing black holes

Here we investigate certain properties of the spin EOB Hamiltonian that are crucial when building the complete EOB model. Specifically, we check the existence and behavior of the innermost stable circular orbit (ISCO), the light ring (photon orbit) and the maximum of the EOB orbital frequency. This study is restricted to circular equatorial orbits in the spin aligned or anti-aligned cases. For convenience, we consider the EOB Hamiltonian written in spherical coordinates; we fix $\theta = \pi/2$ and set the conjugate momentum $P_\theta = 0$.

The ISCO position is obtained by solving $\partial H(R, P_{R^*} = 0, P_\Phi)/\partial R = 0, \partial^2 H(R, P_{R^*} =$

$0, P_\Phi)/\partial R^2 = 0$ where P_{R^*} and P_Φ are conjugate momenta of the tortoise radial coordinate R^* and the orbital phase Φ, respectively. In the nonspinning limit, we find the following ν-correction of the ISCO frequency relative to the Schwarzschild value,

$$\hat{\Omega}_{\rm ISCO} \quad = \quad 6^{-3/2}\left[1 + 0.9837\nu + 1.2543\nu^2 + 5.018\nu^3 + \mathcal{O}(\nu^4)\right], \tag{6.29}$$

where $\mathcal{O}(\nu^4)$ terms contribute less than 1% to the correction. In the test-particle limit, the coefficient of the linear ν-correction term, 0.9837, should be compared to the recently available self-force result [34] (transformed to the gauge condition and mass convention used in the EOB formalism by Ref. [35]) of 1.2513. The relative difference of 21% is due to the fact that our nonspinning EOB Hamiltonian, although calibrated to equal-mass numerical simulations, does not capture all the ν-dependence correctly at 4PN order.[5] The improved spin EOB Hamiltonian [36] will incorporate consistently the self-force result (e.g., Ref. [35]) and can be better constrained by new numerical simulations.

In the spin aligned or anti-aligned case, we find that the ISCO exists for all spin magnitudes. However, in the spin aligned case, when $a > 0.8M$, the ISCO radius (frequency) starts to increase (decrease) with increasing a. This is contrary to the monotonic dependence of the ISCO radius (frequency) on the spin magnitude in the test-particle limit. This unusual behaviour will be overcome by the improved spin EOB Hamiltonian of Ref. [36]. Nevertheless, since this problem occurs only at extreme spin magnitudes and here we have numerical waveforms of moderate spins ($|a| < 0.5M$), we choose to use this spin EOB Hamiltonian in the current calibration.

The light ring is the unstable circular orbit of a massless particle (such as a photon) and can be computed from the deformed EOB metric or from $H_{\rm eff\,Kerr}(\boldsymbol{R}, \boldsymbol{P}, \boldsymbol{S}_{\rm Kerr})$. As in the nonspinning case, we do find a light ring with our spin EOB Hamiltonian. However, in contrast to the nonspinning case, for several values of the spin parameters (including the DD configuration) our spin EOB Hamiltonian does not yield a maximum orbital frequency. It is worth mentioning that if we were using only the "Kerr" part of the spin EOB Hamiltonian, i.e., we ignore $H_{\rm eff\,part}(\boldsymbol{R}, \boldsymbol{P}, \boldsymbol{\sigma})$, then we do find a maximum of the orbital frequency and its value is quite close to the light ring position. A more detailed study has revealed that the absence of the maximum of the orbital frequency for the full spin EOB Hamiltonian is due

[5] We notice that if we used the 4PN and 5PN coefficients, a_5 and a_6, suggested in Ref. [35], we would obtain poles in the function $\Delta_t(R)$ for $|a| > 0.75M$. Moreover, if we adopted the values of a_5 and a_6, suggested in Ref. [35] for the spin configurations analyzed in this work, for which there are no poles in $\Delta_t(R)$, we would obtain phase disagreements on the same order of the ones we have found.

to the spin-orbit coupling term $H_{\rm eff\,part}(\boldsymbol{R},\boldsymbol{P},\boldsymbol{\sigma})$ defined in Eq. (6.13), which as discussed above does not reduce to the test-particle limit prediction at PN orders higher than 2.5PN. In the improved spin EOB Hamiltonian [36], $H_{\rm eff\,part}(\boldsymbol{R},\boldsymbol{P},\boldsymbol{\sigma})$ will be consistent with the test-particle limit prediction at all PN orders linear in the particle spin. Analyses using the improved spin EOB Hamiltonian [36] have shown a reasonable agreement between the position of the EOB light ring and the maximum of the EOB orbital frequency.

Quite interestingly, when the numerical and EOB waveforms are aligned at low frequency, as discussed in detail in section 6.3.1, we find that the EOB light ring is reached at time $0.6M$ before the peak of the numerical h_{22} amplitude. Therefore, a nice property of the nonspinning EOB model [16, 15] holds also in the spinning case, i.e., the EOB light ring position is a good approximation of the peak position of the numerical h_{22} amplitude. The latter property will be a key ingredient in the EOB waveform model, as described later in section 6.2.4.

6.2.3 EOB waveform: Inspiral and Plunge

Having described the inspiral dynamics, we now turn to the gravitational waveforms $h_{\ell m}$. The latter can also be employed to compute consistently the inspiral dynamics through the radiation-reaction force [15]. In the nonspinning case, Refs. [15, 16] have shown that the resummed, factorized PN waveforms proposed in Ref. [29] are in excellent agreement with the numerical waveforms. In Ref. [28] we have generalized the resummed factorized waveforms to include spin effects.

The resummed waveforms are written as the product of five factors,

$$h_{\ell m} = h_{\ell m}^{(N,\epsilon)}\,\hat{S}_{\rm eff}^{(\epsilon)}\,T_{\ell m}\,e^{i\delta_{\ell m}}\,f_{\ell m}\,, \tag{6.30}$$

where ϵ denotes the parity of the multipolar waveform. In the circular-orbit case, ϵ is the parity of $\ell+m$: $\epsilon=\pi(\ell+m)$. These factors are discussed extensively in Ref. [29]. Here we simply write down the expressions used in our spin EOB model, valid for spins aligned or anti-aligned with the orbital angular momentum. Thus, we restrict ourselves to the equatorial plane ($\theta=\pi/2$ and $p_\theta=0$). The leading term $h_{\ell m}^{(N,\epsilon)}$ is the Newtonian contribution

$$h_{\ell m}^{(N,\epsilon)} = \frac{M\nu}{\mathcal{R}} n_{\ell m}^{(\epsilon)}\,c_{\ell+\epsilon}(\nu)\,v_\Phi^{(\ell+\epsilon)}\,Y^{\ell-\epsilon,-m}\left(\frac{\pi}{2},\Phi\right)\,, \tag{6.31}$$

where $\mathcal{R}$ is the distance from the source. The $n_{\ell m}^{(\epsilon)}$ and $c_{\ell+\epsilon}(\nu)$ are functions given in Eqs. (5)–(7) of Ref. [29]. The $Y^{\ell m}(\theta,\Phi)$ are the scalar spherical harmonics. The tangential

velocity v_Φ is the non-Keplerian velocity of a spherical orbit defined by $v_\Phi = r_\Omega \hat{\Omega}$ where

$$r_\Omega \equiv \hat{\Omega}_{\rm cir}^{-2/3} = \left(M \left. \frac{\partial H_{\rm eff}(P_R = 0)}{\partial P_\Phi} \right|_{P_\Phi = P_{\Phi,{\rm cir}}} \right)^{-2/3} , \tag{6.32}$$

and $P_{\Phi,{\rm cir}}$ is the solution of the spherical orbit condition $\partial H_{\rm eff}(R, P_R = 0, P_\Phi)/\partial R = 0$. As in the nonspinning case, the functions $\hat{S}^{(\epsilon)}_{\rm eff}$, $T_{\ell m}$, $e^{i\delta_{\ell m}}$ and $f_{\ell m}$ appearing in the right-hand side of Eq. (6.30) are computed using the Keplerian velocity $v = \hat{\Omega}^{1/3}$. Moreover, $\hat{S}^{(\epsilon)}_{\rm eff}$ is an effective source term that in the test-particle, circular-motion limit contains a pole at the EOB light ring. It is given in terms of the EOB dynamics as

$$\hat{S}^{(+)}_{\rm eff} = \hat{H}_{\rm eff} \qquad \hat{S}^{(-)}_{\rm eff} = \hat{L}_{\rm eff} \equiv |\boldsymbol{r} \times \boldsymbol{p}^*| \, . \tag{6.33}$$

Setting $\hat{S}^{(-)}_{\rm eff}$ to $|\boldsymbol{r} \times \boldsymbol{p}^*|$ in Eq. (6.33) is not the only possible choice; for example, one may instead choose $\hat{S}^{(-)}_{\rm eff}$ to be $\hat{H}_{\rm eff}$. The effect of this choice on the spin EOB model investigated in this work is marginal, since in the equal-mass, equal-spin, nonprecessing binary configurations, odd parity modes contribute only a tiny fraction of the total energy flux (see section 6.3.4 for details). Although we choose to use the source term defined in Eq. (6.33), there is no evidence indicating that this choice is better or worse than others for those binary configurations in which odd parity modes are more important.

The function $T_{\ell m}$ in the right hand side of Eq. (6.30) resums leading logarithms of tail effects, and $e^{i\delta_{\ell m}}$ is a phase correction due to subleading logarithms. Through 2PN order, there are no tail contributions due to spin effects and $T_{\ell m}$ and $e^{i\delta_{\ell m}}$ do not differ from the nonspinning case. Their explicit expressions are given in Eqs. (19)–(29) of Ref. [29]. Finally, the functions $f_{\ell m}$ in the right hand side of Eq. (6.30) collect the remaining PN terms. We computed [28] the spin terms in $f_{\ell m}$ by Taylor expanding the $h_{\ell m}$ in Eq. (6.30) and comparing it to the Taylor-expanded $h_{\ell m}$ calculated in PN theory, including the test-particle spin effects through 4PN order. In the test-particle limit, we choose $\boldsymbol{S}_{\rm Kerr}$ as the spin variable of the spacetime. Expressions of $f_{\ell m}$ can be read from Ref. [28].[6]

Following Refs. [29, 16], we resum all the nonspinning terms in $f_{\ell m}$ in the functional form $f^{\rm NS}_{\ell m} = (\rho_{\ell m})^\ell$ that holds at known PN orders, where $f^{\rm NS}_{\ell m}$ collects the nonspinning terms in $f_{\ell m}$, and $\rho_{\ell m}$ can be read from Appendix C of Ref. [29]. The motivation for this ρ-resummation is to reduce the magnitude of the 1PN coefficients in $f_{\ell m}$ that grow linearly

[6] For odd parity modes, depending on the choice of the source term among $\hat{H}_{\rm eff}$ and $\hat{L}_{\rm eff}$, the corresponding choice of $f_{\ell m}$ should be made among the expressions of $f^H_{\ell m}$ and $f^L_{\ell m}$.

with ℓ (see section IID of Ref. [29]). Since at leading order we did not find such dependence on ℓ in the spinning terms [28], we do not apply the ρ-resummation to them.

Furthermore, since we are trying to reproduce effects in the numerical simulations that go beyond the quasi-circular motion assumption, motivated by the PN expansion for generic orbits, we include nonquasicircular (NQC) effects in $h_{\ell m}$ in the form

$$h_{\ell m}^{\rm insp-plunge} \equiv {}^{\rm NQC}h_{\ell m} = \widehat{h}_{\ell m} \left[1 + a_1^{h_{\ell m}} \frac{p_{r^*}^2}{(r\,\hat{\Omega})^2} + a_2^{h_{\ell m}} \frac{p_{r^*}^2}{(r\,\hat{\Omega})^2}\frac{1}{r} + a_3^{h_{\ell m}} \frac{p_{r^*}^2}{(r\,\hat{\Omega})^2}\frac{1}{r^{3/2}} + a_4^{h_{\ell m}} \frac{p_{r^*}^2}{(r\,\hat{\Omega})^2}\frac{1}{r^2}\right] . \tag{6.34}$$

A similar expression was used in Ref. [16] except that there we used $\dot{r}$ instead of p_{r^*}. For a test-particle plunging in the Kerr geometry, $\dot{r}$ goes to zero at the horizon. We observe a similar behavior in the EOB ν-deformed Kerr geometry. Therefore, in contrast to the nonspinning case, the evolution of $\dot{r}$ is not monotonic during the inspiral-plunge: $\dot{r}$ increases during the inspiral, reaches a peak, and then starts decreasing during the plunge. By replacing $\dot{r}$ with p_{r^*}, we keep the NQC correction terms in Eq. (6.34) monotonic in time; thus, they can successfully model the monotonically increasing amplitude differences between the quasi-circular EOB and numerical waveforms. As in Ref. [16], we fix two of the four adjustable parameters $a_i^{h_{22}}$ by requiring that the peaks of the numerical and EOB h_{22} waveforms coincide in both time and amplitude, where the peak time of the numerical h_{22} waveform is accurately predicted by the EOB light ring, as discussed above. The other two $a_i^{h_{22}}$ parameters are determined by minimizing the overall amplitude difference with respect to the numerical waveform as explained in detail below. The NQC corrections in Eq. (6.34) also depend on spins. However, there is not enough numerical information in this work (we have only the DD configuration) to discriminate between the spinning and nonspinning contribution.

6.2.4 EOB waveform: Merger and Ringdown

The merger-ringdown waveform in the spin EOB model is built in the same way as in the nonspinning EOB model. Details on building merger-ringdown waveforms can be found in section IIC of Ref. [16]. Here we briefly summarize the key points.

In the spin EOB model, we model the ringdown waveform as a linear combination of

the eight quasinormal modes (QNMs) of the final Kerr black hole that correspond to ${}_{-2}Y^{22}$ with overtone numbers $0, \ldots, 7$. The ring-down waveforms can be accurately modeled with fewer QNM modes; we nevertheless choose to include all the eight QNMs whose frequency has been calculated [37] to improve the smoothness of the matching between merger and ring-down waveforms. Mass and spin of the final black hole are computed from numerical data. In particular, for the numerical simulation of the DD configuration, we use $M_{\rm BH}/M = 0.961109 \pm 0.000003$ and $a_{\rm BH}/M_{\rm BH} = 0.54781 \pm 0.00001$ computed in Ref. [30]. Frequencies of the QNMs are computed by interpolating data from Ref. [37]. The eight complex coefficients of the linear combination are fixed by the *hybrid comb matching* described in section IIC of Ref. [16]. The matching time $t^{\ell m}_{\rm match}$ is fixed to be the EOB light ring position. The matching interval $\Delta t^{\ell m}_{\rm match}$ is an adjustable parameter that is fixed by reducing the difference against numerical merger-ringdown waveforms.

6.3 Calibrating the EOB waveforms to numerical relativity simulations

We now calibrate the spin EOB model against the numerical UU and DD spin configurations. We extract both the Newman-Penrose (NP) scalars $\Psi_4^{\ell m}$ and the strain waveforms $h_{\ell m}$ from the simulations. The strain waveforms are extracted with the Regge-Wheeler-Zerilli (RWZ) formalism [38, 39, 40, 41] (see Appendix of Ref. [16] for details of the numerical implementation used to obtain $h_{\ell m}$). We use the RWZ $h_{\ell m}$ to calibrate the EOB model, and use the NP $\Psi_4^{\ell m}$ to check the consistency between the two wave-extraction schemes and to estimate the numerical error associated with the wave extraction schemes.

We will use the $\ell = 2, m = 2$ component of the numerical waveform for tuning the EOB model. Thus, we calibrate in total the following six adjustable EOB parameters: $b(\nu)$, $a_{\rm SS}^{\rm 3PN}$, $a_1^{h_{22}}$, $a_2^{h_{22}}$, $a_3^{h_{22}}$ and $\Delta t^{22}_{\rm match}$.

6.3.1 Uncertainties in numerical waveforms

In this section, we compare numerical waveforms computed at different numerical resolutions and/or using different extrapolation procedures, or with different wave-extraction schemes. Estimates of numerical errors in the waveforms will set our standards when calibrating the EOB model.

First, we adopt the same waveform-alignment procedure used in Ref. [16], that is we

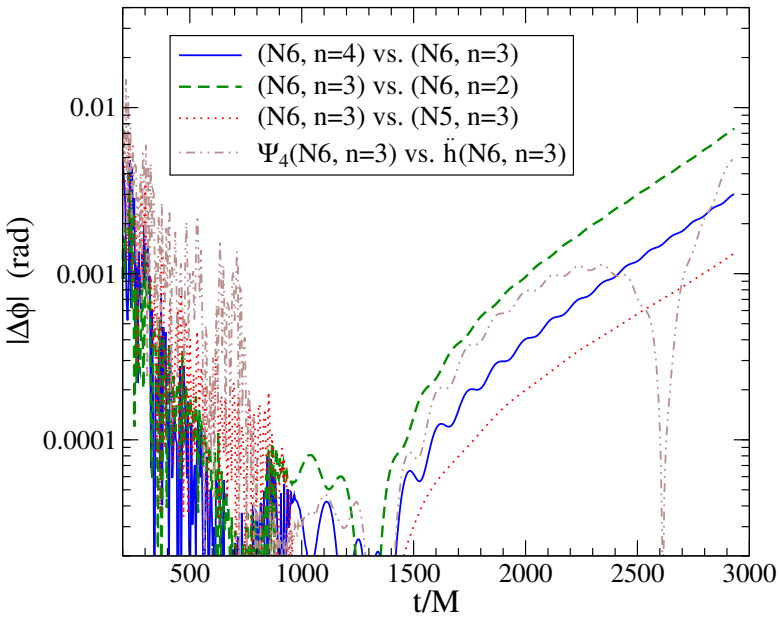

Figure 6.1: Numerical error estimates for the UU configuration. We show the phase difference between several numerical Ψ_4^{22} waveforms aligned using the procedure defined by Eq. (6.35).

align waveforms at low frequency by minimizing the quantity

$$\Xi(\Delta t, \Delta\phi) = \int_{t_1}^{t_2} \left[\phi_1(t) - \phi_2(t - \Delta t) - \Delta\phi\right]^2 \, dt \,, \tag{6.35}$$

over a time shift Δt and a phase shift $\Delta\phi$, where $\phi_1(t)$ and $\phi_2(t)$ are the phases of the two waveforms. The range of integration (t_1, t_2) is chosen to be as early as possible to maximize the length of the waveform but late enough to avoid the contamination from junk radiation present in the numerical initial data. The range of integration should also be large enough to average over numerical noise. We fix $t_1 = 500M$ and $t_2 = 1500M$ in Eq. (6.35).

Using this alignment procedure, we estimate the errors on the numerical Ψ_4^{22}. Figs. 6.1 and 6.2 summarize the phase errors for numerical Ψ_4^{22}. The numerical waveform labeled "(N6, n=3)" [or "Ψ_4(N6, n=3)"] is the reference numerical waveform used throughout this work. Each waveform is extracted on a set of spheres at fixed distances from the source, and then extrapolated to future null infinity; the labels n refer to different orders of this extrapolation and are used to quantify the uncertainty in the phase due to extrapolation. The waveform labeled by N5 (as opposed to N6) is from a simulation with a lower numerical resolution and is used to quantify the uncertainty due to numerical truncation errors. The waveform labeled by "$\ddot{h}$(N6, n=3)" is generated by twice differentiating the RWZ-extracted

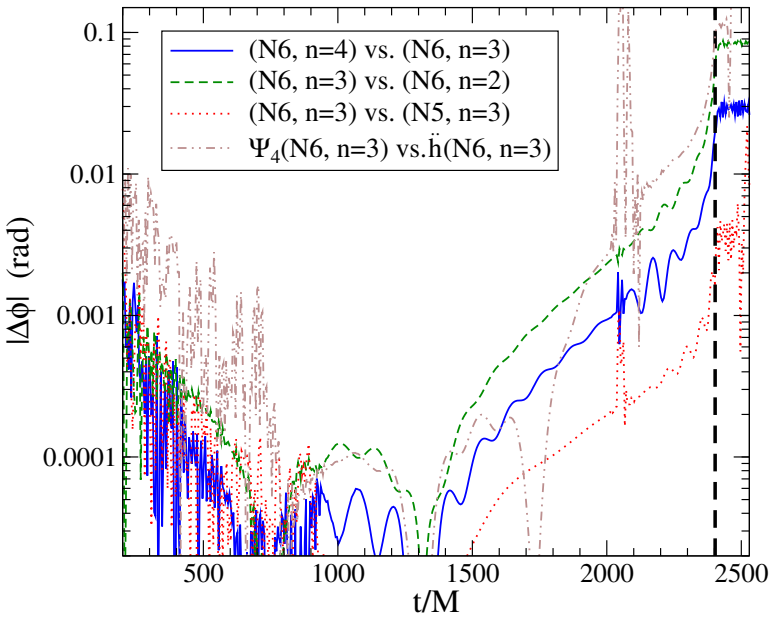

Figure 6.2: Numerical error estimates for the DD configuration. We show the phase difference between several numerical Ψ_4^{22} waveforms aligned using the procedure defined by Eq. (6.35). The dashed vertical line marks the peak amplitude time of the reference numerical strain waveform h_{22} (N6, n=3).

"h(N6, n=3)" waveform, and is used to quantify the uncertainty due to the systematic difference between extracting the NP scalar and extracting the strain waveform via the RWZ formalism.

The noise before $t = 500M$ is due to spurious radiation from initial conditions. The features around $t \approx 2100M$ in Fig. 6.2 are due to a change of gauge in the numerical simulation. Extrapolation with $n = 2$ leads to systematic errors in the extrapolated waveform which in turn results in a systematic error in Δt. Therefore, the green dashed lines in Figs. 6.1 and 6.2 represent a possibly overly conservative error estimate. There is a tiny frequency difference between the NP and RWZ extracted waveforms, which is magnified into a substantial time shift when the waveforms are aligned at low frequency. As a consequence, the dot-dashed brown line in Fig. 6.2 shows a larger phase difference which builds up during the late inspiral. It provides us with the most conservative error estimate for the DD configuration. This is better illustrated in Figs. 6.3 and 6.4, where we compare the RWZ h_{22} and NP Ψ_4^{22} waveforms without any time or phase shift. In blue solid lines, we show the phase and relative amplitude differences $\Delta\phi_{\rm NP}$ and $\Delta A_{\rm NP}/A$ between the RWZ h_{22} waveform differentiated twice with respect to time and Ψ_4^{22}. In red dashed lines, we show the phase and relative amplitude differences $\Delta\phi_{\rm RWZ}$ and $\Delta A_{\rm RWZ}/A$ between Ψ_4^{22} integrated twice in

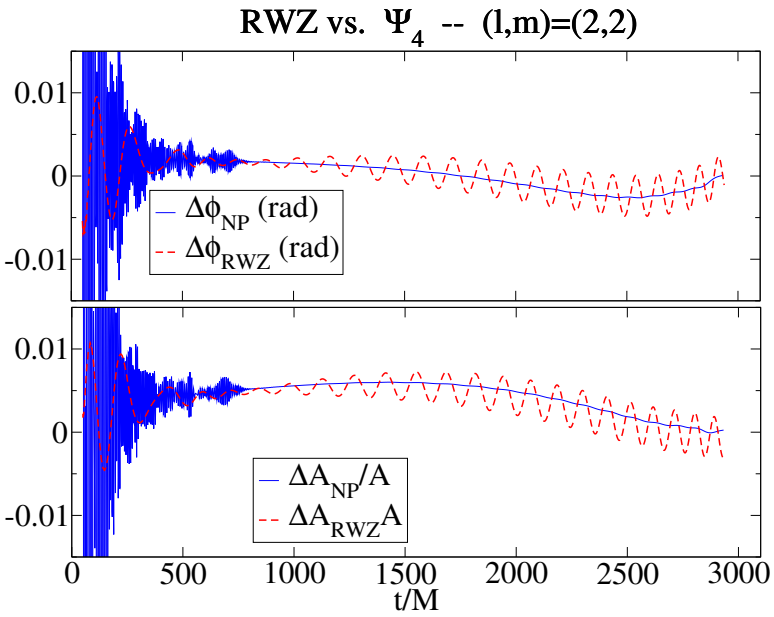

Figure 6.3: Phase and relative amplitude difference between the $(l, m) = (2, 2)$ modes of the RWZ waveform $h_{\rm RWZ}$ and NP scalar Ψ_4 for the UU case.

time and the RWZ h_{22}. In Fig. 6.4, $\Delta\phi_{\rm NP}$ shows a slope between $t = 500M$ and $1500M$. When we apply the alignment procedure, this slope is removed through a time shift, which is transformed into a larger phase difference during late inspiral where the wave frequency is large.

6.3.2 Calibrating the EOB adjustable parameters

Here we adopt the procedure suggested in Ref. [16], augmented with the iterative scheme suggested in Ref. [15] when calibrating the adjustable parameters.

We divide the adjustable parameters into three groups and calibrate them in two steps. The first group, EOB-dynamics parameters, consists of $b(\nu)$ and $a_{\rm SS}^{\rm 3PN}$ in the EOB Hamiltonian (there is no adjustable parameter in the model of the EOB energy flux). These parameters determine the inspiral and plunge dynamics of the EOB model and affect the merger-ringdown waveform only indirectly through the waveform's phase and frequency around the matching point. The second group, EOB-NQC parameters, consists of $a_i^{h_{\ell m}}$, which enter both the EOB dynamics (through the energy flux) and the EOB waveform (through the NQC correction). The third group, EOB-waveform parameters, consists of $\Delta t_{\rm match}^{\ell m}$, which affect the EOB merger-ringdown waveform but not the EOB inspiral-plunge waveform. All the EOB adjustable parameters are calibrated to the numerical RWZ h_{22}. In

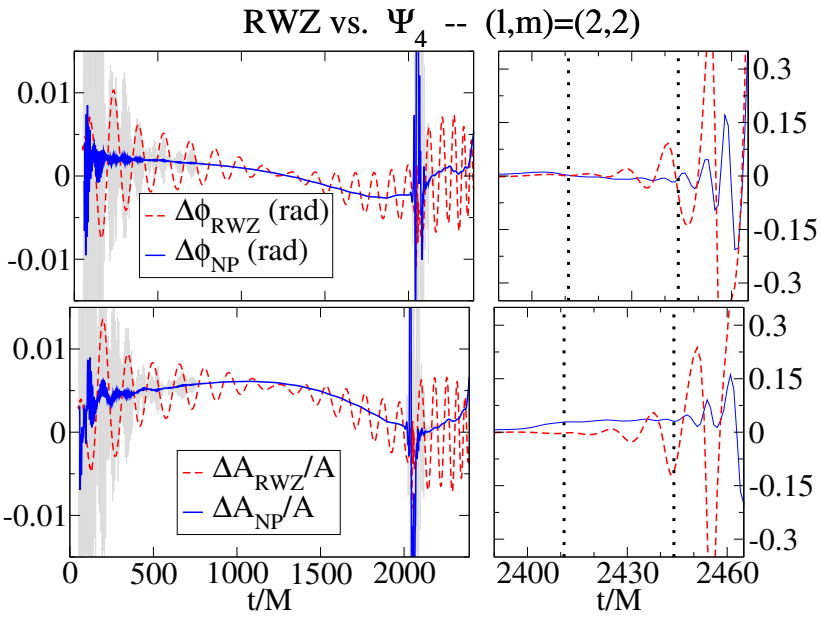

Figure 6.4: Phase and relative amplitude difference between the $(l, m) = (2, 2)$ modes of the RWZ waveform $h_{\rm RWZ}$ and NP scalar Ψ_4 for the DD case. The right panel shows an enlargement of merger and ringdown, with the dotted vertical lines indicating time of maximum of $|\Psi_4|$, and where $|\Psi_4|$ has decayed to 10% of the maximal value. (The blue lines are smoothed; the grey data in the background represents the unsmoothed data.)

the first step of calibration, we simultaneously reduce the difference in waveforms against the numerical UU and DD configurations by calibrating the EOB-dynamics and the EOB-NQC adjustable parameters. In the second step, using the adjustable parameters fixed in the first step, we calibrate the EOB-waveform adjustable parameters.

We adopt the iterative scheme suggested in Ref. [15] to fix the EOB-dynamics and the EOB-NQC parameters in the first step of calibration. In each iteration, we first minimize the phase difference $\Delta\phi(t) \equiv \phi_{\rm EOB}(t) - \phi_{\rm NR}(t)$ by calibrating the EOB-dynamics adjustable parameters. Specifically, we minimize the span of the phase difference $\Delta\phi_{\rm span} \equiv \max_t \Delta\phi(t) - \min_t \Delta\phi(t)$, where the time intervals are different for the UU and DD configurations. Time intervals start at $t_i = 500M$ for both configurations, in order to avoid junk radiation from numerical initial data. However, the time interval ends at the end of the numerical simulation $t_e = 2934.8M$ in the UU configuration, while in the DD configuration, it ends at the peak amplitude time of the h_{22} waveform $t_e = 2402.6M$.

Most of the phase difference between the EOB and NR waveforms accumulates monotonically in the last 10–20M (about half a gravitational-wave cycle) before the merger. Our goal in calibrating the EOB dynamics is to reduce this late-time phase difference under the

condition that the EOB and NR phase difference during the inspiral is strictly less than the numerical error. This goal is better achieved by minimizing the span of the phase difference $\Delta\phi_{\rm span}$ instead of the absolute value $\max_t |\Delta\phi(t)|$ or the norm $\int_{t_i}^{t_e} \Delta\phi(t)^2\, dt$. As a matter of fact, if we choose to minimize either the absolute value or the norm, we obtain a phase difference $\Delta\phi(t)$ whose inspiral part and late-time part average roughly around zero and are comparable in absolute value.

By comparing the EOB model to both the UU and DD configurations, it is possible to calibrate the parameters $b(\nu)$ and $a_{\rm SS}^{\rm 3PN}$ separately. This is because $b(\nu)$ alters a 3.5PN spin-orbit coupling term that depends on the spin orientation, so the phases of the UU and DD waveforms change in opposite directions when varying $b(\nu)$, but $a_{\rm SS}^{\rm 3PN}$ alters a 3PN spin-spin coupling term, so the phases of the UU and DD waveforms change in the same direction when varying $a_{\rm SS}^{\rm 3PN}$.

The EOB-NQC adjustable parameters are calibrated only to the numerical h_{22} waveform of the DD configuration, because we did not run the UU case through merger and ringdown. We first fix $a_1^{h_{22}}$ and $a_2^{h_{22}}$ by requiring that a local extremum of the EOB h_{22} amplitude coincides with the peak of the numerical h_{22} in time and amplitude (the peak time is predicted by the EOB light ring). We expect that in the future, the peak amplitude of the numerical h_{22} will be predicted by numerical relativity with high accuracy as an interpolation function on the physical parameters. Therefore, $a_1^{h_{22}}$ and $a_2^{h_{22}}$ can be determined without a least-squares fit to the NR waveform, reducing by two the number of parameters to be determined by a least-squares fit. The other two NQC parameters, $a_3^{h_{22}}$ and $a_4^{h_{22}}$, are calibrated to the numerical waveform to further reduce the disagreement in amplitude. The NQC parameters will enter the flux through the NQC waveform ${}^{\rm NQC}h_{22}$ in the next iteration. They are set to zeros initially to start the iteration and they usually converge within five iterations.

In the third step, we calibrate the EOB-waveform adjustable parameter $\Delta t_{\rm match}^{22}$ by reducing the difference in the DD configuration merger-ringdown h_{22} waveform.

6.3.3 Comparing the gravitational-wave modes h_{22}

Before calibrating the EOB adjustable parameters, we investigate the phase difference for the EOB uncalibrated waveforms. For the uncalibrated model, we set $a_5 = 1.775$ and all six of our adjustable parameters to zero. We find that during the inspiral, the phase agreement between the numerical and spin EOB uncalibrated waveforms is already substantially better than the agreement between numerical and Taylor-expanded PN waveforms. For the latter,

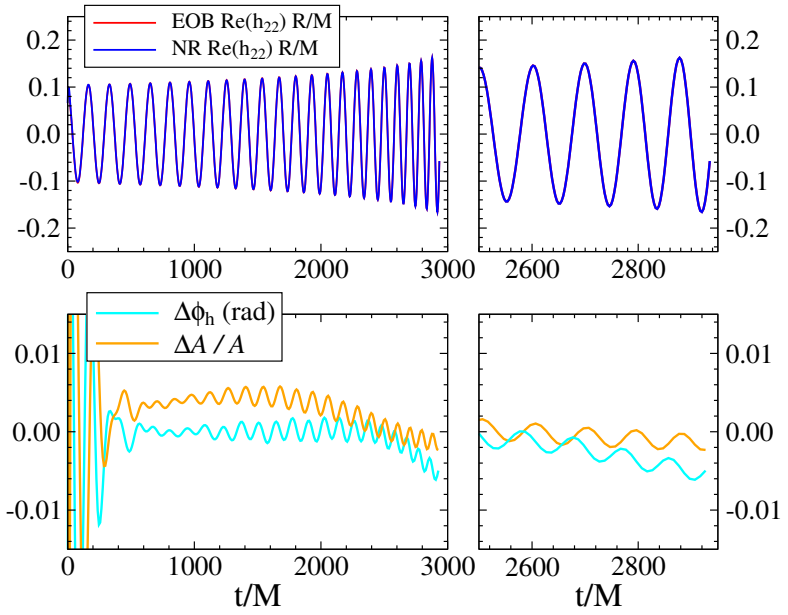

Figure 6.5: Comparison between the numerical and EOB waveform for the UU configuration using $b(\nu) = -1.65$ and $a_{\rm SS}^{\rm 3PN} = 1.5$. The top panels show the real part of the numerical and EOB h_{22}, the bottom panels show amplitude and phase differences between them. The left panels show times $t = 0$ to $2950M$, whereas the right panels present an enlargement of the later portion of the waveform. The EOB waveforms in the top panels are not quite visible since it is covered by the very similar NR waveforms.

we consider the 3.5PN spin Taylor model (T4) of Ref. [42] with amplitude corrections through the highest PN order currently known [43, 28]. In fact, using the uncalibrated spin EOB model and aligning the waveforms with the procedure defined by Eq. (6.35), we find that the phase differences against the numerical UU and DD waveforms, at the end of the simulation and at merger, respectively, are -0.2 and 4.3 radians.[7] Using the spin Taylor T4 model, the corresponding phase differences are 2.0 and -10.0 radians. Therefore, the spin EOB model, even uncalibrated, improves the phase agreement with numerical waveforms of Taylor-expanded PN models by resumming the PN dynamics.

When calibrating the EOB model, we find that the difference in phase and amplitude between the numerical and EOB waveforms is minimized when fixing the EOB-dynamics parameters $b(\nu) = -1.65$ and $a_{\rm SS}^{\rm 3PN} = 1.5$.

[7] If in the uncalibrated EOB model, we chose to include both a_5 and a_6, as discussed in section 6.2.1, and adopted the values $a_5 = -15.5$ and $a_6 = 223$ (calibrated to equal-mass nonspinning numerical waveforms and consistent with the constraint derived from self-force results in Ref. [35]), we would find for the phase differences -0.3 and 3.5 radians. They are comparable with the differences found in the spin EOB model with only a_5.

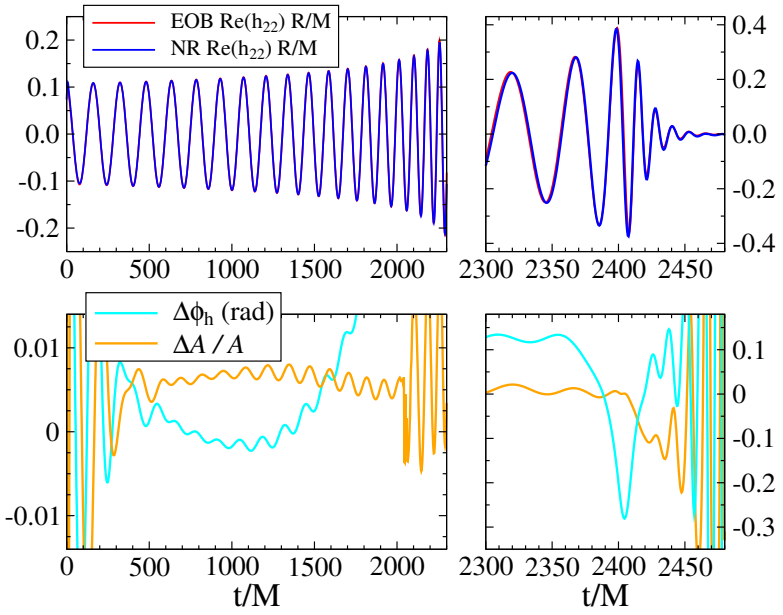

Figure 6.6: Comparison between the numerical and EOB waveform for the DD configuration using $b(\nu) = -1.65$ and $a_{\rm SS}^{\rm 3PN} = 1.5$. The top panels show the real part of the numerical and EOB h_{22}, the bottom panels show amplitude and phase differences between them. The left panels show times $t = 0$ to $2300M$, and the right panels show times $t = 2300M$ to $t = 2480M$ on a different vertical scale.

In Fig. 6.5, we compare numerical and EOB h_{22} waveforms for the UU configuration. The phase difference and relative amplitude difference are strictly within 0.01 radians and 1%, respectively. The systematic error in the EOB waveform in the UU configuration is therefore smaller than the numerical errors.

In Fig. 6.6, we compare numerical and EOB h_{22} waveforms for the DD configuration. Using $b(\nu) = -1.65$ and $a_{\rm SS}^{\rm 3PN} = 1.5$ again, we find that the best phase and amplitude agreement is obtained when the matching occurs at an interval of $\Delta t^{22}_{\rm match} = 3.5M$ ended at $t^{22}_{\rm match} = 2402.0M$, which is the EOB light ring position and is $0.6M$ before the merger, i.e., the peak of the numerical h_{22} at $t = 2402.6M$. The NQC parameters are $a_1^{h_{22}} = -16.1052$, $a_2^{h_{22}} = -1124.43$, $a_3^{h_{22}} = 4529.21$ and $a_4^{h_{22}} = -4587.53$. The relative amplitude difference is strictly within 1% until $2000M$. After $2000M$, although oscillations due to numerical gauge effects in the RWZ h_{22} waveform are at the level of 2% until the merger, the average difference is still less than 1%. After the merger, the amplitude difference grows to about -5% and starts oscillating with increasing magnitude. The latter phenomenon is due to gauge effects in the RWZ h_{22} waveform as discussed in section 6.3.1 and the Appendix of Ref. [16]. The phase difference is within 0.01 radians until about $1800M$ and grows

to -0.28 radians until merger and settles to about 0.1 radians before the exponentially decaying amplitude results in increased errors in the extracted gravitational-wave phase.

In the spin DD configuration, the error in the EOB waveform (especially in the phase) is not within the numerical errors. The phase difference of $\sim$0.13 radians at late inspiral around $t = 2300M$ can be reduced to within the numerical errors of $\sim$0.01 radians by calibrating the EOB-dynamics adjustable parameters, i.e., $b(\nu)$ and $a_{\rm SS}^{\rm 3PN}$. However, this leads to an increase of the phase difference around the merger. Since we choose to minimize the span of the phase difference $\Delta\phi_{\rm span}$ over the time interval that ends at the merger, the phase difference at late inspiral is larger than what it could have been if $\Delta\phi_{\rm span}$ was minimized over a time interval that ends about $100M$ before the merger. The largest phase difference around merger can not be removed by calibrating the chosen adjustable parameters. Nevertheless, we can substantially reduce the phase difference if we allow one of the EOB-dynamics parameters $b(\nu)$ and $a_{\rm SS}^{\rm 3PN}$ to be different in the UU and DD cases, or if we add one more spin-independent adjustable parameter. For instance, there can be a NQC correction factor on the right-hand side of Eq. (6.34) that contributes solely to the phase of the waveform in the form of [32]

$$h_{\ell m}^{\rm insp-plunge} = {}^{\rm NQC}h_{\ell m}\, e^{i\, b_1^{h_{\ell m}}\, p_{r^*}/(r\hat{\Omega})}. \tag{6.36}$$

We can reduce the phase difference at merger to $<$0.05 radians by calibrating this extra EOB-NQC adjustable parameter $b_1^{h_{\ell m}}$. However, until we study a larger number of waveforms, we will not overtune parameters, since the main purpose of this preliminary and exploratory study on the spin EOB model is to show that by making a very simple and minimal choice of adjustable parameters, we can achieve a quite fair agreement with the numerical simulations.

We shall emphasize that, despite the small phase difference that exceeds the numerical errors in the DD configuration, the faithfulness of the EOB waveforms with the numerical waveforms is very good. Using the noise curves of Enhanced LIGO and Advanced LIGO,[8] for both the UU and DD configurations, we find that the faithfulness is always better than 0.999 for black-hole binaries with a total mass of 30–200$M_\odot$. Note that the numerical waveforms start roughly at 40Hz for binaries with total mass $30M_\odot$ and at 10Hz for binaries with total mass $100M_\odot$. Since the Advanced LIGO noise curve has a low frequency cutoff at 10Hz, the numerical waveforms are not long enough to cover the Advanced LIGO sensitivity

[8] For Enhanced LIGO, we use the power spectral density given at `http://www.ligo.caltech.edu/~rana/NoiseData/S6/DCnoise.txt`; for Advanced LIGO, we use the broadband configuration power spectral density given at `http://www.ligo.caltech.edu/advLIGO/scripts/ref_des.shtml`.

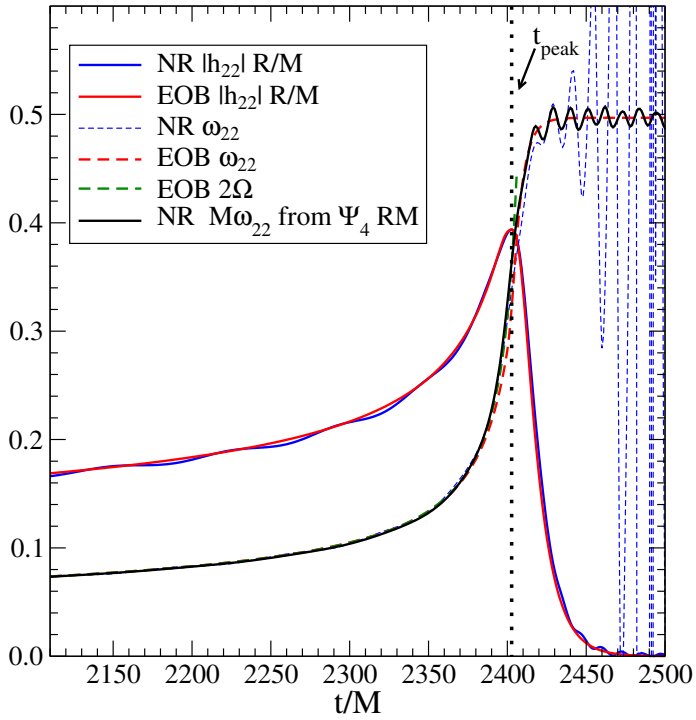

Figure 6.7: We show the amplitude and frequency of the numerical and EOB mode h_{22}, the EOB orbital frequency and the frequency of the numerical mode Ψ_4^{22} for the DD configuration. The vertical line labeled t_{peak} marks the peak of the amplitude of the numerical waveform. The EOB light ring is $0.6M$ before the peak and is too close to be shown in the figure.

band for binaries with total mass smaller than $100M_{\odot}$. When computing overlaps for these lower mass binaries using Advanced LIGO noise curve, we start the integration at the starting frequency of the numerical waveforms instead of 10 Hz. For the available numerical waveforms, the overlaps with EOB waveforms are well above the requirement on the accuracy of binary black-hole waveforms for detection purpose in gravitational-wave observations [44]. The overlaps are also above the measurement requirement for binary black-hole coalescence events observed with signal-to-noise ratio below 1000, which are likely to cover all possible detections by current or advanced ground-based gravitational-wave detectors.

In Fig. 6.7, we compare the amplitude and frequency of numerical and EOB h_{22} waveforms together with the orbital frequency of the EOB model, for the DD configuration. Unlike the nonspinning case [16], the orbital frequency Ω continues to grow during the plunge. However, the EOB light ring is very close to the peak of the numerical h_{22}, as discussed in section 6.2.1. Note that during the ringdown, the frequency computed from

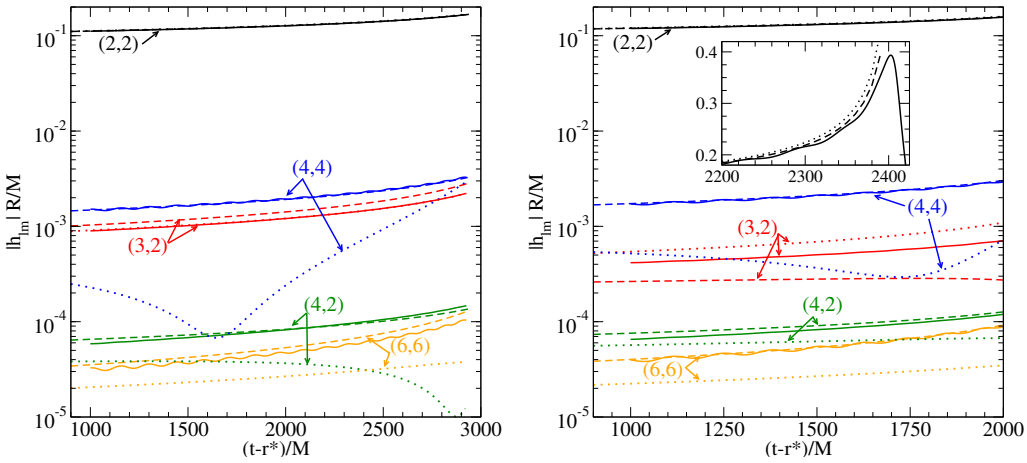

Figure 6.8: Comparison of the numerical (solid lines), EOB (dashed lines) and Taylor-expanded (dotted lines) amplitudes of the dominant and leading subdominant (l, m) modes for the UU (left panel) and DD (right panel) configurations. The inset shows the amplitudes for the dominant $(2, 2)$ mode during the late-inspiral and plunge in the DD configuration, without the addition of EOB-NQC and EOB-waveform adjustable parameters.

the numerical h_{22} shows increasingly large oscillations. We also plot the frequency computed from the numerical Ψ_4^{22} model. This frequency shows much smaller, and bounded, oscillations deep into the ringdown regime.

In Fig. 6.7, the curve labeled "NR $|h_{22}|R/M$" shows noticable oscillations. These oscillations start at $t/M \sim 2100$ coincident with the change of gauge conditions in the numerical simulation (coincident features are also visible in Fig. 6.4). We therefore attribute these features to gauge effects, which apparently contaminate the RWZ waveform h_{22} more strongly than the Newman-Penrose waveform ψ_4.

6.3.4 Comparing the gravitational-wave modes $h_{\ell m}$

Here we generate inspiral higher-order modes, $h_{\ell m}$, using the same dynamics-adjustable parameters calibrated to the numerical h_{22} mode in the previous section. The EOB-NQC parameters and the EOB-waveform parameters for these modes are not calibrated, since higher-order numerical waveforms show large numerical errors before reaching their peaks. For this reason, we constrain the comparison between numerical and EOB higher-order modes to the inspiral stage. The higher-order modes are aligned at low frequencies using the same time and phase shifts (modulo a factor of $m/2$ in the phase shifts) applied to the EOB h_{22} mode.

In Fig. 6.8, we compare the EOB (dashed lines) and numerical (solid lines) amplitudes

of the first five modes that dominate the signal power. In the DD case we show results only until $t = 2000M$ because at later times the numerical data are affected by large oscillations, likely due to gauge effects. Except for the h_{32} mode in the DD configuration, the agreement is very good for all the subdominant modes, as well as for the h_{22} mode, in both the UU and DD waveforms. We believe that the difference seen for the DD h_{32} mode is due to the lack of knowledge of PN spin couplings in the amplitude of the higher modes. In fact, only the leading-order PN spin term is known in the amplitude of the h_{32} mode, and no PN spin terms are known in the amplitudes of the other subdominant modes shown in Fig. 6.8. Being resummed in the form of Eq. (6.30), the leading spin term in h_{32} leaves a residual term in f_{32} at the leading order. We test two choices of the odd-parity source term in Eq. (6.33), $\hat{L}_{\rm eff}$ and $\hat{H}_{\rm eff}$, and find this residual term always dominating over all the nonspinning terms and causing f_{32} to decrease and cross zero at high frequency, thus showing the odd behavior in the DD (3,2) mode of Fig. 6.8. We also try to apply the ρ-resummation discussed in section 6.2.3 on the spin terms of the f_{32}. Although when applying the ρ-resummation, the leading order residual term in ρ_{32} is reduced by $1/\ell = 1/3$ with respect to the residual term in f_{32}, it still dominates over other terms and causes $(\rho_{32})^3$ to cross zero at high frequency.

In Fig. 6.8, we also show the Taylor-expanded PN amplitudes (dotted lines). Their expressions can be read from Refs. [43] and [28], and they depend on dynamical variables only through the orbital velocity. We calculate these amplitudes using the non-Keplerian orbital velocity defined in Eq. (6.32) for the leading term and the Keplerian orbital velocity for all the next-to-leading terms. We calculate the non-Keplerian and Keplerian velocities using the EOB dynamics. That is to say, these amplitudes and the resummed amplitudes are calculated using exactly the same dynamical evolutions. In particular, the energy flux in the dynamics is always modeled by resummed waveforms, even when we calculate the Taylor-expanded PN amplitudes. These Taylor-expanded PN amplitudes are not to be confused with the amplitudes of the adiabatic PN approximants, such as the TaylorT1 and TaylorT4 approximants [45], because the underlying dynamics of the latter is completely different. In Fig. 6.8, although the Taylor-expanded PN amplitudes work reasonably well for the h_{22} mode during inspiral, and probably by chance also for the h_{32} mode in the UU configuration, their performance is not as good as that of the resummed amplitudes in general. Especially, for the h_{44} and h_{42} modes, the Taylor amplitudes are not monotonic. This unpleasant behavior is caused by their 1PN-order nonspinning terms. Furthermore, the insert of Fig. 6.8 shows that the performance of Taylor-expanded PN amplitudes becomes worse for the h_{22} mode during the late inspiral and plunge in the DD configuration.

Given the current information from PN theory and numerical simulations, we consider the agreement in Fig. 6.8 reasonable and do not dwell further on the choice of the waveform modeling options. The differences have little impact on the EOB model since the largest difference in h_{32} affects the energy flux by less than 10^{-4}, which is overwhelmed by other uncertainties in the EOB dynamics.

For the five dominant modes, the relative differences between the numerical and EOB $h_{\ell m}$ frequencies are within 0.5%, except for the $(3,2)$ mode in the DD configuration where the difference is within 1%. Since the $h_{\ell m}$ frequency depends on both the orbital frequency and its amplitude, the larger amplitude difference in the $(3,2)$ mode affects its gravitational-wave frequency. Except for the $(3,2)$ mode in the DD configuration, all frequency agreement is within the numerical errors.

6.4 Conclusions

In this chapter, we carried out the first calibration of the spin EOB model to accurate numerical-relativity simulations of spinning, nonprecessing black-hole binaries. We focused on two equal-mass black-hole binaries having spins both aligned, or both anti-aligned with the orbital angular momentum, and dimensionless magnitude $\sim$0.44 [30].

For the EOB conservative dynamics, we adopted the spin EOB Hamiltonian suggested in Refs. [21, 22], augmented with the 4PN-order nonspinning parameter a_5 and two adjustable parameters. For the EOB nonconservative dynamics, we employed the gravitational-wave energy flux which includes spin effects and which has been computed using the factorized multipolar waveforms of Ref. [28].

As in previous cases [14, 16], we aligned the EOB and numerical waveforms at low frequency over a time interval of $1000M$, and minimized the difference between numerical and EOB waveforms by calibrating a handful of EOB-adjustable parameters. In particular, in this first exploration, we calibrated two EOB-dynamics adjustable parameters [$b(\nu)$ in Eq. (6.16b) which introduces a spin-orbit term at 3.5PN order, and $a_{\rm SS}^{\rm 3PN}$ in Eq. (6.19) which introduces a 3PN spin-spin term], and three EOB-NQC adjustable parameters [see Eq. (6.34)] which enter the gravitational-wave energy flux and the EOB gravitational-wave (2,2) mode. Finally, we also calibrated the EOB-waveform adjustable parameter $\Delta t^{22}_{\rm match}$. Quite interestingly, similar to the case of nonspinning waveforms, we found that for spinning waveforms, once the EOB-dynamics adjustable parameters are calibrated at low frequency, the EOB light ring coincides with the peak of the numerical-relativity waveform. Thus,

for both spinning and nonspinning binary black holes, the EOB light ring marks the most natural point at which to match the EOB inspiral-plunge waveform to the EOB merger-ringdown waveform.

In the equal-mass, spin aligned case, we found that phase and fractional amplitude differences between the numerical and EOB $(2, 2)$ mode can be reduced to 0.01 radians and 1%, respectively, over the entire inspiral waveforms. In the equal-mass, spin anti-aligned case, these differences can be reduced to 0.13 radians and 1% during inspiral, and to 0.4 radians and 10% during merger and ringdown. The waveform agreement is within numerical errors in the spin aligned case while slightly over numerical errors in the spin anti-aligned case. Despite this difference, we found that using Enhanced LIGO and Advanced LIGO noise curves, the overlap maximized with respect to reference time and phase between the EOB and the numerical (2,2) mode, is larger than 0.999 for binaries with total mass 30–200$M_{\odot}$. This is well above the accuracy requirement of binary black-hole waveforms for detection and measurement purposes in gravitational-wave observations [44].

In addition to comparing the numerical and EOB waveforms for the leading (2,2) mode, we also compared them for the next four subleading modes. Except for the h_{32} mode in the DD configuration, the amplitude and frequency agreements are very good for all the subdominant modes, as well as for the h_{22} mode, in both the UU and DD waveforms. We believe that the difference seen for the DD h_{32} mode is due to the lack of knowledge of PN spin couplings in the amplitude of the subleading modes.

The spin EOB Hamiltonian [21, 22] adopted in this work was an excellent starting point to explore the calibration of the EOB model against spinning numerical simulations; however, as discussed above, and in particular in section 6.2.2, the spin EOB Hamiltonian we used exhibits some unusual behaviour. Especially when extended at 4PN and 5PN, in some regions of the parameter space the Hamiltonian does not have an ISCO or the ISCO radius grows as the spin magnitude increases. This is opposite to the result in the test-particle limit case. Moreover, although the spin EOB Hamiltonian has a light ring, in some regions of the parameter space (including the anti-aligned case discussed in this chapter) the orbital frequency does not reach a maximum. Those features turned out to be crucial when calibrating the EOB model to nonspinning numerical waveforms, and we believe will be crucial also when modeling spinning numerical waveforms. We found that the lack of those features in the current EOB Hamiltonian is due to the *ad hoc* spin coupling term $H_{\text{eff part}}(\boldsymbol{R}, \boldsymbol{P}, \boldsymbol{\sigma})$, defined in Eq. (6.13). This spin coupling term does not reproduce the results of a spinning test-particle at PN orders higher than 2.5PN. Analyses using an

improved spin EOB Hamiltonian [36] obtained by building on Ref. [27] have shown that those features can be recovered.

6.5 Appendix: Tortoise coordinate in Cartesian implementation

We start with the definition of the radial tortoise coordinate given in Eq. (6.28): $dR^*/dR = 1/\xi_a(R)$. The invariance of the action gives $P_{R^*} = P_R\, dR/dR^* = P_R\, \xi_a(R)$. In evolving the EOB dynamics, we adopt the dynamical variables $\boldsymbol{R}$, $\boldsymbol{P^*}$, $\boldsymbol{S_1}$ and $\boldsymbol{S_2}$. The transform from $\boldsymbol{P}$ to $\boldsymbol{P^*}$ is a coordinate transform, not a canonical transform. In this section, we derive explicitly the transform to tortoise coordinate for the Hamiltonian and Hamilton equations of motion implemented in Cartesian coordinates.

The transform between $\boldsymbol{P}$ and $\boldsymbol{P^*}$ is determined by the invariance in their tangential components and the rescaling in their radial components, that is

$$\begin{aligned} \boldsymbol{R}\times\boldsymbol{P} &= \boldsymbol{R}\times\boldsymbol{P^*}\,, \\ \xi_a(R)\,\boldsymbol{R}\cdot\boldsymbol{P} &= \boldsymbol{R}\cdot\boldsymbol{P^*}\,. \end{aligned} \tag{6.37}$$

Choosing three independent equations out of the four above, we can write the transform in components as

$$\begin{pmatrix} -Y & X & 0 \\ 0 & -Z & Y \\ X & Y & Z \end{pmatrix} \begin{pmatrix} P_X^* \\ P_Y^* \\ P_Z^* \end{pmatrix} = \begin{pmatrix} -Y & X & 0 \\ 0 & -Z & Y \\ \xi_a(R)X & \xi_a(R)Y & \xi_a(R)Z \end{pmatrix} \begin{pmatrix} P_X \\ P_Y \\ P_Z \end{pmatrix} \tag{6.38}$$

or explicitly as

$$\begin{aligned} \boldsymbol{P^*} &= \begin{pmatrix} P_X^* \\ P_Y^* \\ P_Z^* \end{pmatrix} \\ &= \begin{pmatrix} 1+\frac{X^2}{R^2}\,[\xi_a(R)-1] & \frac{XY}{R^2}\,[\xi_a(R)-1] & \frac{XZ}{R^2}\,[\xi_a(R)-1] \\ \frac{XY}{R^2}\,[\xi_a(R)-1] & 1+\frac{Y^2}{R^2}\,[\xi_a(R)-1] & \frac{YZ}{R^2}\,[\xi_a(R)-1] \\ \frac{XZ}{R^2}\,[\xi_a(R)-1] & \frac{YZ}{R^2}\,[\xi_a(R)-1] & 1+\frac{Z^2}{R^2}\,[\xi_a(R)-1] \end{pmatrix} \begin{pmatrix} P_X \\ P_Y \\ P_Z \end{pmatrix} \\ &\equiv T\boldsymbol{P}\,. \end{aligned} \tag{6.39}$$

In the spin EOB Hamiltonian, we shall replace $\boldsymbol{P}$ with $T^{-1}\boldsymbol{P^*}$. The equations of motion for $\boldsymbol{R}$ and $\boldsymbol{P^*}$ are

$$\frac{dX^i}{dt} = \frac{\partial H_{\rm real}}{\partial P_i}\bigg|_{X^i} = \frac{\partial H_{\rm real}}{\partial P_j^*}\bigg|_{X^j} \frac{\partial P_j^*}{\partial P_i} = \frac{\partial H_{\rm real}}{\partial P_j^*}\bigg|_{X^j} T_j{}^i\,, \tag{6.40}$$

and

$$\begin{aligned}
\frac{dP_i^*}{dt} &= \frac{\partial P_i^*}{\partial P_j}\frac{dP_j}{dt} + \frac{\partial P_i^*}{\partial X^j}\frac{dX^j}{dt} \\
&= T_i{}^j \left(-\frac{\partial H_{\rm real}}{\partial X^j}\bigg|_{P_j} + \frac{1}{\Omega|\boldsymbol{L}|}\frac{dE}{dt}P_j \right) + \frac{\partial P_i^*}{\partial X^j}\frac{\partial H_{\rm real}}{\partial P_k^*}\bigg|_{X^k} T_k{}^j \\
&= -T_i{}^j \frac{\partial H_{\rm real}}{\partial X^j}\bigg|_{P_j} + \frac{1}{\Omega|\boldsymbol{L}|}\frac{dE}{dt}P_i^* + \frac{\partial P_i^*}{\partial X^j}\frac{\partial H_{\rm real}}{\partial P_k^*}\bigg|_{X^k} T_k{}^j\,,
\end{aligned} \tag{6.41}$$

where the matrix $\partial P_i^*/\partial X^j$ can be written in T and $\boldsymbol{P^*}$ as $\partial P_i^*/\partial X^j = \partial T_i{}^k/\partial X^j \left(T^{-1}\right)_k{}^l P_l^*$.

Bibliography

[1] B. C. Barish and R. Weiss, Phys. Today **52**, 44 (1999).

[2] S. J. Waldman, Class. Quantum Grav. **23**, S653 (2006).

[3] F. Acernese et al., Class. Quantum Grav. **23**, S635 (2006).

[4] B. F. Schutz, Class. Quantum Grav. **26**, 094020 (2009).

[5] P. C. Peters and J. Mathews, Phys. Rev. **131**, 435 (1963).

[6] A. Buonanno, G. B. Cook, and F. Pretorius, Phys. Rev. D **75**, 124018 (2007).

[7] Y. Pan et al., Phys. Rev. D **77**, 024014 (2008).

[8] P. Ajith et al., Class. Quantum Grav. **24**, S689 (2007).

[9] P. Ajith et al., Phys. Rev. D **77**, 104017 (2008).

[10] A. Buonanno et al., Phys. Rev. D **76**, 104049 (2007).

[11] T. Damour and A. Nagar, Phys. Rev. D **77**, 024043 (2008).

[12] T. Damour, A. Nagar, E. N. Dorband, D. Pollney, and L. Rezzolla, Phys. Rev. D **77**, 084017 (2008).

[13] T. Damour, A. Nagar, M. Hannam, S. Husa, and B. Brügmann, Phys. Rev. D **78**, 044039 (2008).

[14] M. Boyle et al., Phys. Rev. D **78**, 104020 (2008).

[15] T. Damour and A. Nagar, Phys. Rev. D **79**, 081503 (2009).

[16] A. Buonanno et al., Phys. Rev. D **79**, 124028 (2009).

[17] N. Yunes, A. Buonanno, S. A. Hughes, M. Coleman Miller, and Y. Pan, Phys. Rev. Lett. **104**, 091102 (2010).

[18] A. Buonanno and T. Damour, Phys. Rev. D **59**, 084006 (1999).

[19] A. Buonanno and T. Damour, Phys. Rev. D **62**, 064015 (2000).

[20] T. Damour, P. Jaranowski, and G. Schäfer, Phys. Rev. D **62**, 084011 (2000).

[21] T. Damour, Phys. Rev. D **64**, 124013 (2001).

[22] T. Damour, P. Jaranowski, and G. Schäfer, Phys. Rev. D **78**, 024009 (2008).

[23] P. Ajith et al., Phys. Rev. Lett. **106**, 241101 (2009).

[24] L. Blanchet, Living Rev. Rel. **9** (2006).

[25] G. Schafer, Post-Newtonian methods: Analytic results on the binary problem, in *Mass and Motion in General Relativity*, edited by L. Blanchet, A. Spallicci, and B. Whiting, pages 167–210, Springer, New York, 2011.

[26] A. Buonanno, Y. Chen, and T. Damour, Phys. Rev. D **74**, 104005 (2006).

[27] E. Barausse, E. Racine, and A. Buonanno, Phys. Rev. **D80**, 104025 (2009).

[28] Y. Pan, A. Buonanno, R. Fujita, E. Racine, and H. Tagoshi, (2010).

[29] T. Damour, B. R. Iyer, and A. Nagar, Phys. Rev. D **79**, 064004 (2009).

[30] T. Chu, H. P. Pfeiffer, and M. A. Scheel, Phys. Rev. **D80**, 124051 (2009).

[31] M. Scheel, M. Boyle, T. Chu, L. Kidder, K. Matthews and H. Pfeiffer, Phys. Rev. D **79**, 024003 (2009).

[32] T. Damour and A. Nagar, Phys. Rev. D **76**, 064028 (2007).

[33] L. Blanchet, A. Buonanno, and G. Faye, Phys. Rev. D **74**, 104034 (2006).

[34] L. Barack and N. Sago, Phys. Rev. Lett. **102**, 191101 (2009).

[35] T. Damour, Phys. Rev. **D81**, 024017 (2010).

[36] E. Barausse and A. Buonanno, Phys. Rev. **D81**, 084024 (2010).

[37] E. Berti, V. Cardoso, and A. O. Starinets, Class. Quantum Grav. **26**, 163001 (2009).

[38] T. Regge and J. A. Wheeler, Phys. Rev. **108**, 1063 (1957).

[39] F. J. Zerilli, Phys. Rev. Lett. **24**, 737 (1970).

[40] O. Sarbach and M. Tiglio, Phys. Rev. D **64**, 084016 (2001).

[41] O. Rinne, L. T. Buchman, M. A. Scheel, and H. P. Pfeiffer, Class. Quantum Grav. **26**, 075009 (2009).

[42] Y. Pan, A. Buonanno, Y. Chen, and M. Vallisneri, Phys. Rev. D **69**, 104017 (2004).

[43] L. E. Kidder, Phys. Rev. D **77**, 044016 (2008).

[44] L. Lindblom, B. J. Owen, and D. A. Brown, Phys. Rev. D **78**, 124020 (2008).

[45] M. Boyle et al., Phys. Rev. D **76**, 124038 (2007).

Chapter 7

Horizon dynamics of distorted rotating black holes

We present numerical simulations of a rotating black hole distorted by a pulse of ingoing gravitational radiation. For strong pulses, we find up to five concentric marginally outer trapped surfaces. These trapped surfaces appear and disappear in pairs, so that the total number of such surfaces at any given time is odd. The world tubes traced out by the marginally outer trapped surfaces are found to be spacelike during the highly dynamical regime, approaching a null hypersurface at early and late times. We analyze the structure of these marginally trapped tubes in the context of the dynamical horizon formalism, computing the expansion of outgoing and incoming null geodesics, as well as evaluating the dynamical horizon flux law and the angular momentum flux law. Finally, we compute the event horizon. The event horizon is well behaved and approaches the apparent horizon before and after the highly dynamical regime. No new generators enter the event horizon during the simulation.

Originally published as T. Chu, H. P. Pfeiffer, and M. I. Cohen, Phys. Rev. D **83**, 104018 (2011).

7.1 Introduction

In the efforts by the numerical relativity community leading up to the successful simulation of the inspiral and merger of two black holes, analyses of single black holes distorted by gravitational radiation have offered a convenient and simpler setting to understand the nonlinear dynamics during the late stages of binary black hole coalescence. For this purpose,

initial data for a Schwarzschild black hole plus a Brill wave was presented in [1], which was both time symmetric and axisymmetric. In highly distorted cases, the apparent horizon could develop very long, spindlelike geometries. If the event horizon can show similar behavior, this would raise intriguing questions related to the hoop conjecture [2]. The work of [1] was extended to distorted rotating black holes in [3], where the apparent horizon served as a useful tool to examine the quasinormal oscillations of the black hole geometry as it relaxed in an evolution. Further studies have extracted the gravitational waves emitted by the black hole [4], and compared the apparent and event horizons [5].

We continue this line of investigation here, while incorporating various modern notions of quasilocal horizons that have emerged in recent years. Our emphasis is on horizon properties during the highly dynamical regime, and no symmetries are present in our initial data and evolutions. The utility of quasilocal horizons can be immediately appreciated when one wants to perform a numerical evolution of a black hole spacetime. One must be able to determine the surface of the black hole at each time, in order to track the black hole's motion and compute its properties, such as its mass and angular momentum. However, the event horizon, which is the traditional notion of a black hole surface, can only be found after the entire future history of the spacetime is known.

Quasilocal horizons can be computed locally in time, and so are used instead to locate a black hole during the evolution. Of particular interest is a marginally outer trapped surface (MOTS), which is a spatial surface on which the expansion of its outgoing null normal vanishes [6]. The use of MOTSs is motivated by several results. When certain positive energy conditions are satisfied, an MOTS is either inside of or coincides with an event horizon [6, 7]. The presence of an MOTS also implies the existence of a spacetime singularity [8]. In an evolution, the MOTSs located at successive times foliate a world tube, called a marginally trapped tube (MTT). MTTs have been studied in the context of trapping horizons [9, 10], isolated horizons [11, 12, 13], and dynamical horizons [14, 15, 16].

Both the event horizon and an MTT react to infalling matter and radiation, although their behaviors can be quite different in highly dynamical situations. Being a null surface, the evolution of the event horizon is governed by the null Raychaudhuri equation [17], so that even though its area never decreases, in the presence of infalling matter and radiation the rate of growth of its area decreases and can even become very close to zero [18]. Since an MTT is determined by quasilocal properties of the spacetime, its reaction to infalling matter and radiation is often much more intuitive. A MTT is usually spacelike (e.g., a dynamical horizon) in such situations, although further scrutiny has revealed that MTTs

can exhibit various intriguing properties of their own. For example, an MTT may become timelike and decrease in area [19], or even have sections that are partially spacelike and partially timelike [20]. In a numerical simulation, such behavior is often indicated by the appearance of a pair of new MTTs at a given time, accompanied by a discontinuous jump in the world tube of the apparent horizon, or outermost MOTS.

In this chapter, we investigate the behavior of MTTs and the event horizon in the context of a rotating black hole distorted by an ingoing pulse of gravitational waves. First, we construct a series of initial data sets in which the amplitude of the gravitational waves varies from small to large, which are then evolved. We focus on the evolution with the largest distortion of the black hole, in which the mass of the final black hole is more than double its initial value. During the evolution, the world tube of the apparent horizon jumps discontinuously when the gravitational waves hit the black hole, and as many as five MTTs are found at the same time. Some of these MTTs decrease in area with time, although we find that all the MTTs during the dynamical stages of our evolution are spacelike and dynamical horizons. Moreover, all these MTTs join together as a single dynamical horizon. Their properties are further analyzed using the dynamical horizon flux law [15], which allows one to interpret the growth of the black hole in terms of separate contributions. We also evaluate the angular momentum flux law based on the generalized Damour-Navier-Stokes equation [21]. Finally, we locate the event horizon and contrast its behavior with that of the MTTs.

The organization of this chapter is as follows. Section 7.2 details the construction of the initial data sets and section 7.3 describes the evolutions. Section 7.4 introduces some definitions about MOTSs, and the methods used to locate them. Section 7.5 discusses the MTTs foliated by the MOTSs, the determination of their signatures, and the fluxes of energy and angular momentum across them. The emphasis is on the case with the largest distortion of the initial black hole, as is the remainder of the chapter. Section 7.6 explains how we find the event horizon, and contrasts its properties with the MTTs. Section 7.7 presents some concluding remarks. Finally, the Appendix offers some insight on our results in light of the Vaidya spacetime.

7.2 Initial Data

Initial data sets are constructed following the method of [22], which is based on the extended conformal thin sandwich formalism. First, the 3+1 decomposition of the spacetime metric

is given by [23, 24]

$$
\begin{aligned}
{}^{(4)}ds^2 &= g_{\mu\nu}dx^\mu dx^\nu, && (7.1)\\
&= -N^2dt^2 + g_{ij}\left(dx^i + \beta^i dt\right)\left(dx^j + \beta^j dt\right), && (7.2)
\end{aligned}
$$

where g_{ij} is the spatial metric of a t = constant hypersurface Σ_t, N is the lapse function, and β^i is the shift vector. (Here and throughout this chapter, Greek indices are spacetime indices running from 0 to 3, while Latin indices are spatial indices running from 1 to 3.) Einstein's equations (here with vanishing stress-energy tensor $T_{\mu\nu} = 0$) then become a set of evolution equations,

$$
\begin{aligned}
(\partial_t - \mathcal{L}_\beta)g_{ij} &= -2NK_{ij}, && (7.3)\\
(\partial_t - \mathcal{L}_\beta)K_{ij} &= N\left(R_{ij} - 2K_{ik}K^k{}_j + KK_{ij}\right) - \nabla_i\nabla_j N, && (7.4)
\end{aligned}
$$

and a set of constraint equations,

$$
\begin{aligned}
R + K^2 - K_{ij}K^{ij} &= 0, && (7.5)\\
\nabla_j\left(K^{ij} - g^{ij}K\right) &= 0. && (7.6)
\end{aligned}
$$

In the above, $\mathcal{L}$ is the Lie derivative, ∇_i is the covariant derivative compatible with g_{ij}, $R = g^{ij}R_{ij}$ is the trace of the Ricci tensor R_{ij} of g_{ij}, and $K = g^{ij}K_{ij}$ is the trace of the extrinsic curvature K_{ij} of Σ_t.

Next, a conformal decomposition of various quantities is introduced. The conformal metric $\tilde{g}_{ij}$ and conformal factor ψ are given by

$$
g_{ij} = \psi^4\tilde{g}_{ij}, \tag{7.7}
$$

the time derivative of the conformal metric is denoted by

$$
\tilde{u}_{ij} = \partial_t\tilde{g}_{ij}, \tag{7.8}
$$

and satisfies $\tilde{u}_{ij}\tilde{g}^{ij} = 0$, while the conformal lapse is given by $\tilde{N} = \psi^{-6}N$. Equations (7.5), (7.6),

and the trace of (7.4) can then be written as

$$\tilde{\nabla}^2\psi - \frac{1}{8}\psi\tilde{R} - \frac{1}{12}\psi^5 K^2 + \frac{1}{8}\psi^{-7}\tilde{A}_{ij}\tilde{A}^{ij} = 0, \tag{7.9}$$

$$\tilde{\nabla}_j\left(\frac{1}{2\tilde{N}}\left(\mathbb{L}\beta\right)^{ij}\right) - \tilde{\nabla}_j\left(\frac{1}{2\tilde{N}}\tilde{u}^{ij}\right) - \frac{2}{3}\psi^6\tilde{\nabla}^i K = 0, \tag{7.10}$$

$$\tilde{\nabla}^2\left(\tilde{N}\psi^7\right) - \left(\tilde{N}\psi^7\right)\left(\frac{1}{8}\tilde{R} + \frac{5}{12}\psi^4 K^2 + \frac{7}{8}\psi^{-8}\tilde{A}_{ij}\tilde{A}^{ij}\right) = -\psi^5\left(\partial_t K - \beta^k\partial_k K\right). \tag{7.11}$$

In the above, $\tilde{\nabla}_i$ is the covariant derivative compatible with $\tilde{g}_{ij}$, $\tilde{R} = \tilde{g}^{ij}\tilde{R}_{ij}$ is the trace of the Ricci tensor $\tilde{R}_{ij}$ of $\tilde{g}_{ij}$, $\tilde{\mathbb{L}}$ is the longitudinal operator,

$$\left(\tilde{\mathbb{L}}\beta\right)^{ij} = \tilde{\nabla}^i\beta^j + \tilde{\nabla}^j\beta^i - \frac{2}{3}\tilde{g}^{ij}\tilde{\nabla}_k\beta^k, \tag{7.12}$$

and $\tilde{A}^{ij}$ is

$$\tilde{A}^{ij} = \frac{1}{2\tilde{N}}\left(\left(\tilde{\mathbb{L}}\beta\right)^{ij} - \tilde{u}^{ij}\right), \tag{7.13}$$

which is related to K_{ij} by

$$K_{ij} = \psi^{-10}\tilde{A}_{ij} + \frac{1}{3}g_{ij}K. \tag{7.14}$$

For given $\tilde{g}_{ij}$, $\tilde{u}_{ij}$, K, and $\partial_t K$, Eqs. (7.9), (7.10), and (7.11) are a coupled set of elliptic equations that can be solved for ψ, $\tilde{N}$, and β^i. From these solutions, the physical initial data g_{ij} and K_{ij} are obtained from (7.7) and (7.14), respectively.

To construct initial data describing a Kerr black hole initially in equilibrium, together with an ingoing pulse of gravitational waves, we make the following choices for the free data,

$$\tilde{g}_{ij} = g^{\mathrm{KS}}_{ij} + Ah_{ij}, \tag{7.15}$$

$$\tilde{u}_{ij} = A\partial_t h_{ij} - \frac{1}{3}\tilde{g}_{ij}\tilde{g}^{kl}A\partial_t h_{kl}, \tag{7.16}$$

$$K = K^{KS}, \tag{7.17}$$

$$\partial_t K = 0. \tag{7.18}$$

In the above, g^{KS}_{ij} and K^{KS} are the spatial metric and the trace of the extrinsic curvature in Kerr-Schild coordinates, with mass parameter $M_{\mathrm{KS}} = 1$ and spin parameter $a_{\mathrm{KS}} = 0.7M_{\mathrm{KS}}$ along the z-direction. The pulse of gravitational waves is denoted by h_{ij}, and is chosen to be an ingoing, even parity, $m = 2$, linearized quadrupole wave in a *flat* background as given by Teukolsky [25] (see [26] for the solution for all multipoles). The explicit expression for

the spacetime metric of the waves in spherical coordinates is

$$\begin{aligned} h_{ij}dx^i dx^j = &\left(R_1 \sin^2\theta\cos 2\phi\right) dr^2 \\ &+ 2R_2 \sin\theta\cos\theta\cos 2\phi r dr d\theta \\ &- 2R_2 \sin\theta\sin 2\phi r \sin\theta dr d\phi \\ &+ \left[R_3\left(1+\cos^2\theta\right)\cos 2\phi - R_1\cos 2\phi\right] r^2 d^2\theta \\ &+ \left[2\left(R_1 - 2R_3\right)\cos\theta\sin 2\phi\right] r^2\sin\theta d\theta d\phi \\ &+ \left[-R_3\left(1+\cos^2\theta\right)\cos 2\phi + R_1\cos^2\theta\cos 2\phi\right] r^2\sin^2\theta d^2\phi, \end{aligned} \tag{7.19}$$

where the radial functions are

$$R_1 = 3\left[\frac{F^{(2)}}{r^3} + \frac{3F^{(1)}}{r^4} + \frac{3F}{r^5}\right], \tag{7.20}$$

$$R_2 = -\left[\frac{F^{(3)}}{r^2} + \frac{3F^{(2)}}{r^3} + \frac{6F^{(1)}}{r^4} + \frac{6F}{r^5}\right], \tag{7.21}$$

$$R_3 = \frac{1}{4}\left[\frac{F^{(4)}}{r} + \frac{2F^{(3)}}{r^2} + \frac{9F^{(2)}}{r^3} + \frac{21F^{(1)}}{r^4} + \frac{21F}{r^5}\right], \tag{7.22}$$

and the shape of the waves is determined by

$$F = F(t+r) = F(x) = e^{-(x-x_0)^2/w^2}, \tag{7.23}$$

$$F^{(n)} \equiv \left[\frac{d^n F(x)}{dx^n}\right]_{x=t+r}. \tag{7.24}$$

We choose F to be a Gaussian of width $w/M_{\rm KS} = 1.25$, at initial radius $x_0/M_{\rm KS} = 15$. The constant A in Eq. (7.15) is the amplitude of the waves. We use the values $A = 0.1$, 0.2, 0.3, 0.4, and 0.5, each resulting in a separate initial data set.

Equations (7.9), (7.10), and (7.11) are solved with the pseudospectral elliptic solver described in [27]. The domain decomposition used in the elliptic solver consists of three spherical shells with boundaries at radii $r/M_{\rm KS} = 1.5$, 12, 18, and 10^9, so that the middle shell is centered on the initial location of the gravitational wave pulse. The inner boundary lies inside the apparent horizon and Dirichlet boundary conditions appropriate for the Kerr black hole are imposed. It should be noted that these boundary conditions are only strictly appropriate in the limit of small A and large x_0, when the initial data corresponds to an ingoing pulse of linearized gravitational waves on an asymptotically flat background, with a Kerr black hole at the origin. As A is increased and x_0 is reduced, we expect this property to remain qualitatively true, although these boundary conditions become physically less well

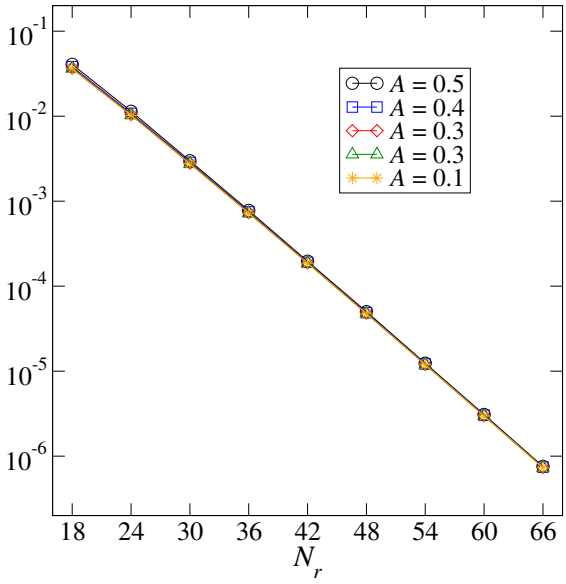

Figure 7.1: Convergence of the elliptic solver for different amplitudes A. Plotted is the square-sum of the Hamiltonian and momentum constraints, Eqs. (7.5) and (7.6), as a function of numerical resolution, measured here by the number of radial basis functions in the spherical shell containing the gravitational waves.

motivated. Nonetheless, we show below by explicit evolution that most of the energy in the pulse moves inward and increases the black hole mass.

At the lowest resolution, the number of radial basis functions in each shell is (from inner to outer) $N_r = 9$, 18, and 9, and the number of angular basis functions in each shell is $L = 5$. At the highest resolution, the number of radial basis functions in each shell is (from inner to outer) $N_r = 41$, 66, and 41, and the number of angular basis functions in each shell is $L = 21$. Figure 7.1 shows the convergence of the elliptic solver. The expected exponential convergence is clearly visible. Curves for each A lie very nearly on top of each other, indicating that convergence is independent of the amplitude of the waves. We evolve the initial data sets computed at the highest resolution of the elliptic solver.

We locate the apparent horizon (the outermost marginally outer trapped surface defined in section 7.4.1) in each initial data set using the pseudospectral flow method of Gundlach [28] (explained briefly in section 7.4.2), and compute the black hole's initial quasilocal angular momentum S_i and Christodoulou mass M_i (the subscript "i" denotes initial values). The quasilocal angular momentum S is defined in Eq. (7.48), which we calculate with

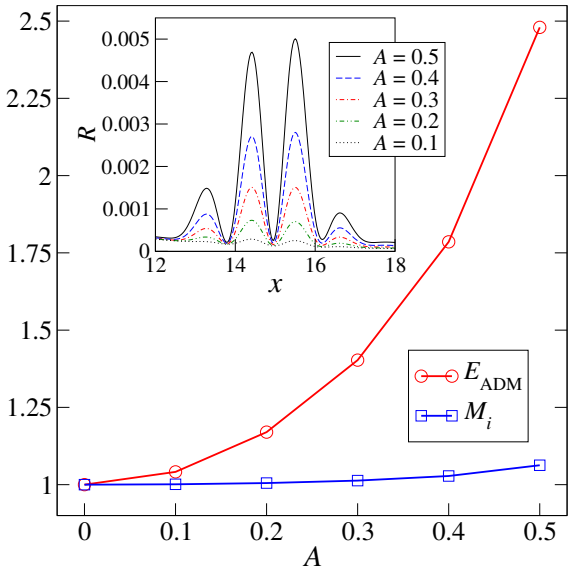

Figure 7.2: ADM energy $E_{\rm ADM}$ and Christodoulou mass M_i of the initial data sets, versus the gravitational wave amplitude A. The inset shows the Ricci scalar R along the x-axis. All quantities are given in units of the mass of the background Kerr-Schild metric.

approximate Killing vectors [29] (see also [30]). The Christodoulou mass M is given by

$$M = \sqrt{{M_{\rm H}}^2 + \frac{S^2}{4{M_{\rm H}}^2}}, \tag{7.25}$$

where $M_{\rm H} = \sqrt{A_{\rm H}/16\pi}$ is the Hawking or irreducible mass [31], with $A_{\rm H}$ being the area of the marginally outer trapped surface of interest. The main panel of Fig. 7.2 shows M and the Arnowitt-Deser-Misner (ADM) energy $E_{\rm ADM}$, as a function of the amplitude A of each initial data set. The difference between $E_{\rm ADM}$ and M is a measure of the energy contained in the ingoing gravitational waves. For $A \gtrsim 0.4$, this energy is comparable to or greater than M, so the black hole will become strongly distorted in the subsequent evolution. The inset of Fig. 7.2 shows the Ricci scalar R of g_{ij} along the x-axis at the initial location of the gravitational wave pulse. The sharp features of R necessitate the use of the higher N_r as labeled in Fig. 7.1.

7.3 Evolutions

Each of the initial data sets are evolved with the Spectral Einstein Code (`SpEC`) described in [32, 33]. This code solves a first-order representation [34] of the generalized harmonic

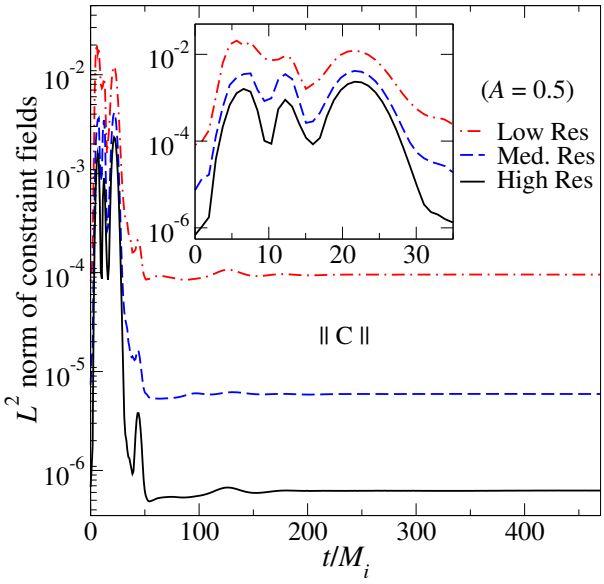

Figure 7.3: Constraint violations for the evolution with $A = 0.5$. Plotted is the L^2 norm of all constraints, normalized by the L^2 norm of the spatial gradients of all dynamical fields.

system [35, 36, 37]. The gauge freedom in the generalized harmonic system is fixed via a freely specifiable gauge source function H_μ that satisfies

$$H_\mu(t,x) = g_{\mu\nu}\nabla_\lambda\nabla^\lambda x^\nu = -\Gamma_\mu, \tag{7.26}$$

where $\Gamma_\mu = g^{\nu\lambda}\Gamma_{\mu\nu\lambda}$ is the trace of the Christoffel symbol. In 3+1 form, the above expression gives evolution equations for N and β^i [34],

$$\partial_t N - \beta^i\partial_i N = -N\left(H_t - \beta^i H_i + NK\right), \tag{7.27}$$

$$\partial_t\beta^i - \beta^k\partial_k\beta^i = Ng^{ij}\left[N\left(H_j + g^{kl}\Gamma_{jkl}\right) - \partial_j N\right], \tag{7.28}$$

so there is no loss of generality in specifying H_μ instead of N and β^i, as is more commonly done. For our evolutions, H_μ is held fixed at its initial value.

The decomposition of the computational domain consists of eight concentric spherical shells surrounding the black hole. The inner boundary of the domain is at $r/M_{\rm KS} = 1.55$, inside the apparent horizon of the initial black hole, while the outer boundary is at $r/M_{\rm KS} = 50$. The outer boundary conditions [34, 38, 39] are designed to prevent the influx of unphysical constraint violations [40, 41, 42, 43, 44, 45, 46] and undesired incoming gravitational radiation [47, 48], while allowing the outgoing gravitational radiation to pass

freely through the boundary. Interdomain boundary conditions are enforced with a penalty method [49, 50]. The evolutions were run on up to three different resolutions–low, medium, and high. For the low resolution, the number of radial basis functions in each shell is $N_r = 23$, and the number of angular basis functions in each shell is $L = 15$. For the high resolution, $N_r = 33$ and $L = 21$ in each shell.

We will be mainly interested in the case where the gravitational waves have an amplitude $A = 0.5$. As a measure of the accuracy of this evolution, the constraints of the first-order generalized harmonic system are plotted in Fig. 7.3. Plotted is the L^2 norm of all constraint fields, normalized by the L^2 norm of the spatial gradients of the dynamical fields (see Eq. (71) of [34]). The L^2 norms are taken over the entire computational volume. The constraints increase at first, as the black hole is distorted by the gravitational waves. As the black hole settles down to equilibrium, the constraints decay and level off. The results presented in the following sections use data from the high resolution runs only.

7.4 Marginally Trapped Surfaces

7.4.1 Basic Definitions and Concepts

Let $\mathcal{S}$ be a closed, orientable spacelike 2-surface in Σ_t. There are two linearly independent and future-directed outgoing and ingoing null vectors l^μ and k^μ normal to $\mathcal{S}$. We write these vectors in terms of the future-directed timelike unit normal n^μ to Σ_t and the outward-directed spacelike unit normal s^μ to $\mathcal{S}$ as

$$l^\mu = \frac{1}{\sqrt{2}}\left(n^\mu + s^\mu\right) \quad \text{and} \quad k^\mu = \frac{1}{\sqrt{2}}\left(n^\mu - s^\mu\right), \tag{7.29}$$

normalized so that $g_{\mu\nu} l^\mu k^\nu = -1$. Then the induced metric $\bar{q}_{\mu\nu}$ on $\mathcal{S}$ is

$$\bar{q}_{\mu\nu} = g_{\mu\nu} + l_\mu k_\nu + l_\nu k_\mu, \tag{7.30}$$

$$= g_{\mu\nu} + n_\mu n_\nu - s_\mu s_\nu. \tag{7.31}$$

The extrinsic curvatures of $\mathcal{S}$ as embedded in the full four-dimensional spacetime are

$$\bar{K}^{(l)}_{\mu\nu} = \bar{q}^\lambda_\mu \bar{q}^\rho_\nu \nabla_\lambda l_\rho \quad \text{and} \quad \bar{K}^{(k)}_{\mu\nu} = \bar{q}^\lambda_\mu \bar{q}^\rho_\nu \nabla_\lambda k_\rho. \tag{7.32}$$

The null vectors l^μ and k^μ are tangent to a congruence of outgoing and ingoing null geodesics,

respectively. The traces of the extrinsic curvatures give the congruences' *expansions*

$$\theta_{(l)} = \bar{q}^{\mu\nu}\nabla_\mu l_\nu \;\text{ and }\; \theta_{(k)} = \bar{q}^{\mu\nu}\nabla_\mu k_\nu, \tag{7.33}$$

and the *shears* are the trace-free parts,

$$\sigma^{(l)}_{\mu\nu} = \bar{q}^\lambda_\mu \bar{q}^\rho_\nu \nabla_\lambda l_\rho - \frac{1}{2}\bar{q}_{\mu\nu}\theta_{(l)} \;\text{ and} \tag{7.34}$$

$$\sigma^{(k)}_{\mu\nu} = \bar{q}^\lambda_\mu \bar{q}^\rho_\nu \nabla_\lambda k_\rho - \frac{1}{2}\bar{q}_{\mu\nu}\theta_{(k)}. \tag{7.35}$$

The geometrical interpretation of the expansion is the fractional rate of change of the congruence's cross-sectional area [17]. We will mainly be interested in 2-surfaces $\mathcal{S}$ on which $\theta_{(l)} = 0$, called *marginally outer trapped surfaces* (MOTSs) following the terminology in [20]. If $\theta_{(l)} < 0$ on $\mathcal{S}$, then outgoing null normals will be converging toward each other, as one expects to happen inside a black hole. If $\theta_{(l)} > 0$ the situation is reversed, so the condition $\theta_{(l)} = 0$ provides a reasonable quasilocal prescription for identifying the surface of a black hole. In practice, an MOTS will generally lie inside the event horizon, unless the black hole is stationary. The outermost MOTS is called the *apparent horizon*, and is used to represent the surface of a black hole in numerical simulations. In the next subsection, we briefly describe how we locate MOTSs.

7.4.2 MOTS Finders

We use two different algorithms to locate MOTSs in Σ_t. Both algorithms expand an MOTS "height function" in spherical harmonics

$$r_{\rm MOTS}(\theta,\phi) = \sum_{l=0}^{L_{\rm MOTS}} \sum_{m=-l}^{l} A_{lm} Y_{lm}(\theta,\phi). \tag{7.36}$$

Our standard algorithm is the pseudospectral fast flow method developed by Gundlach [28], which we use during the evolution. This method utilizes the fact that the MOTS condition $\theta_{(l)} = 0$ results in an elliptic equation for $r_{\rm MOTS}(\theta,\phi)$. The elliptic equation is solved using a fixed-point iteration with the flat-space Laplacian on S^2 on the left-hand side, which is computationally inexpensive to invert given the expansion Eq. (7.36). The fixed-point iteration is coupled to parameterized modifications which allow for tuning of the method to achieve fast, but still reasonably robust convergence. In Gundlach's nomenclature, we use the N flow method, and have found the parameters $\alpha = 1$ and $\beta = 0.5$ satisfactory (see [28]

for definitions).

Gundlach's algorithm (as well as MOTS finders based on flow methods in general [51, 52]) incorporates a sign assumption on the surfaces near the MOTS, namely that $\theta_{(l)}$ is *positive* for a surface which lies somewhat *outside* of the MOTS. This assumption is satisfied for the apparent horizon. However, this sign assumption is not satisfied for some inner MOTSs in Σ_t that we discover below. Therefore, these inner MOTSs are unstable fixed-points for Gundlach's algorithm, so that this algorithm cannot locate these MOTSs.

To find these inner MOTSs, we employ an older algorithm that is based on a minimization technique [53, 54, 55]: The coefficients A_{lm} in Eq. (7.36) are determined by minimizing the functional

$$\Theta \equiv \int_{\mathcal{S}} \theta_{(l)}^2 \sqrt{\bar{q}} d^2x, \tag{7.37}$$

where the surface integral is over the current trial surface with area element $\sqrt{\bar{q}}$. This technique is insensitive to the sign assumption in Gundlach's method. However, it is much slower, especially for large L_{MOTS}.

When multiple MOTSs are present in Σ_t, the choice of an initial surface determines the final surface the MOTS finder converges to. Therefore, both MOTS finders require judicious choices of these initial surfaces. We typically track MOTSs from time step to time step, and use the MOTS at the previous time step as an initial guess for the MOTS finder at the current time.

7.5 Marginally Trapped Tubes

7.5.1 Basic Definitions and Concepts

During an evolution, the MOTSs found at successive times foliate a world tube, or a *marginally trapped tube* (MTT). The type of MTT that is foliated by a series of MOTSs depends on the physical situation. A null MTT is an *isolated horizon* [12, 13, 56, 11, 57] if $-R_{\mu\nu}l^\nu$ is future causal, and certain quantities are time independent on it. An isolated horizon describes a black hole in equilibrium. On the other hand, a *dynamical horizon* describes a black hole that is absorbing matter or gravitational radiation [14, 15], and is physically the most relevant. A dynamical horizon is a spacelike MTT foliated by MOTSs on which $\theta_{(k)} < 0$, called *future marginally outer trapped surfaces*. For a given slicing of spacetime by spatial hypersurfaces Σ_t, the foliation of a dynamical horizon by future marginally outer trapped surfaces on Σ_t is unique [16]. Since the location of a MOTS is a property of Σ_t,

different spacetime slicings will in general give different MTTs. Also, a timelike MTT is called a *timelike membrane* [58]. Since causal curves can traverse it in both inward and outward directions, it cannot represent the surface of a black hole.

An additional characterization of MTTs is based on trapping horizons [9]. A *future outer trapping horizon* is an MTT foliated by MOTSs that have $\theta_{(k)} < 0$ and $\mathcal{L}_k\theta_{(l)} < 0$ for some scaling of l^μ and k^μ. Such an MOTS is called a *future outer trapping surface*. If the null energy condition holds, a future outer trapping horizon is either completely null or completely timelike. It was shown in [59] that if $\mathcal{L}_k\theta_{(l)} \neq 0$ for at least one point on these future outer trapping surfaces, then the future outer trapping horizon is spacelike, or a dynamical horizon, in a neighborhood of the future outer trapping surfaces. Otherwise the future outer trapping horizon is null.

Interestingly, an MTT may not fall into either of the categories described above, but can have sections of mixed signatures as demonstrated in the head-on collision of two black holes [20]. At merger, a common apparent horizon appears in Σ_t that surrounds the MOTSs of the individual black holes. This common horizon then bifurcates into outer and inner common horizons. The outer common horizon grows in area and is spacelike. However, the inner common horizon decreases in area and foliates an MTT that is briefly partly spacelike and partly timelike, before becoming a timelike membrane later on.

7.5.2 Multiple MTTs

We now discuss the MOTSs that occur during the five evolutions of the distorted black hole, with amplitude $A = 0.1$, 0.2, 0.3, 0.4, or 0.5 for the ingoing gravitational wave pulse. The MOTSs we find are indicated in Fig. 7.4 by their Christodoulou masses M. Early in each simulation, M is approximately constant, and begins to increase when the gravitational wave hits the black hole around $t \approx 12M_i$. The effect is more pronounced for larger A. The horizontal dotted lines in Fig. 7.4 indicate the ADM energy of the initial data. Although we do not explicitly calculate the energy carried away by gravitational waves, we can still see that the final *Christodoulou* mass is close to $E_{\rm ADM}$, indicating that the energy in the gravitational wave pulse predominantly falls into the black hole, and only a small fraction of this energy propagates to null infinity. Even for the highest amplitude case of $A = 0.5$, the final value of M is about 99.1% of the ADM energy. These results are as expected. However, for both $A = 0.4$ and $A = 0.5$, a very interesting new feature arises: *multiple* concentric MOTSs are present at the *same* coordinate time.

The evolution with $A = 0.5$ shows the multiple MOTSs more distinctly, hence we will

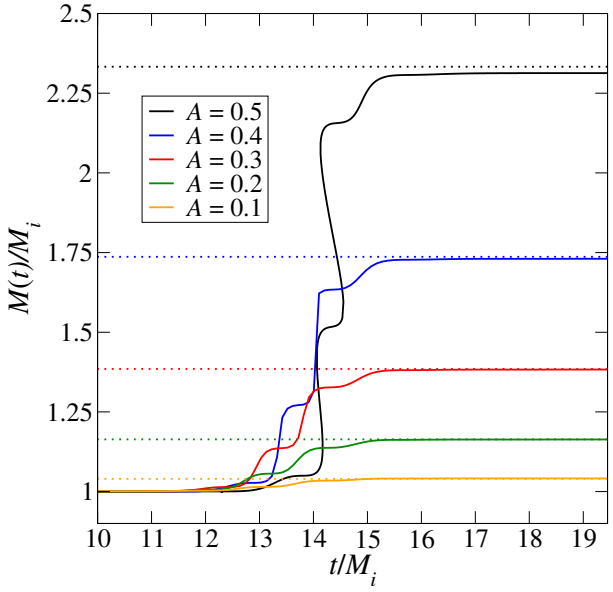

Figure 7.4: The solid curves are the Christodoulou masses $M(t)$ divided by their initial values M_i for the five evolutions with different amplitudes $A = 0.1$, 0.2, 0.3, 0.4, and 0.5 for the ingoing pulse of gravitational waves. The horizontal dotted lines denote the ADM energy of each data set, $E_{\rm ADM}/M_i$.

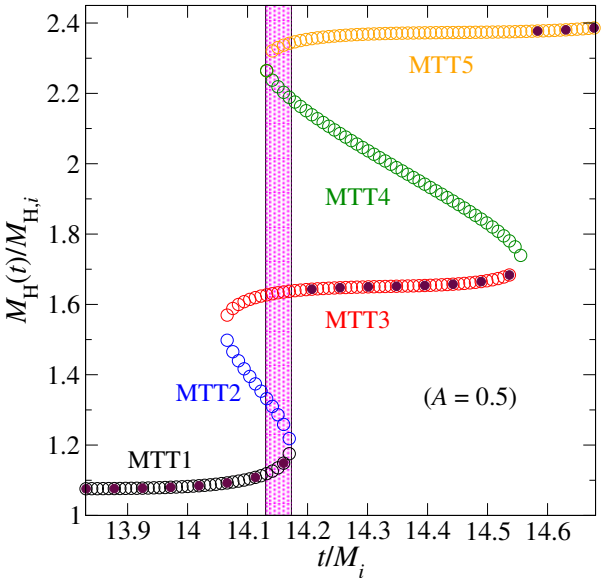

Figure 7.5: Irreducible mass $M_{\rm H}$ divided by its initial value $M_{{\rm H},i}$ for the evolution with $A = 0.5$. The solid circles are the values of $M_{\rm H}$ for MOTSs found during the evolution. The completed curve is traced out by open circles. The vertical shaded region indicates when five MOTSs exist at the same time.

focus on it in the remainder of this chapter. Figure 7.5 presents a closer look at the *irreducible* masses $M_{\rm H}$ for this case. Locating all MOTSs shown in Fig. 7.5 requires considerable care. The starting point was the output of the MOTS finder that was run during the evolution, using Gundlach's fast flow algorithm [28]. Because of the computational expense involved, the MOTS finder was not run very frequently, resulting in the solid circles in Fig. 7.5. The MOTS at the previous time was used as the initial guess for the current time, resulting in a series of MOTSs which is as continuous as possible. The curve traced out by these points has sharp jumps, which was the first indication of the presence of multiple MOTSs at these times. Then to find the remainder of MTT3 and MTT5, an MOTS corresponding to one of these solid circles on MTT3 or MTT5 was used as an initial guess and the MOTS finder was also run more frequently. At this stage, we had completely traced out MTT1, MTT3, and MTT5. Next we found MTT2 and MTT4 to be unstable fixed points for Gundlach's algorithm, so it was necessary to use our older MOTS finder based on a minimization technique [53, 54, 55] to find these MTTs. As an initial guess for finding an MOTS on MTT2 for instance, a sphere with radius equal to the average radii of MTT1 and MTT3 sufficed. Once an MOTS on MTT2 was located, it was used as an initial guess for the MOTS finder to locate the MOTSs on neighboring time slices (both later and earlier). The same procedure was used to locate MTT4.

After finding all the MTTs in Fig. 7.5, a clearer picture of their structures in relation to each other emerged. MTT1 corresponds to the surface of the initial black hole. Shortly after $t = 14M_i$, a new MOTS with $M_{\rm H}/M_{{\rm H},i} \approx 1.525$ appears and bifurcates into two MTTs. $M_{\rm H}$ decreases along MTT2, which promptly annihilates with MTT1, while MTT3 persists slightly longer. A similar process then takes place again, and MTT5 is left over as the surface of the final black hole, with $M_{\rm H}$ more than double its initial value. The vertical shaded region indicates the time interval when five MTTs exist simultaneously. Notice that $M_{\rm H}$ of the apparent horizon jumps discontinuously in time from the curve of MTT1 to MTT3, and then to MTT5. This indicates that the apparent horizon itself is discontinuous across these times.

The apparent horizon is the outermost MOTS, and when only one MOTS is present in a black hole evolution, the MOTS and apparent horizon are identical. Here this is not the case, and Fig. 7.6 shows the apparent horizon in relation to the various MTTs. This figure also highlights another potential pitfall when locating MOTSs. MOTS finders are typically run during the evolution fairly infrequently, using the MOTS from the last MOTS computation as an initial guess (to minimize computational cost). If this had been done for

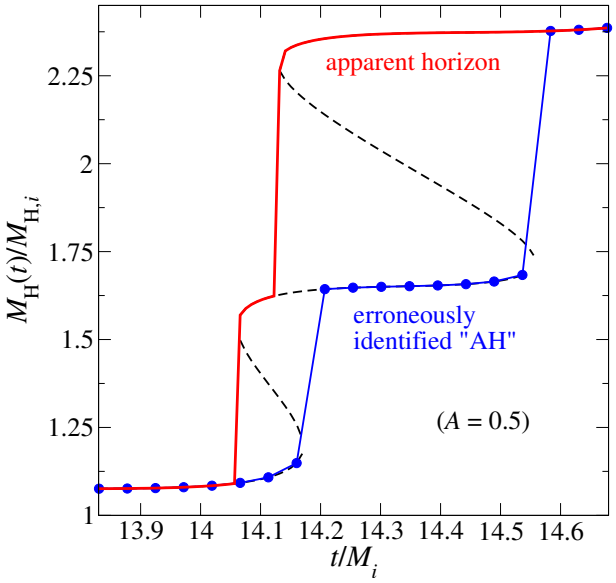

Figure 7.6: The solid red line denotes the apparent horizon for the evolution with $A = 0.5$. The solid blue circles denote an erroneous "apparent horizon," which is found when the apparent horizon finder is run during the evolution in larger time intervals. The black dashed lines denotes all five MTTs as shown in Fig. 7.5.

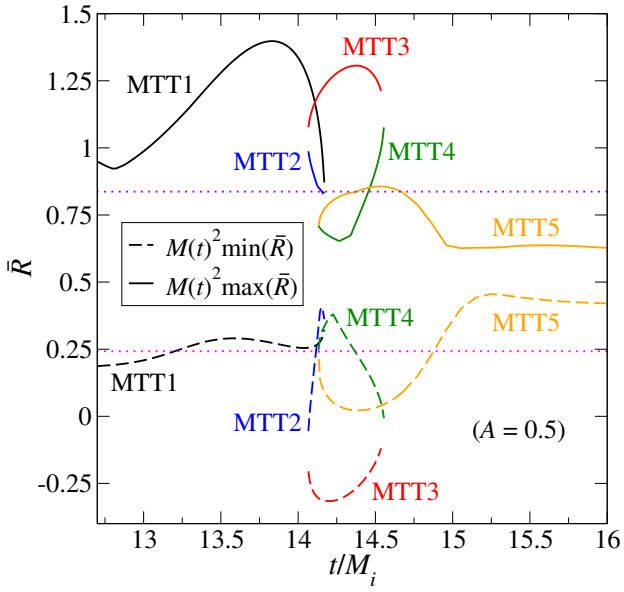

Figure 7.7: Extrema of the intrinsic scalar curvature $\bar{R}$ of MOTSs during the evolution with $A = 0.5$. The horizontal dotted lines are the values for the apparent horizon in the initial data. Around $t = 14.25M_i$, the MOTSs have regions of negative $\bar{R}$.

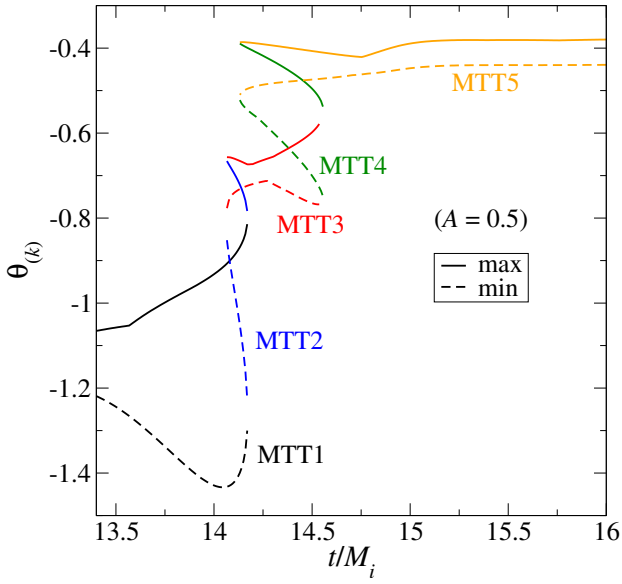

Figure 7.8: Extrema of $\theta_{(k)}$ on each MOTS along the MTTs during the evolution with $A = 0.5$. For the time shown, $\theta_{(k)} < 0$.

the $A = 0.5$ case shown in Figs. 7.5 and 7.6, the solid blue circles would have been obtained. Because the previously found MOTS is used as an initial guess, newly appearing MOTSs are generally missed. For instance, the solid blue circles follow MTT1 until it disappears, instead of jumping to MTT3. Therefore, the output of the "apparent horizon finder" (the more widely used name, but technically less precise than "MOTS finder"), is sometimes *not* the apparent horizon.

A measure of the distortion of the black hole is provided by the intrinsic scalar curvature $\bar{R}$ of the MOTSs. The extrema of $\bar{R}$ is shown in Fig. 7.7, along with those of the initial apparent horizon. It is interesting to point out that around $t = 14.25M_i$, the distortion caused by the gravitational waves with $A = 0.5$ is sufficiently strong to produce regions of negative $\bar{R}$.

7.5.3 Dynamical Horizons

We determine the signatures of the multiple MTTs during the highly dynamical period. First we compute $\theta_{(k)}$ and $\mathcal{L}_k\theta_{(l)}$ using the null normals in Eq. (7.29), and find that both quantities are negative. So our MTTs are future outer trapping horizons, which must be either spacelike or null, and we can immediately rule out the possibility of there being sections of mixed signatures. Figure 7.8 shows the extrema of $\theta_{(k)}$ along each MTT. The

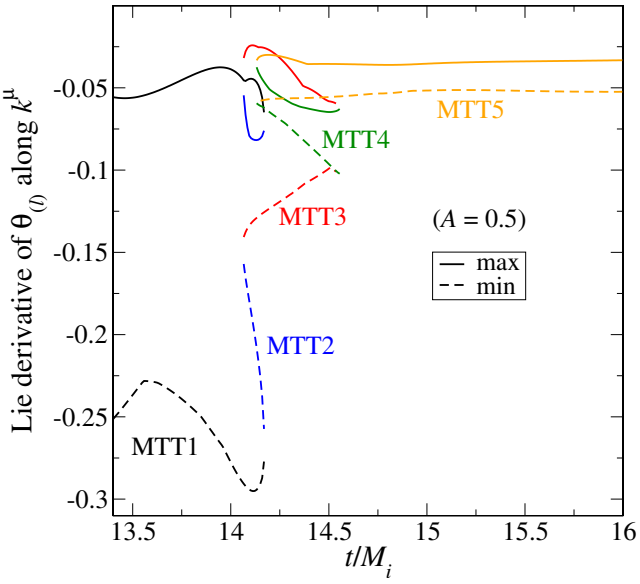

Figure 7.9: Extrema of $\mathcal{L}_k\theta_{(l)}$ on each MOTS along the MTTs during the evolution with $A = 0.5$. For the time shown, $\mathcal{L}_k\theta_{(l)} < 0$.

quantity $\mathcal{L}_k\theta_{(l)}$ is evaluated from the expression [59]

$$\mathcal{L}_k\theta_{(l)} = -\bar{R}/2 + \omega_\mu\omega^\mu - d_\mu\omega^\mu + 8\pi T_{\mu\nu}l^\mu k^\nu, \tag{7.38}$$

where

$$\omega_\mu = -\bar{q}^\nu_\mu k_\lambda \nabla_\nu l^\lambda \tag{7.39}$$

is the *normal fundamental form*, and d_μ is the covariant derivative compatible with $\bar{q}_{\mu\nu}$. Figure 7.9 shows the extrema of $\mathcal{L}_k\theta_{(l)} < 0$ along each MTT.

Next we compute $\mathcal{L}_l\theta_{(l)}$ to determine whether the MTTs are spacelike or null. We evaluate this using the null Raychaudhuri equation [17],

$$\mathcal{L}_l\theta_{(l)} = -\sigma^{(l)\mu\nu}\sigma^{(l)}_{\mu\nu} - 8\pi T_{\mu\nu}l^\mu l^\nu. \tag{7.40}$$

Figure 7.10 shows that during the times when there are multiple MTTs, $\mathcal{L}_l\theta_{(l)} \neq 0$ somewhere on each MOTS. Thus all of the MTTs are dynamical horizons at these times.

Here we also mention the *extremality parameter* e of a MTT introduced in [60]. In

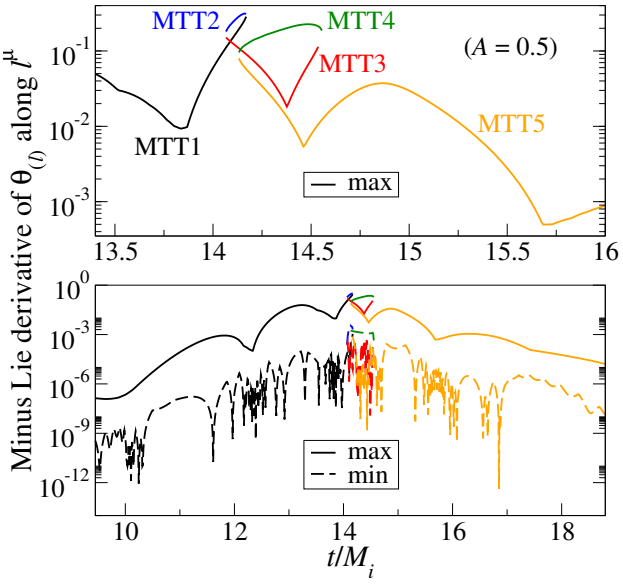

Figure 7.10: Extrema of $-\mathcal{L}_l\theta_{(l)}$ on each MOTS along the MTTs during the evolution with $A = 0.5$. Near $t = 14M_i$, $\mathcal{L}_l\theta_{(l)} \neq 0$ somewhere on $\mathcal{S}_v$.

vacuum, it is given by

$$e = \frac{1}{4\pi}\int_{\mathcal{S}} \omega_\mu \omega^\mu \sqrt{\bar{q}} d^2x, \tag{7.41}$$

$$= 1 + \frac{1}{4\pi}\int_{\mathcal{S}} \mathcal{L}_k\theta_{(l)} \sqrt{\bar{q}} d^2x, \tag{7.42}$$

where the integral is over an MOTS $\mathcal{S}$ that foliates the MTT. When $\mathcal{S}$ is axisymmetric, this can be regarded as the sum of the squares of all angular momentum multipoles. Because a future outer trapping horizon, which is either spacelike or null, has $\mathcal{L}_k\theta_{(l)} < 0$, it is always subextremal ($e < 1$). So a timelike membrane foliated by future MOTSs (with $\theta_{(k)} < 0$) must have $\mathcal{L}_k\theta_{(l)} > 0$, and is superextremal ($e > 1$). Therefore, it was suggested in [60] that an MTT's transition from being spacelike to timelike can be detected when $e \to 1$.

Figure 7.11 shows e along each MTT, and we see that nowhere does $e \to 1$, confirming that our MTTs do not become timelike. The value of e shows a substantial decrease after the distortion has left, which is not due to a loss of quasilocal angular momentum J (defined in Eq. (7.48)), but to the large gain in irreducible mass $M_{\rm H}$. It may seem that e in Fig. 7.11 is already rather small to start out with, but one must recall that e depends on the scaling of the null normals l^μ and k^μ. That is, we can define new null normals $\bar{l}^\mu = f l^\mu$ and $\bar{k}^\mu = k^\mu/f$, rescaled by some function f such that the normalization $\bar{l}^\mu \bar{k}_\mu = -1$ is preserved. Then e

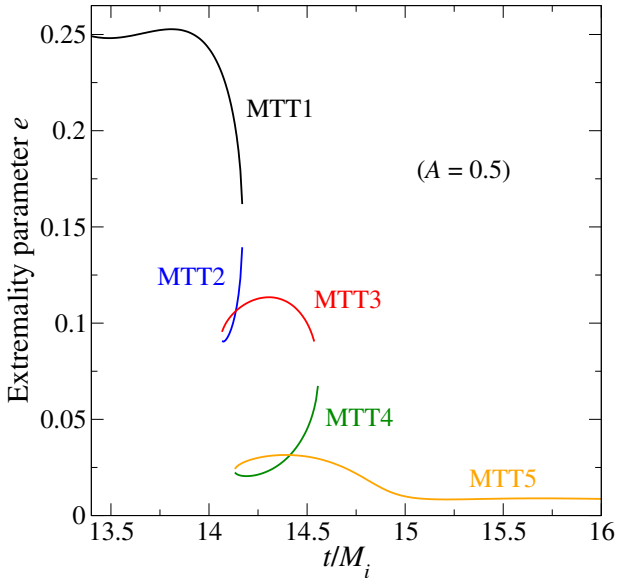

Figure 7.11: Extremality parameter e along the MTTs during the evolution with $A = 0.5$. For the time shown, the MTTs are subextremal with $e < 1$, indicating that the MTTs have no timelike sections.

will change as

$$\bar{e} = e + \frac{1}{4\pi}\int_{\mathcal{S}} [2\omega^\mu d_\mu \ln f + (d_\mu \ln f)(d^\mu \ln f)]\ \sqrt{\bar{q}}d^2x. \tag{7.43}$$

Nevertheless, the extremality classification of the MTTs is invariant.

It is known that the irreducible mass $M_{\rm H}$ of an MOTS must increase along a dynamical horizon [15], so at first it may seem surprising that MTT2 and MTT4, with decreasing $M_{\rm H}$ during the evolution, are also dynamical horizons. However, all these MTTs can be viewed as sections of a single dynamical horizon $\mathcal{H}$ that weaves forwards and backwards in time. Then it is clear that the tangent vector to $\mathcal{H}$ along MTT2 and MTT4 points backwards in time, so that $M_{\rm H}$ is actually increasing along $\mathcal{H}$ as expected. Our simple choice of holding the gauge source function H_μ equal to its initial value leads to a spacetime foliation that interweaves $\mathcal{H}$. This could be avoided by an alternative choice of H_μ that results in a single dynamical horizon that only grows in time.

The situation here resembles an example of a Tolman-Bondi spacetime considered in [19], where multiple spherically symmetric dust shells fall into a black hole. For their chosen matter distribution, multiple MTTs also formed (up to three at the same time), which were either completely spacelike, or null when the matter density vanished between successive dust shells. In our case the role of the matter density is replaced by the shear $\sigma^{(l)}_{\mu\nu}$ due to the gravitational waves. Since this is always nonvanishing somewhere on the multiple MTTs

that form, we only have dynamical horizons.

In [16], it was shown that for a regular dynamical horizon (which is achronal and also a future outer trapping horizon), no weakly trapped surface (on which $\theta_{(l)} \leq 0$ and $\theta_{(k)} \leq 0$) can exist in its past domain of dependence. This helps to explain the difficulty in locating MOTSs along MTT2 and MTT4 using flow methods. For example, consider locating an MOTS on MTT2 at $t = 14.1M_i$ shown in Fig. 7.5. If we use a trial surface $\mathcal{S}$ located between the MOTSs on MTT1 and MTT2, it must have $\theta_{(l)} > 0$ because it lies in the past domain of dependence of $\mathcal{H}$. This means that $\mathcal{S}$ will be moved inwards when using flow methods, away from MTT2. If we switch to having $\mathcal{S}$ lie between the MOTSs on MTT2 and MTT3, then having $\theta_{(l)} > 0$ is desired. Unfortunately, now $\mathcal{S}$ lies in the future domain of dependence of $\mathcal{H}$, and we are no longer guaranteed that $\mathcal{S}$ is not a weakly trapped surface.

7.5.4 Dynamical Horizon Flux Law

The growth of a black hole in full, nonlinear general relativity can be described by the dynamical horizon flux law of Ashtekar and Krishnan [14, 15], which relates the increase in area or mass along a dynamical horizon to fluxes of matter and gravitational energy across it. Here, we will evaluate this flux law for the dynamical horizon $\mathcal{H}$ that consists of the multiple MTT sections we found earlier, using the form given in [59].

To state the dynamical horizon flux law, let us specifically consider the change in the irreducible mass $M_{\rm H}$ along $\mathcal{H}$. Denote an MOTS that foliates $\mathcal{H}$ by $\mathcal{S}_v$, which is labeled by a foliation parameter v that is constant on $\mathcal{S}_v$. Then choose a tangent vector V^μ to $\mathcal{H}$ that is normal to each $\mathcal{S}_v$, and such that

$$\mathcal{L}_V v = 1. \tag{7.44}$$

This vector V^μ can be written as

$$V^\mu = \bar{B}\bar{l}^\mu - \bar{C}\bar{k}^\mu, \tag{7.45}$$

in terms of coefficients $\bar{B}$ and $\bar{C}$, and null normals $\bar{l}^\mu = f l^\mu$ and $\bar{k}^\mu = k^\mu/f$ that are rescaled by a function f (but still having $\bar{l}^\mu \bar{k}_\mu = -1$) so that

$$\bar{C} = 2\frac{dM_{\rm H}}{dv}. \tag{7.46}$$

The dynamical horizon flux law is then

$$\frac{dM_{\rm H}}{dv} = \int_{\mathcal{S}_v} \left[T_{\mu\nu} \bar{l}^\mu \tau^\nu + \frac{\bar{B}}{8\pi} \sigma^{(\bar{l})}_{\mu\nu} \sigma^{(\bar{l})\mu\nu} + \frac{\bar{C}}{8\pi} \bar{\omega}_\mu \bar{\omega}^\mu \right] \sqrt{\bar{q}} d^2x, \tag{7.47}$$

where $\sigma^{(\bar{l})}_{\mu\nu}$ and $\bar{\omega}_\mu$ are given by Eqs. (7.34) and (7.39) but in terms of $\bar{l}^\mu$ and $\bar{k}^\mu$, and $\tau^\mu = \bar{B}\bar{l}^\mu + \bar{C}\bar{k}^\mu$ is the normal vector to $\mathcal{H}$.

The first term in Eq. (7.47) involving $T_{\mu\nu}$ is the energy flux of matter across $\mathcal{S}_v$, and the second term involving $\sigma^{(\bar{l})}_{\mu\nu}$ is a flux of gravitational energy [15]. The last term has been interpreted differently by various authors. The normal fundamental form ω_μ (or $\bar{\omega}_\mu$) enters into the definition of the quasilocal angular momentum S of a black hole mentioned at the end of section 7.2, which is given by [15],

$$S = -\frac{1}{8\pi} \int_{\mathcal{S}_v} \phi^\mu \omega_\mu \sqrt{\bar{q}} d^2x, \tag{7.48}$$

for any choice of rotation vector field ϕ^μ on $\mathcal{S}_v$. Because of this relation, this term has been interpreted as a flux of rotational energy [15, 20]. However, it has been pointed out in [59] that this is unlikely, as ω_μ is related to S itself and not its flux. Indeed, this may be illustrated by considering a Kerr black hole that is distorted by an ingoing spherically symmetric dust shell (which carries no angular momentum). So even though there will be no flux of rotational energy, the last term in Eq. (7.47) will still be nonzero whenever $\bar{C} \neq 0$, which is necessarily true on a dynamical horizon. This last term also closely resembles the extremality parameter e mentioned in section 7.5.3.

Another interpretation of the last term in Eq. (7.47) has been given by Hayward [61] as a flux of longitudinal gravitational radiation, by examining the components of an effective gravitational radiation energy tensor in spin-coefficient form. At future null infinity, the outgoing longitudinal gravitational radiation is negligible relative to the outgoing transverse radiation, but near the black hole this is generally not so.

To evaluate the dynamical horizon flux law, we first construct a tangent vector X^μ to $\mathcal{H}$ that connects $\mathcal{S}_v$ in Σ_t to $\mathcal{S}_{v'>v}$ in $\Sigma_{t'}$ as

$$X^\mu = \pm \left(1, \frac{\partial x^i_v}{\partial t} \right), \tag{7.49}$$

where x^i_v are the coordinates of $\mathcal{S}_v$, and the plus sign is for $t' > t$ while the minus sign is for $t' < t$. The latter occurs along MTT2 and MTT4. The spatial components of the tangent vector X^μ diverge when two MTT sections meet. This may be avoided by a different choice

of X^μ, but here we employ the simple one described above. For this reason, we also consider the corresponding foliation parameter v along each section of $\mathcal{H}$ separately. Since

$$\mathcal{L}_X v = \pm \frac{\partial v}{\partial t}, \tag{7.50}$$

and we would like this to be unity, it follows that $v = \pm t + v_0$, where v_0 is some constant along each MTT section. We choose $v = t$ along MTT1. Along the other MTT sections, we choose v_0 so that $v = 0$ on the first $\mathcal{S}_v$ we find on those sections.

Next we make X^μ orthogonal to $\mathcal{S}_v$ to obtain V^μ (while leaving the time component unchanged, so Eq. (7.44) is still satisfied with the choice of v described above). To achieve this, we use the unit tangent vectors to $\mathcal{S}_v$,

$$p^\mu = N_p \left(0, \frac{\partial x^i_v}{\partial \theta}\right) \text{ and } q^\mu = N_q \left(0, \frac{1}{\sin\theta}\frac{\partial x^i_v}{\partial \phi}\right). \tag{7.51}$$

Here, $x^i_v(\theta,\phi) = c^i_{\mathrm{MOTS}} + r_{\mathrm{MOTS}}(\theta,\phi) d^i(\theta,\phi)$ where $r_{\mathrm{MOTS}}(\theta,\phi)$ is given in Eq. (7.36) and d^i is the coordinate unit vector pointing from the origin c^i_{MOTS} of the expansion along the (θ,ϕ)-directions. Also, N_p and N_q are normalization factors such that $p^2 = q^2 = 1$. Orthogonalizing q^μ against p^μ gives the vector

$$Q^\mu = N_Q \left(q^\mu - p^\nu q_\nu p^\mu\right), \tag{7.52}$$

where N_Q is again a normalization factor such that $Q^2 = 1$. Then we obtain the desired tangent vector to $\mathcal{H}$ as

$$V^\mu = X^\mu - \left(p^\nu X_\nu\right) p^\mu - \left(Q^\nu X_\nu\right) Q^\mu. \tag{7.53}$$

This can be also be expressed in terms of our standard null normals of Eq. (7.29) as

$$V^\mu = B l^\mu - C k^\mu, \tag{7.54}$$

with coefficients $B = -V^\mu k_\mu$ and $C = V^\mu l_\mu$.

Now we determine the rescaled null normals $\bar{l}^\mu$ and $\bar{k}^\mu$ appearing in Eq. (7.45). Since V^μ must be the same vector whether it is written in terms of l^μ and k^μ, or $\bar{l}^\mu$ and $\bar{k}^\mu$, we have the relations

$$\bar{B} = B/f \text{ and } \bar{C} = fC, \tag{7.55}$$

which together with Eq. (7.46) gives

$$f = \frac{B}{\bar{B}} = \frac{\bar{C}}{C} = \frac{2}{C}\frac{dM_{\rm H}}{dv}. \tag{7.56}$$

Evaluating the scale factor f requires knowledge of $dM_{\rm H}/dv$. It is straightforward to show that the area element $\sqrt{\bar{q}}$ of $\mathcal{S}_v$ changes along $\mathcal{H}$ as

$$\mathcal{L}_V \sqrt{\bar{q}} = -C\theta_{(k)}\sqrt{\bar{q}}, \tag{7.57}$$

so the change in the cross-sectional area $A_{\rm H}$ along $\mathcal{H}$ is

$$\frac{dA_{\rm H}}{dv} = -\int_{\mathcal{S}_v} C\theta_{(k)}\,\sqrt{\bar{q}}d^2x. \tag{7.58}$$

From the definition $M_{\rm H} = \sqrt{A_{\rm H}/16\pi}$, it then follows that

$$\frac{dM_{\rm H}}{dv} = \frac{1}{\sqrt{64\pi A_{\rm H}}}\frac{dA_{\rm H}}{dv}. \tag{7.59}$$

The terms in the dynamical horizon flux law (7.47) are calculated by noting that under the rescaling of the null normals l^μ and k^μ,

$$\sigma^{(\bar{l})}_{\mu\nu} = f\sigma^{(l)}_{\mu\nu} \;\text{ and }\; \bar{\omega}_\mu = \omega_\mu + d_\mu \ln f. \tag{7.60}$$

The results are shown in Fig. 7.12 from $t = 10M_i$ to $t = 20M_i$. The energy flux of matter is neglected since we have $T_{\mu\nu} = 0$. The flux associated with $\bar{B}\sigma^{(\bar{l})}_{\mu\nu}\sigma^{(\bar{l})\mu\nu}$, labeled as "$\sigma^{(\bar{l})}$ flux," is always the larger contribution to the growth of $M_{\rm H}$, which is expected from the interpretation of this term as a flux of gravitational energy. This is most pronounced along MTT2 and MTT4, with decreasing $M_{\rm H}$ during the evolution, and clearly indicates that their appearance is a consequence of the sufficiently high gravitational energy flux across them. We have seen in section 7.5.2 that for weak gravitational waves and with the same gauge condition for the evolution, no such MTTs appear. The maximum number of MTTs that can exist at the same time may also be linked to the structure of the gravitational waves, as shown in the inset of Fig. 7.2, although we have not explored this aspect further.

The fluxes increase rapidly near each bifurcation point. This is because of our choice of normalization for X^μ in Eq. (7.49), which propagates into V^μ. To understand this, let us write as x^μ_c the spacetime coordinates of $\mathcal{S}_c$ that bifurcates, with foliation parameter $v = c$

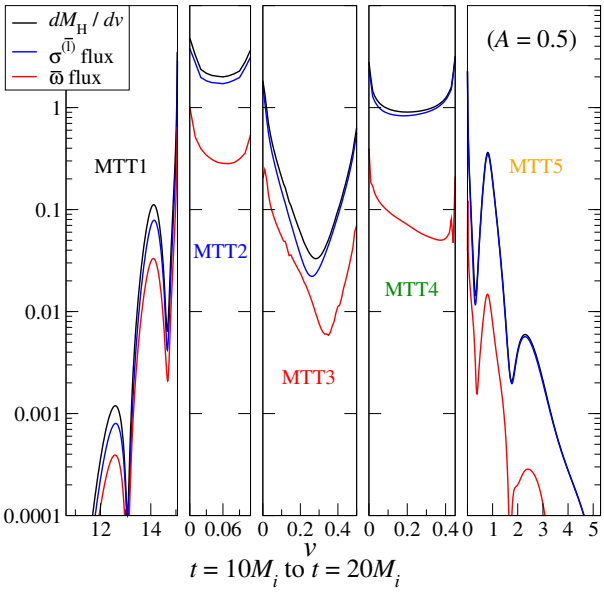

Figure 7.12: Terms in the dynamical horizon flux law of Eq. (7.47) plotted against the foliation parameter v along each section of $\mathcal{S}_v$. Along MTT1, we choose $v = t$. Along the other MTT sections, we choose $v = 0$ on the first $\mathcal{S}_v$ we find.

say. Then on a nearby $\mathcal{S}_v$, we can approximate $\partial x^i_v/\partial t$ by

$$\frac{\partial x^i_v}{\partial t} \approx \frac{\partial}{\partial t}\left(x^i_c \pm \lambda\sqrt{|t-t_c|}\right) = \pm\frac{\lambda}{2}\frac{1}{\sqrt{|t-t_c|}}, \tag{7.61}$$

where λ is some function. As $t \to t_c$, this quantity diverges as does the norm of V^μ, and leads to the higher values of the fluxes measured along V^μ. This singular behavior could be absorbed into a redefined foliation parameter $v' = v'(v)$. Also, any visible discontinuities in the fluxes across different sections of $\mathcal{H}$ in Fig. 7.12 are due to the difficulty in finding $\mathcal{S}_c$ exactly (as indicated by the data points in Fig. 7.5, even searching for MOTSs at every $\Delta t = 0.01$ is insufficient for this purpose).

7.5.5 Angular Momentum Flux Law

The angular momentum S defined in Eq. (7.48) depends on a choice of rotation vector ϕ^μ on $\mathcal{S}_v$. If $\mathcal{S}_v$ is axisymmetric, the natural choice of ϕ^μ is the axial Killing vector. In general spacetimes no such Killing vector exists, but one can nevertheless define a suitable ϕ^μ [62] by requiring it to have closed orbits, and be divergence-free

$$d_\mu \phi^\mu = 0. \tag{7.62}$$

This notion has been further refined to calculate approximate Killing vectors [29, 30] in black hole simulations, and we will make use of this choice here. They were also used to compute S of the initial data sets in section 7.2.

Gourgoulhon has generalized the Damour-Navier-Stokes equation for null hypersurfaces to trapping horizons and used it to derive a flux law for the change in S along a hypersurface $\mathcal{H}$ foliated by 2-surfaces $\mathcal{S}_v$ (not necessarily MOTSs) with foliation parameter v [21],

$$\begin{aligned}\frac{dS}{dv} =& -\int_{\mathcal{S}_v} T_{\mu\nu}\phi^\mu\tau^\nu\,\sqrt{\bar{q}}d^2x \qquad (7.63)\\ &-\frac{1}{16\pi}\int_{\mathcal{S}_v}\sigma^{(\tau)\mu\nu}\mathcal{L}_\phi\bar{q}_{\mu\nu}\,\sqrt{\bar{q}}d^2x\\ &+\int_{\mathcal{S}_v}\frac{1}{8\pi}\left[\theta_{(k)}\phi^\mu d_\mu C-\omega_\mu\mathcal{L}_V\phi^\mu\right]\,\sqrt{\bar{q}}d^2x\\ =& -\int_{\mathcal{S}_v} T_{\mu\nu}\phi^\mu\tau^\nu\,\sqrt{\bar{q}}d^2x \qquad (7.64)\\ &-\int_{\mathcal{S}_v}\frac{1}{8\pi}\left[B\sigma^{(l)}_{\mu\nu}\sigma^{(\phi)\mu\nu}+C\sigma^{(k)}_{\mu\nu}\sigma^{(\phi)\mu\nu}\right]\,\sqrt{\bar{q}}d^2x\\ &+\int_{\mathcal{S}_v}\frac{1}{8\pi}\left[\theta_{(k)}\phi^\mu d_\mu C-\omega_\mu\mathcal{L}_V\phi^\mu\right]\,\sqrt{\bar{q}}d^2x,\end{aligned}$$

where the vectors $V^\mu = Bl^\mu - Ck^\mu$ and $\tau^\mu = Bl^\mu + Ck^\mu$ are tangent and normal to $\mathcal{H}$, respectively. The first integral in Eq. (7.64) is the angular momentum flux due to matter. The second integral can be thought of as the flux due to gravitational radiation and vanishes if $\mathcal{S}_v$ is axisymmetric. In addition, it is usually required that ϕ^μ be Lie transported along the dynamical horizon,

$$\mathcal{L}_V\phi^\mu = 0, \qquad (7.65)$$

so that the last integral in Eq. (7.64) vanishes when $\mathcal{S}_v$ is an MOTS [21]. This requirement ensures that in the absence of matter and gravitational radiation, the angular momentum flux will be zero along an MTT as expected, instead of there being some physically unmeaningful flux simply due to measuring S about different axes.

Here we evaluate the angular momentum flux law for the dynamical horizon $\mathcal{H}$ found in section 7.5.3 for $A = 0.5$. Because we calculate S with ϕ^μ being an approximate Killing vector, Eq. (7.65) is not satisfied in general, and so we must keep the last integral in Eq. (7.64). We use the same tangent vector V^μ and foliation parameter v along each section of $\mathcal{H}$ as in section 7.5.4, and the null normals to $\mathcal{S}_v$ given in Eq. (7.29). The values of the terms in Eq. (7.64) are shown in Fig. 7.13 from $t = 10M_i$ to $t = 20M_i$. The first integral is neglected since $T_{\mu\nu} = 0$. The two terms in the second integral are labeled as

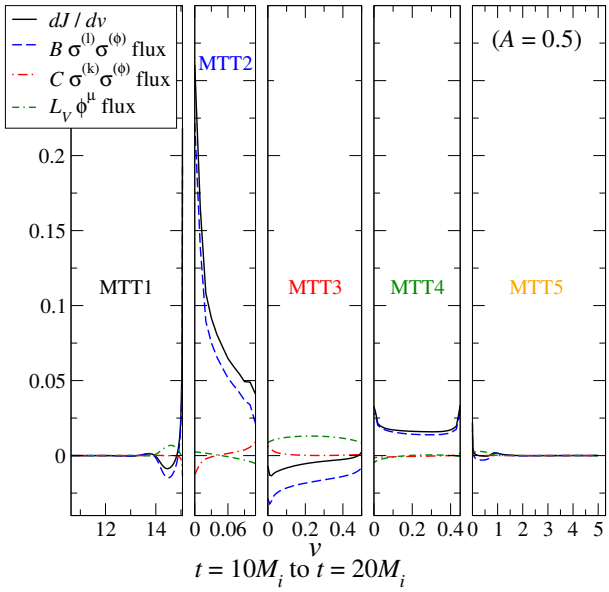

Figure 7.13: Terms in the angular momentum flux law of Eq. (7.64) plotted against the foliation parameter v along each section of $\mathcal{H}$. Along MTT1, we choose $v = t$. Along the other MTT sections, we choose $v = 0$ on the first $\mathcal{S}_v$ we find.

"$B\sigma^{(l)}\sigma^{(\phi)}$ flux" and "$C\sigma^{(k)}\sigma^{(\phi)}$ flux." The last integral is labeled as "$\mathcal{L}_V\phi^\mu$ flux." The angular momentum flux dS/dv is dominated by the flux associated with $B\sigma^{(l)}_{\mu\nu}\sigma^{(\phi)\mu\nu}$, due to the large $\sigma^{(l)}_{\mu\nu}$ produced by the gravitational waves. The magnitude of dS/dv vanishes initially, becomes largest along the end of MTT1 and the beginning of MTT2 when the gravitational waves reach the black hole, and settles back down to zero again along the successive MTT sections. Because dS/dv alternates sign along $\mathcal{H}$, the net change in S turns out to be small. The terms in the angular momentum flux law also diverge near each $\mathcal{S}_v$ that bifurcates into two MTTs, just like the terms in the dynamical horizon flux law in Fig. 7.12, and again is a consequence of our choice of V^μ as discussed at the end of section 7.5.4.

7.6 The Event Horizon

7.6.1 Basic Definitions and Concepts

The standard definition of the surface of a black hole is the *event horizon*, the boundary of the set of all points that are not in the causal past of future null infinity [7]. It is a null hypersurface, generated by null geodesics that have no future endpoints. As defined, the event horizon is a 3-surface, but it is common to refer to the intersection of this surface with

Σ_t as the event horizon as well. In contrast to an MOTS, the event horizon can only be found after the entire future history of the spacetime is known. Because of its teleological nature, the event horizon can behave nonintuitively. For instance, before a gravitational collapse has occurred an event horizon already forms, even though there is no flux of energy or angular momentum across it yet. In this section we describe our method of finding the event horizon, and contrast its properties with those of the MTTs found in section 7.5.

7.6.2 Event Horizon Finder

The event horizon is located in a spacetime by following geodesics backward in time. It is well known [5, 63] that null outgoing geodesics in the vicinity of the event horizon, when followed backwards in time, will converge onto the event horizon exponentially. Therefore, given a well-chosen congruence of geodesics, one can trace the event horizon of the spacetime with exponentially (in time) improving accuracy.

Our event horizon finder [64] tracks a set of geodesics backwards in time. The initial guess for the event horizon is chosen at some late time when the black hole is in a quasistationary state. At this time, the apparent horizon and event horizon coincide closely, and the apparent horizon is used as the initial guess. The initial direction of the geodesics is chosen to be normal to the apparent horizon surface, and the geodesics are integrated backwards in time. The geodesic equation requires values for the metric and its derivatives for each geodesic at each point in time. These values are obtained by interpolation from the values computed during the evolution. With an appropriate form of the geodesic equation, we can follow a geodesic as a function of coordinate time t, rather than the affine parameter along the geodesic.

7.6.3 Contrasting the Event Horizon with MTTs

We find the event horizon for the evolution in which the ingoing gravitational waves have the largest amplitude $A = 0.5$. The surface area $A_{\rm EH}$ of the event horizon is computed by integrating the metric induced on its surface by the spatial metric g_{ij}. The irreducible mass of the event horizon is then given as $M_{\rm EH} = \sqrt{A_{\rm EH}/16\pi}$. This is shown in Fig. 7.14, together with the irreducible mass $M_{\rm H}$ along the MTTs. An obvious difference is that $M_{\rm EH}$ always increases in time, and the event horizon does not bifurcate like the MTTs shortly after $t = 14M_i$. The event horizon is also already growing at the very beginning of the evolution, before the gravitational waves have hit the black hole. By $t = 14M_i$, the value of $M_{\rm EH}$ has almost doubled while $M_{\rm H}$ is still fairly close to its initial value. In fact, during

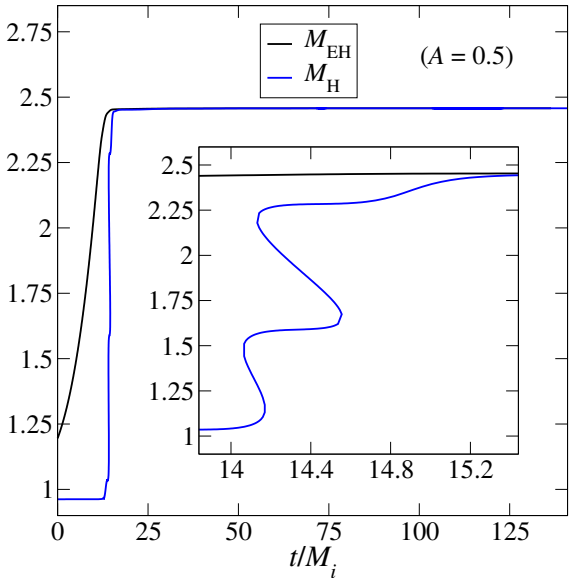

Figure 7.14: Irreducible masses of the event horizon $M_{\rm EH}$ and the MOTSs $M_{\rm H}$ during the evolution with $A = 0.5$. At the very beginning of the evolution $M_{\rm EH}$ is already increasing, while $M_{\rm H}$ is still fairly constant. As the inset shows, $M_{\rm EH}$ grows very slightly when $M_{\rm H}$ changes the most.

the time when multiple MTTs are present and one would intuitively expect the black hole to be the most distorted, the event horizon shows very little growth.

This peculiar behavior of the event horizon was also illustrated in [18] for the gravitational collapse of spherical dust shells, and explained with the null Raychaudhuri equation [17],

$$\frac{d\theta_{(l)}}{d\lambda} = -\frac{1}{2}\theta_{(l)}^2 - \sigma_{\mu\nu}^{(l)}\sigma^{(l)\mu\nu} - 8\pi T_{\mu\nu}l^\mu l^\nu, \tag{7.66}$$

where λ is an affine parameter along the congruence of null geodesics that generate the event horizon, with tangent vector l^μ. The area element $\sqrt{h}$ of the event horizon is related to the expansion $\theta_{(l)}$ by $d\sqrt{h}/d\lambda = \theta_{(l)}\sqrt{h}$, and substituting this into Eq. (7.66) gives

$$\frac{d^2\sqrt{h}}{d\lambda^2} = \left(\frac{1}{2}\theta_{(l)}^2 - \sigma_{\mu\nu}^{(l)}\sigma^{(l)\mu\nu} - 8\pi T_{\mu\nu}l^\mu l^\nu\right)\sqrt{h}. \tag{7.67}$$

In dynamical situations we will generally have $\theta_{(l)} \neq 0$ on the event horizon, and this accounts for its accelerated growth, which is evident even at early times in our evolution when the shear $\sigma_{\mu\nu}^{(l)}$ is negligible. When the pulse of gravitational waves hits the black hole, $\sigma_{\mu\nu}^{(l)}$ on the event horizon becomes large, and according to Eq. (7.67) this will decelerate its growth, even causing the growth to become very small in our case.

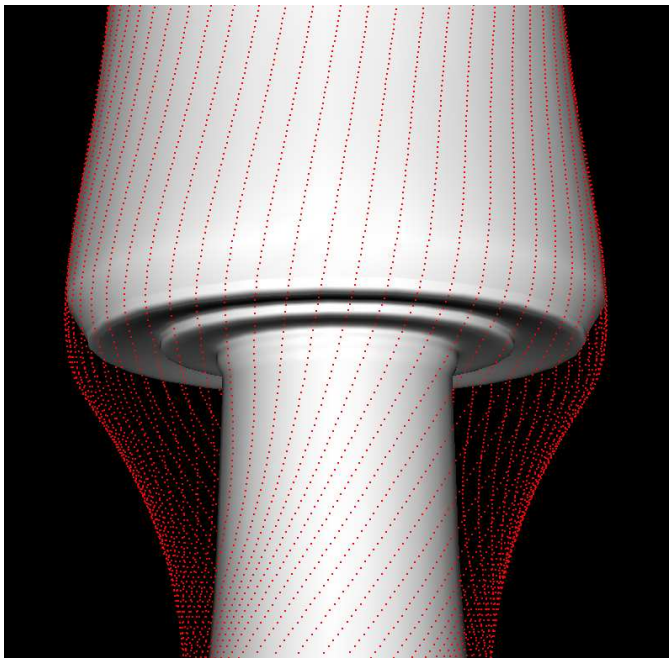

Figure 7.15: Spacetime diagram of the event horizon and dynamical horizons for $A = 0.5$. The dotted red lines are the null generators of the event horizon, while the solid grey surface represents the dynamical horizons.

At late times, the event and apparent horizons eventually coincide as both $\sigma^{(l)}_{\mu\nu}$ and $\theta_{(l)}$ go to zero on the event horizon while the apparent horizon becomes null. Finally, Fig. 7.15 shows a spacetime diagram of the event horizon and the dynamical horizon $\mathcal{H}$, with the spatial dimension along the $z-$direction suppressed. The null generators of the event horizon are shown as dotted red lines, and lie outside the solid grey surface of $\mathcal{H}$, except when they coincide at late times. In Fig. 7.15 the event horizon's cross section appears to be shrinking at late times. The constancy of the area of the event horizon (cf. Fig. 7.14) shows that this is merely a coordinate effect.

7.7 Discussion

In this chapter, we investigate marginally trapped tubes and the event horizon for rotating black holes distorted by a pulse of ingoing gravitational waves. For small distortions (low amplitude A), the simulations do not exhibit any unexpected behavior: the area of the apparent horizon is initially approximately constant, it grows when the gravitational radiation reaches the black hole, and then settles down to a constant value after the highly dynamical regime is over. However, for strong distortions, we find much more interesting

behaviors of the MOTSs. A new pair of MOTSs appears outside the original MOTS. These new surfaces are initially close together and move rapidly away from each other, indicating that at the critical time when they first appear they are coincident (although this particular event cannot be resolved in an evolution with finite time step). The inner surface of such a pair shrinks, eventually approaches the original MOTS, and then these two surfaces annihilate each other. For amplitude $A = 0.4$ this process happens once, for $A = 0.5$ this happens *twice*, and there is a short time interval during which *five* MOTSs are present in the simulation.

The MTTs traced out by the MOTSs are smooth, and appear to combine into one smooth hypersurface (although the critical points where different marginally trapped tubes combine with each other cannot be resolved). When the black hole is distorted, we find that this hypersurface is everywhere spacelike and a dynamical horizon. We investigate how the black hole grows by evaluating the dynamical horizon flux law of Ashtekar and Krishnan [15, 59], and find that the gravitational energy flux is largest across the sections of the dynamical horizon that decrease in cross-sectional area with increasing time. We also evaluate the angular momentum flux law of Gourgoulhon [21] along the dynamical horizon, but instead of using a rotation vector ϕ^μ that is Lie transported along the dynamical horizon, we use an approximate Killing vector [29], since we prefer to calculate the angular momentum itself in this way. The angular momentum flux law is based on the generalized Damour-Navier-Stokes equation, which treats the black hole as a viscous fluid. Evaluating the generalized Damour-Navier-Stokes equation itself could aid in developing physical intuition about black holes in numerical spacetimes.

In illustrating the procedure for finding multiple MOTSs, caution must be taken to locate the apparent horizon with MOTS finders when the MOTS found at a previous time is used as an initial guess. If the MOTS finder is not run frequently enough, new MOTSs will be missed and an erroneous apparent horizon will be identified. This raises the issue of whether the true apparent horizon was indeed located in similar work involving highly distorted black holes in the past (e.g., [3]). A better understanding of the slicing dependence of the MOTSs in our simulations would also be helpful in choosing a more natural slicing condition that gives a single dynamical horizon that only grows in the cross-sectional area with time in highly dynamical situations.

When computing the event horizon, we find it to be smooth, and enveloping the complicated structure of the MOTSs. As can be seen in Figs. 7.14 and 7.15, the event horizon is very close to the apparent horizon at late times, as one would expect. The motion of

the event horizon is restricted by the fact that it is foliated by null geodesics. Therefore, in order to encompass the MOTSs, the event horizon begins to grow much earlier, and even at the start of our simulation the event horizon is already considerably larger than the apparent horizon. At early times, $t \lesssim 10M_i$, the event horizon approaches the apparent horizon exponentially. The rate of approach should be given by the surface gravity of the initial black hole, but we have not verified this in detail, as our simulation does not reach sufficiently far into the past. This could be checked by placing the initial pulse of gravitational radiation at a larger distance from the black hole. The growth of the event horizon is described by the Hawking-Hartle formula [65], which may also be evaluated to give a more complete comparison of MTTs and the event horizon.

Our findings are analogous to the behavior of MOTSs and event horizons in the Vaidya spacetime, as worked out in detail in the appendix. In particular, for strong accretion, the Vaidya spacetime can also exhibit multiple MOTSs at the same time, all of which foliate dynamical horizons. Both in the Vaidya spacetime and our distorted Kerr spacetimes, the event horizon begins to grow much earlier before multiple MOTSs appear. By choosing a mass functions $m(v)$ that has two strong pulses of accretion, the Vaidya example in the appendix would also produce five concentric MOTSs similar to that seen in Fig. 7.5.

7.8 Appendix: Multiple horizons in the Vaidya spacetime

The ingoing Vaidya spacetime is a spherically symmetric spacetime describing a black hole that accretes null dust [66]. It shares similar features to the distorted Kerr spacetimes presented in this paper, which we mention here briefly. The ingoing Vaidya metric in ingoing Eddington-Finkelstein coordinates (v, r, θ, ϕ) is

$$ds^2 = -\left(1 - \frac{2m(v)}{r}\right) dv^2 + 2dvdr + r^2 d\Omega^2, \tag{7.68}$$

where $v = t + r$ is advanced time (not to be confused with the foliation parameter v of dynamical horizon in the main text). From the Einstein equations, the stress-energy tensor is

$$T_{\mu\nu} = \frac{dm/dv}{4\pi r^2} (\partial_\mu v)(\partial_\nu v). \tag{7.69}$$

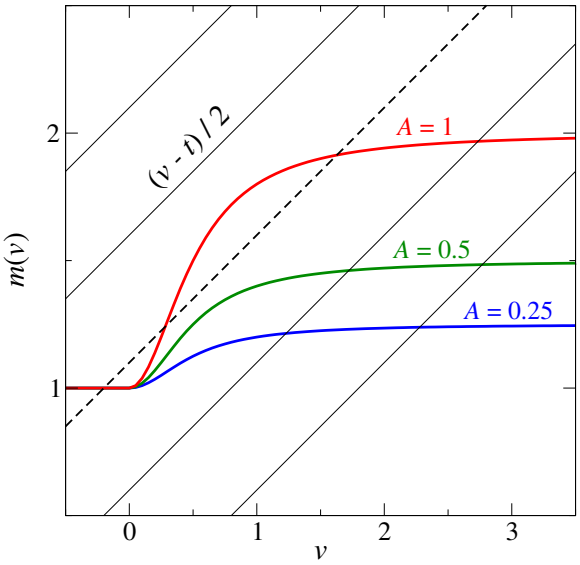

Figure 7.16: Mass functions $m(v)$ of the Vaidya spacetime for three amplitudes $A = 0.25, 0.5$, and 1, along with the straight lines $(v-t)/2$. MOTSs exist at the intersections of these functions. For $A = 0.5$ and 1, there are up to three intersections, as illustrated by the dashed black line which intersects the $A = 1$ mass curve three times.

With the choice of radial outgoing and ingoing null vectors

$$l^\mu = \left[1, \frac{1}{2}\left(1 - \frac{2m(v)}{r}\right), 0, 0\right] \quad \text{and} \quad k^\mu = (0, -1, 0, 0) \tag{7.70}$$

normalized so that $l^\mu k_\mu = -1$, the expansions of the null normals are

$$\theta_{(l)} = \frac{1}{r}\left(1 - \frac{2m(v)}{r}\right) \quad \text{and} \quad \theta_{(k)} = -\frac{2}{r}. \tag{7.71}$$

From this, we see that MOTSs are located at $r = 2m(v)$, or

$$m(v) = \frac{1}{2}(v - t). \tag{7.72}$$

The number of solutions to Eq. (7.72), i.e., the number of MOTSs, can be conveniently discussed with the diagram shown in Fig. 7.16. The thick solid lines represent three different mass functions[1] $m(v)$ plotted vs. v. The right-hand side of Eq. (7.72) is a family of straight lines (one for each t) represented by the thin diagonal lines in Fig. 7.16. For a given t, the number of intersections between the $(v-t)/2$ and the $m(v)$ curve gives the number of MOTSs at that particular t. The straight line $\frac{1}{2}(v-t)$ has slope $1/2$, so if $dm/dv < 1/2$ for

[1] These correspond to Eq. (7.77) with the different parameters described below it.

all v, then there will be exactly one intersection[2] for every t. If

$$\frac{dm}{dv} > \frac{1}{2} \qquad \text{for some } v, \tag{7.73}$$

then the $m(v)$ curve will have regions that are steeper than the straight line. By adjusting the vertical intercept of the straight line, equivalent to choosing a suitable t, the straight line will pass through a point with $dm/dv > 1/2$. At this point, $m(v)$ passes from below to above the straight line, so there must be an additional intersection at both smaller and larger v, for a total of three MOTSs. Thus, sufficiently rapid mass accretion (large dm/dv) results in multiple MOTSs.

The signature of a spherically symmetric MTT depends on the sign of [19]

$$C = \frac{T_{\mu\nu} l^\mu l^\nu}{1/(2A_{\mathrm{H}}) - T_{\mu\nu} l^\mu k^\nu}, \tag{7.74}$$

where A_{H} is the cross-sectional area of the MTT. The MTT is spacelike if $C > 0$, null if $C = 0$, and timelike if $C < 0$. From Eq. (7.69) and Eq. (7.70),

$$T_{\mu\nu} l^\mu l^\nu = \frac{dm/dv}{4\pi r^2} \quad \text{and} \quad T_{\mu\nu} l^\mu k^\nu = 0, \tag{7.75}$$

so we see that $C > 0$ for the Vaidya spacetime as long as $dm/dv > 0$. Furthermore, since $\theta_{(k)} < 0$, these MTTs will also be dynamical horizons.

The event horizon is generated by radial outgoing null geodesics satisfying

$$\frac{dr}{dv} = \frac{1}{2}\left(1 - \frac{2m(v)}{r}\right). \tag{7.76}$$

Integrating this differential equation requires knowledge of the event horizon location at some point. This is usually supplied by the final state of the black hole, when accretion has ended.

To close, we illustrate these considerations with a concrete example. We choose the mass function

$$m(v) = \begin{cases} m_0, & v \le 0 \\ m_0 + \dfrac{A m_0 v^2}{v^2 + W^2}, & v > 0 \end{cases} \tag{7.77}$$

similar to that presented in [67] (Am_0 is the mass accreted by the black hole, and W determines the time scale of accretion). We set $m_0 = 1$, $W = 0.5$, and consider three

[2] Assuming $m(v)$ is nondecreasing, and has finite bounds for $v \to \pm\infty$.

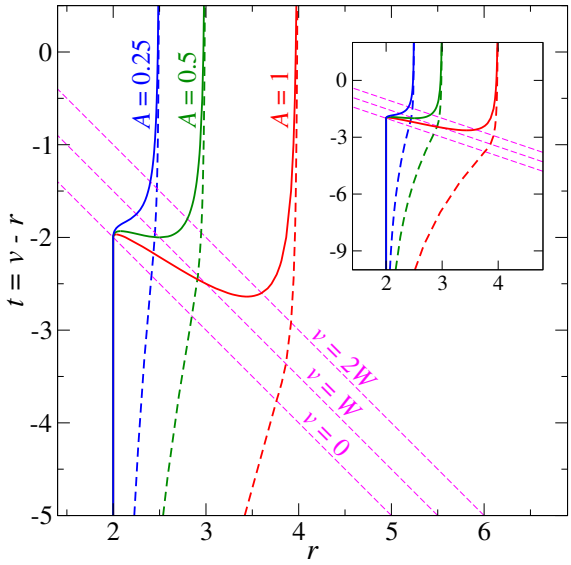

Figure 7.17: Locations of MOTSs (solid lines) and event horizons (dashed lines) in the Vaidya spacetime. For $A = 0.25$ there is one MOTS at all times. For $A = 0.5$ and 1, up to three MOTSs exist at a time t. The event horizons approach the MTTs at very early and late times, and start growing much earlier than the MTTs. The inset shows a larger interval in t.

different amplitudes $A = 0.25, 0.5$, and 1. Figure 7.16 shows the respective mass functions, and we see that $A = 0.25$ never leads to multiple MOTSs, while $A = 1$ clearly exhibits three MOTSs for certain t. It is easy to show that Eq. (7.73) implies $Am_0 > 4W/(3\sqrt{3})$. The locations of the MOTSs in (r, t) coordinates are shown in Fig. 7.17. For $A = 0.25$, there is only one MOTS at all times. For $A = 0.5$, there are up to three MOTSs at a single time. A new MOTS appears at $r = 2.5$ immediately after $t = -2$, and bifurcates into two MTTs. One of these MTTs shrinks and annihilates with the innermost MTT at $t = -1.93256$, while only the outermost MTT remains at late times and grows toward $r = 3$. For $A = 1$, there are again up to three MOTSs at a single time, but a new MOTS appears earlier at $t = -2.63822$. After $t = -1.96824$, only one MOTS remains and grows toward $r = 4$. Also shown in Fig. 7.17 are lines of constant v indicating when accretion begins ($v = 0$), and when $m(v)$ has increased by 50% and 80%, respectively ($v = W$ and $v = 2W$).

The event horizons for the three cases are computed by integrating Eq. (7.76) *backward* in time, starting with $r_{\rm EH}(v \to \infty) = 2(1 + A)m_0$. The resulting surfaces are shown as the dashed curves in Fig. 7.17. The event horizon is located at $r = 2$ in the far past, starts growing long before $m(v)$ increases, and asymptotically approaches the MTT of the final black hole for all amplitudes A.

Bibliography

[1] D. Bernstein, D. Hobill, E. Seidel, and L. Smarr, Phys. Rev. D **50**, 3760 (1994).

[2] K. S. Thorne, in *Magic Without Magic; John Archibald Wheeler*, edited by J. Klauder, Frieman, San Francisco, 1972.

[3] P. Anninos et al., Phys. Rev. D **50**, 3801 (1994).

[4] S. R. Brandt and E. Seidel, Phys. Rev. D **52**, 870 (1995).

[5] P. Anninos et al., Phys. Rev. Lett. **74**, 630 (1995).

[6] S. W. Hawking and G. F. R. Ellis, *The large scale structure of space-time*, Cambridge University Press, Cambridge, England, 1973.

[7] R. M. Wald, *General Relativity*, University of Chicago Press, Chicago and London, 1984.

[8] R. Penrose, Phys. Rev. Lett. **14**, 57 (1965).

[9] S. A. Hayward, Phys. Rev. D **49**, 6467 (1994).

[10] S. A. Hayward, Phys. Rev. Lett. **93**, 251101 (2004).

[11] A. Ashtekar, C. Beetle, and S. Fairhurst, Class. Quantum Grav. **17**, 253 (2000).

[12] A. Ashtekar et al., Phys. Rev. Lett. **85**, 3564 (2000).

[13] A. Ashtekar, C. Beetle, and J. Lewandowski, Phys. Rev. D **64**, 044016 (2001).

[14] A. Ashtekar and B. Krishnan, Phys. Rev. Lett. **89**, 261101 (2002).

[15] A. Ashtekar and B. Krishnan, Phys. Rev. D **68**, 104030 (2003).

[16] A. Ashtekar and G. J. Galloway, Advances in Theoretical and Mathematical Physics **9**, 1 (2005).

[17] E. Poisson, *A Relativist's Toolkit: The Mathematics of Black-Hole Mechanics*, Cambridge University Press, 2004.

[18] I. Booth, Can. J. Phys. **83**, 1073 (2005).

[19] I. Booth, L. Brits, J. A. Gonzalez, and C. V. D. Broeck, Class. Quantum Grav. **23**, 413 (2006).

[20] E. Schnetter, B. Krishnan, and F. Beyer, Phys. Rev. D **74**, 024028 (2006).

[21] E. Gourgoulhon, Phys. Rev. D **72**, 104007 (2005).

[22] H. P. Pfeiffer, L. E. Kidder, M. A. Scheel, and D. Shoemaker, Phys. Rev. D **71**, 024020 (2005).

[23] R. Arnowitt, S. Deser, and C. W. Misner, The dynamics of general relativity, in *Gravitation: An Introduction to Current Research*, edited by L. Witten, Wiley, New York, 1962.

[24] J. W. York, Jr., Kinematics and dynamics of general relativity, in *Sources of Gravitational Radiation*, edited by L. L. Smarr, pages 83–126, Cambridge University Press, Cambridge, England, 1979.

[25] S. A. Teukolsky, Phys. Rev. D **26**, 745 (1982).

[26] O. Rinne, Class. Quantum Grav. **26**, 048003 (2009).

[27] H. P. Pfeiffer, L. E. Kidder, M. A. Scheel, and S. A. Teukolsky, Comput. Phys. Commun. **152**, 253 (2003).

[28] C. Gundlach, Phys. Rev. D **57**, 863 (1998).

[29] G. Lovelace, R. Owen, H. P. Pfeiffer, and T. Chu, Phys. Rev. D **78**, 084017 (2008).

[30] G. B. Cook and B. F. Whiting, Phys. Rev. D **76**, 041501(R) (2007).

[31] S. W. Hawking, J. Math. Phys. **9**, 598 (1968).

[32] M. A. Scheel et al., Phys. Rev. D **74**, 104006 (2006).

[33] `http://www.black-holes.org/SpEC.html`.

[34] L. Lindblom, M. A. Scheel, L. E. Kidder, R. Owen, and O. Rinne, Class. Quantum Grav. **23**, S447 (2006).

[35] H. Friedrich, Commun. Math. Phys. **100**, 525 (1985).

[36] D. Garfinkle, Phys. Rev. D **65**, 044029 (2002).

[37] F. Pretorius, Class. Quantum Grav. **22**, 425 (2005).

[38] O. Rinne, Class. Quantum Grav. **23**, 6275 (2006).

[39] O. Rinne, L. Lindblom, and M. A. Scheel, Class. Quantum Grav. **24**, 4053 (2007).

[40] J. M. Stewart, Class. Quantum Grav. **15**, 2865 (1998).

[41] H. Friedrich and G. Nagy, Commun. Math. Phys. **201**, 619 (1999).

[42] J. M. Bardeen and L. T. Buchman, Phys. Rev. D **65**, 064037 (2002).

[43] B. Szilágyi, B. Schmidt, and J. Winicour, Phys. Rev. D **65**, 064015 (2002).

[44] G. Calabrese, J. Pullin, O. Reula, O. Sarbach, and M. Tiglio, Commun. Math. Phys. **240**, 377 (2003).

[45] B. Szilágyi and J. Winicour, Phys. Rev. D **68**, 041501(R) (2003).

[46] L. E. Kidder, L. Lindblom, M. A. Scheel, L. T. Buchman, and H. P. Pfeiffer, Phys. Rev. D **71**, 064020 (2005).

[47] L. T. Buchman and O. C. A. Sarbach, Class. Quantum Grav. **23**, 6709 (2006).

[48] L. T. Buchman and O. C. A. Sarbach, Class. Quantum Grav. **24**, S307 (2007).

[49] D. Gottlieb and J. S. Hesthaven, J. Comput. Appl. Math. **128**, 83 (2001).

[50] J. S. Hesthaven, Appl. Num. Math. **33**, 23 (2000).

[51] T. Nakamura, Y. Kojima, and K. ichi Oohara, Phys. Lett. **106A**, 235 (1984).

[52] K. P. Tod, Class. Quantum Grav. **8**, L115 (1991).

[53] T. W. Baumgarte, G. B. Cook, M. A. Scheel, S. L. Shapiro, and S. A. Teukolsky, Phys. Rev. D **54**, 4849 (1996).

[54] H. P. Pfeiffer, S. A. Teukolsky, and G. B. Cook, Phys. Rev. D **62**, 104018 (2000).

[55] H. P. Pfeiffer, G. B. Cook, and S. A. Teukolsky, Phys. Rev. D **66**, 024047 (2002).

[56] A. Ashtekar, C. Beetle, and S. Fairhurst, Class. Quantum Grav. **16**, L1 (1999).

[57] A. Ashtekar, S. Fairhurst, and B. Krishnan, Phys. Rev. D **62**, 104025 (2000).

[58] A. Ashtekar and B. Krishnan, Living Rev. Rel. **7** (2004), 10.

[59] I. Booth and S. Fairhurst, Phys. Rev. D **75**, 084019 (2007).

[60] I. Booth and S. Fairhurst, Phys. Rev. D **77**, 084005 (2008).

[61] S. Hayward, Class. Quantum Grav. **23**, L15 (2006).

[62] I. Booth and S. Fairhurst, Class. Quantum Grav. **22**, 4515 (2005).

[63] J. Libson et al., Phys. Rev. **D53**, 4335 (1996).

[64] M. Cohen, H. P. Pfeiffer, and M. A. Scheel, Class. Quant. Grav. **26**, 035005 (2009).

[65] S. W. Hawking and J. B. Hartle, Commun. Math. Phys. **27**, 283 (1972).

[66] P. C. Vaidya, Phys. Rev. **83**, 10 (1951).

[67] E. Schnetter and B. Krishnan, Phys. Rev. D **73**, 021502(R) (2006).